

**SCHOOL OF ELECTRONICS, ELECTRICAL AND SYSTEMS  
ENGINEERING**

**INTERNAL MODEL CONTROL (IMC) DESIGN FOR A STALL-REGULATED  
VARIABLE-SPEED WIND TURBINE SYSTEM**

**By**

**Norzanah Rosmin**

**A Doctoral Thesis**

Submitted in partial fulfilment  
of the requirements for the award of

**Doctor of Philosophy**  
**of**  
**Loughborough University**

February 2015

Copyright 2015 Norzanah Rosmin



## Contents

Thesis Access Conditions and Deposit Agreement	i
Figures in text	vi
Tables in text	x
Abstract	xi
Acknowledgement	xii
Used Acronyms/Abbreviations	xiii
Used Symbols	xv
<b>1 Introduction..... 1</b>	<b>1</b>
1.1 Introduction to Wind Energy Conversion System..... 1	1
1.2 Approaches to Improve Power Control Performance ..... 6	6
1.2.1 Fixed Speed Operation ..... 6	6
1.2.2 Variable Speed Operation ..... 11	11
1.3 Background of the Study ..... 19	19
1.4 Research Objectives ..... 23	23
1.5 Scope of the Study ..... 23	23
1.6 Major Contributions..... 24	24
1.7 Thesis Layout..... 26	26
<b>2 SRVSWT with Stator-Controlled SCIG ..... 27</b>	<b>27</b>
2.1 SRVSWT with Fully-Rated Power Converter Control ..... 27	27
2.2 SRVSWT Control Aims and Strategies ..... 29	29
2.2.1 SCIG-based SRVSWT Control Aims ..... 29	29
2.2.2 SCIG-based SRVSWT Control Strategies ..... 43	43
2.3 Description of SCIG-based SRVSWT ..... 48	48
2.3.1 SCIG Steady-state Model ..... 48	48
2.3.2 The SCIG Dynamic d-q Model ..... 53	53
2.3.3 SCIG State-space Equation Dynamic Model ..... 57	57
2.4 Chapter Summary ..... 61	61

3	Description and Validation of Wind Energy Conversion System (WECS) Modelling .....	<b>62</b>
3.1	Wind Energy Conversion System (WECS) Modeling.....	62
3.1.1	Wind Speed Dynamics Model.....	64
3.2	Aerodynamic Model .....	70
3.3	Drivetrain Model .....	72
3.3.1	Estimation of the Drivetrain Parameter .....	77
3.4	Induction Generator and Full-Rated Power Converter Model .....	79
3.4.1	Estimation of the Generator Parameter .....	87
3.5	Summary of Wind Turbine Data/Parameter .....	90
3.6	Validation of the Fixed-Speed SRWT Simulation Model .....	91
3.6.1	Validation of Turbine Operation at 50 Hz .....	92
3.6.2	Validation of Turbine Operation at 43.5 Hz .....	99
3.6.3	Details of the Fixed-speed SRWT Control .....	103
3.7	Chapter Summary .....	108
4	Description of Controllers, Tuning Procedure and Performance Index .....	<b>109</b>
4.1	Chapter Overview .....	109
4.2	Description of Controllers .....	109
4.2.1	Indirect Vector Control .....	114
4.2.2	Testing Models.....	119
4.3	Controller Tuning Procedure .....	123
4.3.1	I/O Pairing Using the RGA Approach .....	124
4.4	Proportional (P) and Integral (I) Parameter Tuning Method .....	128
4.4.1	Ziegler-Nichols (M1) .....	129
4.4.2	Tyreus and Luyben (M2) .....	130
4.4.3	IMC-PI (M3) .....	130
4.4.4	IMC-PI-IP (M4).....	136
4.5	Performance Index.....	138
4.5.1	Robustness Measure .....	139
4.5.2	Performance Measure .....	140

4.6	Chapter Summary .....	141
<b>5</b>	<b>Results and Discussion.....</b>	<b>142</b>
5.1	Chapter Overview .....	142
5.2	Results of the Proposed Tuning Methods .....	142
	5.2.1 Step Change Performance Assessment.....	143
	5.2.2 Dynamic Performance Assessment.....	152
5.3	Results for the Proposed Control Strategies during Intermediate Load (IL).....	166
5.4	Results for the Indirect Vector Control (IVC) and Sensorless Indirect Vector Control (SLIVC) Model Algorithms .....	169
5.5	Chapter Summary .....	172
<b>6</b>	<b>Conclusions, Contributions to Knowledge and Suggestions for Future Studies .....</b>	<b>173</b>
6.1	Chapter Overview .....	173
6.2	Conclusions.....	173
6.3	Suggestions for Future Studies .....	179
	<b>APPENDIXES .....</b>	<b>181</b>
	<b>LIST OF PUBLICATIONS.....</b>	<b>182</b>
	<b>REFERENCES.....</b>	<b>184</b>

## Figures and tables in text

### Figures in text

Figure 1-1 Electrical conversion concepts of the typical power converter arrangements of a modern variable speed wind turbine: (a) reduce-rated back-to-back power converter (b) half-rated back-to-back power converter	2
Figure 1-2 Typical configuration of a fixed-pitch variable-speed wind turbine with a fully-rated converter	5
Figure 1-3 Control strategy on SRWT	7
Figure 1-4 The aerodynamic power versus rotor speed, for different wind speeds	7
Figure 1-5 Control strategy on SRVSWT: (a) power versus wind speed, (b) power versus rotor speed	14
Figure 1-6 SRVSWT strategies during partial and full loads	16
Figure 2-1 $C_p - \lambda$ curve	32
Figure 2-2 Control aims and laws for the proposed SCIG-based SRVSWT system	34
Figure 2-3 The aerodynamic power versus wind speed, with various efficiencies	36
Figure 2-4 Forces on a blade element	40
Figure 2-5 Per-phase equivalent circuit of a SCIG with respect to the stator	49
Figure 2-6 Stationary frame a-b-c to $d^s - q^s$ axes transformation	55
Figure 2-7 Transformation of stationary frame $d^s - q^s$ into synchronously rotating frame $d^e - q^e$	56
Figure 2-8 Dynamic or d-q equivalent circuit of an induction generator	58
Figure 3-1 (a) Installed 25 kW Carter wind turbines with close-up, (b) Turbine control panels	63
Figure 3-2 Structure of the Wind Turbine Modelling System	64
Figure 3-3 Annual wind speed at West Beacon Farm based on the Rayleigh distribution	65
Figure 3-4 Equivalent wind speed simulation model	67

Figure 3-5 (a) white noise signal, (b) gust/turbulence signal, (c) equivalent or instantaneous velocity signal (d) modified equivalent or instantaneous velocity signal for all wind speed conditions	69
Figure 3-6 The SIMULINK model of the aerodynamic model	70
Figure 3-7 Power coefficient versus tip speed ratio ( $C_p - \lambda$ )	71
Figure 3-8 Equivalent drivetrain model	72
Figure 3-9 The SIMULINK model of the drivetrain	76
Figure 3-10 Dynamic interaction diagram between the SCIG and the full-rated power converter	79
Figure 3-10 The MATLAB/SIMULINK model of the power converter	74
Figure 3-11 (a) The MATLAB/SIMULINK model of the power converter, (b) Simplified flux control, and (c) Simplified current (torque) control	80
Figure 3-12 (a) Rotor field-oriented SCIG model (b) d-q decoupling by state feedback plus decoupling terms	82
Figure 3-13 The MATLAB/SIMULINK model of the SCI	84
Figure 3-14 Components of the MATLAB/SIMULINK SCIG model: (a) mechanical speed (b) rotor flux (c) d-axis stator current (d) q-axis stator current	85
Figure 3-15 (a) Components of the MATLAB/SIMULINK SCIG model: Block C, (b) Components of the MATLAB/SIMULINK SCIG model: Block D	86
Figure 3-16 Power flow in a three-phase induction motor	87
Figure 3-17 Equivalent circuit of a three-phase induction motor	88
Figure 3-18 (a) Power versus wind speed (b) ramp wind speed (c) realistic wind speed	93
Figure 3-19 $C_p - \lambda$ curves with and without the stall modification	95
Figure 3-20 Power versus wind speed after the stall modification for high winds	97
Figure 3-21 (a) $C_p - \lambda$ curve, (b) $\lambda$ - wind speed curve, (c) torque - speed curve, (d) power - speed curve	98
Figure 3-22 Power versus wind speed after the stall modification at an operating frequency at 43.5 Hz	100

Figure 3-23 (a) Power vs. generator speed, (b) torque vs. generator speed, (c) phase current vs. wind speed ( $f = 43.5$ Hz), (d) phase current vs. wind speed ( $f = 50$ Hz)	101
Figure 3-24 Snapshot current vs wind speed (a) at $t = 3$ to 3.5 seconds ( $f=43.5$ Hz) (b) at $t = 13$ to 13.5 seconds ( $f=43.5$ Hz ) (c) at $t = 3$ to 3.5 seconds ( $f=50$ Hz) (d) at $t = 13$ to 13.5 seconds ( $f=50$ Hz )	102
Figure 3-25 Schematic diagram of the fixed-speed SRWT control system	103
Figure 3-26 Graphs of power spectral density versus vibration frequency of the Carter wind turbine (a) taken from [131,153] (b) taken from [115]	104
Figure 3-27 Generated electrical power, flux, stator current and speed responses when the fixed-speed SRWT system model is controlled by the $\psi_{dr}$ flux controller, the $I_{qs}$ current controller and the speed controller	107
Figure 4-1 Vector control steady-state phasor: (a) Torque component of current control and (b) Flux component of current control	112
Figure 4-2 Implementation of transformation and inverse transformation of vector control in a machine	114
Figure 4-3 (a) Standard indirect vector control for IVC (b) The classical design control loop for standard indirect vector control	121
Figure 4-4 SRVSWT with the SLIVC method [136]	123
Figure 4-5 MIMO model of the SRVSWT system	124
Figure 4-6 Step response of a FOPTD system and the graphical construction used to estimate the FOPTD parameters	125
Figure 4-7 Step response of a FOPTD system and the graphical construction used to estimate the FOPTD parameters [168]: (a) Obtaining $\lambda_{open}$ and (b) Obtaining $\lambda_{closed}$	127
Figure 4-8 (a) Classical feedback structure and (b) IMC structure	131
Figure 4-9 Configuration of a typical cascade system	134
Figure 4-10 Block diagram with I-P controller	136
Figure 4-11 Sustained periodic oscillation signal	138
Figure 4-12 Graphical interpretation of the sensitivity function from the Nyquist curve	140
Figure 5-1 Step change response at the set point	145
Figure 5-2 Disturbance response at the input plant	148

Figure 5-3 Comparison between high-order model and the FOPTD model	150
Figure 5-4 Different output signals based on different values of the controller tuning parameter $\varepsilon$	151
Figure 5-5 The sustained periodic oscillation signal for $\varepsilon = 0.22$	151
Figure 5-6 The SRVSWT behaviour in a realistic wind speed profile: (a) the realistic wind speed profile, (b) the generator mechanical speed, (c) the power coefficient, and (d) the tip-speed ratio	153
Figure 5-7 The SRVSWT behaviour in the low wind speed region: (a) the realistic wind speed profile, (b) the generator mechanical speed, (c) the power coefficient, and (d) the tip speed ratio	154
Figure 5-8 The SRVSWT behaviour in the medium wind speed region: (a) the realistic wind speed profile, (b) the generator mechanical speed, (c) the power coefficient, and (d) the tip speed ratio	155
Figure 5-9 The behaviour of the SRVSWT in the high wind speed region: (a) the realistic wind speed profile, (b) the generator mechanical speed, (c) the power coefficient, and (d) the tip speed ratio	156
Figure 5-10 The behaviour of the SRVSWT in a realistic wind speed profile: (a) the dq-stator voltage, (b) the stator voltage, (c) the dq-stator current, and (d) the stator current	158
Figure 5-11 The behaviour of the SRVSWT in a realistic wind speed profile: (a) the generated torque, (b) the generated power, (c) the rotor flux, and (d) the stator angular frequency	161
Figure 5-12 Generated torque versus wind speed	162
Figure 5-13 Generated power versus wind speed	163
Figure 5-14 Generated power versus mechanical rotor speed	164
Figure 5-15 The mechanical rotor speed strategies: constant speed (CS) and modified power tracking (MoPT)	166
Figure 5-16 The control performance of the SRVSWT system using CS and MoPT strategies: (a) power-wind speed curve and (b) power-angular mechanical rotor speed curve	167
Figure 5-17 The control performance of the SRVSWT system using the CS and MoPT strategies: (a) torque-wind speed curve and (b) torque-angular mechanical rotor speed curve	168
Figure 5-18 'Power-wind speed' curve: (a) SLVC and (b) IVC	170
Figure 5-19 'Power-wind speed' curve: (a) IMC-PI and (b) IMC-PI-IP	171

## Tables in text

Table 1-1 Summary of research attempted on SRVSWT considering the control strategy for each wind speed region, the adopted controller, the technique and the generator employed	18
Table 3-1 Drive parameters	87
Table 3-2 Wind Turbine Characteristics	91
Table 3-3 Details of the new tip speed ratio and power coefficient	97
Table 4-1 Summary of the differences among the designs of IVC	116
Table 4-2 Tuning of PID controller parameters according to the ZN method	130
Table 4-3 Tuning of PID controller parameters according to the TL method	130
Table 5-1 Performance measures for the ZN, TL and IMC-PI tuning rules	143
Table 5-2 Details of the tuning parameters for the Ziegler-Nichols and Tyreus-Luyben tuning procedures	144
Table 5-3 Details of the tuning parameters and the FOPTD model for the IMC-PI and IMC-PI-IP tuning rules	144
Table 5-4 Details of the transient response for the ZN, TL, IMC-PI and IMC-PI-IP tuning rules	146
Table 5-5 Details of the high-order and reduced-order model transfer function for the MIMO plant	149

# Abstract

A stall-regulated wind turbine with fixed-speed operation provides a configuration which is one of the cheapest and simplest forms of wind generation and configurations. This type of turbine, however, is non-optimal at low winds, stresses the component structure and gives rise to significant power peaks during early stall conditions at high wind speeds. These problems can be overcome by having a properly designed generator speed control. Therefore, to track the maximum power locus curve at low winds, suppress the power peaks at medium winds, limit the power at a rated level at high winds and obtain a satisfactory power-wind speed curve performance (that closely resembles the ideal power-wind speed curve) with minimum stress torque simultaneously over the whole range of the wind speed variations, the availability of active control is vital. The main purpose of this study is to develop an internal model control (IMC) design for the squirrel-cage induction generator (SCIG), coupled with a full-rated power converter of a small (25 kW), stall-regulated, variable-speed wind-turbine (SRVSWT) system, which is subject to variations in the generator speed, electromagnetic torque and rotor flux. The study was done using simulations only. The objective of the controller was to optimise the generator speed to maximise the active power generated during the partial load region and maintain or restrict the generator speed to reduce/control the torque stress and the power-peaking between the partial and full load regions, before power was limited at the rated value of 25 kW at the full load region. The considered investigation involved estimating the proportional-integral (PI) and integral-proportional (IP) controllers' parameter values used to track the stator-current producing torque, the rotor flux and the angular mechanical generator speed, before being used in the indirect vector control (IVC) and the sensorless indirect vector control (SLIVC) model algorithms of the SCIG system. The design of the PI and IP controllers was based on the fourth-order model of the SCIG, which is directly coupled to the full-rated power converter through the machine stator, whereas the machine rotor is connected to the turbine rotor via a gearbox. Both step and realistic wind speed profiles were considered. The IMC-based PI and IP controllers (IMC-PI-IP) tuning rule was proven to have smoothed the power curve and shown to give better estimation results compared to the IMC-based PI controllers (IMC-PI), Ziegler-Nichols (ZN) and Tyreus-Luyben (ZN) tuning rules. The findings also showed that for the SRVSWT system that employed the IVC model algorithm with the IMC-PI-IP tuning rule, considering the application of a maintained/constant speed (CS) strategy at the intermediate load region is more profitable than utilizing SRVSWT with the modified power tracking (MoPT) strategy. Besides that, the finding also suggested that, for the IMC-PI-IP approach, the IVC does provide better power tracking performance than the SLIVC model algorithm.

# Acknowledgements

First of all, I would like to express my gratitude to all those who have given me support and strength to complete this thesis.

I am deeply indebted to my supervisor: Professor Dr Simon. J. Watson for his guidance, advice, encouragement and patience in supervising this research. His positive thinking, very understanding, very kind-hearted, belief and willingness to support me in completing this research and thesis are very much appreciated.

My appreciation goes to my sponsor Universiti Teknologi Malaysia (UTM) and the Ministry of Higher Education (MOHE) for giving me the opportunity to have full scholarships to further my study abroad.

To my dear parents Hj Rosmin and Hajjah Alminah, my father and mother in-law, Hj Musta'amal and Zaharah, my brothers, my sisters, my nieces, my nephews and all my relatives who constantly pray for my success, special thanks goes to all of you.

To the people that are very important to my life, to my husband, Dr Aede Hatib Musta'amal, for his endless love, unparalleled patience, understanding and unwavering support, and my wonderful children, Muhammad Aqil Fathulah, Muhammad Nabil Wajihuddin, Muhammad Arif Fakhrullah, Nur Hajidah Aqilah, Muhammad Warid Waquiuddin and my new born little princess Nur Qisya Humaira, I am grateful to have all of you as my family.

To all who have helped me, Dr Hanan, Dr John Barton, Dr Murray, Dr Hazlina, Dr Norhaliza, Dr Yusri, Dr Sazalinsyah, Mashanum, Faridah, and many more than can be mentioned, I will be forever grateful and perpetually indebted to you. Thank you.

# Used Abbreviations

AC	Alternate current
APOC	Active power optimal control
CPS	Constant power strategy
CS	Constant speed
DC	Direct Current
DFIG	Doubly-fed Induction Generator
DVC	Direct vector control
FL	Full load
FOPTD	First order plus time delay
GSC	Generator-side converter
HAWT	Horizontal-axis wind turbine
I	Integral
IAE	Integral absolute error
IG	Induction Generator
IL	Intermediate load
IMC	Internal model control
IMC-PI	IMC model-based employing PI controllers
IMC-PI-IP	IMC model-based employing PI and IP controllers
IP	Integral-proportional
IVC	Indirect vector control
LPV	Linear Parameter-Varying
LQ	Linear quadratic
LQG	Linear quadratic Gaussian
MIMO	Multiple-input multiple-output
MoPT	Modified power tracking
MPPT	maximum power point tracking
NM	Not mentioned
NSC	Network-side converter
OP	Operating point
ORC	Optimal rotor control
P	Proportional
PI	Proportional-integral
PL	Partial load
PM	Permanent magnet
PM	Phase margin
PWM	Pulse width modulation
RE	Renewable energy
RGA	Relative gain array
RHP	Right half plane
RSOC	Rotational speed optimal control

SC	Scalar control
SCIG	Squirrel-cage induction generator
SLIVC	Sensorless indirect vector control
SR	Switch Reluctance
SRVSWT	Stall-regulated (fixed-pitch) variable speed wind turbine
SRWT	Stall-regulated wind turbine
TL	Tyreus-Luyben
TSR	Tip speed ratio
TV	Total variation
V&V	Verification and validation
VAWT	Vertical-axis wind turbine
VC	Vector control
WECS	Wind energy conversion system
ZN	Ziegler-Nichols

## Used symbols

$a$	Axial induction factor
$a'$	Angular induction factor
$A$	Area
$\alpha$	Angle of attack
$\beta$	Pitch angle
$B$	Beta function
$B$	Magnetic field
$\vec{B}$	Magnetic flux density vector
$\cos\theta$	Power factor
$C_p$	Power coefficient
$C_{pmax}$	Maximum power coefficient
$d$	Direct-axis
$d^e$	Direct-axis synchronous frame
$d^s$	Direct-axis stationary frame
$e$	Error
$\varepsilon$	The controller tuning parameter
$E$	Voltage
$f_{c,PI}$	Cut-off frequency in Hz
$f_D$	Drag force
$f_L$	Lift force
$f_{pdf}(v)$	Rayleigh probability function
$f_n$	Natural frequency
$f_r$	Frequency of rotor speed
$f_R$	Rated frequency
$f_s$	Electrical frequency
$F_{ij}$	Flux linkage ( $i = q$ or $d$ and $j = s$ or $r$ )
$F_{mq}, F_{md}$	$q$ and $d$ -axis magnetizing flux linkages
$G$	Element material modulus of rigidity (90 Gpa for steel)
$G_p$	Process/plant model
$G_{p-}(s)$	Invertible minimum phase
$G_{p+}(s)$	Non-invertible minimum phase
$i_{qr}, i_{dr}$	$q$ and $d$ -axis rotor currents
$i_{qs}, i_{ds}$	$q$ and $d$ -axis stator currents
$i_{sa}, i_{sb}, i_{sc}$	Three-phase stator current measurement, phase a, b and c, respectively
$I$	Turbulence intensity
$I_r$	Rotor current
$I_R$	Rated current
$I_s$	Stator current
$\tilde{I}_s$	The terminal current

$J$	Moment of inertia
$J_g$	Generator inertia
$J_r$	Rotor inertia
$K$	Gain
$K_c$	Critical gain
$K_i$	Integral control gain
$K_p$	Proportional control gain
$K_p$	Model gain ( $\frac{\Delta y}{\Delta u}$ )
$K_s$	Shaft stiffness
$K_u$	Ultimate gain
$k_T$	Torque gain
$k\omega^2$	Torque law
$\lambda$	Adjustable parameter for filter
$\lambda_{opt}$	Optimum tip speed ratio
$\lambda_{target}$	Target tip speed ratio
$l$	Length of conductor in the magnetic field
$L$	Turbulence lengths scale
$L_m$	Magnetizing leakage inductance
$L_r$	Rotor inductance
$L_s$	Stator inductance
$L_s'$	Stator transient inductance
$m_{1-blade}$	Mass for 1-blade turbine
$m_{2-blade}$	Mass for 2-blade turbine
$m_i$	Mass
$M_s$	Maximum sensitivity
$n_r$	Rotational speed in rpm
$n_s$	Synchronous speed in rpm
$N$	Number of turns
$N_1$	Number of gear teeth connected to the low-speed shaft
$N_2$	Number of gear teeth connected to the high-speed shaft
$N_g$	Gearbox ratio
$\Omega_r$	Blade rotation
$\psi_{dr}$	d-axis rotor flux
$\psi_{dr}^*$	Reference d-axis rotor flux
$\hat{\psi}_r$	Rotor flux, which is aligned on the direct-axis synchronously rotating frame
$p$	Number of poles
$P_{aero}$	Aerodynamic power
$P_{ag}$	Air-gap power
$P_{core}$	Core loss
$P_{developed}$	Conversion/developed power
$P_D$	Developed power
$P_g$	Generated power
$P_{in}$	Input power
$P_{losses}$	Total power losses
$P_{max}$	Maximum power

$P_R$	Rated power
$P_{out}$	Output power
$P_{rated}$	Rated power
$P_{rcl}$	Rotor copper loss
$P_{rot}$	Rotational loss
$P_{scl}$	Stator copper loss
$P_{stray}$	Stray loss
$P_{turbine}$	Power from turbine
$P_u$	Ultimate period
$P_{wind}$	Power from wind
$q$	Quadrature-axis
$q^e$	Quadrature-axis synchronous frame
$q^s$	Quadrature-axis stationary frame
$\rho$	Air density
$r$	Order of the filter
$r_i$	Radial distance
$r_{ref}$	Reference from input
$R$	Radius
$R_r$	Rotor resistance
$R_s$	Stator resistance
$s$	Stator variable
$S$	Slip
$SD$	The standard deviation
$\mathcal{S}(s)$	Sensitivity function
$\bar{\sigma}_v$	The wind standard variance
$\theta$	Angle
$\theta$	Time delay
$\tau$	Time constant
$T$	Sampling time
$T_F$	Time constant of the shaping filter
$T_{aero}$	Aerodynamic torque
$T_{ag}$	Air-gap torque
$T_d$	Derivative control time constant
$T_e$	Electrical output torque
$T_g$	Generated torque
$T_i$	Integral control time constant
$T_l$	Load torque
$T_{load}$	Load torque
$T_{out}$	Output torque
$T_r$	Rise time
$T_s$	Settling time
$T_s'$	Stator transient time constant
$u(t)$	Control signal
$U$	Wind speed
$U_{high}$	High wind velocity
$U_{low}$	Low wind velocity
$v$	instantaneous wind speed
$\bar{v}$	Velocity of the bar relative to the magnetic field

$v_{eq}(t)$	Equivalent or actual instantaneous wind speed velocity
$v_m$	Mean wind speed
$v_{\bar{m}}$	Long time scale of the mean wind speed
$v_{qr}, v_{dr}$	$q$ and $d$ -axis rotor voltages
$v_{qs}, v_{ds}$	$q$ and $d$ -axis stator voltages
$v_t$	Wind gust/turbulence
$v_t(t)$	Turbulence component
$v_b$	Wind speed at b point
$v_{cut-in}$	Cut-in wind speed
$v_{cut-out}$	Cut-out wind speed
$v_{rated}$	Rated wind speed
$V_F$	Amplification factor
$\hat{V}_m$	Air gap voltage, which is aligned on the quadrature-axis synchronously rotating frame
$\hat{V}_s$	The terminal voltage
$V_R$	Rated voltage
$\omega_{FL}$	Rotational speed at FL region
$\omega_{slip}$	Slip speed
$\omega_a$	Speed at point a
$\omega_b$	Generator angular electrical base frequency
$\omega_b$	Speed at point b
$\omega_{c,PI}$	Cut-off frequency in rad/s
$\omega_c$	Speed at point c
$\omega_e$	Stator angular electrical frequency
$\omega_{fix}$	Fixed speed
$\omega_m$	Mechanical rotor speed
$\omega_m^*$	Reference mechanical rotor speed
$\omega_{ms}$	Frequency where the sensitivity function has its maximum
$\omega_{opt}$	Optimum speed
$\omega_r$	Rotational speed in rad/s
$\omega_r$	Rotor angular electrical speed
$\omega_{ref}$	Reference speed
$\omega_s$	Synchronous speed in rad/s
$\omega_{sc}$	Sensitivity crossover frequency where the sensitivity function becomes greater than 1 for the first time
$\omega_t$	Rotational speed of the rotor blade
$W$	Relative wind
$x_M$	Magnetising reactance
$x_{lr}$	Rotor leakage resistance ( $\omega_e L_{lr}$ )
$x_{ls}$	Stator leakage resistance ( $\omega_e L_{ls}$ )
$y$	Output
$z$	Height of the wind turbine hub
$\%OS$	Percent overshoot

# 1 Introduction

## 1.1 Introduction to Wind Energy Conversion System

The increment of renewable energy (RE) penetration within electric power systems is currently an important issue [1, 2], particularly in the wind energy sector, as it is the most efficient and competitive of RE technologies [3]. To achieve a high level of wind energy penetration while providing the lowest possible cost and energy sell price, the system security, reliability and power quality should be carefully considered. The management of the entire power plant system, including the generation, transmission [4, 5] and distribution sides, [1, 5, 6] needs to be balanced. Several approaches have been proposed to improve the quality of system management, for instance, wind forecasting, the energy storage system and the modern control system between the generation and distribution sides. The first and second approaches have been found to potentially solve the short term problems, such as load matching and power conditioning, but they still fail to send the pure constant power signal to the mains while maintaining the system stability [4, 6]. However, the third approach may solve additional system management issues, such as power quality improvement, fault ride-through, generator-grid uncoupling, voltage regulation and maintenance of the system stability of the network [4, 6-8].

Modern control equipment allows power electronic converters and variable speed drives to be installed in the wind energy system. The power converter allows active generator control, enabling efficient electromagnetic torque control *via* various control algorithms and technologies. Electrical conversion concepts of typical power converter arrangements of a modern variable speed wind turbine are shown in Figure 1-1(a), whilst Figure 1-1(b) shows the further improvement of the former system.

In general, each variable speed wind turbine has four essential elements, namely, the turbine rotor, drive train, generator and back-to-back power converter. Each turbine rotor usually has two or three blades mounted on a front

shaft of a drive train. In the drive train, a gearbox is connected to two shafts called the front shaft and the end shaft. A gearbox with a 1:N multiplier ratio is connected between the front and end shafts, which causes the end shaft to turn at the higher (1 x N) angular speed. This high-speed shaft is then connected to a generator.

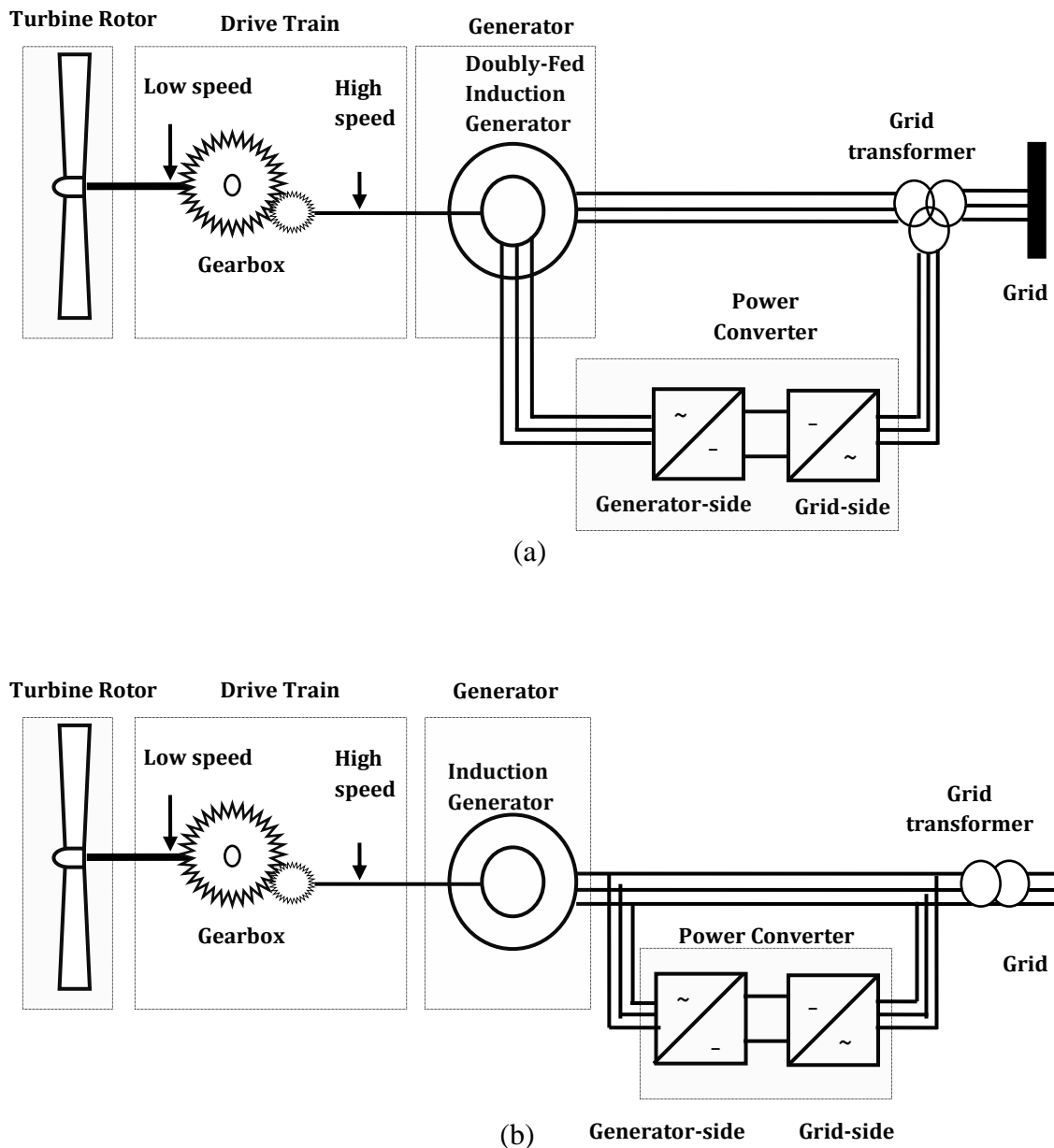


Figure 1-1 Electrical conversion concepts of the typical power converter arrangements of a modern variable speed wind turbine: (a) reduce-rated back-to-back power converter (b) half-rated back-to-back power converter

The generator is included in the system to transform the mechanical-rotational energy from the high-speed shaft (end shaft) into electrical energy. Electrical signals from the rotor winding in the generator are fed to the grid transformer via variable-frequency, back-to-back, power converters or directly (through the stator) before sending the voltage signals to the grid. The variable-frequency, back-to-back, power converter consists of two converters: the generator-side converter (GSC) and the network-side converter (NSC), and is separated by a DC-voltage intermediate link between them. These converters work independently depending on the configuration arrangement. GSC can be a diode-based rectifier or a pulse-width modulation (PWM) voltage source converter depending on the type of wind turbine technology. In contrast, NSC is typically a PWM voltage source converter.

Figure 1-1(a) shows the first configuration that uses the power converter to control the partial power sent to the grid. This configuration is popularly known as the Doubly-Fed Induction Generator (DFIG) and is the first configuration that controls the generator speed and power factor. One-third of the nominal power is fed from the rotor, and two-thirds of the power is fed from the stator [6]. This configuration uses a wound rotor induction generator where the stator is directly connected to the grid, whilst the rotor circuit is connected to the grid via the converter using slip rings and brushes. To allow variable speed operation in the rotor, controllable voltage from the GSC will be injected into the rotor at the slip frequency, whereby the NSC decouples the electrical grid frequency from the rotor mechanical frequency.

Shown in Figure 1-1(b), the power converter is designed to work at half-rated power using a squirrel-cage induction generator. This system is designed to improve the weakness of the DFIG system. The stator-grid connection is disconnected from the system when the wind turbine works at low or medium power. This connection is specially designed for power optimisation and power transfer to the mains. At high power, GSC is disconnected from the system for reactive power and harmonics compensation. However, during fault occurrence, under such an operating condition, the controllability of GSC is almost lost and the controllability on active and reactive power becomes inactive [9]. Hence, only

NSC handles the reactive power control, but NSC can only manage a part of the power due to its small power converter rating.

DFIG with partial-rated power converter is the most popular arrangement installed in the wind turbine application [10, 11] because the system has little energy loss and can perform better than a fixed-speed wind turbine. However, because of its power converter connection, this system has introduced extra complexity because the brush can easily wear out and needs to be replaced every six months or more often [12, 13]. During normal operation, the power converter allows the rotor to work under optimal conditions to obtain maximum power through active and reactive power control [14]. However, in the case of heavy loads and fault occurrences, this system may disengage frequently from the grid because the stator is directly coupled to the grid. During the fault, high current is induced and the system protection then disconnects the line and reconnects it again once the system is assured stable. A certain amount of time must pass before confirming that the system is stable and can safely be reconnected. However, in the worst conditions, the current may also damage the converters and insulation materials [11, 14]. This undesirable high current will flow inrush into the stator winding and then flow into the rotor due to the magnetic coupling effects between them. As a consequence, a protection circuit needs to be installed in the system to block the GSC [15], which may result in additional circuit complexity and cost for operation and maintenance. In terms of generator control, this system has a limited speed range ( $\pm 30\%$ ) due to its smaller converter size.

Due to the drawbacks of the DFIG system, the full-rated power converter was designed as an alternative. The typical configuration of this full-rated, converter-based, wind turbine is depicted in Figure 1-2. In this arrangement, a full-rated power converter is directly coupled to a squirrel-cage induction generator through the machine stator whilst the machine rotor is connected to the turbine rotor via a gearbox, which allows the drive train and induction generator to be completely decoupled from the grid. All the generated power is sent to the grid through the power converter, which leads to the reduction of mechanical shocks on the turbine if a fault/disturbance occurs at the grid side. Furthermore, during fault occurrence, this system can work under standby and

in an island [6], unlike in the DFIG system where the wind turbine generator will be tripped due to the voltage instability, particularly if connected to the weak grid [9, 16]. Additionally, this system enables a wider speed control because of its larger converter size [6, 17].

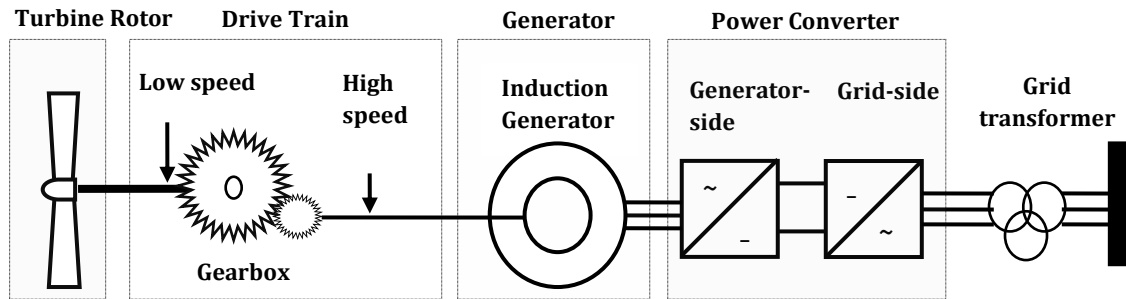


Figure 1-2 Typical configuration of a fixed-pitch variable-speed wind turbine with a fully-rated converter

Although power converter control currently focuses upon the grid side rather than the generator side to improve the power management, generator-side control should also be investigated in the variable speed wind turbine to solve the conflict between dynamic stability and torque/speed management capability, for improved active power control performance, which allows power to be extracted at maximum during low wind velocities and limited at the rated power during high wind velocities. Additionally, generator-side control can allow a simpler fixed-pitch (stall-regulated) wind turbine with a robust and rugged induction machine to be used. For example, the blade-pitching system can be removed altogether, resulting in a mechanically simpler and lighter wind turbine configuration. This type of wind turbine is known as a stall-regulated (fixed-pitch) variable speed wind turbine (SRVSWT) and is as shown in Figure 1-2. This type of configuration has drawn the attention of many researchers and the renewable energy industry, and the model is used in the control algorithms design studied in this project.

## 1.2 Approaches to Improve Power Control Performance

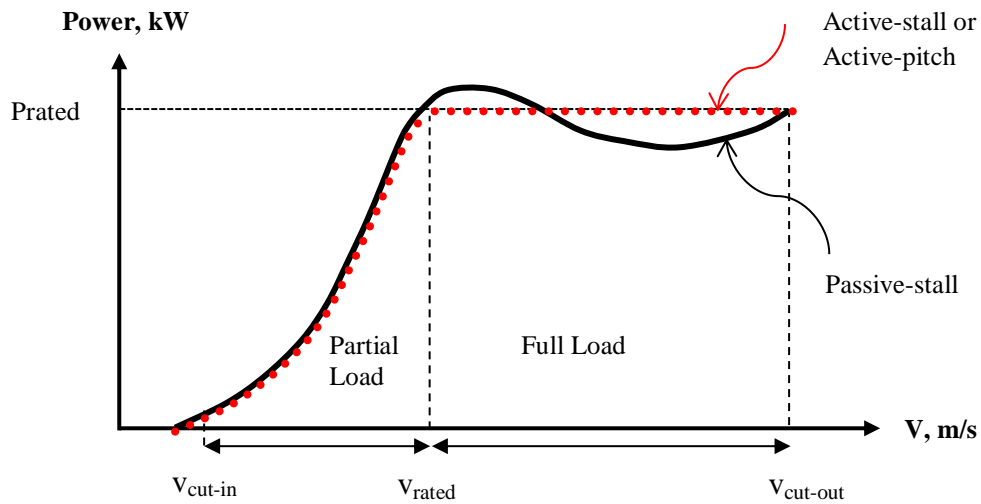
As this research focuses on the application of active control to the generator of a stall-regulated wind turbine system, only the generator-side control of the power converter is discussed. This section reviews the development and research being performed to enhance the active power control of SRWT systems.

### 1.2.1 Fixed Speed Operation

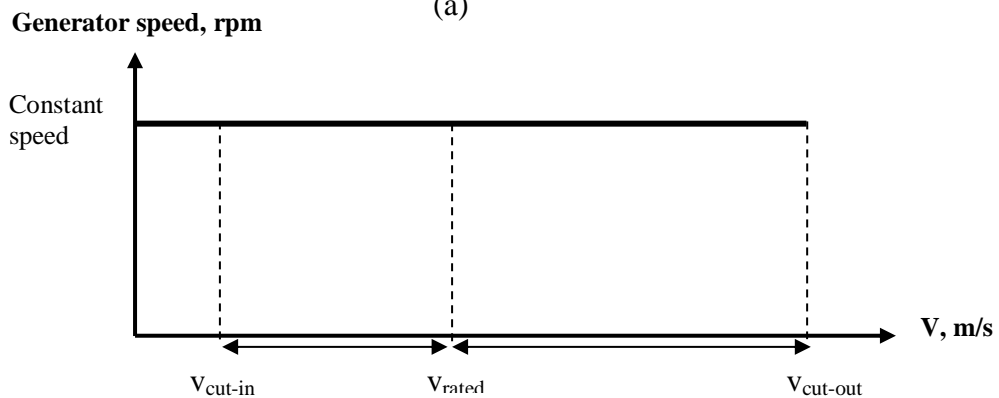
#### 1.2.1.1 Passive Stall

It is well known that the first commercial wind turbine using fixed blade and fixed speed operation, known as the 'passive stall wind turbine' or 'stall-regulated wind turbine (SRWT)', causes a conflict between dynamic stability and power optimisation ability. In this scheme, the power or torque characteristic cannot be modified because the speed of the generator is locked to the grid line frequency. However, in reality, the generator's torque characteristic varies by a few per cent due to its slip.

The basic power control strategy of this SRWT is uncontrolled, and its behaviour is depicted in Figure 1-3 (see the thick black line). Power starts to be generated when the wind speed reaches the cut-in wind speed ( $v_{\text{cut-in}}$ ) and will be shut down when the cut-off wind speed ( $v_{\text{cut-out}}$ ) is exceeded. As Figure 1-3(a) shows, there are two regions: partial load and full load, each involving a different behaviour. The 'partial load' region represents the zone of low wind velocities ( $v_{\text{cut-in}} < \text{partial load} < v_{\text{rated}}$ ), whereas the 'full load' region represents the zone of high wind velocities ( $v_{\text{rated}} < \text{full load} < v_{\text{cut-out}}$ ). During partial load, the generated power cannot be controlled at the optimum level. Because the rotational speed is almost constant (Figure 1-3(b)), only one operating point could reach maximum power when power is optimised at only one wind speed (see Figure 1-4). Hence, the efficiency level of the power production is poor. The power is more or less dependent on the torque created along the operating locus.



(a)



(b)

Figure 1-3 Control strategy on SRWT

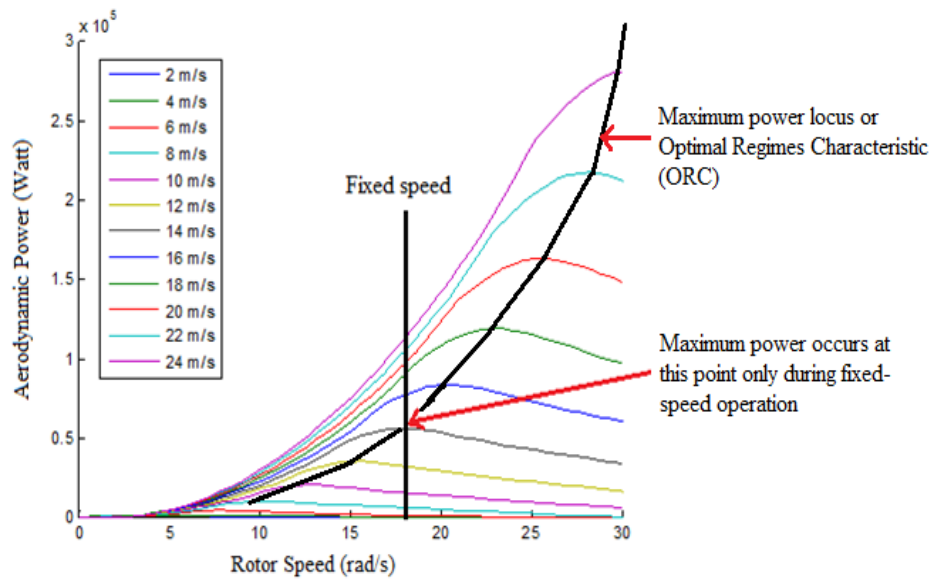


Figure 1-4 The aerodynamic power versus rotor speed, for different wind speeds

In the full load region, when the wind speed is near  $v_{rated}$ , power is automatically reduced while the turbine is automatically stalled by the blade aerodynamics. As a consequence, a power peak occurs when the wind reaches  $v_{rated}$ , and then exhibits a power reduction and an increase again when the winds blow stronger, before the turbine is shut down. Hence, the behaviour and safety factors of this scheme highly depends on the blade profile design [18, 19]. With this passive control, there is a drawback in terms of the complexity of the aerodynamic design problems and how to confront the wind turbine's structural dynamic's behaviours [20]. The right aerofoils must be carefully designed. Because the turbine generator runs at a chosen fixed speed, the stress induced in the turbine structure increases as the wind speed increases. Additionally, noise will be an inherent consequence of the increasing wind speeds, where more the increased turbulence occurs during stall. It is good if the appropriate  $v_{cut-in}$ ,  $v_{rated}$ ,  $v_{cut-out}$  and maximum power ceiling of a turbine can be well-determined before designing the blade profile, but unfortunately, each turbine is not tailored to the conditions at each site.

Various standard designs have been developed and tested to achieve satisfactory aerofoil characteristics. To develop a standard benchmark, the aerofoil design was classified into two classes: horizontal-axis wind turbines (HAWTs) and vertical-axis wind turbines (VAWTs). The details of the HAWT class are described by Tangler and Somers in [21], and the VAWT class is described by Klimas in [22].

Initially, *NACA 230XX* series aerofoils have been used in many commercial HAWTs. The *XX* stands for the percentage value of the thickness-to-chord ratio. For VAWTs, the thickness ratio is usually designed within the 12% to 15% range, and the code has a four-digit series, e.g., *NACA 00XX*. For HAWTs, however, the aerofoils have *XX* ranging from approximately 28% at the root to approximately 12% at the tip of the blade [19]. This design, however, produces unsatisfactory features because its performance is reduced when the blade thickness increases and it is very sensitive to surface fouling. The *NACA 44XX* series was designed to improve the surface fouling problem but still presents significant power reduction when experiencing higher sensitivity to the surface roughness. Surface roughness is a condition where the blade surface smoothness has been degraded

due to rain, dirt, dust, or insect debris. Another design was proposed to reduce roughness losses, and the power is improved substantially when the *NACA 63-2XX* series is introduced. A smaller upper surface thickness was proposed in *NACA 63-425* to reduced roughness sensitivity [23].

To further improve the aerodynamic performance, the aerofoil design is occasionally modified. A performance enhancement of the stall-regulated rotors is achieved when the blade outboard aerofoils with low lift coefficient were considered in the design [21]. Lift coefficient is a function of the incident angle defined as the angle that the flow makes with the chord. For stall-regulated wind turbine, a low lift coefficient in the outboard blade region helps control peak rotor power. This modified design enables the use of 10% to 15% more swept area for a given generator size. Other improvements have also been obtained using different blades thicknesses and rotor diameter classifications [19, 21]. As an example, for the *NACA* case, nine aerofoil families consisting of different blade lengths ranging from 1 metre to 25 metres was proposed. For each blade length, various blade thicknesses (from thin to thicker) and various generator sizes (from 2 to 1000 kW) were designed and tested. The diameter classification approach has also been tested on the *SERI 80Y* series. By this classification, the thickness-to-chord ratio appropriate for the blade length is designed. The selection of the right thickness-to-chord ratio is important because this value influences the turbine strength and stiffness. Improvements in terms of structural performance and the minimum blade cost have also been made. Hence, a family of thicker aerofoils has been designed for longer rotor diameters (ranging from 21-35 metres), for instance, the *SERI* aerofoil families.

In addition to the traditional aerofoils designed by Tangler and Somers, aerofoil designs for wind turbines, such as the inverse and direct design methods by Drela in [24], Timmer and van Rooy in [25], and Obayshi and Tanakashi in [26], were also proposed. Using the inverse design method, the aerofoil surface flow is predetermined for indicated operational conditions and the aerofoil contour (the separation bubble transition and associated losses) is then defined. Using direct design, a simpler algorithm was developed in the design of transonic aerofoils, where numerical optimisation with rational multidisciplinary design was considered whilst multiple constraints were imposed. Using a flexible blade

is also suggested to improve the operational range of wind turbines [27]. Unfortunately, none of these designs have fundamentally solved the power optimisation issue during partial load and smoothed the power limitation in the full load region. The problems with the passive stall solutions have therefore motivated the application of active stall control and active pitch control to provide better power control during high winds [18].

### **1.2.1.2 Active Stall**

There are basically two methods of power regulation by pitch control, namely 'pitch-to-stall' and 'pitch-to-feather'. In fixed speed operation, pitch control is usually used in above rated wind speeds. For better understanding, the 'pitch-to-stall' will be referred to in this thesis as 'active stall' control and will be explained in this subsection, whereas the 'pitch-to-feather' will be referred as 'active pitch' and will be explained in the next subsection.

Using 'active stall' control, the blade pitch angle is decreased to increase the blade angle of attack, which causes the blades to go into a deeper stall [28]. By restricting the rotational speed and controlling the blade pitch angle, the incident angle can be adjusted and hence power can be controlled [17]. During this time, the drag force rises whilst the lift force drops abruptly. Hence, excessive energy in the wind can be dissipated when power overshoot during rated power can be avoided at the beginning of the wind gusts. Also, as a result, power can be maintained at its rated level when the force in the rotor plane can remain constant because of the composition between the drag and lift forces. However, a weakness of this method, is when turbine goes into a stall, the thrust force increases drastically, inducing heavier aerodynamic loads. A comparison of the aerodynamic power behaviour between the passive stall and the active stall control is shown in Figure 1-3(a) [8].

### **1.2.1.3 Active Pitch**

Like 'active stall/pitch-to-stall' control, 'active pitch/pitch-to-feather' control works by altering the blade angle to reduce aerodynamic power [28]. The blades are feathered as wind speed increases. However, in active pitch control, the pitch angle tends to increase (up to 35° from the pitch reference) [17, 29], so that the incident angle decreases. During this time, the lift coefficient drops whilst the drag coefficient remains low. Contrary to the passive stall, when using this method, the thrust force decreases as wind speed increases. However, using this method, larger control effort is needed compared to active stall control, where larger gains are needed in the control loop to provide fast pitching response (approximately 5°/s) [17]. Faster response is important for preventing the rotor from reaching the maximum pitch limit [30]. The comparison between this active pitch control and the other types of passive and active stall control is illustrated in Figure 1-3(a).

If passive stall and fixed-speed is used, optimum power only occurs at one wind speed. The power optimisation issue during partial load has not been solved [31]. Additionally, the power during high winds cannot be limited at a constant rated power. To use active stall and active pitch control, more complex circuitry is needed due to blade pitching. The problems with the solutions mentioned above have therefore motivated the application of active speed control to provide new levels of performance that cannot be achieved with conventional fixed-speed operation [18].

### **1.2.2 Variable Speed Operation**

The level of interest in using active speed control for the wind energy system has grown steadily due to the market expansion [32] since the mid-nineties [33]. Wind energy systems, for instance, mostly use computer controlled electronic systems that require electronic components. Wind turbines use a form of adjustable speed drive that allows variable speed operation during partial load and blade pitching during full load. The concept is now well established and examples of this technology can now be found in many countries, including China, USA, Germany, Spain and India [34].

Variable speed control research has been well implemented on the wind turbine system to improve power management, irrespective of whether an induction or synchronous generator is used. Numerous studies have been carried out to apply variable speed to the pitch-blade wind turbine system. In fact, almost all modern wind turbines at present are operated with variable speed. Unlike the stall-blade wind turbine (also known as SRWT), the fixed-speed concept is popularly used in the operation system, whilst the application of the variable speed concept is actively proposed and discussed only in the literature. The main reason for using the SRWT with variable speed is to design a control system that can produce maximum available power during partial load whilst limiting the accessible power at a rated power during full load, which is not possible with purely fixed-speed, fixed-blade/passive stall control. The power curve resembling active stall/active pitch can be obtained, as depicted in Figure 1-3(a).

Mostly, studies involving wind energy conversion system (WECS) emphasize the selection of the control objectives. Commonly, control objectives are based on the wind turbine operating regions: partial load (PL), intermediate load (IL) and full load (FL), as illustrated in Figure 1-5(a). The PL region represents the zone of power optimisation, whereas the IL and FL regions represent the zone of power limitation. In the PL region, power is controlled to be optimised when maximum power needs to be generated, that is, when wind speeds range from  $v_{\text{cut-in}}$  to  $v_b$ . In the IL region, when the wind speed is greater than  $v_b$  and lower than  $v_{\text{rated}}$ , power control will be applied to limit the power from increasing cubically. The power of a turbine is directly proportional to the cube of the wind speed, and also influenced by the power coefficient ( $C_p$ ) and the power constant ( $k_T$ ). The power constant depends on the rotating blade area and the air density. Meanwhile, the power coefficient represents the ratio of the turbine aerodynamic power to the power available in the wind [18], [35]. To capture the maximum power, the power coefficient should be maintained at the maximum value, at which state the power coefficient is usually referred to as  $C_{pmax}$ . To obtain  $C_{pmax}$ , the tip speed ratio ( $\lambda$ ) of the turbine should be controlled to be at the optimal condition. Tip speed ratio is the ratio between the tangential speed of the tip of a blade and the actual velocity of the wind. At optimal tip

speed ratio ( $\lambda_{opt}$ ), the power coefficient is at the maximum value. But, if the  $\lambda$  moves away from the point of  $\lambda_{opt}$ , the  $C_p$  will begin to decrease. In the FL region, power limitation will take over when power is maintained at the rated power, where the wind speeds are between  $v_{rated}$  and  $v_{cut-out}$ .

The relationship between power controls and the speed control for each region can be depicted as in Figure 1-5(b). During PL, the speed is allowed to increase corresponding to the increment of the wind speeds. Then, during IL, two concepts are usually employed. The first concept is the use of constant speed (CS) control, and the second concept uses modified power tracking (MoPT), which is also called 'soft stall control', by restricting the rotor speed. In the FL region, the constant power strategy (CPS) needs to be applied to limit the excessive power by actively reducing the speed. However, in this FL region, the CS and MoPT are also applied depending on the design control aims.

The following is a review of the control approach that has been proposed in the previous research on the SRVSWT controller during partial load and full load.

### **1.2.2.1 Partial Load (PL)**

For the SRVSWT system, the aim of control during the partial load region is to optimise the aerodynamic power or to follow the locus of optimal rotor control (ORC). In certain references, this locus also called the 'optimal regime characteristic' where power is expected to be maximally captured; see Figure 1-4.

Several strategies have been proposed to achieve ORC, such as controlling the aerodynamic/drive train torques, continuously setting these torques at the optimum rotor speed where the maximum power coefficient ( $C_{pmax}$ ) or optimum tip speed ratio ( $\lambda_{opt}$ ) is achieved [36]. The ORC can be achieved by one of three approaches: maximum power point tracking (MPPT), rotational speed optimal control (RSOC), and active power optimal control (APOC) [17].

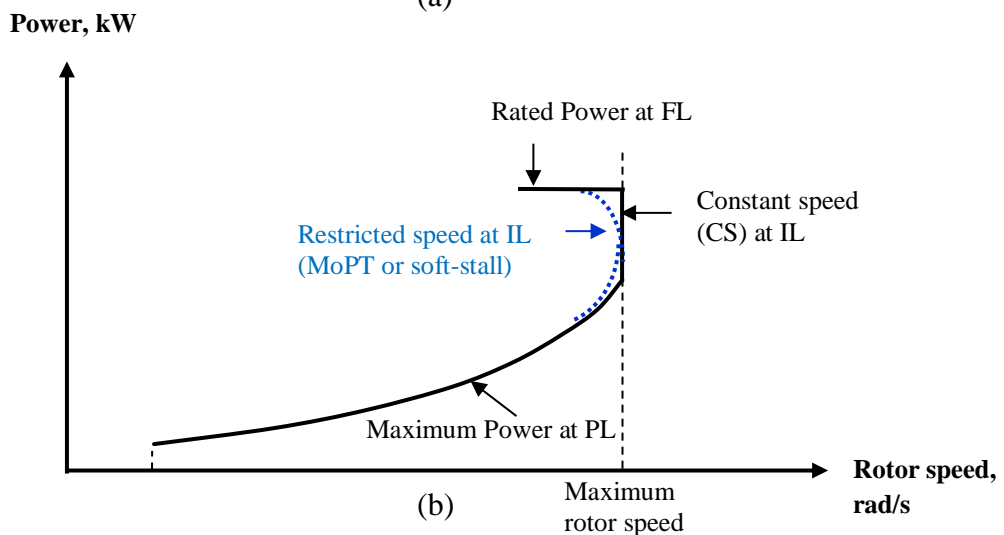
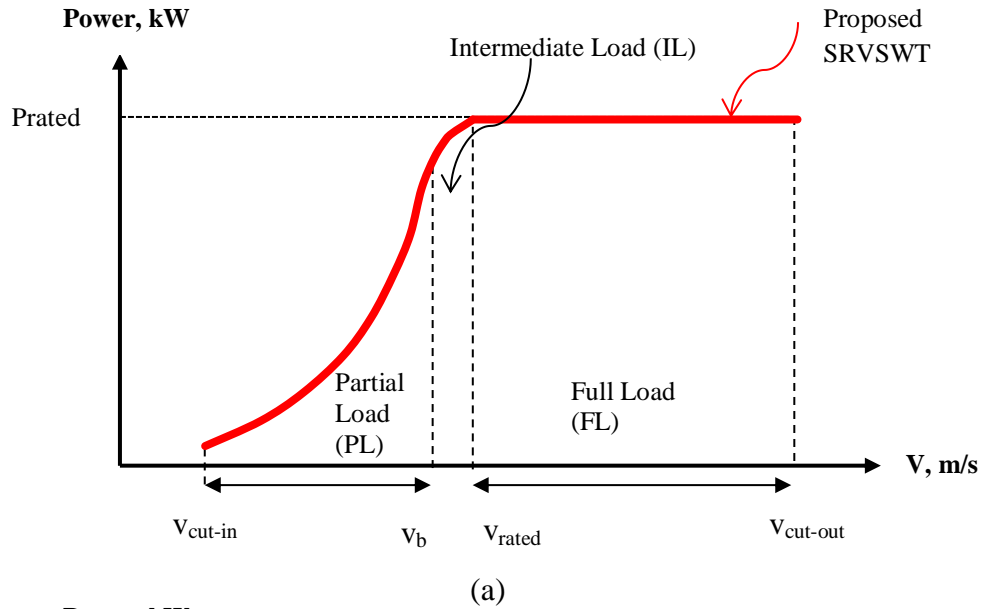


Figure 1-5 Control strategy on SRVSWT: (a) power versus wind speed, (b) power versus rotor speed

MPPT is used when the parameters of  $C_{pmax}$  and  $\lambda_{opt}$  are not known [17, 37]. These parameters are estimated by searching for an intersect point where maximum power ( $P_{max}$ ) is attained when the rotor speed is increased. Though this method is simple because it needs little information, its operating point (OP) may differ quite significantly from the optimal OP during turbulent winds, which is due to the ignorance of wind turbulence and system dynamics during the design. RSOC is performed when  $\lambda_{opt}$  is known and the control system uses wind speed information as the reference set point, whilst APOC is performed when  $C_{pmax}$  and  $\lambda_{opt}$  are known and the control system uses the shaft rotational speed

information as the reference set point [17]. Due to the inaccuracy of wind speed measurement in RSOC, APOC is more widely used than RSOC. This inaccuracy is due to the time lag caused by the tower shadow and wind shear. The wind speed measurement by the anemometer is different from the actual wind speed experienced by the blade. If the classical/PI design is used for ORC, it is common to adopt the speed loop [38], [39], [40], [41],  $k\Omega^2$  law (torque) loop [42], [39] and power loop [43, 44], where the generator torque was usually chosen as the control input of the plant model. In some reference, cascade control comprising two/three loops was also demonstrated.

However, other strategies for the partial load region were also proposed in the literature, for instance, tracking the 99% efficiency of the ORC curve, tracking constant torque and tracking constant speed [36], as shown in Figure 1-6.

### **1.2.2.2 Full Load (FL)**

In the full load region, several theoretical approaches have been proposed by Leithead and Connor to reduce the efficiency of power extraction. These approaches are tracking by constant power, tracking by modified power, tracking by constant torque and tracking by constant speed, as illustrated in Figure 1-6. To track the constant power, the rotor speed must be actively reduced, but abrupt deceleration must be avoided because the torque may increase abruptly, stressing the drive train. By modifying the rated power curve, energy capture may be slightly reduced, but the turbine dynamics can be improved [36, 43]. If the constant torque strategy is chosen, considerable loss occurs compared to the rated power tracking, but losses are markedly more reduced if a fixed speed is selected [36]. To improve the fixed speed performance, two discrete speed operations were also suggested. When wind speeds increase (as a certain proportion of the maximum speed), another lower rotor speed is set.

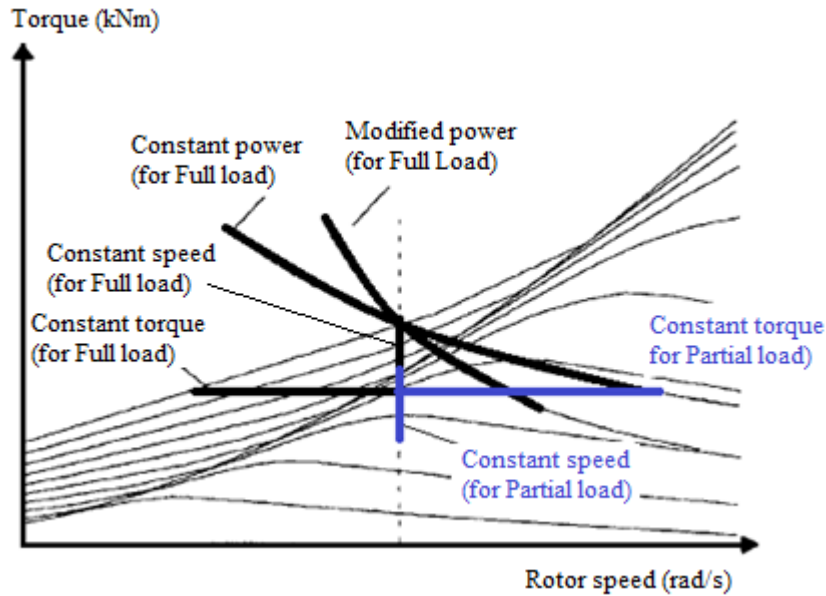


Figure 1-6 SRVSWT strategies during partial and full loads [36]

### 1.2.2.3 Previous Work on SRVSWT

The previous research on SRVSWT considering wind speed regions, adopted controllers, used techniques and employed generators as summarised in Table 1-1. From this table, the gaps where further work can be performed (relating SRVSWT, SCIG and fully-rated power converters) can be more clearly observed. In the table, items 1 to 8 employed DFIG in their studies. Though stall blade and variable speed were chosen, the power converter considered was a partially-rated configuration. All works considered PL, IL and FL control, except Salameh [45] and Battista *et al.* [46] who only considered power optimisation work in their research.

For items 15 to 24, fully-rated power converters were used in the studies, but the types of generators employed, including a synchronous generator [47], switch reluctance [48], DC [37], permanent magnet [49] and others, were not mentioned. Some of these studies used linear control (P, I, PI, LQ, LPV and gain scheduling) and the remaining used nonlinear controllers (MPPT, fuzzy and adaptive). Certain studies used combinations of several sensors and cascade control loops in the controller design. The speed loop is most often chosen to be cascaded with the power or torque loop. The cascaded PI loop is usually

employed to improve global performance [50] and has been proven to perform equivalently to certain modern controllers [51].

From Table 1-1, it can be observed that studies are mostly focused (more than 90%) on partial load instead of intermediate and full load regions. When observation is focused on the full load region only, CPS and MoPT were preferred over CS due to the power-loss factor. For the SRVSWT system with a fully rated converter, most of the studies preferred MoPT to CPS. MoPT is the modified version of CPS where the power peaking during the rated wind speed can reduce smoothly. In Muljadi *et al.*[32], which uses MoPT, the turbine is stalled before reaching the maximum permitted speed, reducing the power efficiency and torque stress [32, 36, 52] and requiring some sort of speed control action to ensure that the rotor properly follows the designed curves. Hence, the speed loop is needed to control the reaction torque.

Pierce and Migliore [38] then improved work that has been performed by Muljadi *et al.* A comparison between CPS and MoPT has been performed. For CPS, the speed was regulated actively between 32 and 58 rpm. For MoPT, the soft stall is occupied by the regulating rotational speed below the permitted maximum where the rated power occurs only at one wind speed. Three years later, Muljadi *et al.* [43] presented the soft stall concept using the vector control concept to control the rotor current. However, these works used partial-rated and not fully-rated power converter.

Cardenas *et al.* [48]and Ekelund [51] also focused solely on the power limitation. Both studies used MoPT control. Cardenas *et al.* used a small signal model in the control system. The PI controller, used to correct the errors, was designed by using the root locus method. The results of power and rotational speed responses based on two wind steps were presented. Ekelund employed PI and the linear quadratic (LQ) optimal control model to keep the power at a constant rated value. In his work, he measured the level of variance of the drive train torque and the captured power using the LQ criterion. He then compared the LQ performance with classical PI and PI cascade-compensated design performance. Ekelund found that the cascade design exhibited good results, coequal to the LQG approach. However, the cascade design is more convenient without changing the controller's parameters variables.

Table 1-1 Summary of research attempted on SRVSWT considering the control strategy for each wind speed region, the adopted controller, the technique and the generator employed

**Note:**

PL – Partial load

MoPT – Modified Power Tracking

AC – Alternate current

DFIG- Double-fed induction generator

IL – Intermediate load

CPS – Constant Power Strategy

PM – Permanent magnet

FL – Full load

NM – Not mentioned

IG – Induction Generator

CS – Constant speed

SR – Switch Reluctance

DC – Direct Current

No	Reference	Wind Speed Region						Specific Controller	Technique & Tracking Loop	Generator
		PL	IL		FL					
		C <sub>pmax</sub>	C <sub>pmax</sub>	CS	CS	CPS	MoPT			
1	Muljadi, E., Pierce, K.G. & Migliore, P.G. [42]	x	x				x		Torque control, $k\Omega^2$	DFIG
2	Xin-Fang, Z., Da-Ping, X. & Yi-Bing, L. [53]	x		x		x		Adaptive optimal fuzzy, PI	Speed control	DFIG
3	Pierce, K.G., Migliore, P.G. [38]	x		x		x	x	PI	Torque control: speed loop	DFIG
4	Salameh, Z.M. [45]	x							External resistance control	DFIG
5	Battista, H.D. <i>et al.</i> [46]	x						Sliding-mode		DFIG
6	Muljadi, E., Pierce, K. and Migliore, P. [43]	x	x				x		Torque control: power loop	DFIG
7	Muljadi, E., Pierce, K. and Migliore, P. [44]	x	x				x		Torque control: power loop	DFIG
8	Datta, R. and Ranganathan, V.T. [54]	x								DFIG SCIG
9	Senjyu [55]	x						PI	Voltage & current observer (sensorless vector control)	SCIG
10	Novak, P. <i>et al.</i> [39]	x						LQG, PI + low pass filter, P + low pass filter + high pass filter, nonlinear TS & TQ	Torque control, $k\Omega^2$ : speed loop	SCIG
11	Pournaras, C. <i>et al.</i> [56]	x	x					Robust controller	Torque control	SCIG
12	Thiringer, T. & Linders, J. [57]	x		x					Power control	SCIG
13	Bianchi, F.D., Mantz, R.J. & Christiansen, C.F. [40]	x		x		x		LPV	Speed control: speed loop	SCIG
14	Bourlis, D. [58]	x				x		I, P (gain scheduling)	Torque control	SCIG
15	Bongers, P. M. M. <i>et al.</i> [47]						x	Linear quadratic (LQ)		SG
16	Vihriala, H. [49]	x			x			PI, feedforward fuzzy	Torque control. Cascade: displacement, speed & current control	PM
17	Bianchi, F., Battista, H. & Mantz, R.J. [41]	x						Gain scheduling, LPV	Speed control: speed loop, torque loop	NM
18	Leithead, W.E. [52]	x					x		Torque control	NM
19	Muljadi, E., Butterfield, C.P. & Buhl, M.L. [32]	x		x			x		Speed control	NM
20	Boukhezzer, B. & Siguerdidjane, H. [50]	x		x			x	Nonlinear	Torque control. Cascade loop: speed and power.	NM
21	Cardenas, R. <i>et al.</i> [48]						x	P	Torque control: speed loop. Small signal model.	SR
22	Ekelund, T. [51]						x	Adaptive LQ, P, I	Torque control. Cascade loop: speed and power	NM
23	Arnaltes, S. [59]	x						PI	Torque control: speed and torque loop	NM
24	Neammanee, B. <i>et al.</i> [37]	x				x		Nonlinear MPPT, fuzzy		DC

Additional work by Boukhezzar and Siguerdidjane [50] also employed a cascade controller to regulate the electric power during full load. The authors dealt with the nonlinear cascade controller in an effort to upgrade Ekelund's work in [51]. The proposed nonlinear model comprises two tracking loops where the inner loop is the speed loop and the outer loop is the power loop. The input of the inner loop is controlled by the outer loop, in which the main demanded reference is the generated power. By employing this cascade structure, the operating point could track the demanded generator power.

The part of Table 1-1 containing items 8 to 14 (the shaded columns/rows) is the most interesting because it really demonstrates the purpose and novelty of this research. For these items, SCIG with fully rated power converter was employed. These studies worked on power optimisation and used a linear controller, except Pournaras *et al.* [56] which used a robust nonlinear controller. From these seven studies, only Thiringer and Linders [57] and Bianchi *et al.* [40] considered studies on the intermediate region and used CS control, whilst only Bianchi *et al.* [40] and Bourlis [58] considered the study of the full load region and used CPS to limit the power. Thiringer and Linders emphasised that the correct maximum permitted speed must be chosen for the power limitation during intermediate load to avoid over-power risk. In their work, comparison of generated power at six different rotor speeds was demonstrated. In Bianchi's work, the general torque ( $k\omega^2$  law) that was proposed by Novak *et al.* [60] is improved by applying quasi-linear control with the adaptability of gain scheduling, for both the IL and FL regions. The most recent work by Bourlis represents the power control using P and I controllers with the gain-scheduling approach where switching devices are used to change the gain parameters during region transitions.

### **1.3 Background of the Study**

The most unique component of a variable speed wind turbine system is its converter. The back-to-back power converter enables not only variable speeds in a wind energy system but also the establishment of power optimisation and a protection scheme. By employing a SRVSWT with a full-rated power converter, control of the generator speed can be achieved for an extensive range of speeds.

If a stall-regulated (fixed-pitch) wind turbine is equipped with variable speed control in the partial-load and full-load regions, variable speeds enable optimal region control for the partial loads and reduced power efficiency for the intermediate and full loads.

For a partial load, the turbine speed should be regulated to track the maximum power efficiency, which enables the rotational speed of the wind turbine to be continuously adapted (accelerate or decelerate) for different wind speeds. This situation, however, can produce deviations in the operating point from the  $C_{pmax}$  or the  $\lambda_{opt}$ , particularly during rapid variations in wind speed [36, 58]. Thus, considerable power loss is induced, specifically when the turbine exhibits a narrow power coefficient ( $C_p$ ) curve [58, 61]. Another consequence of the accelerations/decelerations due to a continuous generator speed is the significant supplementary stress to the turbine structure, including the drive train and the generator [6]. The frequent changing and braking of the generator speeds induces tension, particularly during turbulence and rapid changes in wind speed [36, 62, 63]. These situations can cause difficult power modifications and abrupt power reduction [6], whereas overspeeding may occur, or the machine may exhibit abnormal behaviour, such as motoring, instead of generating action [52, 64]. Overvoltage or undervoltage conditions may also occur.

For intermediate and full loads, the turbine speed should be restricted to enable power reduction (or to release stored kinetic energy), and the speed should be reduced when the blade stall begins to create power-peaking. During this situation, the tendency of the generator speed to resist changes from its state of motion is greater than the tendency to resist changes during the partial-load condition. If the speed deviation is large, the inertia constant is also large before a new steady state speed is attained [65, 66]. If the generated power needs to be limited at a rated value during full load, the speed should be restricted. However, highly nonlinear dynamics are significantly involved where the rotor aerodynamics are insensitive to changes in wind speed [36, 63, 67]. The stall blade (fixed pitch) also undergoes a natural stalling process in which the power is automatically reduced, diverting from continuously increasing the captured power.

With passive stall control, the power limitation during high wind velocities is naturally and inexpensively obtained. However, with passive stall control, power could not be limited at a rated level when wind speeds reach the full-load region [8] where a power overshoot occurs at the beginning of the rated wind speed. Then, the power decreases and subsequently increases before the cut-out wind speed is attained. For a complete turbine operation, which ranges from the cut-in wind speed to the cut-out wind speed, the worst situation is expected during the transition between the partial-load region and the full-load region, in which power overshoots usually occur [35] due to the transition in the control goal from a continuously followed ORC curve to the speed restriction curve. This phenomenon results in stress on the generator and gearboxes, strong vibrations, increased fatigue and tear, noise and, in extreme cases, breakdown [68].

As explained in section 1.2, several solutions to the problem of partial loads are provided; they incorporate the blade design, the linear controller, the nonlinear controller and different control approaches (speed, power and torque loop tracking). The control approach proposed for the partial load can be extended to the intermediate-load and full-load regions. Few studies of the performance of these regions have been conducted for the SCIG with a fully-rated power converter. No studies of the MoPT have been performed for the intermediate load.

To address these problems, active control for partial, intermediate and full loads must also be employed. The active control strategy employed in this study involves the design of advanced controllers for active generator control, which can optimise and limit the active power (in the partial-load and full-load regions) by controlling the generator torque and the generator speed. For intermediate and full loads, management of the speed control and the natural characteristics of the stall process of the SRVSWT, which are unknown, are difficult to understand without specific investigation or field testing. Thus, the trade-off between a reasonable transient response of speed and management of the frequent torque fluctuations for intermediate and full loads for the SRVSWT system offers a new challenge and provides the opportunity for investigation.

Vector control (VC) was the natural choice as it comprises a sophisticated approach to controlling the active power by controlling the machine rotor flux and the rotor speed [69]. Using VC, active power is controlled *via* independent rotor flux and rotor speed control. To perform the VC model algorithms, simple IMC-based proportional-integral (PI) and integral-proportional (IP) controllers were used in the proposed model as they have performed well in servomotors and can be employed in many algorithms and modelling techniques. These controllers can also be easily implemented, require minimal feedback information, and offer robust control [17].

Although some studies of the design of control algorithms have been performed to improve the active power quality of the SRVSWT for partial loads, few studies have focused on the intermediate-load and full-load regions. An intensive review of the literature has also demonstrated that no studies of the application of active power control have focused on VC during high winds. Only the study by Senjyu [55] has considered VC; however, only power optimisation was considered in his study. The sensorless approach, in which position and speed measurements were not utilised, was employed.

Therefore, this study focuses on the design of active power control for all regions of the SRVSWT system, with the objective of maximising power capture in the partial-load region, suppressing power-peaking during the transition from the partial-load and the full-load region, maintaining generated power in the full-load region, and reducing the mechanical stress within the operating range of the safe mode. Two types of VC model algorithms, namely, indirect vector control (IVC) and sensorless indirect vector control (SLIVC), are proposed and implemented. Tracking by the modified power approach, which has been proposed by Leithead and Connor in [36], is also employed to obtain smoother dynamic loads during the transition from the partial-load region and the full-load region. As no real implementation work has been tested, the success of these control algorithms for the proposed SRVSWT system is significantly dependent on the validation of the developed SRWT simulation model. Thus, the study focuses on the validation process for the SRWT model, the control algorithm, the design of the parameter gain selection and the quadratic equation for the modified power curve.

## **1.4 Research Objectives**

The main objectives of the study were as follows:

1. To design an IMC-based control algorithm that can effectively estimate the parameter values of proportional-integral (PI) and integral-proportional (IP) controllers.
2. To apply the IMC-based approach for the PI and IP controllers to the squirrel-cage induction generator that is coupled with the fully-rated power converter of a stall-regulated variable-speed wind turbine (SRVSWT) system. The goal of the controller was to maximise the generated active power during the partial-load region and maintain or restrict the generator speed to reduce/control power-peaking between the partial-load region and the full-load region before power is limited at the rated value of 25 kW in the full-load region.

## **1.5 Scope of the Study**

The study addresses the following:

1. Description of a SRVSWT system with a squirrel-cage induction generator with a fully-rated power converter.
2. Description and design of IVC and its application to the SRVSWT system.
3. Description and design of SLIVC and its application to the SRVSWT system.
4. Description, design and application of IMC to the squirrel-cage induction generator system of the SRVSWT.
5. Detailed description of the property of the proposed IMC, which employs first-order and time delay models, in the estimation of the proportional and integral parameter values. Only a first-order filter is considered.
6. Detailed description of the property of the proposed IP controller in the IVC model algorithm of a squirrel-cage induction generator.
7. The controller design requirements are as follows:

- Small maximum sensitivity ( $M_s$ ).
  - Small integral absolute error (IAE).
  - Small total variation (TV).
  - Phase margin between 50 and 70 degrees.
  - Minimum overshoot (< 20%).
8. Computer simulation study of a SRVSWT system:
- Step input test.
  - Realistic wind speed profile for speeds ranging from 3 m/s to 20 m/s.
9. Detailed description of the properties of the proposed MoPT approach for power smoothing in the stall region.
10. Comparative study of the effectiveness of the following items:
- controllers (Nichol-Ziegler (ZN), Tyreus-Luyben (TL), IMC-PI and IMC-PI-IP)
  - model algorithm (IVC and SLIVC)
  - power limitation strategy for the intermediate load (constant speed (CS) and MoPT)
- in optimising the available aerodynamic power, restricting the power during the power-peaking zone and limiting power in the high wind-speed region.
11. Wind speeds ranging from 3 to 8 m/s, 8 to 11 m/s, and 11 to 20 m/s were considered in the partial-load region, the intermediate-load region, and the full-load region, respectively.

## 1.6 Major Contributions

The major contributions or novelties of this research are as follows:

1. Modelling development of the fixed-speed stall-regulated wind-turbine (SRWT) system and the variable-speed stall-regulated wind-turbine (VSSRWT) system, in which using the squirrel-cage induction generator (SCIG) that is coupled with the fully-rated power converter. The fixed-speed SRWT simulation model is built up systematically from the simplest

sub-models to the largest content block using Matlab/SIMULINK software environment. The model is intended to represent a 25 kW Carter wind turbine, a machine that is still in operation at West Beacon Farm in Loughborough, UK. The authenticity of the SRWT model has been validated using manufacturer's specification and the on-site measurement data. The fixed-speed SRWT will be then used to develop a variable speed SRWT with the addition of designed indirect vector control (IVC) and sensorless indirect vector control (SLIVC) model algorithms.

2. Estimation of the modified tip speed ratio ( $\lambda_{stall} = \frac{\omega R + (\Delta\omega_{stall} R_{stall})}{U}$ ) of the dynamic stall model of the fixed-speed SRWT system. This estimation is developed to show the effect of tip speed ratio deviation is less reduced when wind speed increases from one state to another state during deep stall. Using this estimation, the power coefficient also demonstrated less reduced compared to the behavior before the tip speed ratio is modified. This exhibits the real turbine behavior when experiencing very high winds where the blades become less sensitive due to turbulence factor. The effectiveness of this model has been proven when the developed SRWT model is validated with the manufacturer and the on-site data measurement.
3. New placement of integral-proportional (IP) controller in the speed controller of the proposed IVC and SLIVC model algorithms of the SRVSWT system is proposed; a single proportional term is applied to the feedback signal and a single integral term is applied to the cumulative errors between the reference signal and feedback signal to obtain a more robust speed controller. An estimation of integral parameter controller value using Internal Model Control (IMC) based design is proposed where two steps are introduced to obtain the integral gain,  $K_i$ ; obtaining the zero pole gain from the open-loop transfer function matrix plant and selecting the controller tuning parameter of  $\varepsilon$ .
4. Modified power tracking (MoPT) strategy at medium wind speeds has been proposed and the success of its reduction peak power has been proven. Using this strategy, the power peaking that naturally occurs on the SRWT during early stall be able to be reduced below the machine

rated power. Additionally, the performance of the MoPT strategy has been compared with the used constant speed (CS) strategy for this wind speed region.

## **1.7 Thesis Layout**

The thesis is divided into six chapters. The basic concepts of WECS and approaches to improve the power control performance of the SRVSWT system have been introduced in this chapter. This chapter has also included the problem background to highlight the importance of the study for the application of active speed control in the SRVSWT system.

Chapter 2 details the adopted SRVSWT system and its theories and components and describes the adopted control schemes and the application of direct and quadrature axis transformation of the SCIG, which is connected to a fully-rated power converter to control the generator speed and torque.

Chapter 3 presents the process of wind turbine modelling of the SRWT system. A step-by-step explanation of the method for developing the model is provided in this chapter. The preliminary results of the characteristics for each sub-model are also presented. The process of validating the sub-model and the complete model is also described and explained. The comparison of the modelling results using the data from the manufacturer with the modelling results using the data from the field test is also included.

The descriptions of the proposed model algorithm (IVC and SLIVC) and the proposed tuning rules (ZN, TL, IMC-PI and IMC-PI-IP) for the SRVSWT system are described in Chapter 4. The reasons for selecting these methods are also discussed.

The simulation results are presented in Chapter 5. Chapter 6 concludes the research findings, states the research contributions and recommends future studies.

## **2 SRVSWT with Stator-Controlled SCIG**

### **2.1 SRVSWT with Fully-Rated Power Converter Control**

For a fully-rated power converter connected to the stator winding, a synchronous or induction generator is typically utilised [6]. Each technology has its advantages and drawbacks. In wind turbine design, the correct selection of generator and drive is very significant because non-optimal selection may lead to poor system performance and increased installation and maintenance costs.

A synchronous generator is a self-excited machine that can manage the active and reactive power by itself. No winding rotor circuit is needed in the configuration system, and the electromagnetic torque can be directly controlled using the generator's total stator current. However, the synchronous generator has some drawbacks, e.g. it is not a self-starting machine. Therefore, a special winding in the rotor poles, known as damper winding, must be provided to solve this problem. Damper winding is auxiliary winding connected in series with the field windings to provide smooth starting torque to a synchronous machine. In a synchronous machine, damper winding is placed in the coil slots and short circuited. This connection enables this additional winding to carry the high starting current needed to create magnetic flux. Thus, better starting torque is provided before the synchronous machine has reached synchronism. Damper winding in the synchronous machine also provides a compensation effect when the synchronous machine has a stability problem during transients and disturbances from the external load. In contrast, for an induction machine, the function of damper winding is obtained naturally without the need for the additional circuit due to its original design (squirrel cage winding in the rotor part). With a synchronous machine, demagnetisation may occur when the machine has a high temperature during heavy loads or short-circuit conditions. The power converter must also be oversized to handle the voltage and power factor control because the synchronous generator cannot handle these by itself.

In a SRWT system, for a fully-rated power converter connected to the wind turbine generator, a solid SCIG may have an equivalent performance to the

synchronous generator [19]. Unlike the synchronous generator, the SCIG is not a self-exciting machine and therefore requires an external reactive power supply [70]. However, this problem can be overcome by commutating the system with the power converter [71]. In fact, the generator torque of an induction machine may also be controlled independently using the same power converter. Under certain conditions, the grid-connected induction generator performs better than the grid-connected synchronous generator in terms of lower torque spikes and softer response [18] because, with the use of a SCIG, speed may be varied by a few per cent of the synchronous speed, unless the synchronous generator is coupled to the power electronics to decouple the synchronous generator from the grid. Indeed, using a SCIG, the speed can be set to almost any desired value. The demanded frequency, phase, and voltage of the current flowing from the generator are determined by the power converter. Thus, when all these required values are established, the generator torque is controlled automatically [18].

As discussed in Chapter 1, for the SRVSWT system, the power control described can be achieved by using generator torque and speed control across the full range of operational wind speeds. Based on the advantages offered by the SCIG, explained above, the advent of the fully-rated power converter has been the key to exploiting the advantages of matching the speed to the changing load torque requirements during wind speed variations. Additionally, SCIGs are well known and are popularly proposed for the SRVSWT configuration as they are generally simple, robust, quite rugged, very reliable, brushless and economical [72]. SCIGs also can also work well under fast transient conditions and with excited programmable inverters or rectifiers [40, 73, 74]. The size of the power converter is smaller than that required if a synchronous generator is used because SCIGs can manage voltage and power factor control, unlike a wind turbine with constant-speed operation, for which a capacitor bank is needed to overcome the problem of poor reactive power control and a soft-starter is needed to manage the in-surge in reactive power from the grid at start-up [70],[75]. In addition, with the power converter, the turbine nacelle can have a lighter design with the power converter set up on the ground, completely separate from the wind generator. For these reasons, the SCIG is being strongly considered as a good option in conjunction with the SRVSWT with fully-rated

power converter control. However, to commercialise the SCIG, this system must be proven practical and reliable. To demonstrate practicality and reliability, the correct control aims and the appropriate design strategies must be chosen before designing the sophisticated control system that needs to be installed in the SRVSWT system.

## **2.2 SRVSWT Control Aims and Strategies**

### **2.2.1 SCIG-based SRVSWT Control Aims**

To design a wind turbine controller, the control aims and the control strategy must be identified. For control aim identification, the turbine regions and the modes of operation are usually determined. The primary aim of this research is to control the active power generated by the SRVSWT for the whole operating region. To be specific, the operating region is divided into three wind regions. Regions of operation depend on the boundary of the wind speeds, for instance, the low (PL), intermediate (IL) or high (FL) wind speed conditions, see Figure 1-5. In wind energy production, power is generated when the wind speeds operate between the cut-in and cut-out wind speeds. Different turbines have different cut-in and cut-out wind speeds depending on their designs. Certain designs will consider 3.5 or 4 m/s as the cut-in wind speed while cut-out wind speed might be as high as 40 m/s, though 25 m/s is more usual. Thus, the modes of operation always refer to a fixed speed, a variable speed, or a combination to ensure that the control objectives can be reached over the full range of operational wind speeds [17].

In this study, the control aims were divided into three main regions: Region I (PL), Region II (IL) and Region III (FL). For SRVSWT, the power optimisation and limiting can be changed by accelerating or decelerating the rotor for low, intermediate or extreme winds. Therefore, the method for obtaining the target reference speed for all regions is explained in section 2.2.2.1 to section 2.2.2.3.

### 2.2.1.1 Region I: Partial Load (PL)

In the PL region, the turbine will start to generate energy when the wind speeds reach  $v_{cut-in}$  and the turbine successfully absorbs and overcomes the existing windage, friction, core and copper losses. In this region, the maximum power from the wind should be captured for each wind-speed condition. For a given wind speed, the aerodynamic efficiency varies with rotor speed. The maximum power occurs at a different speed point. A unique point on the power/rotor speed plane exists where the maximum aerodynamic efficiency is reached. The maximum aerodynamic efficiency corresponds to the maximum value of the aerodynamic power coefficient ( $C_{pmax}$ ). The locus of the points of maximum aerodynamic efficiency, implicitly parameterised by wind speed, together with the curves of constant wind speed from 2 m/s to 24 m/s are shown in Figure 1-4 in Chapter One.

In this study, for the PL region (Region I), the maximum power is aimed to be absorbed when the wind speed is 3 to 8 m/s. For this region, the wind turbine operating point should be kept at the peak of its power coefficient. The power coefficient ( $C_p$ ) of a turbine is defined as the ratio of the turbine aerodynamic power ( $P_{turbine}$ ) to the power available in the wind ( $P_{wind}$ ) [18], [35]:

$$C_p = \frac{P_{turbine}}{P_{wind}} \quad (2-1)$$

where

$$P_{wind} = \frac{1}{2} \rho \pi A U^3 \quad (2-2)$$

where  $\rho$  is the air density,  $A$  is the area swept by blade rotation and  $U$  is the wind speed.

From Equation (2-1), the turbine power ( $P_{turbine}$ ) seems to be directly proportional to  $C_p$ . Thus, to obtain the maximum rotor power, operation at the peak of the power coefficient ( $C_{pmax}$ ) is clearly desirable.  $C_{pmax}$  is the maximum power coefficient or the maximum power extraction efficiency of a wind turbine. Hence, the maximum turbine power can be expressed as

$$P_{turbine} = \frac{1}{2} \rho \pi A U^3 C_{pmax} \quad (2-3)$$

However, for general use, the turbine power beyond the state of maximum power can be estimated using Equation (2-3), with  $C_{pmax}$  being replaced by the  $C_p$ .

Because the aerodynamic performance of a wind turbine is usually characterised by the variation of the non-dimensional power coefficient ( $C_p$ ) versus the tip speed ratio ( $\lambda$ ), the power extracted by a wind turbine with a blade length of  $R$  in Region I can be written as

$$P_{turbine} = \frac{1}{2}\rho(\pi R^2)C_{pmax}U^3 \quad (2-4)$$

To relate the shaft rotational speed with Equation (2-4), the wind speed term can be arranged by inserting Equation (2-5), where the wind speed, blade speed and the tip speed ratio are correlated, as defined in [18], [35]:

$$U = \frac{\omega_t R}{\lambda_{opt}} \quad (2-5)$$

where  $\omega_t$  is the rotational speed of the rotor blade (the front shaft rotational speed) in rad/s and  $\lambda_{opt}$  is the optimum value of  $\lambda$  when  $C_p$  has a well-determined maximum at  $C_{pmax}$ .

Thus, the final equation used to extract the maximum turbine power in the PL region  $P_{C-Law1}$  is as found in Equation (2-6):

$$P_{C-Law1} = \frac{1}{2}\rho(\pi R^2)C_{pmax}\left(\frac{\omega_t R}{\lambda_{opt}}\right)^3$$

$$P_{C-Law2} = \frac{1}{2}\rho(\pi R^5)C_{pmax}\left(\frac{\omega_t}{\lambda_{opt}}\right)^3 \quad (2-6)$$

The generic relationship between  $C_p$ ,  $C_{pmax}$ ,  $\lambda$  and  $\lambda_{opt}$  is shown in Figure 2-1.

However, the turbine power can also be defined in other ways, e.g. by researchers [18], [35], as

$$P_{C-Law1} = T_{aero}\omega_t \quad (2-7)$$

where  $T_{aero}$  is the aerodynamic torque. Thus, the target aerodynamic torque for this region can be calculated by Equation (2-8).

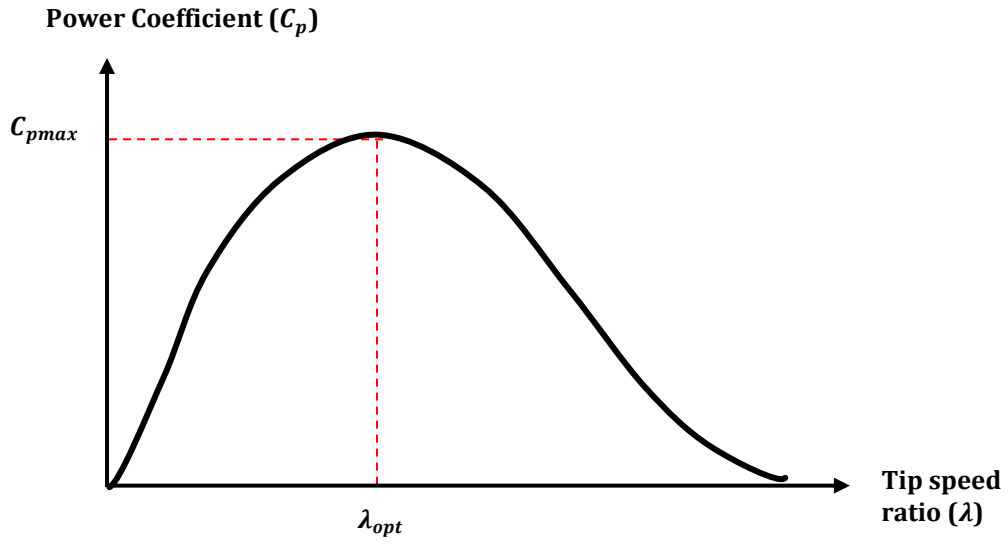


Figure 2-1  $C_p - \lambda$  curve [18]

$$T_{aero} = \frac{P_{C-Law1}}{\omega_t} = \frac{\frac{1}{2}\rho(\pi R^5)C_{pmax}\left(\frac{\omega_t}{\lambda_{opt}}\right)^3}{\omega_t} = \frac{1}{2}\rho(\pi R^5)C_{pmax}\left(\frac{1}{\lambda_{opt}}\right)^3\omega_t^2 \quad (2-8)$$

The equation can be simplified as

$$T_{aero} = \frac{1}{2}\rho(\pi R^5)C_{pmax}\left(\frac{1}{\lambda_{opt}}\right)^3\omega_t^2 = K_T\omega_t^2 \quad (2-9)$$

where

$$K_T = \frac{1}{2}\rho(\pi R^5)C_{pmax}\left(\frac{1}{\lambda_{opt}}\right)^3 \quad (2-10)$$

To ensure that the optimum operating point (OP) occurs regardless of wind speed fluctuation, the turbine rotational speed  $\omega_t$  must be regulated as in Equation (2-11) or Equation (2-12).

$$\omega_t = \omega_{ref} = \omega_{opt} = \sqrt{\frac{T_{aero}}{K_T}} \quad (2-11)$$

or

$$\omega_t = \omega_{ref} = \omega_{opt} = \frac{\lambda_{opt}U}{R} \quad (2-12)$$

The SCIG-based SRVSWT control aims and its adapted laws for Region I for this study involve the control mode, wind speed range, tip speed ratio, and the locus of shaft power, rotor speed and power coefficient. These are summarised in the first column (coloured pink) in Figure 2-2.

### 2.2.1.2 Region II: Intermediate Load (IL)

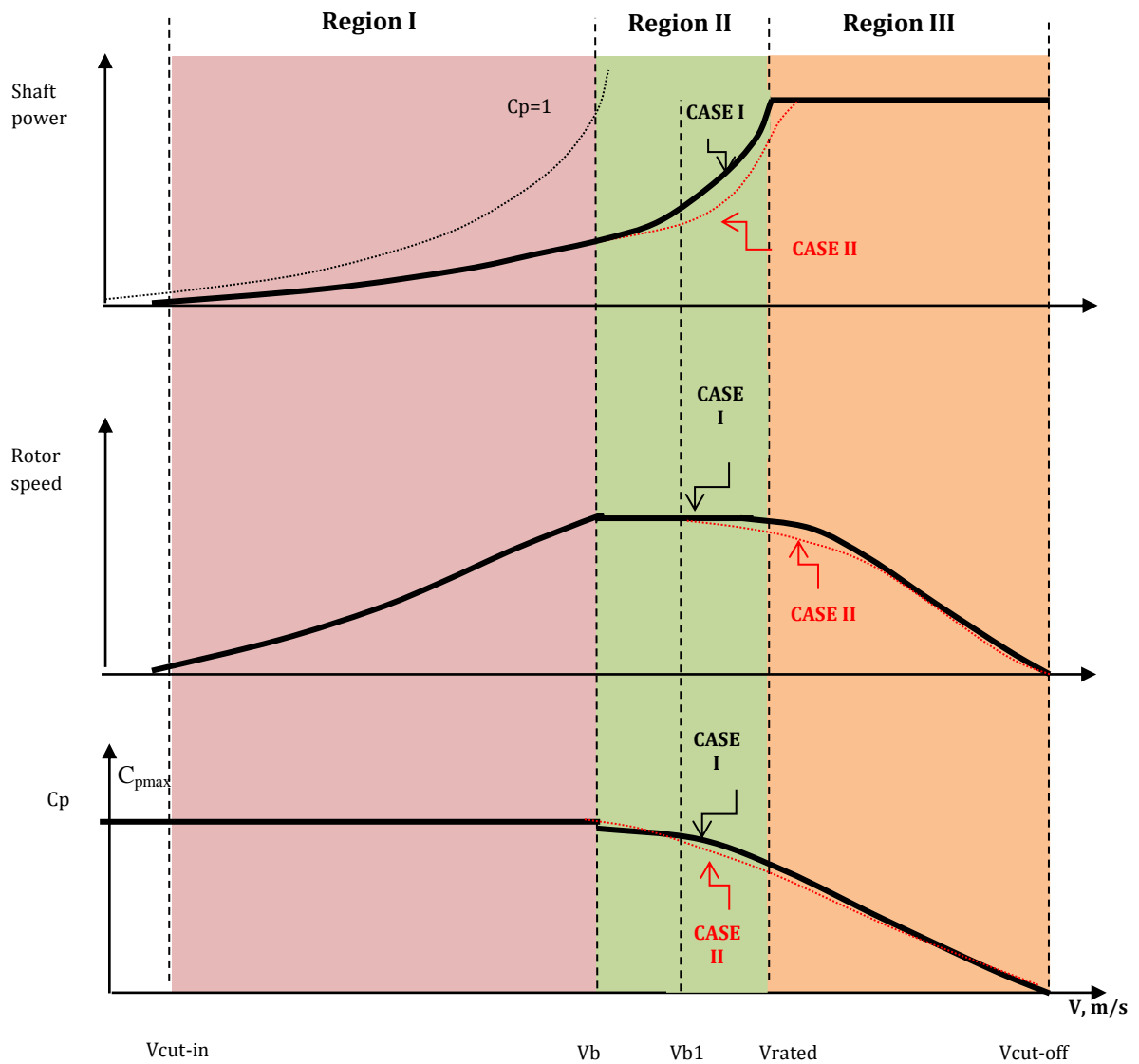
In region II, aerodynamic power and torque deviate from following the maximum power locus. To produce smoother power-peaking during the region transition (from Region I to Region II), a combination of operation modes (variable and fixed speed) are applied. For this region, this research attempted two case studies: Case I (CS) and Case II (MoPT).

#### Case I (CS):

Power reduction from the cube factor is started but power continues to increase by limiting the rotor speed to a constant speed (CS). In this study, the wind speed reached  $v_b$  when the wind speed is greater than 8 m/s. Meanwhile,  $v_{rated}$  is reached when the wind speed is greater than 11 m/s. For Case I, for which the speed should be limited to a fixed speed in the intermediate region, the target rotational speed is as shown in Equation (2-13).

$$\omega_t = \omega_{ref} = \omega_{fixed} \quad (2-13)$$

In this case, the turbine works in fixed-speed mode as long as the wind speeds are between  $v_b$  and  $v_{rated}$ .



	REGION I	REGION II	REGION III
Control Aim	Power optimization	Reduced power	Rated power
Control Mode	Variable speed	CASE I Fixed speed	Variable speed
		CASE II Fixed speed	CASE II Variable speed
Wind speed range	3 to 8 m/s	CASE I 8 to 11 m/s	11 to 20 m/s
		CASE II 8 to 10 m/s	CASE II 10 to 13 m/s
Power coefficient (Cp)	Maximum power coefficient ( $C_{pmax}$ )	$0 < C_p < C_{pmax}$	
Tip speed ratio ( $\lambda$ )	Optimum tip speed ratio ( $\lambda_{opt}$ )	$0 < \lambda < \lambda_{opt}$	

Figure 2-2 Control aims and laws for the proposed SCIG-based SRVSWT system

### Case II (MoPT):

In Case II, power is managed to be diverted from continuously following the maximum power tracking by modifying the maximum power locus (MoPT), which can be achieved by restricting the rotor speed by following a certain track curve. Power can be increased or decreased at each wind speed if the power curve is modified upward or downward, respectively. For this Case II, in which speed should be limited ( $\omega_{ref} = \omega_{fixed}$ ) and restricted ( $\omega_{ref} = \omega_a, \omega_b$  or  $\omega_c$ ) in the IL region, the target rotational speed and the power laws are expressed in Equations (2-14) to (2-17).

$$\omega_t = \omega_{ref} = \omega_{fixed} \quad (P_{C-Law2} \approx 96 - 97\% \times P_{C-Law3}) \quad \text{for } 8 \leq U < 10 \text{ m/s} \quad (2-14)$$

$$\omega_t = \omega_{ref} = \omega_a \quad (P_{C-Law2} \approx 96 - 97\% \times P_{C-Law3}) \quad \text{for } 10 \leq U < 11 \text{ m/s} \quad (2-15)$$

$$\omega_t = \omega_{ref} = \omega_b \quad (P_{C-Law2} \approx 94 - 96\% \times P_{C-Law3}) \quad \text{for } 11 \leq U < 12 \text{ m/s} \quad (2-16)$$

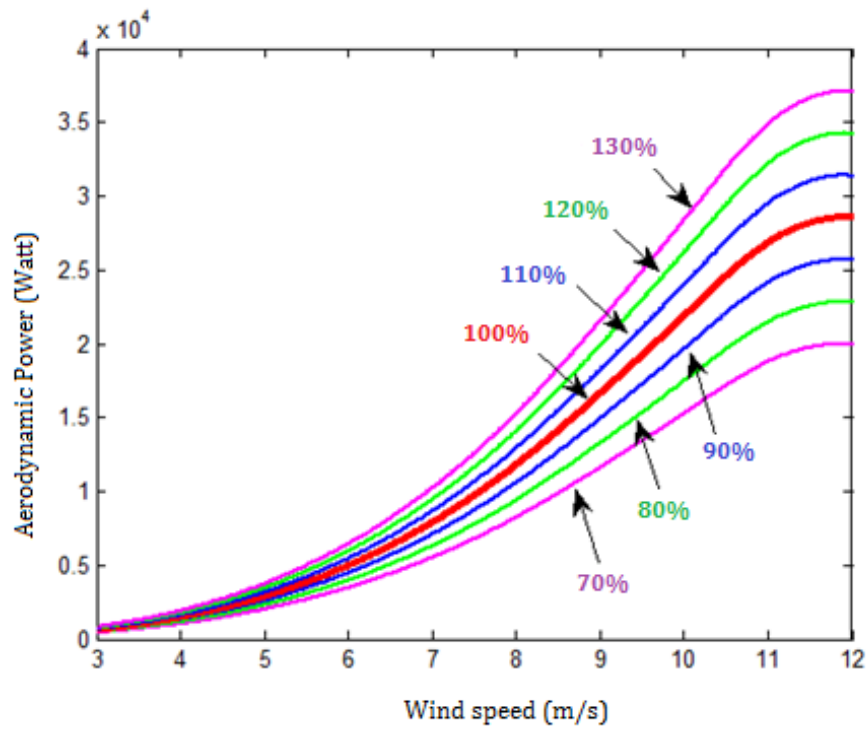
$$\omega_t = \omega_{ref} = \omega_c \quad (P_{C-Law2} \approx 94 - 99\% \times P_{C-Law3}) \quad \text{for } 12 \leq U < 13 \text{ m/s} \quad (2-17)$$

where  $\omega_t$  is turbine speed,  $\omega_{ref}$  is target rotational turbine speed,  $\omega_{fixed}$  is maximum permitted speed and  $U$  is wind speed. In Equations (2-14) to (2-17), two power laws are involved;  $P_{C-Law2}$  and  $P_{C-Law3}$ , where  $P_{C-Law2}$  is the turbine power in the IL region meanwhile  $P_{C-Law3}$  is the rated power or the turbine power in the FL region.

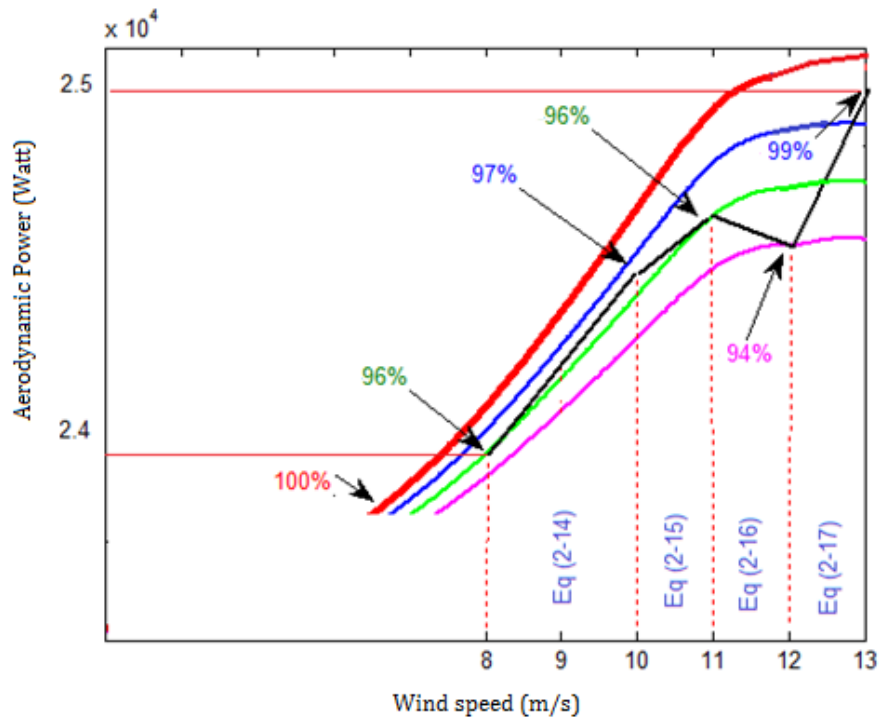
As can be seen in Equation (2-14) and (2-15), these equations are actually look the same. But, they are actually giving different effect to the power control when  $\omega_{ref} = \omega_{fixed}$  and  $\omega_{ref} = \omega_a, \omega_b$  or  $\omega_c$  strategies are applied into the control system. Though the rotor speed is fixed and then changed (reduced), the generated power continues to increase due to the increase in wind speed.

To be specific, for this Case II, when the wind speed reaches  $v_b$ , the turbine speed needs to be limited at the maximum permitted speed,  $\omega_{fixed}$ . During this time, control will follow the rule that written in Equation (2-14).

Power can be reduced up to 4% from the rated power. The generic modified power can be illustrated in Figure 2-3(a).



(a)



(b)

Figure 2-3 The aerodynamic power versus wind speed, with various efficiencies

From the figure, note that, the generated power is at the rated value when the power curve is laid at 100%. At curve 90%, 80% and 70%, power is reduced 10%, 20% and 30% from the rated power, respectively. Similarly, when power curve laid at 110%, 120% and 130%, it meant that power is increased 10%, 20% and 30% from the rated power, respectively. However, for these power curves, where power curves are greater than 100%, operation should be avoided because at this region, stall occurs and certainly turbine must be kept away from the deep stall conditions. Meanwhile, when the wind speed increases and is greater than the specific  $v_{b1}$ , the rotor speed needs to be reduced from the maximum permitted rotor speed until the wind speed reaches  $v_{rated}$ . During this time, control will follow the rule that written in Equation (2-15), then Equation (2-16) and finally Equation (2-17) when wind speed keep increasing linearly from 10 to 13 m/s. When turbine speed is set to  $\omega_{ref} = \omega_a \omega_b$  or  $\omega_c$ , power can be reduced up to 4% to 6% from the rated power. As power captured can be increased or reduced in a large quantity by having small rotor speed change, a careful design must be paid into attention during the design. Small percentage power reduction could reduce some significant amount of captured power. In Figure 2-3(b), the approach on how Equations (2-14) to (2-17) is used is exhibited. In the figure, it can be depicted that power is kept increased from 96% to 97% of the rated power when wind speed reaches 8 m/s. During this range ( $8 \leq U < 10$  m/s), Equation (2-14) is used. When wind speed increases from 10 m/s, power is reduced from 97% to 96% the rated power. When wind speed keeps increases again, power is further reduced by 2% from the previous target where Equation (2-16) is used during this range.

However, for wind speed from 12 to 13 m/s, power is kept increased from 94% up to 99% of the rated power. During this time, Equation (2-17) is employed. From this figure, it can be observed that for wind speed between 11 to 13 m/s, an inverted triangular curve can be observed. From 11 to 12.5 m/s, power needs significantly reduced this time because power peaking is naturally occurred when stall blade is employed. By employing Equation (2-17), power can be managed to be lowered than the rated value. When wind speed reaches 13 m/s, power is controlled to work near the rated power before limited at the rated value when wind speed keeps increases.

With the intention that the power be captured does not exceed the rated power, but at the same time there is only a slight power reduction, estimations based on the percentage values of the rated power are considered. By replacing the  $C_{pmax}$  with the  $C_p$  value in Equation (2-3), the turbine power in general conditions can be estimated. By considering reductions between 94 to 99% from the rated power level, a new  $C_p$  is determined. Using the  $C_p - \lambda$  curve, a new  $\lambda$  is determined. The considered  $C_p$  and  $\lambda$  are in the ranges  $0 < C_p < C_{pmax}$  and  $0 < \lambda < \lambda_{opt}$ , respectively, as shown in the second column (coloured green) in Figure 2-2. With the determined  $\lambda$  value replacing  $\lambda_{opt}$ , Equation (2-12) is used to calculate the target rotational blade speed. From the tests that were conducted on a repetitive basis, it was found that a different percentage for each wind speed (from 8 to 13 m/s) provides the best reasonable power, as targeted by the control design.

In this study, for Region II, the wind speed reaches  $v_b$  when the wind speed is 8 m/s,  $v_{b1}$  when the wind speed is 10 m/s and  $v_{rated}$  when the wind speed is 13 m/s.

The SCIG-based SRVSWT control aims and its adapted laws for Region II for this study, involving the control mode, wind speed range, tip speed ratio, and the locus of shaft power, rotor speed and power coefficient are summarised in the second column (coloured green) in Figure 2-2.

### 2.2.1.3 Region III: Full Load (FL)

During FL, power efficiency is further reduced by prohibiting the turbine from following the  $C_{pmax}$  trajectory to restrict power at the rated value. The turbine is constrained to operate at lower values of  $\lambda$  and  $C_p$ , thereby slowing down the rotor speed, as shown in the third column (coloured orange) in Figure 2-2. By inserting Equation (2-10) into Equation (2-6), the target power in this region ( $P_{C-Law3}$ ) can be calculated using Equation (2-18) or Equation (2-19). The target torque in this region can be estimated using Equation (2-20) or Equation (2-21).

$$P_{C-Law3} = P_{rated} = k_T(\omega_{FL})^3 \quad (2-18)$$

$$P_{C-Law3} = P_{rated} = T_{aero}\omega_{FL} \quad (2-19)$$

$$T_{C-Law3} = \frac{P_{rated}}{\omega_{FL}} = k_T(\omega_{FL})^2 \quad (2-20)$$

$$T_{C-Law3} = \frac{P_{rated}}{\omega_{FL}} = k_T(\omega_{FL})^2 = k_T^{1/3}(P_{rated})^{2/3} \quad (2-21)$$

where  $P_{rated}$  is the maximum or rated power of the SCIG and  $\omega_{FL}$  is the turbine speed for the FL region. Thus, when the power is not optimised and limited at a rated value, the target speed in Region III can be derived from the following equation:

$$\omega_t = \omega_{ref} = \omega_{FL} = \frac{P_{rated}}{T_{aero}} \quad (2-22)$$

Thus, when the turbine experiences a wind speed greater than  $v_{cut-out}$ , the turbine must be shut down to prevent any failure or breakdown of the turbine.

The SCIG-based SRVSWT control aims and its adapted laws for Region III for this study, involving the control mode, wind speed range, tip speed ratio, and the locus of shaft power, rotor speed and power coefficient, are summarised in the third column (coloured orange) in Figure 2-2. To understand how the rotor speed is controlled due to the various velocities at the blade, the relationships between the forces developed at the blade, relative wind, angle of attack and the turbine speed must be understood first. Therefore, in the next section, the theory describing the forces on a blade element is explained.

#### 2.2.1.4 Forces on a Blade Element

To control the power from the SRVSWT system, torque control is required. To control the torque, turbine/generator speed control is necessary. Control of the speed depends on the existing relative wind and the forces developed at the blades. In the blade element, the forces involved are lift ( $f_L$ ) and drag ( $f_D$ ) forces, which are perpendicular and parallel, respectively, to the relative wind,  $W$ . The relative wind is the summation vector of the wind velocity at the rotor,  $U(1 - a)$ , and the wind velocity of the blade rotation,  $\Omega r(1 + a')$ .  $\Omega r$  is the blade section velocity,  $a$  is the axial induction factor and  $a'$  is the angular (tangential) induction factor.  $a$  is a function of the tip speed ratio,  $\lambda$ . The way the

rotor speed is controlled by the various angles and velocities at the blade, from the blade tip orientation, is shown in Figure 2-4.

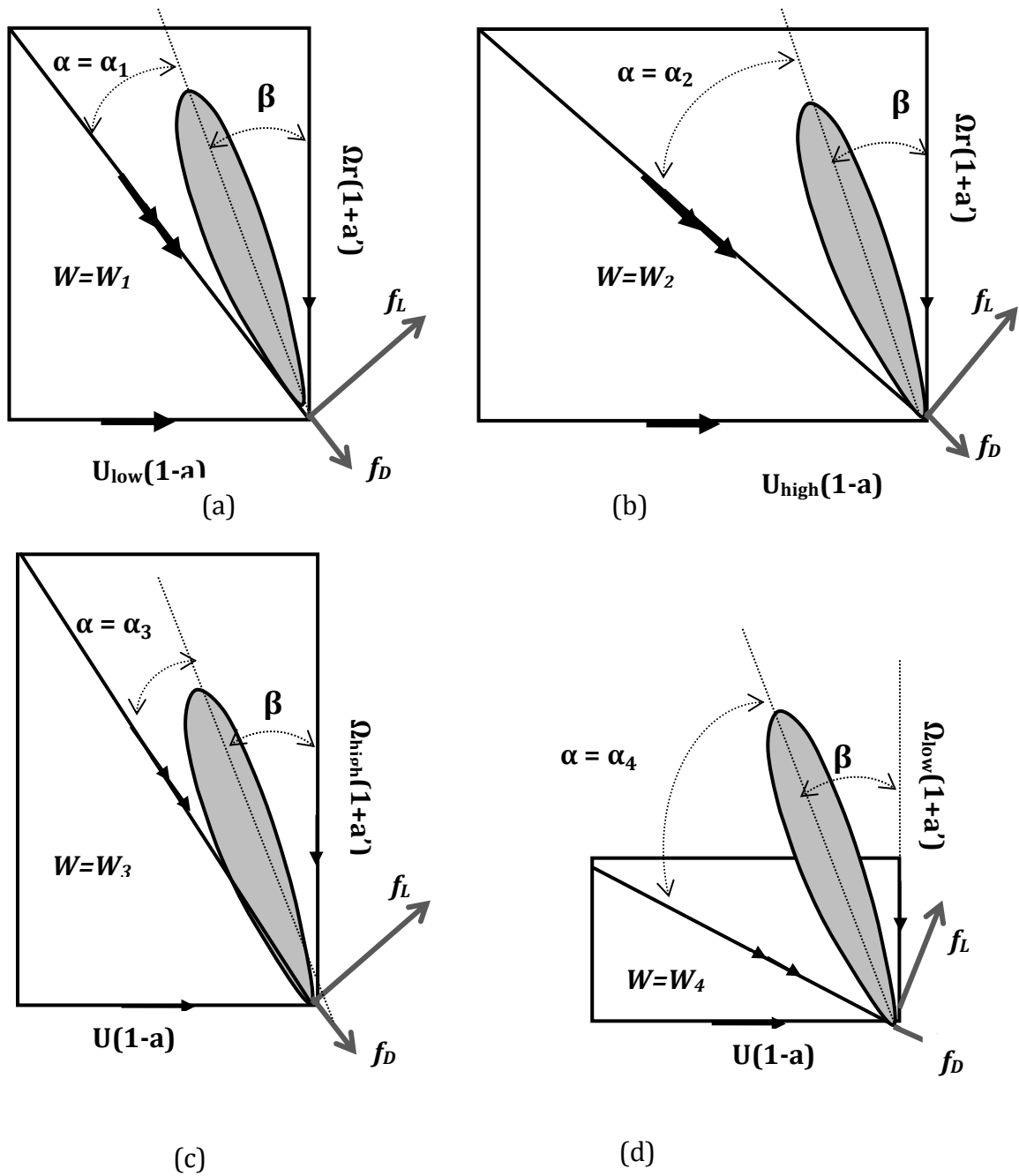


Figure 2-4 Forces on a blade element

Based on Figure 2-4(a) and Figure 2-4(b), which show two conditions of wind velocity,  $U(1-a)$  can be described. The different condition of wind velocity at the rotor at low wind velocity ( $U_{low}$ ) and high wind velocity ( $U_{high}$ )

are shown in Figure 2-4(a) and Figure 2-4(b), respectively. For a fixed-pitch SRWT, the blade pitch angle ( $\beta$ ) is fixed. Assuming that the velocity of the blade rotation  $\Omega r(1 + a')$  is constant, the angle of attack ( $\alpha$ ) created during  $U_{\text{low}}$  is smaller than in  $U_{\text{high}}$  ( $\alpha_1 < \alpha_2$ ). When wind velocity increases ( $U(1 - a) = U_{\text{high}}(1 - a)$ ), the relative wind speed also increases ( $W = W_2$ ), where  $W_2 > W_1$ . Hence, the blade angle of attack also increases ( $\alpha = \alpha_2$ ). At low angles of attack, the wind flow is attached to the upper surface of the blade aerofoil. In this condition of  $\alpha$ , lift ( $f_L$ ) increases relative to the created  $\alpha$ , but drag ( $f_D$ ) is relatively low. However, during high wind velocity, when  $\alpha$  increases and is greater than the critical value of the angle of attack, a wake is formed above the aerofoil, decreasing the lift and increasing the drag force, where the stall occurs. Therefore, these two wind cases show that the condition of stall is influenced by the angles of attack ( $\alpha$ ).

However, from Figure 2-4(c) and Figure 2-4(d), which show two conditions of different blade rotation,  $\Omega r(1 + a')$  is depicted. The different condition of blade rotation - at faster blade rotation ( $\Omega_{\text{high}}(1 + a')$ ), and slower blade rotation ( $\Omega_{\text{low}}(1 + a')$ ) - are shown in Figure 2-4(c) and Figure 2-4(d), respectively. Again, recall that, for a fixed-pitch SRWT, the blade pitch angle ( $\beta$ ) is fixed. Assuming that the wind velocity,  $U(1 - a)$  at the rotor remains constant (the same situation as in the case of Figure 2-4(a)), the created angle of attack ( $\alpha$ ) during blade rotation  $\Omega r(1 + a')$  equal to  $\Omega_{\text{high}}(1 + a')$ , is equal to  $\alpha_3$  ( $\alpha_3 < \alpha_1$ ). Figure 2-4(c) shows that when wind velocity is constant and the blade rotation  $\Omega r(1 + a')$  is equal to  $\Omega_{\text{high}}(1 + a')$ , the angle of attack  $\alpha$  is equal to  $\alpha_3$ . Therefore, the resultant relative wind ( $W$ ) increases from  $W$  to  $W_3$ , as shown in Figure 2-4(c).

If the blade rotation  $\Omega r(1 + a')$  is reduced to  $\Omega_{\text{low}}(1 + a')$ , remember that  $\beta$  is fixed,  $\alpha$  increases to  $\alpha = \alpha_4$ . Hence, the resultant relative wind ( $W$ ) decreases from  $W$  to  $W_4$ , as shown in Figure 2-4(d). Thus, by controlling the blade angles of attack ( $\alpha$ ), which is achieved by changing the magnitude of the velocity of the blade rotation, the turbine condition can be controlled. By increasing the rotational speed of the blade,  $\alpha$  can be decreased; the lift force ( $f_L$ ) can be increased by decreasing the drag force ( $f_D$ ), as shown in Figure 2-4(c).

Thus, from Figure 2-4, it can be concluded that the stall behaviour can be controlled by controlling the blade angles of attack,  $\alpha$ . To control  $\alpha$ , the rotational speed of the rotor blade,  $\Omega$  must be controlled. However,  $\alpha$  and  $\Omega$  need to be controlled within the permitted range. For the fixed-pitch blade ( $\beta$  is fixed), power regulation in this region implies a movement towards the left in the  $C_p - \lambda$  plane, until the rated torque is reached. However, if the turbine loses its stability, the regulation may imply a movement towards the right in the  $C_p - \lambda$  plane (unstable region). As shown in the  $C_p - \lambda$  curve in Figure 2-1, when  $\lambda$  moves away from the  $\lambda_{opt}$ , the  $C_p$  becomes smaller, thus leading to a reduction of power efficiency. When stall begins,  $\lambda$  starts to deviate from the state of  $\lambda_{opt}$ . When wind speeds keep increasing, the  $\lambda$  will be even smaller corresponding to the reaction of the rotor speed and the increasing wind speed. Bear in mind that the air density and turbulence intensity on the blades change significantly during high winds. In fact, during high winds, the high rotor inertia decreases the natural time-constant of the rotor. Longer time is required to change the rotational speed from the previous state to a new rotational speed since the rotor time-constant decreases inversely with the wind speed [76]. Besides, during high winds where  $\lambda$  gets lower, blade vibrations may occur [57]. All these phenomena cause the turbine rotor to become even more difficult to control as expected.

For a fixed-pitch blade with variable speed operation, along the FL region, the early stall domain is the most challenging region to control [57]. If the wind turbine operates above stall speed, the system lacks protection from gusts. Thus, the turbine will rotate at a high rotor speed and with rapid increases of wind speeds, power peaks would be formed.

In the presence of gusts, power typically will increase abruptly. The rotor speed starts to be decelerated when the control system detects the errors. This starting process of this deceleration may lead to the formation of extra power. The same situation may occur when the rotor speed starts to be accelerated when wind speed decreases. These situations, however, show that increases or decreases in wind speed make it difficult to keep power always at the desired level.

## **2.2.2 SCIG-based SRVSWT Control Strategies**

In this research, SCIG was chosen for the SRVSWT system. To perform SCIG control via the power converter requires two types of control strategy; scalar control (SC) and vector control (VC). These advanced strategies have been widely used as modern alternative methods in induction machine control, particularly in motor speed control applications, such as those found in [77], [78], [79] and [80]. The difference between these two strategies is explained next.

### **2.2.2.1 Scalar Control (SC)**

Scalar control is a relatively simple method. It refers to the magnitude of the variation of a control variable only and disregards any phase change of the control variable. In machine operation, there are coupling effects in the machine variables, but using SC, these coupling effects are unnoticed. For instance, to control machine flux, the voltage source and the frequency of the stator machine need to be controlled. Meanwhile, to control the torque, the frequency or the slip of the machine need to be controlled. Therefore, coupling effects in the machine variables exist, this shows that flux and torque are functions of frequency and voltage, respectively.

SC is simpler than VC in terms of variable control and application. In VC, both the magnitude and phase of the control variable are controlled indirectly, unlike in SC where only magnitude is controlled. In SC, the transient performance is not possible, but the steady-state model of an induction machine is mainly used to derive this technique. Due to this, SC is easier to control and implement, but this drive offers somewhat poorer performance due to the inherent coupling effect. To explain more clearly, when the frequency (or slip) is increased, torque can be increased as well as with the increment of frequency (or slip), enabling the decrease in flux. This flux is then compensated for by the flux control loop which is then fed to the control input (voltage). This temporary decrease in flux reduces the torque sensitivity to slip, thereby increasing the response time. In addition, using SC, the magnitude of variables such as the voltage and the

frequency of the stator voltages are determined from the steady-state properties of the machine only and do not consider transient conditions [81].

Hitherto, scalar controlled drives have been widely used in industry. Their importance, however, has diminished recently because of the sophisticated performance of vector controlled drives, which are demanded in many applications.

### **2.2.2.2 Vector Control (VC)**

After the invention of vector control in the 1970s, the analysis of induction machines became easier where the machine could be controlled as the mean of a separately-excited DC machine. In a DC machine, the field flux produced by the field current is perpendicular to the armature flux produced by the armature current. These fields are decoupled and stationary with respect to each other. Consequently, when the armature current is controlled to control the torque, the field flux remains unaffected, thus a fast transient response is achieved.

In an induction machine, with VC, the DC machine operation can be imitated, where the torque and flux can be controlled separately by transforming all controlled variables to DC instead of AC using mathematical transformation. Therefore, machine variables can be decoupled, and then controlled without affecting each other, unlike the SC situation. Using VC, the control variables (such as voltage, current and flux linkage vector) flow in separate windings; flux and torque loop control [82]. For this reason, this technique solves the problems found in SC, particularly in terms of system response time. With VC, fast periodic speed variations can be realized [83]. In fact, using VC, the magnitude, frequency and instantaneous position of the control variables such as voltage, current and flux linkage vector are controlled and valid for both steady state and transient conditions. However, to implement VC, a system that is more complex than SC is required due to the more powerful microcomputer, microprocessor or digital signal processing (DSP) system in the VC drives.

Using the superior VC permits an algebraic transformation that converts the dynamic structure of SCIG into that of a separately-excited, decoupled control structure with independent control of flux and torque. For the SRVSWT system

with SCIG, it is expected that the responses of its system dynamics can be controlled quickly with VC where rapid periodic electrical rotor speed variations can occur, particularly during wind turbulence and gusts.

The application of this control strategy in the SRVSWT proposed in this research is explained in detail in Chapter Four. Work involving the use of SC and VC in the wind turbine application is reviewed next.

### **2.2.2.3 Applications of SC and VC in Wind Turbines**

Active generator control using VC, also known as the field-oriented approach on VSWT models, has been widely investigated by many researchers. In the research of Ohyama et al. [84], a study was performed to control the wind-generated power and generator rotational speed. VC was used and was compared with the slip frequency control system but using sensorless techniques. Speed is not measured but was estimated using the adaptive rotor flux observer, which is a system that provides an estimate of the rotor flux state of a given real system in an online environment from measurements of the input and output of the real system. In this study, the online phase voltage and phase current are used as the input variables whilst the rotor speed and rotor flux are chosen as the output variables. Meanwhile, sensorless slip frequency control is a method where the stator voltage or current is controlled by maintaining the rotor flux at a constant value of  $V/\omega_s$  where  $V/\omega_s$  is the ratio between the stator voltage and the synchronous speed. The synchronous speed is obtained by summing the estimated rotor speed to the slip speed that was produced from the inner PID loop. Research found that VC performed better than the sensorless slip frequency control in terms of speed and power references.

In the autonomous wind turbine application, Idjdarene *et al.* [85] focused on the terminal voltage control of the isolated wind power, which was driven by an induction generator. The effect of generator saturation was considered, and the diphasic model of an induction machine was used. The outcome shows that the saturation level can be maintained and that the DC voltage can be controlled at a constant level through the torque control. Another example of the application of VC to the autonomous wind power system is found in Cardenas *et*

*al.* [86]. Power smoothing was the main objective of this work, in particular, during power surges/sags (from the turbine side) or sudden changes from the load demand side. Smoothing power was executed using a nonlinear controller with feedforward compensation.

From the literature survey, it was found that most of the existing research involving VC on the VSWT focused on the DFIG applications. For example, Babu *et al.* in [87] modelled and simulated the steady-state and transient behaviours of DFIG. The results, including voltage, current, torque and inverter responses, were demonstrated for both conditions. In [88], Mugica also developed and modelled the behaviour of the DFIG wind turbine. However, in Mugica's work, two full models, two simplified models and two steady-state models were developed and compared. The findings show that the steady-state models did not represent the actual behaviour during instability. The research also used PSCAD and MATLAB software to analyse the results. Davijani *et al.* [89] also used PSCAD software in their research on the DFIG wind turbine, but the PSCAD was combined with EMTDC software. In this study, researchers used the combination of adaptive control, namely fuzzy control, of the VC model to give better performance in terms of power quality and stability for fault test design, particularly during abnormal conditions. A test was performed for three line-to-ground short circuits. To improve the power quality on VSWT, Ibrahim [90] proposed VC with a hysteresis current controller. In addition to research in [89], research on DFIG fault analysis is also found in [91] by Xu *et al.* and [92] by Thakre. However, the research in [91] by Xu *et al.* focused on voltage dips and swell effects. Testing was conducted under symmetrical low and high grid voltage faults where the effect of magnetic flux saturation was also considered. The combination of a PI controller with a current regulator was also adopted in this work. Thakre [92] performed VC on the DFIG wind turbine under balanced and unbalanced conditions to control the power flow while handling unbalanced currents and suppressing the torque and reactive power pulsations.

In addition to the issue related to grid connection, many researchers also studied power optimisation and power limitation on a DFIG system. Examples of studies on power optimisation using VC on a DFIG system were performed by Pan *et al.* in [93] and Aouzellag *et al.* in [58]. In [93], nonlinear control

approaches such as sliding mode and extreme seeking control (ESC) were applied to improve performance during maximum power tracking. Active and reactive stator powers were controlled without flux estimation. The authors claimed that the proposed sliding mode performance is similar to the performance of direct power control (DPC), although the sliding mode approach is simpler than the DPC. However, in [58], Aouzellag et al. used an RST regulator with good power tracking performance. The RST is a polynomial regulator. The elements R, S, and T are polynomials in which the degree is fixed according to the degree of the transfer functions of continuation and regulation in an open loop. They are calculated using a strategy of robust pole placement. Arifujjaman *et al.* [94] also undertook research involving power optimisation. However, they include work involving power limitation strategy. During power optimisation, Arifujjaman *et al.* used a speed/current control technique, whereas, during the above-rated wind speed, pitch control was executed. In addition to application to the induction generator, VC was applied to the permanent magnet synchronous generator for wind turbines described in [95] by Mora.

Examples related to the implementation of SC in the DFIG system by Jovanovic *et al.* are available in [96]; these compare the performance of SC and VC for a brushless, doubly-fed, reluctance machine and study the trade-off between machine performance and the converter size. This study was performed for large pump and wind turbine generator applications. In [97], written in 2009, Jovanovic improved upon [96], adding direct torque control for sensorless speed control for applications similar to those studied in [96]. Additionally, Rajaji and Kumar in [98] presented a simulation of a stand-alone DFIG wind turbine using SC and a neural network controller to control the stator voltage so that power can be captured at the optimum power coefficient during power optimisation. Optimisation work using SC can also be found in [99] by Constantin, where SC is used to control the synchronous frequency.

Research on the grid side during disturbance or unbalanced conditions using SC was performed by Wu in [8] and by Bouaziz in [100]. Wu performed a study on harmonic elimination and power factor control while Bouaziz investigated the feasibility of variable-speed pitch-regulated wind turbines using PI controllers and hysteresis controllers. Focus on power quality improvement

on the grid side is also found in the literature. For example, Kanellos et al. [101] used SC to regulate reactive power, which maintains grid voltage to improve the quality of generated power while suppressing the mechanical stress. In [102], Vongmanee experimented with using SC in an emulator of the wind turbine generator using SCIG to improve the quality of wind power and enhance the speed stability.

From the literature survey in this chapter, it was found that the use of VC and SC in SRVSWT is not available, but their use was actively proposed and performed in the DFIG wind turbine system. But, since VC was widely used, proven reliable and provides faster response through decoupling control of torque and speed, this study examines the potential of VC as a control strategy applied to the full-rated power converter on the SCIG-based SRVSWT system. Before demonstrating the modelling work of the SRWT system, the SCIG-based SRVSWT system is described in the next section, which provides useful information on how the VC strategy can be applied through direct- and quadrature-axes control.

## **2.3 Description of SCIG-based SRVSWT**

### **2.3.1 SCIG Steady-state Model**

#### **2.3.1.1 Equivalent Circuit**

Steady state analysis of an induction machine has received considerable attention in the literature to determine a system performance model [103]. The steady state of a model is where the variables of a model are unchanging in time throughout the entire domain. Steady-state performance analysis is important to ensure that the controlled variable of a system is always under control. To predict and analyse a machine's performance in a steady state condition, a simple per-phase equivalent circuit model is usually used [72]. The diagram of the per-phase equivalent circuit of a SCIG, with respect to the stator, is presented in Figure 2-5.

In the squirrel-cage induction machine model, there are two types of impedance in the primary (stator) and secondary (rotor) windings, namely resistance and leakage reactance. The resistance of the stator is called  $R_s$ , and the

leakage of the stator is called  $x_{ls}$ . These two components appear on the left-hand side of the machine model. On the secondary side, the resistance and the reactance of the rotor are called  $R_r$  and  $x_{lr}$ , respectively. Also shown in the figure is the equivalent rotor resistance  $\frac{R_r}{s}$ , which has been broken up into 2 components;  $R_r$  and  $\frac{R_r}{s}(1 - s)$ . The first component corresponds to the losses of the rotor copper whereas the second component corresponds to the power developed by the motor due to the rotation of the turbine rotor. The shunt element,  $x_M$ , which is the magnetising reactance corresponding to the core of the motor, is also included.

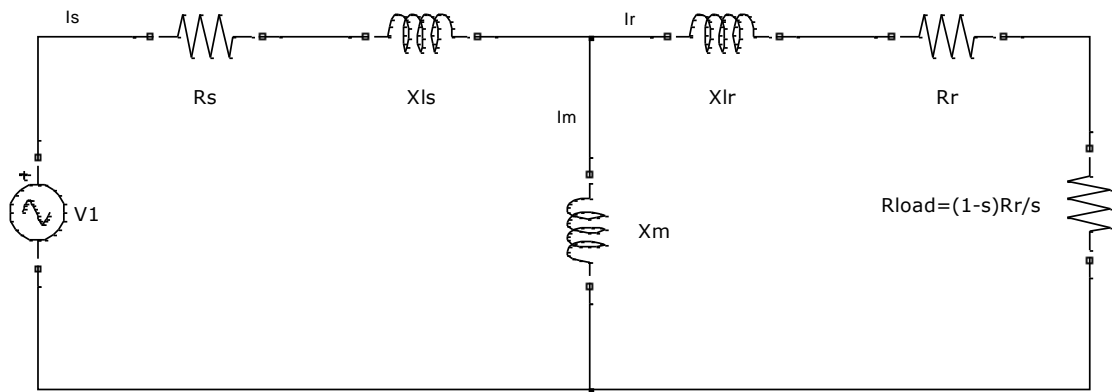


Figure 2-5 Per-phase equivalent circuit of a SCIG with respect to the stator

When a three-phase voltage has been applied to the stator of an induction machine, a three-phase set of stator currents will flow, which produces a magnetic field,  $B$ . This magnetic field's rotation has a speed given by

$$n_s = \frac{120f_s}{p} \quad (2-23)$$

where  $n_s$  is the magnetic field's rotation or the machine synchronous speed, measured in rotations per minute (rpm) and  $f_s$  is the electrical frequency in hertz (Hz) and  $p$  is the number of poles in the machine.

A voltage will be induced in the machine when the rotating magnetic field  $B_s$  passes over the rotor bars. The voltage induced is given by

$$e_{induced} = \bar{v} \cdot \bar{B} \cdot l \quad (2-24)$$

where  $\bar{v}$  is the velocity of the bar relative to the magnetic field,  $\bar{B}$  is the magnetic flux density vector and  $l$  is the length of conductor in the magnetic field.

The behaviour of an induction generator is highly dependent on the rotor's voltage and current. The voltage induced by the rotor bar is based on the speed of the rotor relative to the magnetic fields. Due to this relative movement between the magnetic fields and the rotor, the rotor runs faster than the synchronous speed in generating mode. Meanwhile, the rotor runs more slowly than the synchronous speed in motoring mode. The difference between the speed of the magnetic field and the speed of the rotor is called the *slip*. This slip generates the useful torque in the machine, thereby enabling an induction machine to transfer power to its load. Slip ( $S$ ) can also be referred to the difference between the synchronous speed ( $n_s$ ) and the rotor speed ( $n_r$ ) and can be calculated numerically as in Equation (2-35):

$$S = \frac{\omega_s - \omega_r}{\omega_s} = \frac{n_s - n_r}{n_s} \quad (2-25)$$

where

$$\omega_s = \frac{2\pi n_s}{60} \text{ rad/s} \quad (2-26)$$

$$\omega_r = \frac{2\pi n_r}{60} \text{ rad/s} \quad (2-27)$$

$$n_r = (1 - S)n_s \text{ rpm} \quad (2-28)$$

The synchronous frequency of the induction generator is represented by  $f_s$  and the unit is Hz. Its relationship with the frequency of the rotor speed is given by Equations (2-29) or (2-30).

$$f_r = S f_s \quad (2-29)$$

$$f_r = \frac{p}{120} (n_r - n_s) \quad (2-30)$$

By referring to Figure 2-4, the stator current,  $I_s$  can be calculated as

$$I_s = \frac{V_1}{Z_{in}} \quad (2-31)$$

where  $Z_{in}$  and  $Z_r$  can be computed using Equations (2-32) and (2-33) as

$$Z_{in} = R_s + jX_{ls} + \frac{Z_r(jX_M)}{Z_r + jX_M} \quad (2-32)$$

$$Z_r = R_s + R_s \left( \frac{1-s}{s} \right) + jX_{lr} \quad (2-33)$$

Then, by using the current divider rule, the rotor current is calculated as

$$I_r = \frac{jX_M}{Z_r} I_s \quad (2-34)$$

The input power in the induction generator of the circuit in Figure 2-5 is given by Equation (3-35) as

$$P_{input} = 3V_1 I_1 \cos \theta_1 \quad (2-35)$$

where  $\theta_1$  is the angle difference between the stator current and the stator voltage. It can be obtained directly from the stator current if the angle of the reference voltage is zero.

The electromagnetic power, also known as the *air-gap power*, is equal to

$$P_{ag} = I_r^2 \left( \frac{R_r}{s} \right) \text{ Watts} \quad (2-36)$$

Air-gap power is the total power transferred from the stator to the rotor side through the air-gap after considering all the stator losses. Then, the air-gap torque is equal to

$$T_{ag} = \frac{P_{ag}}{\omega_s} = 3I_2^2 \left( \frac{R_r}{\omega_s s} \right) \text{ Nm} \quad (2-37)$$

where the air-gap torque is the torque produced at the air-gap between the stator and the rotor. Or, it can also be recognised as the power in resistor of  $\frac{R_r}{s}$ , the useful power in the induction generator, known as *developed power* or *converted power*. This is the total mechanical power that has been transformed into the electrical form [82] and is given by Equations (2-38) or (2-39).

$$\begin{aligned}
P_{developed} &= P_{conversion} \\
&= P_{ag} - Rotor_{losses} \\
&= 3I_r^2 \frac{R_r}{S} - 3I_r^2 (R_r) \\
&= 3I_r^2 \left( \frac{R_r}{S} - R_r \right) \\
&= 3I_r^2 R_r \left( \frac{1-S}{S} \right) \\
&= 3I_r^2 \left( \frac{R_r}{S} \right) (1 - S) \\
&= P_{ag}(1 - S) \tag{2-38}
\end{aligned}$$

$$P_g = I_r^2 R_r \frac{1-S}{S} \tag{2-39}$$

where  $P_g$  is the generated power or developed power or converted power,  $S$  is the slip,  $I_r$  is the rotor current,  $I_s$  is the stator current,  $R_r$  is the rotor resistance,  $R_s$  is the stator resistance,  $x_{lr}$  is the rotor reactance,  $x_{ls}$  is the stator reactance and  $x_M$  is the magnetizing reactance.

Hence, the induced torque or developed torque is equivalent to Equations (2-40) or (2-41).

$$T_{ind} = \frac{P_{conv}}{\omega_r} \tag{2-40}$$

$$T_{ind} = \frac{P_{conv}}{\omega_r} = \frac{(1-S)}{(1-S)\omega_s} P_{ag} \tag{2-41}$$

If the value of the rotational losses (e.g. eddy current, hysteresis, frictions) of the induction generator is known, the actual useful power becomes the output power,  $P_{out}$  where

$$P_{out} = P_{developed} = P_{losses} \tag{2-42}$$

So, the output torque,  $T_{out}$  is equal to

$$T_{out} = \frac{P_{out}}{\omega_r} \tag{2-43}$$

### 2.3.2 The SCIG Dynamic d-q Model

The use of the d-q model to help solve a complex problem in machine analysis was introduced by R.H. Park in the 1920s [72]. This complex problem concerns the time-varying parameters such as the machine's inductances. This problem came from the dynamic performance of the machine. In machine dynamics, the rotor windings move with respect to the three-phase stator windings. When the rotor position is changing, the coupling coefficients between the stator and rotor also change continuously. Hence, the variations of these time-varying parameters will affect the values of the voltages, currents and flux linkages of the machine. In Park's work, the d-q technique design is available for synchronous machines with respect to a stationary reference frame. All time-varying inductances, with respect to the varying magnetic reluctance during relative motion, are eliminated.

However, in the 1930s, H.C. Stanley proposed a d-q model for the induction machine with respect to the stationary reference frame. Later, G. Kron proposed an improvement of the d-q model. He used both stator and rotor variables in the synchronously rotating frame, fixed in the stator but with respect to a rotating magnetic field. Then, D. S. Brereton applied stator variable transformation to the rotating reference frame, which was fixed on the rotor. Next, the time-varying parameter transformation for an induction machine was improved by Krause and Thomas. In their work, the varying variables of the stator and rotor refer to a common reference frame, rotating at any speed, which can be achieved by transforming the three-phase stationary reference frame variables into two-phase stationary reference frame variables. Next, the two-phase stationary reference frame is transformed into the synchronously rotating reference frame. To obtain the actual dynamic systems, the reverse transformation is used. The basic idea of this d-q reference frame is introduced to convert the AC components of the vectors in the stator frame into DC signals. Hence, the technique that was proposed by Krause and Thomas is expected to be very useful in the adjustable speed drive application. Using this technique, the time-varying inductances can be eliminated directly even though the speed is varying [104].

Thus, to model the modern adjustable speed drive in the SRVSWT application and analysis, the d-q model must be understood. The main advantage of using the d-q model is that the transient behaviour of a dynamic system can be studied effectively [72] because the feedback loop effects of the tuning errors in the early process, where transients occur, can be observed if this d-q model is used.

### 2.3.2.1 Equivalent Circuit

In the induction generator simulation, several transformations are involved in the d-q model. As mentioned earlier, all three-phase variables need to be converted to two-phase d-q quantities. Before converting these three-phase voltages to the two-phase d-q stationary reference frame, the line voltages are transformed into three-phase voltage variables if the information about the line voltage is available. This transformation can be performed using Equation (2-44) [72],[9].

$$\begin{bmatrix} v_{an} \\ v_{bn} \\ v_{cn} \end{bmatrix} = \begin{bmatrix} +\frac{2}{3} & -\frac{1}{3} & -\frac{1}{3} \\ -\frac{1}{3} & +\frac{2}{3} & -\frac{1}{3} \\ -\frac{1}{3} & -\frac{1}{3} & +\frac{2}{3} \end{bmatrix} \begin{bmatrix} v_{ao} \\ v_{bo} \\ v_{co} \end{bmatrix} \quad (2-44)$$

where  $v_{an}$  is the phase voltage for phase a,  $v_{bn}$  is the phase voltage for phase b,  $v_{cn}$  is the phase voltage for phase c,  $v_{ao}$  is the line voltage for phase a,  $v_{bo}$  is the line voltage for phase b and  $v_{co}$  is the line voltage for phase c.

A phasor diagram can be used to illustrate how the three-phase variables are transformed into the equivalent two-phase stationary reference frame and then into the equivalent synchronous reference frame. From Figure 2-5, the phasor's magnitude and angle of each rotor and stator variables can be observed. The symmetrical three-phase induction machine with stationary as-bs-cs axes is separated by an angle of  $2\pi/3$ .

The two-phase stationary reference frame  $d^s - q^s$  axes can be placed at any angle, where the superscript 's' refers to the stationary frame. By assuming that the  $q^s$  axis is oriented at  $\theta = 0$ , so that the  $q^s$ -axis is aligned with the as-axis, the  $d^s - q^s$  axes can be calculated using Equation (2-45) [72],[9] and placed

as in the Figure 2-6. Now, these three-phase voltage variables have been transformed to the two-phase d-q stationary frame. Here, we have considered voltage as the variable. The current and flux linkages can be transformed by similar equations.

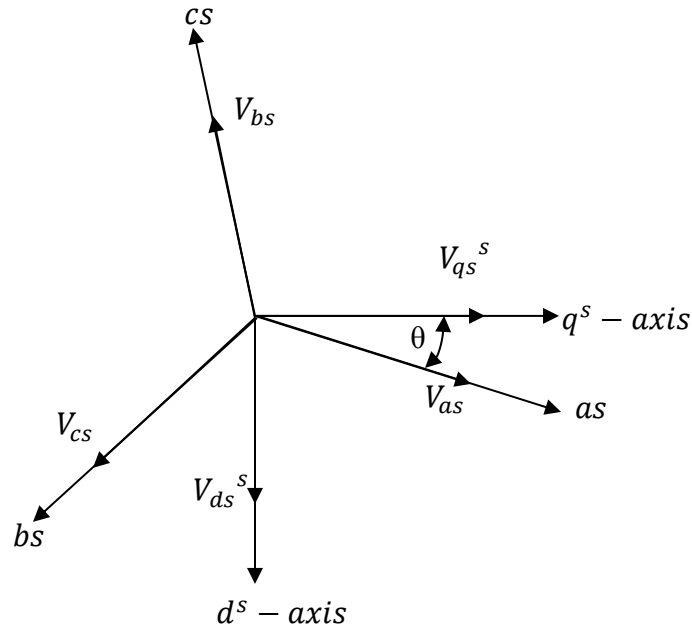


Figure 2-6 Stationary frame a-b-c to  $d^s - q^s$  axes transformation

$$\begin{bmatrix} v_{qs}^s \\ v_{ds}^s \end{bmatrix} = \begin{bmatrix} 1 & 0 & 0 \\ 0 & -\frac{1}{\sqrt{3}} & \frac{1}{\sqrt{3}} \end{bmatrix} \begin{bmatrix} v_{an} \\ v_{bn} \\ v_{cn} \end{bmatrix} \quad (2-45)$$

Then, the two-phase d-q stationary frame is transformed into the synchronous reference frame using Equation (2-46) [72],[9]. The conversion from the synchronous reference frame to the stationary reference frame can be performed using Equation (2-47) [72],[9].

$$\begin{bmatrix} v_{qs}^s \\ v_{ds}^s \end{bmatrix} = \begin{bmatrix} v_{qs}^s \cos\theta_e - v_{ds}^s \sin\theta_e \\ v_{qs}^s \sin\theta_e + v_{ds}^s \cos\theta_e \end{bmatrix} \quad (2-46)$$

$$\begin{bmatrix} v_{qs}^s \\ v_{ds}^s \end{bmatrix} = \begin{bmatrix} v_{qs}^s \cos\theta_e + v_{ds}^s \sin\theta_e \\ -v_{qs}^s \sin\theta_e + v_{ds}^s \cos\theta_e \end{bmatrix} \quad (2-47)$$

where  $\theta_e$  is the angle difference between phase and current synchronous reference frame.

The relation between the two-phase stationary reference frame  $d^s - q^s$  and the two-phase synchronous reference frame  $d^e - q^e$  is depicted in Figure 2-7. Superscript 'e' refers to the synchronous frame.

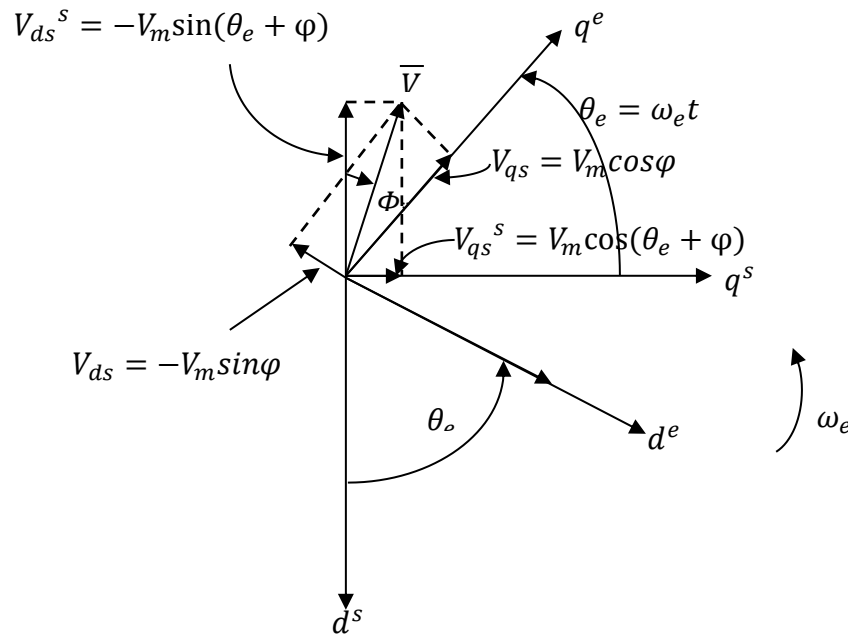


Figure 2-7 Transformation of stationary frame  $d^s - q^s$  into synchronously rotating frame  $d^e - q^e$

To obtain the actual voltage and current variables of the simulated induction generator, all two-phase d-q quantities are then transformed back into the three-phase variables. This conversion can be expressed using Equation (2-48).

$$\begin{bmatrix} v_a \\ v_b \\ v_c \end{bmatrix} = \begin{bmatrix} 1 & 0 \\ -\frac{1}{2} & -\frac{\sqrt{3}}{2} \\ -\frac{1}{2} & \frac{\sqrt{3}}{2} \end{bmatrix} \begin{bmatrix} v_{qs}^s \\ v_{ds}^s \end{bmatrix} \quad (2-48)$$

Detailed explanations of this transformation are available in many references, including [72], [9], [63], [11] and [105].

### 2.3.3 SCIG State-space Equation Dynamic Model

The simple model explained in subsection 2.2.1 is used to form the voltage and torque equations for an induction generator formulated in terms of the magnitudes of the machine variables. This model is known to describe the machine's steady-state performance. Unfortunately, the steady-state model cannot explain the machine's dynamic performance [104]. In this subsection, the equation's formation for voltage and torque are transformed into d-q quantities, in the synchronously rotating reference frame. The dynamic equivalent circuit of the d-q SCIG used for the proposed SRVSWT system in this research is shown in Figure 2-8.

This model is based on equations derived in Krause's model, as explained in section 2.2.2, which is described in [11]. This machine model is very popular in machine modelling work, particularly in simulation work such as that found in [14],[16], [58], [64], [106], [107], and [15]. According to Krause's model, the modelling equations of the derivative of flux linkage form can be expressed as follows:

$$\frac{dF_{qs}}{dt} = \omega_b \left[ v_{qs} - \frac{\omega_e}{\omega_b} F_{ds} + \frac{R_s}{x_{ls}} (F_{mq} + F_{qs}) \right] \quad (2-49)$$

$$\frac{dF_{ds}}{dt} = \omega_b \left[ v_{ds} + \frac{\omega_e}{\omega_b} F_{qs} + \frac{R_s}{x_{ls}} (F_{md} + F_{ds}) \right] \quad (2-50)$$

$$\frac{dF_{qr}}{dt} = \omega_b \left[ v_{qr} - \frac{(\omega_e - \omega_r)}{\omega_b} F_{dr} + \frac{R_r}{x_{lr}} (F_{mq} - F_{qr}) \right] \quad (2-51)$$

$$\frac{dF_{dr}}{dt} = \omega_b \left[ v_{dr} + \frac{(\omega_e - \omega_r)}{\omega_b} F_{qr} + \frac{R_r}{x_{lr}} (F_{md} - F_{dr}) \right] \quad (2-52)$$

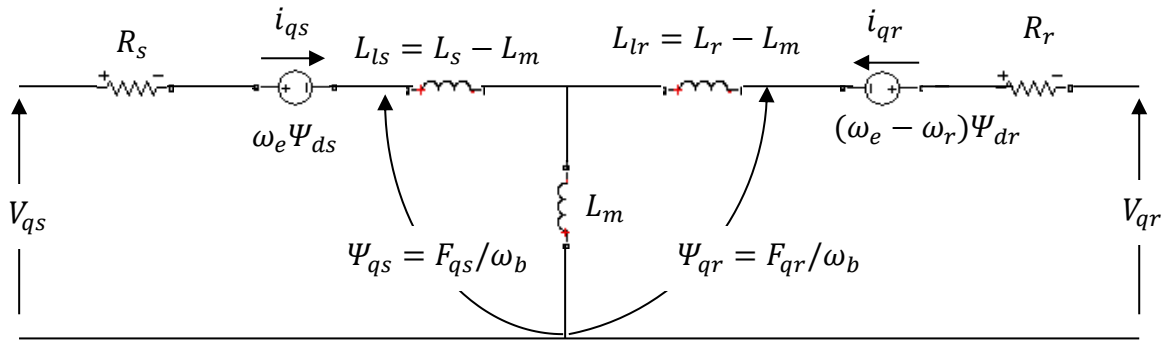
The flux linkage equations are derived as

$$F_{qs} = x_{ls} i_{qs} + F_{mq} \quad (2-53)$$

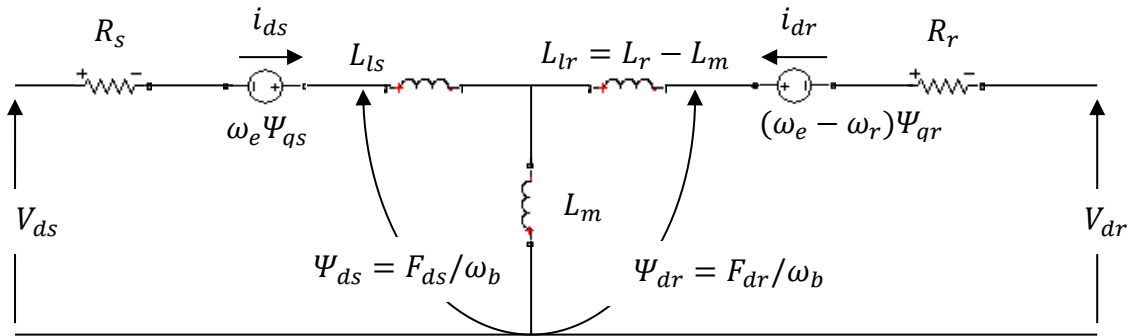
$$F_{qr} = x_{lr} i_{qr} + F_{mq} \quad (2-54)$$

$$F_{ds} = x_{ls} i_{ds} + F_{md} \quad (2-55)$$

$$F_{dr} = x_{lr} i_{dr} + F_{md} \quad (2-56)$$



(a)



(b)

Figure 2-8 Dynamic or d-q equivalent circuit of an induction generator (a) q-axis circuit (b) d-axis circuit

From the flux linkage equations, the rotor and stator linkage currents with relation to the flux linkage are given as

$$i_{qs} = \frac{1}{x_{ls}} (F_{qs} - F_{mq}) \quad (2-57)$$

$$i_{qr} = \frac{1}{x_{lr}} (F_{qr} - F_{mq}) \quad (2-58)$$

$$i_{ds} = \frac{1}{x_{ls}} (F_{ds} - F_{md}) \quad (2-59)$$

$$i_{dr} = \frac{1}{x_{lr}} (F_{dr} - F_{md}) \quad (2-60)$$

By substituting Equations (2-57) and (2-58) into Equations (2-53) and (2-54), which are the flux linkage equations, the mutual flux linkages  $F_{mq}$  and  $F_{md}$  are expressed as

$$F_{mq} = x_{ml} \left[ \frac{F_{qs}}{x_{ls}} + \frac{F_{qr}}{x_{lr}} \right] \quad (2-61)$$

$$F_{md} = x_{ml} \left[ \frac{F_{ds}}{x_{ls}} + \frac{F_{dr}}{x_{lr}} \right] \quad (2-62)$$

Finally, the electromagnetic torque equation in terms of flux linkages can be expressed as

$$T_e = \frac{3}{2} \left( \frac{p}{2} \right) \frac{1}{\omega_b} (F_{ds} i_{qs} - F_{qs} i_{ds}) \quad (2-63)$$

The relations between electrical torque and the load torque in terms of rotational speed from the machine torque are expressed as

$$T_e - T_l = J \left( \frac{2}{p} \right) \frac{d\omega_r}{dt} \quad (2-64)$$

where the variables are defined as follows:

- $d$  is direct-axis,
- $q$  is quadrature-axis,
- $s$  is stator variable,
- $r$  is rotor variable,
- $F_{ij}$  is the flux linkage ( $i = q$  or  $d$  and  $j = s$  or  $r$ ),
- $R_r$  is rotor resistance,
- $R_s$  is stator resistance,
- $x_{ls}$  is stator leakage resistance ( $\omega_e L_{ls}$ ),
- $x_{lr}$  is rotor leakage resistance ( $\omega_e L_{lr}$ ),
- $x_{ml}$  is  $\frac{1}{\left( \frac{1}{x_m} + \frac{1}{x_{ls}} + \frac{1}{x_{lr}} \right)}$ ,
- $p$  is number of poles,
- $J$  is moment of inertia,

$T_e$	is electrical output torque,
$T_l$	is load torque,
$\omega_e$	is stator angular electrical frequency,
$\omega_b$	is generator angular electrical base frequency,
$\omega_r$	is rotor angular electrical speed,
$i_{qs}, i_{ds}$	is $q$ and $d$ -axis stator currents,
$i_{qr}, i_{dr}$	is $q$ and $d$ -axis rotor currents,
$v_{qs}, v_{ds}$	is $q$ and $d$ -axis stator voltages,
$v_{qr}, v_{dr}$	is $q$ and $d$ -axis rotor voltages,
$F_{mq}, F_{md}$	is $q$ and $d$ -axis magnetizing flux linkages.

For the SCIG-based SRVSWT system, the equations of  $v_{qr}$  and  $v_{dr}$  in (2-51) and (2-52) are set to zero. By converting the relevant equations listed from Equation (2-49) to Equation (2-64), the modelling equations of a SCIG in the state-space form are derived as follows:

$$\frac{dF_{qs}}{dt} = \omega_b \left[ v_{qs} - \frac{\omega_e}{\omega_b} F_{ds} + \frac{R_s}{x_{ls}} \left( \frac{x_{ml}}{x_{lr}} F_{qr} + \left( \frac{x_{ml}}{x_{ls}} + 1 \right) F_{qs} \right) \right] \quad (2-65)$$

$$\frac{dF_{ds}}{dt} = \omega_b \left[ v_{ds} + \frac{\omega_e}{\omega_b} F_{qs} + \frac{R_s}{x_{ls}} \left( \frac{x_{ml}}{x_{lr}} F_{dr} + \left( \frac{x_{ml}}{x_{ls}} + 1 \right) F_{ds} \right) \right] \quad (2-66)$$

$$\frac{dF_{qr}}{dt} = \omega_b \left[ -\frac{(\omega_e - \omega_r)}{\omega_b} F_{dr} + \frac{R_r}{x_{lr}} \left( \frac{x_{ml}}{x_{ls}} F_{qs} + \left( \frac{x_{ml}}{x_{lr}} - 1 \right) F_{qr} \right) \right] \quad (2-67)$$

$$\frac{dF_{dr}}{dt} = \omega_b \left[ \frac{(\omega_e - \omega_r)}{\omega_b} F_{qr} + \frac{R_r}{x_{lr}} \left( \frac{x_{ml}}{x_{ls}} F_{ds} + \left( \frac{x_{ml}}{x_{lr}} - 1 \right) F_{dr} \right) \right] \quad (2-68)$$

$$\frac{d\omega_r}{dt} = \left( \frac{p}{2J} \right) (T_e - T_l) \quad (2-69)$$

For the variable-speed drive, two types of the inverter are usually applied; the voltage source inverter (VSI) and the current source inverter (CSI). Because VSI is more commonly used in industry than the CSI [108], the VSI (in terms of control inputs) was considered for this study. By using VSI, the six-step or pulse-

width modulation (PWM) inverter can be used. However, the development model of the VSI is not included in this work. The VSI is assumed to have a unit voltage and current gain, where the voltage and currents are generated as dictated by the corresponding reference voltage and currents from the controller.

## **2.4 Chapter Summary**

The advantages of using the SCIG have been given. The SCIG-based SRVSWT control aims and its adapted laws for each wind regions for this study have been described in detail and summarised. The control strategies of the SCIG connected to the full-rated power converter drive using VC and SC on the proposed SRVSWT system have been described. The application of these VC and SC strategies in the wind turbine system has also been reviewed. VC and SC can yield high efficiency and robust performance in DFIG and GSC regardless of the changes of machine parameters, but their application to the SRVSWT system is not yet available. The comparison between SC and VC has also been explained and since VC offers a higher level of dynamic performance it has, therefore, been chosen as the control model algorithm for this study. Finally, the steady-state, dynamics and state-space equations employing the VC model algorithm used for modelling the SCIG-based SRVSWT system in the next chapter have been given.

### **3 Description and Validation of Wind Energy Conversion System (WECS) Modelling**

#### **3.1 Wind Energy Conversion System (WECS) Modeling**

This chapter explains the modelling development and validation process of the stall-regulated, horizontal-axis, WECS dynamic system. The modelling of a complete stall-regulated wind turbine (SRWT) system using SIMULINK is described step by step. SIMULINK is chosen as the numerical environment for this work because it is a powerful and modern software package that provides a convenient tool for simulations in contrast to the compilation of several individual program codes. The simulation model is built up systematically from the simplest sub-models to the largest content block. However, MATLAB codes are used for certain applications to simplify the experimental analyses and particularly to export the search variables obtained from the codes and transfer the information to the SIMULINK model. The authenticity of each developed sub-model is verified before they are combined to form the full model. Methods for gathering the unavailable data parameters are also discussed.

This modelling is intended to represent a 25 kW Carter wind turbine, a machine that is still in operation at West Beacon Farm in Loughborough, UK. The Carter turbines, as shown in Figure 3-1(a), are two stall-regulated two-bladed wind turbines in which are the largest generators of sustainable energy at West Beacon Farm. These turbines are rated at 25kW each and were installed in 1990 at a cost of £60,000. The wind turbines were direct-on-line AC grid-connected and deliver some 3-phase 415V AC. The status of the turbines drives, switching frequency filters and control gear could be seen at the main control panels in the control room, as shown in Figure 3-1(b). These panels were designed and built by the Control Techniques Inc. Because this turbine is rather old, operational data are not available. Hence, estimates are made based on the limited available data and from other similar-sized turbines. The Carter turbine

consists of a two-bladed, 25-kW, stall-regulated, horizontal axis, fixed-speed wind turbine system.

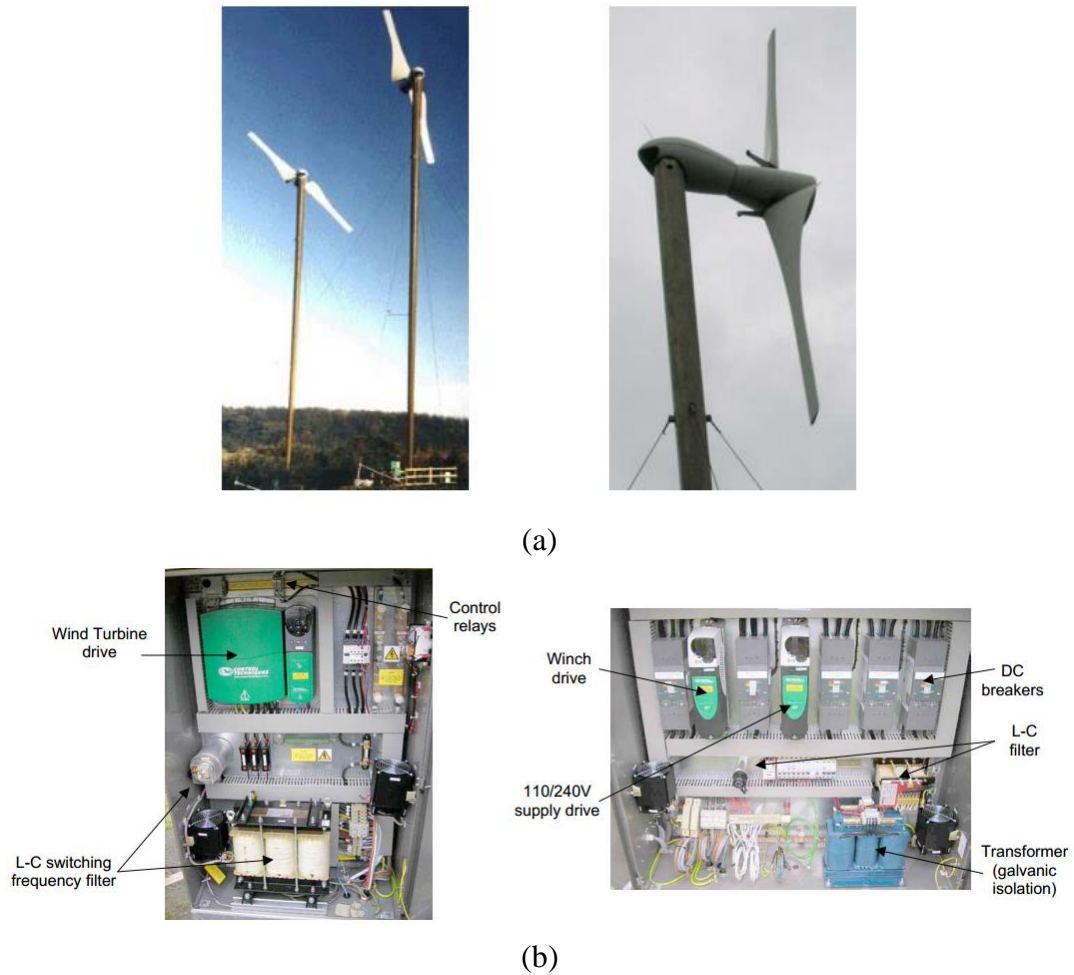


Figure 3-1 (a) Installed 25 kW Carter wind turbines with close-up, (b) Turbine control panels

Figure 3-2 shows a schematic of the SIMULINK model that was developed to model the Carter turbine. The model is composed of four sub-models, which include the wind speed, aerodynamic, drivetrain and SCIG with a full-rated power converter sub-models. The wind speed model is developed as an input to the complete model, whereas the aerodynamic model represents the torque or power that is created at the turbine rotor blades. The drivetrain model depicts the link between the generator/load torque and the turbine/generator shaft speed, and the SCIG sub-model models the behaviour by which power is

generated according to the adopted control strategy. Each model development stage is explained in the following sections of this chapter.

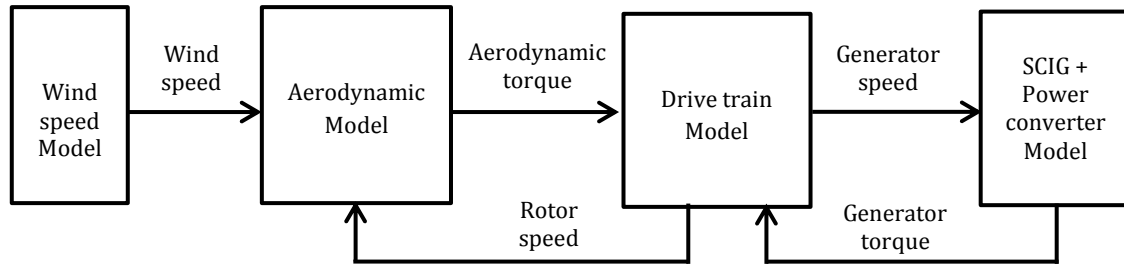


Figure 3-2 Structure of the Wind Turbine Modelling System

### 3.1.1 Wind Speed Dynamics Model

The annual wind speed distribution of West Beacon Farm can be described using the Rayleigh probability function [109]:

$$f_{pdf}(v) = \frac{v}{\alpha^2} \exp\left[-\left(\frac{v}{\sqrt{2}\alpha}\right)^2\right] \quad (3-1)$$

where  $v$  is the instantaneous wind speed and alpha,  $\alpha$ , is given by:

$$\alpha = v_{\bar{m}} \sqrt{2/\pi} \quad (3-2)$$

which relates to the notably long time scale of the mean wind speed,  $v_{\bar{m}}$ , which is measured in m/s.

The standard deviation,  $SD$ , and the turbulence intensity,  $I$ , are calculated using Equations (3-3) and (3-4) [18], respectively

$$SD = \sqrt{\frac{1}{N_s-1} \sum_{i=1}^{N_s} (v - v_{\bar{m}})^2} \quad (3-3)$$

$$I = \frac{\sqrt{\sigma^2}}{v_{\bar{m}}} = \frac{\sigma}{v_{\bar{m}}} \quad (3-4)$$

where  $N_s$  is the number of samples during each short-time interval and  $\sigma$  is the standard deviation.

Figure 3-3 shows the annual Rayleigh distribution for West Beacon Farm , Loughborough (solid line), which has a mean wind speed of 4.5 m/s [110, 111] at 24 metres hub height. Considering that the area under the curve is unity, Equation (3-3) provides the standard deviation,  $SD = 0.59$  m/s. Thus, the turbulence intensity, over ten-minute period,  $I = 0.13$ . Also, from this figure, it should be noted that this mean wind speed is not the most commonly occurring wind speed which is somewhat less than this, at around 3.7 m/s. To verify the authentic of the simulated Rayleigh distribution curve, the simulated curve (solid line) is then compared with the Rayleigh distribution that has been measured at Rutherford Appleton Laboratory (RAL), UK (dashed line)[112] . As RAL is located in England and has almost same mean wind speed and standard deviation as estimated in Loughborough, the simulated curve reveals insignificant difference with the measured curve at RAL.

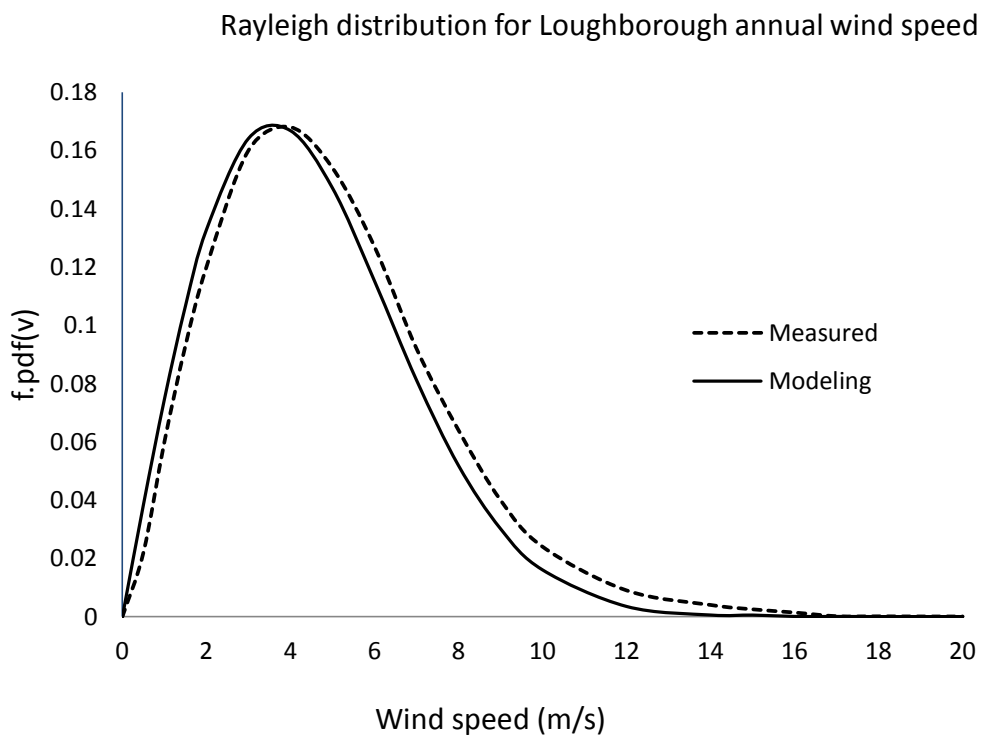


Figure 3-3 Annual wind speed at West Beacon Farm based on the Rayleigh distribution

An equivalent wind speed model is developed to simulate the actual torque experienced by the rotor at West Beacon Farm. The equivalent or actual

instantaneous velocity is a superposition of the turbulence wind and the mean wind speed components and can be written as

$$v_{eq}(t) = v_{\bar{m}}(t) + v_t(t) \quad (3-5)$$

where  $v_{eq}(t)$  is the equivalent or actual instantaneous wind speed velocity,  $v_{\bar{m}}(t)$  is the mean wind speed component that determines the turbine's current operating point,  $v_{\bar{m}}(t)$  is assumed to be constant after several minutes and  $v_t(t)$  is a turbulence component that displays high frequency oscillations near the operating points. The frequency and amplitude of the wind speed variance is limited by  $v_t(t)$ .

The equivalent or actual instantaneous wind speed behaviour can be modelled as shown in Figure 3-4. This model makes the following assumptions:

- (a) The wind shear effect is ignored. Wind shear is the variation of wind speed with elevation. Wind shear is typically influenced by several factors such as atmospheric stability, surface roughness, changes in surface conditions and terrain shape. For wind power developers, these details of wind shear are important to be obtained to determine the actual potential electricity production and economic feasibility study of a candidate wind turbine site [18, 113, 114], particularly if the turbine blade has a diameter more than 100 metres [113]. This is important because the wind shear plays important role in determining the suitable turbine hub height. However, since these issues are not one of the thesis's aims in this study, wind shear effect was disregarded. In addition, for small turbine with 10 metres in diameter and turbine hub height of 24 metres, no significant effect may affect the energy yield estimation [113]. Furthermore, ignorance of wind shear in modelling work is acceptable since wind shear extrapolation may have a large ambiguity because the wind shear models do not always describe reality [18].
- (b) The wind speed variations in the horizontal direction are not considered. Perfect tracking in the yaw direction is assumed; in practice, this is impossible and results in energy losses at least 1-2% [109] and additional stresses on the components.

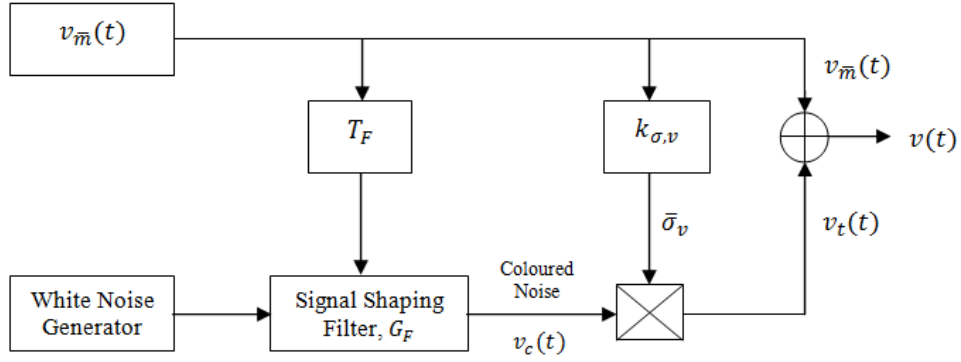


Figure 3-4 Equivalent wind speed simulation model

The mean wind speed, which is also known as the medium- and long-term component, can be denoted as [18, 109]

$$v_{\bar{m}}(t) = \sum_{i=0}^N A_i \cos(\omega_i t + \varphi_i) \quad (3-6)$$

where  $N$  is the number of samples during each medium- and long-term interval and  $\varphi_i$  is the phase of the harmonics, which is generated randomly with a uniform distribution in the range of  $[\pi, -\pi]$ . If  $i = 0$ , and  $\omega_0 = 0, \varphi_0 = 0$ , then  $A_0 = v_{\bar{m}}$  where  $v_{\bar{m}}$  is the mean wind speed.

A distributed white noise signal is generated using a random number generator to denote the driving force of the wind. The white noise signal is subsequently smoothed with a signal-shaping filter to transform the white noise signal into a coloured noise signal. The signal-shaping filter can be designed using the Kaimal or Von Karman spectrum model. These models are popular for modelling short-term turbulence characteristics in wind velocity series simulations [4]. In this work, the von Karman spectrum model is used to shape the white noise signal. The transfer function of the Von Karman shaping filter can be expressed as [109]

$$G_F(j\omega) = \frac{V_F}{(1+j\omega T_F)^{5/6}} \quad (3-7)$$

where  $V_F$  is the amplification factor, and  $T_F$  is the time constant of the shaping filter.

The parameter selection for the shaping filter depends on the annual mean wind speed,  $v_{\bar{m}}$  and the turbulence length scale,  $L$ , which corresponds to the site roughness. The turbulence length scale can be expressed as [4]

$$L = \begin{cases} 150 \text{ m}, & \text{if } z \geq 30 \text{ m} \\ 5z \text{ m}, & \text{if } z < 30 \text{ m} \end{cases} \quad (3-8)$$

where  $z$  is the height of the wind turbine hub.

At West Beacon Farm, the wind turbine hub is located 24 m above ground level, and hence the turbulence length is equal to 120 meters. The amplification factor,  $V_F$ , and the time constant,  $T_F$ , of the shaping-filter parameters can be obtained as

$$V_F \approx \sqrt{\frac{2\pi}{\mathcal{B}\left(\frac{1}{2}, \frac{1}{3}\right)} \cdot \frac{T_F}{T}} \quad (3-9)$$

$$T_F = \frac{L}{v_{\bar{m}}} \quad (3-10)$$

where  $T$  is the sampling time. Equation (3-9) used  $T = 1$  second because this value has been used in several other studies [17].  $\mathcal{B}$  denotes the Beta function, which is also known as the Euler integral function. The Beta function can be defined in many forms; in this study, it was defined as

$$\mathcal{B}(x, y) = \frac{(x-1)!(y-1)!}{(x+y-1)!}$$

The wind gust or turbulence,  $v_t$ , is subsequently acquired by multiplying the coloured noise signal by the wind's standard variance,  $\bar{\sigma}_v$  (a constant), and can be calculated as

$$v_t(t) = \bar{\sigma}_v \cdot v_c(t) \quad (3-11)$$

where

$$\bar{\sigma}_v = k_{\sigma,v} \cdot v_{\bar{m}} \quad (3-12)$$

$$k_{\sigma,v} = \begin{cases} 0.10 \sim 0.15 & \text{off shore} \\ 0.15 \sim 0.25 & \text{others} \end{cases} \quad (3-13)$$

The equivalent or actual instantaneous wind speed velocity,  $v_{eq}$ , can be calculated using Equation 3-5. The white noise, turbulence and the created equivalent velocity signal at West Beacon Farm with  $k_{\sigma,v} = 0.25$  and  $v_{\bar{m}} = 4.5$  m/s for 600 seconds with 1 second time step of simulation can be depicted as shown in Figure 3-5(a) to (c).

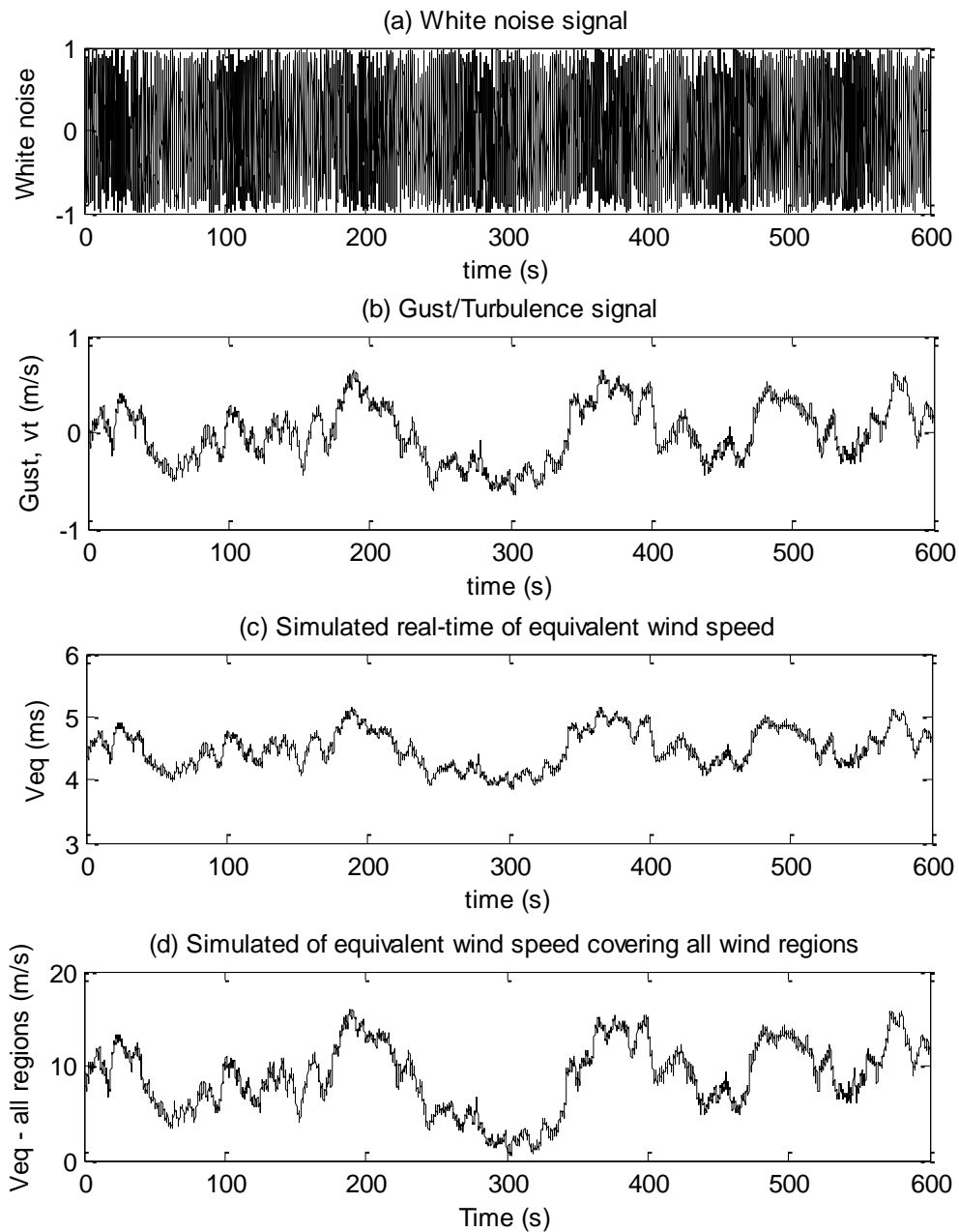


Figure 3-5 (a) white noise signal, (b) gust/turbulence signal, (c) equivalent or instantaneous velocity signal (d) modified equivalent or instantaneous velocity signal for all wind speed conditions

However, because this study is focused on the behaviour of a SRVSWT, in the PL, IL and FL regions, the equivalent or instantaneous wind velocity is modified by changing the value of the mean wind speed and the coloured noise signal. Consequently, the designed turbine can be tested at all wind speeds, from approximately 0 m/s to 16 m/s. Figure 3-5(d) depicts the equivalent or actual instantaneous wind speed velocity,  $v_{eq}$ , which covers all wind speeds and has a mean wind speed of 10.4 m/s for a 600 seconds simulation.

### 3.2 Aerodynamic Model

The aerodynamic model represents the interaction between the turbine rotor and the wind field. The extraction of useful mechanical power from the wind depends on the blade profiles. The developed SIMULINK model of the rotor aerodynamics model is shown in Figure 3-6. The inputs for this model are the turbine rotor speed and the equivalent wind speed that was generated in Section 3.2. The outputs of this model are the aerodynamic torque,  $T_{aero}$ , and the aerodynamic power,  $P_{aero}$ . Equations (2-2) and (2-7) are used to calculate  $P_{aero}$  and  $T_{aero}$ , respectively [35],[75],[5],[18].

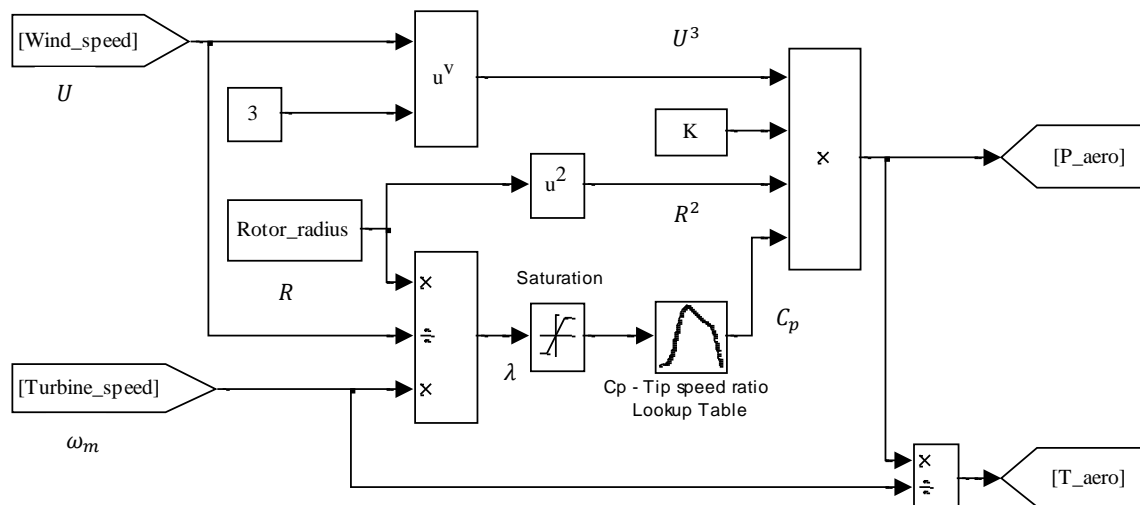


Figure 3-6 The SIMULINK model of the aerodynamic model

In the aerodynamic model, the relationship between the power coefficient and the tip speed ratio is established by the  $C_p - \lambda$  curve. A lookup table of the  $C_p - \lambda$  function is added to the model to obtain the  $C_p$  value for the value of  $\lambda$  for each change in either the wind speed or the rotor speed. To create the  $C_p - \lambda$  lookup table, the  $C_p - \lambda$  intersection points are estimated and plotted based on the curve taken from [115], which was approximated by [116] using the power versus wind speed curve that is provided in the manufacturer's brochure; refer to **Appendix 3A**.

Figure 3-7 shows the  $C_p - \lambda$  curve that was reproduced based on the curve taken from [115]. Based on this figure, the  $C_p$  of the turbine used in this study has a maximum power coefficient,  $C_{pmax}$  of 0.478 at  $\lambda_{opt}$  of 6.78. The response of the torque coefficient,  $C_t$ , can also be estimated from the values of  $C_p$  and  $\lambda$ . The relation between  $C_t$  and  $C_p$  can be represented by Equation (3-14) [17]

$$C_t = \frac{C_p}{\lambda} \quad (3-14)$$

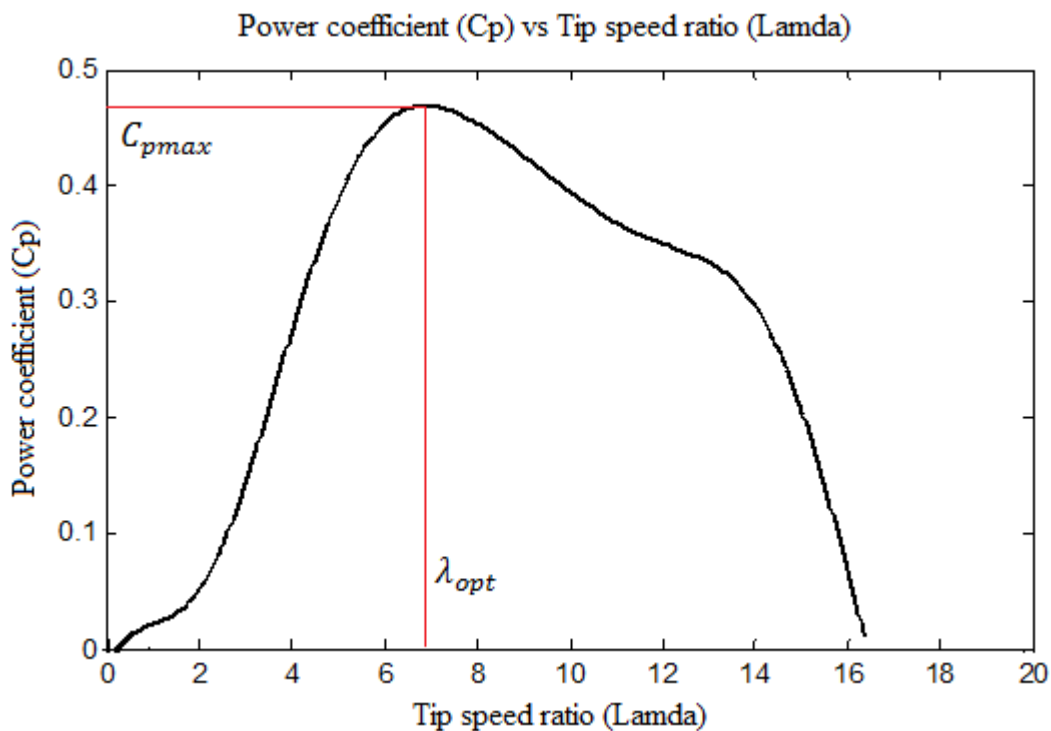


Figure 3-7 Power coefficient versus tip speed ratio ( $C_p - \lambda$ )

### 3.3 Drivetrain Model

This section explains modelling of the drivetrain of the wind turbine system. The speed of the generator shaft can be increased by a factor of  $N:1$  from the turbine rotor shaft speed. The relationship between the turbine rotor torque and the generator torque is also described by the  $N$  factor. In the actual physical system, the wind speed can vary rapidly, even over timescale of a second. When the wind speed changes, the inertia of the wind turbine will respond instantaneously to resist the change. If the rotor accelerates, the electrical systems will generate power to the grid. However, if the rotor decelerates, the electrical systems will absorb the generated kinetic energy from the turbine rotor.

Figure 3-8 depicts the drive train model of the wind turbine system. In the drive train model, the difference in rotation between the low-speed shaft and the high-speed shaft is controlled by the gearbox ratio. In a wind turbine system, unbalanced torque occurs if the turbine torque is not matched to the generator torque. As a result, the shaft will accelerate or decelerate. The shaft will accelerate if the aerodynamic torque is greater than the load torque ( $T_{aero} > T_{load}$ ), whereas the shaft decelerates if the aerodynamic torque is less than the load torque ( $T_{aero} < T_{load}$ ).

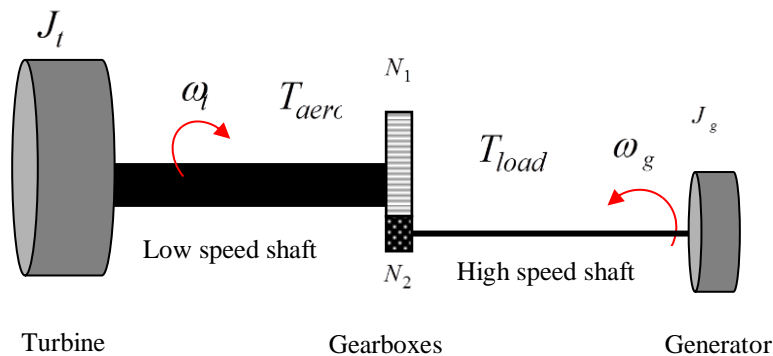


Figure 3-8 Equivalent drivetrain model

In stability power system studies, many researchers have employed a two-mass shaft model to evaluate the transient behaviour of a wind turbine generator [117],[118],[51],[2]. Several studies

[117],[119],[36],[120],[121],[118],[122] have investigated three-mass and higher-order models of wind turbine generator systems for transient stability and fault occurrence studies. A six-mass drivetrain model has also been considered [118]. To avoid an overly complex analysis, the drivetrain model in this study is developed using a simple motion equation in which only rotational inertia is considered. The effects of damping and the stiffness of the shaft are ignored. The reasons why these damping and stiffness are ignored will be explained below.

Stiffness of a shaft can be defined as the resistance of an elastic body to deformation or deflection when a force is applied [123]. In general, for an intact shaft, it has a constant stiffness. It is important to form a stiff shaft in permissible limits because it could detect the crack initialization and propagation. Meanwhile, damping of a shaft is the energy dissipation properties in the rotating shaft. .

In modelling work, the stiffness and damping of a rotating machine such as steam turbines, compressors and generators cannot be ignored if the size of wind turbine is large [124]. For large wind turbines, the stiffness and damping must be considered because they have high polar moment of inertia and material damping. Additionally, torsional resonance will be took place when the excitation frequency of the machine is equal to the torsional natural frequency of the shaft system. Hence, it is very important to ensure that the machine's excitation frequencies are designed far from the natural frequency. However, for a small-sized wind turbine, the stiffness and damping effects are very minor [124].

In certain applications, for example in the torsional vibration analysis (e.g. for aerospace and other structures such as the engine and shaft), considering the damping constant in the design model is necessary. This is important, particularly if the actual torsional vibration behaviour such as reducing dynamic response, reducing fatigue loads and ensuring aeroelastic stability, is mainly focused in the executed analysis [125], since damping can act as an energy dissipation mechanism [126, 127]. If damping is ignored, the undamped signal usually produces higher oscillations in the model [128]. However, certain applications, such as wind turbine systems, can be modelled in two different ways. If the modelling concerns the transient stability of a fixed-speed system, a

two-mass drivetrain (at least) is required to produce a realistic model [126, 128]. For a variable speed wind turbine system, the damping and stiffness constants can be ignored and still provide realistic behaviour; for example, several authors [106, 117-119] have found that a single lumped mass drivetrain model is sufficient to model variable speed wind turbines. This is because the damping and stiffness constants have almost no effect on the power output due to the effect of the decoupling algorithm considered in the power converter model.

In this study however, the safety of the system is also inspected when the stiffness and damping are ignored during the modelling work. Please see Section 3.6.3 on page 105 to 106 for the estimation of the first mode of turbine's natural frequency. From the estimation, it was found that the first mode of the resonant frequency of the studied wind turbine system is 4 Hz. Hence, the details of the first, second and third resonant frequencies are as the followings.

$$\begin{aligned}
 1^{\text{st}} \text{ mode of frequency} &= 4 \times (1)^2 = 4 \text{ Hz} = 25.13 \text{ rad/s} \\
 2^{\text{nd}} \text{ mode of frequency} &= 4 \times (2)^2 = 16 \text{ Hz} = 100.53 \text{ rad/s} \\
 3^{\text{rd}} \text{ mode of frequency} &= 4 \times (3)^2 = 36 \text{ Hz} = 226.19 \text{ rad/s}
 \end{aligned}$$

To ensure that the machine's operating speeds are not exciting the resonance condition, it must be ensured that the natural frequency should not fall within 5% of the operating speeds. Assume that there is no damping in the rotor system. For the studied wind turbine, the synchronous operating speed of the generator is at 157.08 rad/s and this machine has 2% of slip and this is controlled by the frequency converter. Hence, the operating speed range is between 153.94 to 160.22 rad/s as estimated below [124].

Lower operating speed:

$$157.08 \text{ rad/s} - 2\% \text{ slip} = 157.08 \text{ rad/s} - 3.14 \text{ rad/s} = 153.94 \text{ rad/s}$$

Upper operating speed:

$$157.08 \text{ rad/s} + 2\% \text{ slip} = 157.08 \text{ rad/s} + 3.14 \text{ rad/s} = 160.22 \text{ rad/s}$$

Five percent (5%) of the lower operating speed would be 146.24 rad/s, meanwhile the 5% of the upper operating speed would be 168.23 rad/s, as calculated below.

$$5\% \text{ of the lower operating speed: } 153.94 - (153.94 \times 5\%) = 146.24 \text{ rad/s}$$

$$5\% \text{ of the upper operating speed: } 160.22 - (160.22 \times 5\%) = 168.23 \text{ rad/s}$$

From the estimated resonant frequencies and the 5% operating speeds, it is clearly shown that the natural frequencies are not equal or not fall within the operating speed in the range of 146.24 and 168.23 rad/s. It is therefore, the stiffness and damping can be ignored in this modelling study.

In terms of gear train, many researchers, such as Muljadi et al. [32], Kundur [129], Salman et al. [10] and Li et al. [3] and [7], have employed one mass models to represent the gear train. Hence, the single lumped mass drivetrain (with a constant inertia consisting of the blade and generator inertias) is sufficient and was used in this study. To optimise the design of the drive train, torsional vibration analysis is normally carried out to measure the strength of the drive train system. For example, if the shaft is forced to accelerate or decelerate too quickly, will the stiffness of the shaft prevent it from breaking? This however is not considered in the research scope, and is one of the limitations of this study..

In the single lumped mass model, the turbine and its hub were modelled as one summed rotor inertia,  $J_r$ , and the gears and the generator were combined to form another inertia known as the generator inertia,  $J_g$ . The following simple dynamic equations depict the relationship between the wind turbine rotor and the machine generator [17, 32, 129, 130]:

$$J \frac{d\omega_t}{dt} = T_{acc} = T_{aero} - T_{load} \quad (\text{if referring to the low speed shaft})$$

(3-15)

$$J \frac{d\omega_m}{dt} = T_{acc} = T_{aero} - T_{load} \quad (\text{if referring to the high speed shaft})$$

(3-16)

$$J = J_r + G^2 \cdot J_g \quad (\text{if referring to the low speed shaft})$$

$$(3-17)$$

$$J = \frac{J_r}{G^2} + J_g \quad (\text{if referring to the high speed shaft})$$

$$(3-18)$$

$$G = \frac{\omega_g}{\omega_m} = \frac{N_1}{N_2} \quad (3-19)$$

where  $J$  is the combined moment of inertia of turbine and generator ( $\text{kgm}^2$ ),  $\omega_m$  is angular velocity of the rotor ( $\text{rad/s}$ ),  $t$  is time ( $\text{s}$ ),  $T_{acc}$  is accelerating or decelerating torque ( $\text{N.m}$ ),  $T_{aero}$  is aerodynamic torque ( $\text{N.m}$ ),  $T_{load}$  is load torque or generator torque ( $\text{N.m}$ ),  $J_r$  is rotor inertia ( $\text{kgm}^2$ ),  $J_g$  is generator inertia ( $\text{kgm}^2$ ),  $G$  is gearbox ratio,  $N_1$  is number of gear teeth connected to the low-speed shaft and  $N_2$  is number of gear teeth connected to the high-speed shaft.

The drive-train model is developed in SIMULINK using Equations (3-16), (3-18) and (3-19) as depicted in Figure 3-9. The inputs to the drive-train model are the aerodynamic torque ( $T_{aero}$ ) and the generator torque ( $T_{load}$ ), whereas the turbine rotor speed ( $\omega_t$ ), generator mechanical speed ( $\omega_m$ ) and electrical rotor speed ( $\omega_r$ ) are the outputs of the model before feedback to the aerodynamic model and the induction generator model.

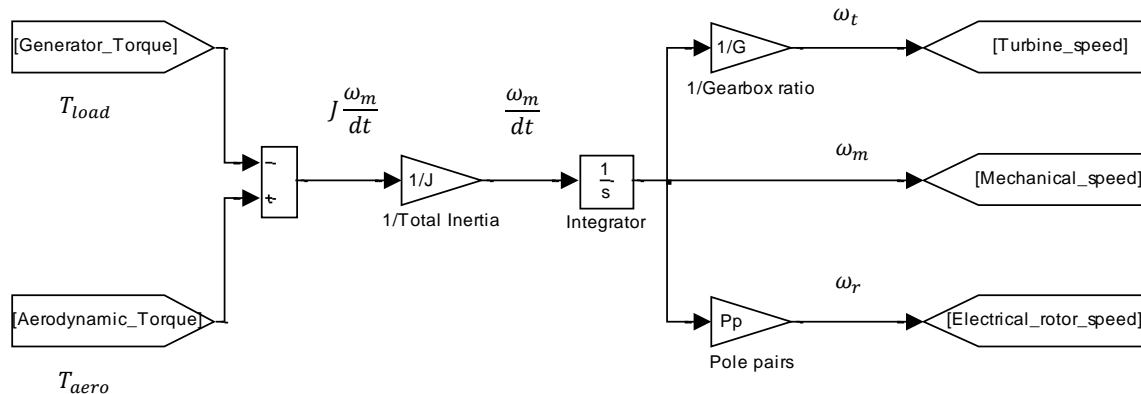


Figure 3-9 The SIMULINK model of the drivetrain

### 3.3.1 Estimation of the Drivetrain Parameter

This section presents the calculations and estimations carried out to obtain the operational data for the wind turbine's gearbox ratio and the total inertia of the wind turbine, which consists of the turbine rotor and generator inertias.

Information about the gearbox ratio of the drivetrain was gathered by counting the numbers of teeth of the components of a damaged gearbox from one of the turbines at WBF which had been opened. It was found that the high-speed shaft has a ratio of 12.748:1 ( $N_1:N_2$ ) to the low-speed shaft. This ratio also was noted by Barton, J and Harson, A. H. in [131] and [115], respectively. However, the gearbox inertia, was not calculated or estimated in this study because there was no opportunity to measure the gearbox weight since no special or suitable equipment is available in the West Beacon Farm. Due to that, the effect of gearbox inertia will be considered during estimating the generator inertia,  $J_g$ .

Again, there was also no opportunity to measure the generator's dimensions and weight to determine its inertia. Thus, the inertia of the Carter turbine was estimated from a turbine of similar size [132]. This turbine has a rated power capacity of 22 kW and can reach a maximum power of 30 kW. The generator inertia ( $J_g$ ) of the induction generator (with the gearbox inertia) in this turbine as given in [132] is 0.78 kgm<sup>2</sup>. Then, this value is used in this modelling work.

In the turbine rotor portion, the moment of inertia is defined as the rotational inertia of a rigid body with respect to its axis and was obtained by multiplying the body mass by the square of its distance from the axis of rotation. The structure of the body mass plays an important role and determines the actual moment of inertia. In the wind turbine system, the moment of inertia of the turbine rotor can be calculated as

$$J_r = \sum m_i r_i^2 \quad (3-20)$$

where  $r_i$  is the radial distance from the inertia axis to the representative particle of mass  $m_i$ .

This equation considers all particles of the body; however, an assumption is made in estimating the turbine inertia. The mass is considered to be concentrated in the centre  $\frac{1}{3}$  of the radius rather than at the outside of the radius [65]. This concept can be illustrated by imagining the blade as a rectangular plate with a straight line as its axis along the edge [133], [134]. The inertia of one blade of the turbine, is equal to

$$J_r = m_{1-blade} \left(\frac{r}{3}\right)^2 \quad (3-21)$$

The total turbine rotor inertia for two blades is equivalent to

$$J_r = 2 \times m_{1-blade} \left(\frac{r}{3}\right)^2 = \frac{2}{9} \times m_{1-blade} r^2 = \frac{1}{9} \times m_{2-blades} r^2 \quad (3-22)$$

where  $m_{1-blade}$  is the mass of one blade and  $m_{2-blades}$  is the total mass of two blades.

Based on the brochure from the manufacturer in [135], the mass of the two blades of the Carter 25 wind turbine is 220 lbs, and the hub mass is 75 lbs. These values imply that the total mass of the rotor blades and hub is equal to 295 lbs or approximately 133.81 kg. The radius of the rotor blade is 32 feet or approximately 5 metres [135]. To confirm these values, the actual blade geometry was also measured during maintenance. Therefore, the entire turbine rotor inertia involving the rotors and hub is calculated as

$$J_r = \frac{1}{9} \times m_{2-blade} r^2 = \frac{1}{9} (133.81)(5)^2 = 372 \text{ kgm}^2$$

Therefore, the inertia of the two masses ( $J$ ) corresponding to the total turbine rotor inertia and the small generator inertia is estimated as 3.068 kgm<sup>2</sup> using Equation (3-18) and using the parameters of the high speed shaft. To verify this estimate, the value calculated using Equation (3-18) and the value estimated

from an approximation that is often used in practice, which is shown in Equation (3-23), are compared [76].

$$J = \frac{14500}{9} P_{rated}^{1.2} r^2 \quad (3-23)$$

where  $P_{rated}$  is the rated power in  $10^6$  watts. In this study, the turbine has a rated power of 25 kW. Hence, Equation (3-23) used a value of  $P_{rated}$  of  $25 \times 10^{-3}$ .

Using Equation (3-23), the total turbine inertia is estimated as  $482 \text{ kgm}^2$  (referring to the low speed shaft). This value is not significantly different from the total turbine inertia of  $498 \text{ kgm}^2$  that is calculated from the estimated inertia of the low speed shaft of  $3.068 \text{ kgm}^2$ .

### 3.4 Induction Generator and Full-Rated Power Converter Model

This sub-chapter presents the SIMULINK model for the dynamic interaction between the SCIG and the full-rated power converter. Figure 3-10 shows a diagram of this model.

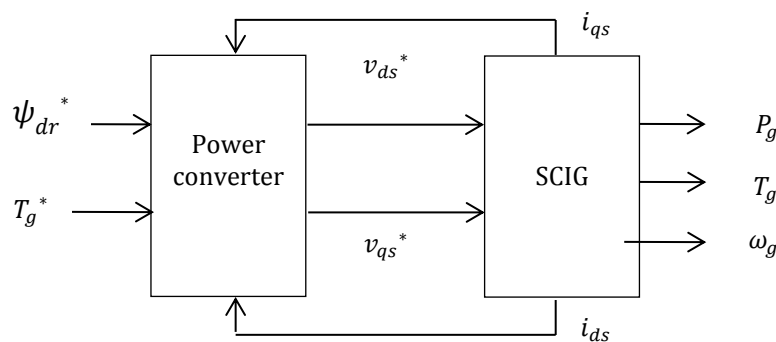
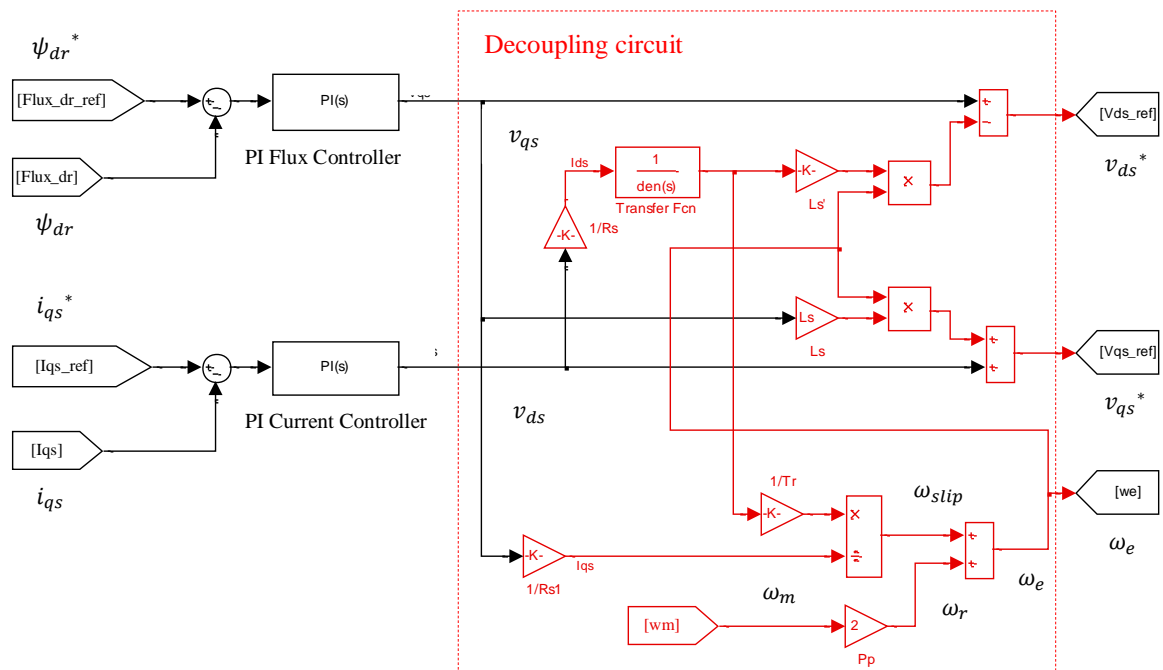


Figure 3-10 Dynamic interaction diagram between the SCIG and the full-rated power converter

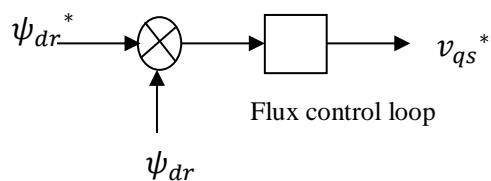
The inputs of the power converter are the reference rotor flux, the demanded generator torque and the dq-stator currents that are fed back from the SCIG model. The reference rotor flux and the demanded generator torque are derived from the rated rotor flux and the output of the generator speed controller, respectively. The output of the converter is the demanded dq-stator

voltages, which are also the inputs of the SCIG model. The signals of the generated power, torque and generator speed are the other final outputs obtained from the SCIG model.

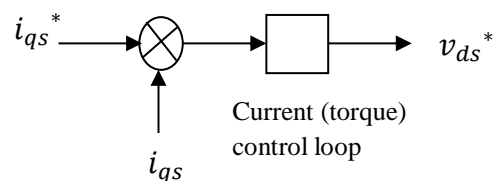
Figure 3-11(a) represents the interior of the power converter model. To create the decoupled output reference of the stator voltages, the outputs of the flux and current controller ( $v_{ds}, v_{qs}$ ) are fed into the decoupling circuit, as shown in red in Figure 3-11(a).



(a)



(b)



(c)

Figure 3-11(a) The MATLAB/SIMULINK model of the power converter, (b) Simplified flux control, and (c) Simplified current (torque) control

Figure 3-11(a) shows the coupling effect in which  $\psi_{dr}$  is controlled through  $v_{qs}$  and  $i_{qs}$  is controlled through  $v_{ds}$ . Thus, to create an independent control of the d-axis current component and the q-axis current component, these unwanted coupling terms need to be cancelled. A schematic of this coupling effect is shown in Figure 3-11(b) and Figure 3011(c).

Before presenting how the decoupling is performed, the procedure for this coupling is explained. The coupling terms obtained from the SCIG state model are

$$\dot{x} = A(\Omega_h).x + Bu \quad (3-24)$$

$$y \equiv T_g = \frac{3pL_m}{2}(i_{qs}i_{dr} - i_{ds}i_{qr})$$

Using the stator voltage components as the input vector and the rotor flux  $\psi_{dr}$  and stator current  $i_{qs}$  as the state vectors [17], the method of adding these coupling terms to the output from the flux and current controllers can be shown as

$$u = [v_{ds} \quad v_{qs}]^T \quad (3-25)$$

$$x = [\psi_{dr} \quad i_{qs}]^T \quad (3-26)$$

where

$$\psi_{dr}(s) = M(s).(v_{ds}(s) + N(s)i_{qs}(s)) \quad (3-27)$$

$$i_{qs}(s) = P(s).(v_{qs}(s) - R(s)\psi_{dr}(s)) \quad (3-28)$$

where  $R(s) = \omega_e . (\sigma L_s . \frac{1+L_r/R_r . s}{L_m} + \frac{L_m}{L_r})$ ,  $\sigma = \text{sigma} = 1 - L_m^2 / (L_s L_r)$ ,  $R_s$  is the stator resistance,  $L_s$  is the stator inductance,  $R_r$  is the rotor resistance,  $L_r$  is the rotor inductance and  $L_m$  is the magnetising leakage inductance.

Equations (3-24) to (3-26) can be represented as a block diagram, as shown in Figure 3-12(a). By inverting the function for which the expected

outputs are the stator voltage components  $v_{ds}$  and  $v_{qs}$ , the coupling terms are obtained as shown in Figure 3-12(b).

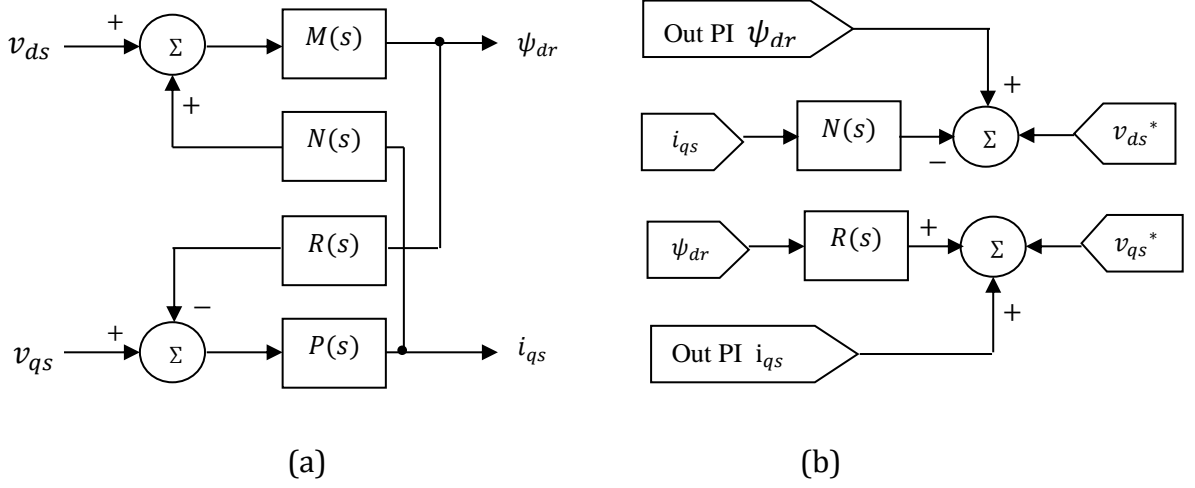


Figure 3-12 (a) Rotor field-oriented SCIG model (b) d-q decoupling by state feedback plus decoupling terms [17]

To obtain the reference stator voltage of the d-axis,  $v_{ds}^*$ , the output of the flux control loop,  $v_{qs}$ , needs to be added to  $-N(s)i_{qs}$  or  $-\omega_e L_s' i_{qs}$ . A similar method can be used to obtain the reference stator voltage of the q-axis,  $v_{qs}^*$ ; the output of the current control loop,  $v_{ds}$ , needs to be added to  $-R(s)\psi_{dr}$  or  $\omega_e L_s i_{ds}$ . Because this equation represents steady state conditions, the derivative term of  $(\sigma L_s \cdot \frac{1+L_R/R_r \cdot s}{L_m})$  is equal to zero.

To cancel the coupling effect between the d- and q-axes, the outputs of the Flux  $\psi_{dr}$  PI controller and the output of the Current  $i_{qs}$  PI controller will be added to the decoupling terms ( $\omega_e L_s' i_{qs}$  and  $\omega_e L_s i_{ds}$ ). The reference d-q stator voltages ( $v_{ds}^*$  and  $v_{qs}^*$ ) can then be obtained using Equations (3-29) and (3-30). Thus,  $\psi_{dr}$  or  $i_{ds}$  is controlled by  $v_{ds}$ , and  $i_{qs}$  is controlled by  $v_{qs}$ , which are independent of each other.

$$v_{ds}^* = v_{qs} - \omega_e L_s' i_{qs} \quad (3-29)$$

$$v_{qs}^* = v_{ds} + \omega_e L_s i_{ds} \quad (3-30)$$

where  $L_s'$  is the stator transient inductance

$$L_s' = L_s - \frac{L_m^2}{L_r} \quad (3-31)$$

Referring back to Figure 3-10, a transfer function is included in the decoupling circuit. This first order transfer function  $\frac{1}{T_s' s + 1}$  (where  $T_s' = \frac{L_s'}{R_s} =$  stator transient time constant) is multiplied by  $i_{ds}$  to show the delay in the current; this occurs in the real system, where unwanted overshoots can be avoided during the transient period [136].

The SCIG based on the wind turbine system involved in this study was explained briefly in Chapter Two. The SCIG based on a wind turbine model is developed based on the appropriate equations shown in the subsection 2.3.3 in the preceding chapter. However, because this study is focused on a SRVSWT that is equipped with an SCIG, only suitable differential equations for the turbine side and the generator side are chosen. Figure 3-13 shows the design of the complete SIMULINK model of a SCIG. Four blocks are needed inside the complete SCIG model to produce the output signals. These blocks are the mechanical speed (Block A), the rotor flux (Block B), the d-axis of the stator current (Block C) and the q-axis of the stator current (Block D). Each block will be explained in a more detail next with assistance of Figures 3-14 to 3-15.

The nonlinear equations for these four models that relate to the appropriate design outputs are expressed in Equations (3-32) to (3-35).

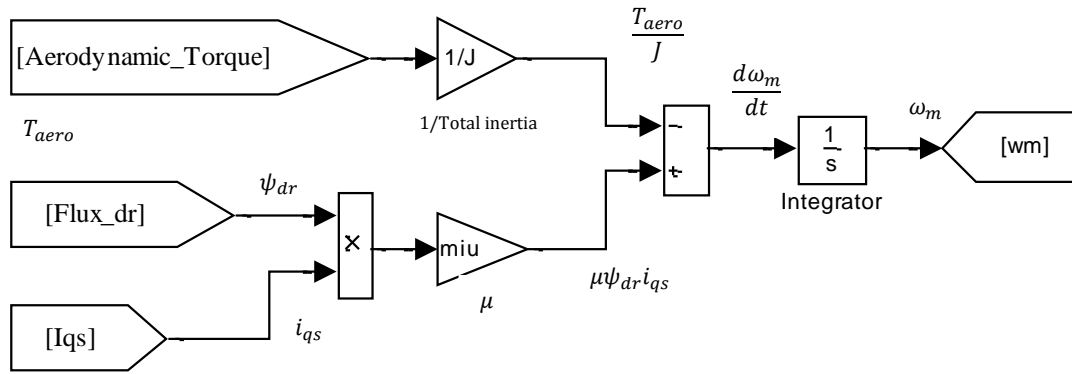
$$\frac{d\omega_m}{dt} = \mu F_{dr} i_{qs} - \frac{T_l}{J} \quad (3-32)$$

$$\frac{dF_{dr}}{dt} = -\alpha F_{dr} + \alpha M i_{ds} \quad (3-33)$$

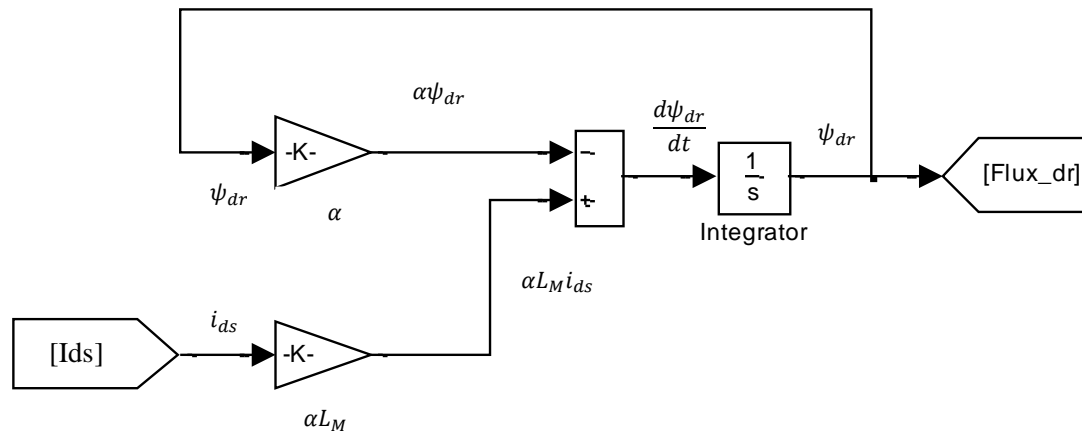
$$\frac{di_{ds}}{dt} = -\gamma i_{ds} + \omega_m i_{qs} + \frac{\alpha M i_{qs}^2}{F_{dr}} + \beta \alpha F_{dr} + \frac{v_{ds}}{\sigma} \quad (3-34)$$

$$\frac{di_{qs}}{dt} = -\gamma i_{qs} - \omega_m i_{ds} - \frac{\alpha M i_{qs} i_{ds}}{F_{dr}} - \beta \omega_m F_{dr} + \frac{v_{qs}}{\sigma} \quad (3-35)$$





(a)



(b)

Figure 3-14 (a) Components of the MATLAB/SIMULINK SCIG model: Block A, (b) Components of the MATLAB/SIMULINK SCIG model: Block B

The models of the stator currents  $i_{ds}$  and  $i_{qs}$  are developed as illustrated in Figure 3-15(a) and Figure 3-15(b) using Equations (3-34) and (3-35), respectively. Finally, the generated torque,  $T_g$ , and the generated power,  $P_g$ , of the SCIG are estimated using Equations (3-36) and (3-37), respectively.

$$T_g = \frac{L_m}{L_r} F_{rd} i_{qs} \quad (3-36)$$

$$P_g = T_g \omega_m \quad (3-37)$$

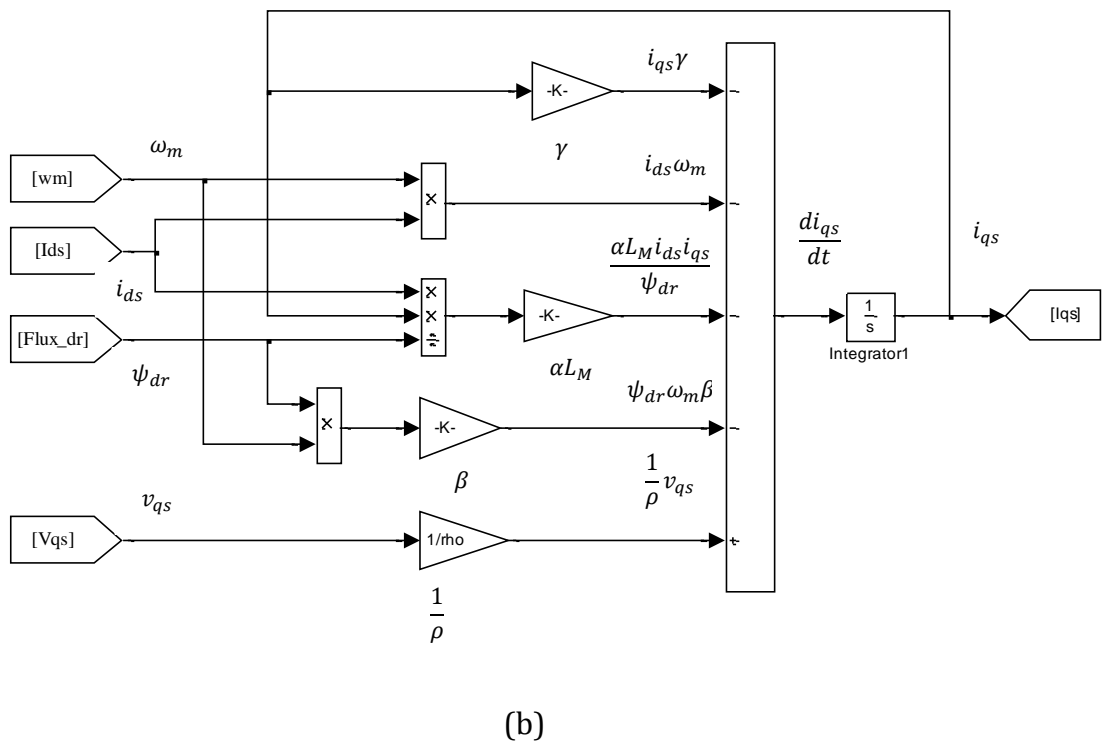
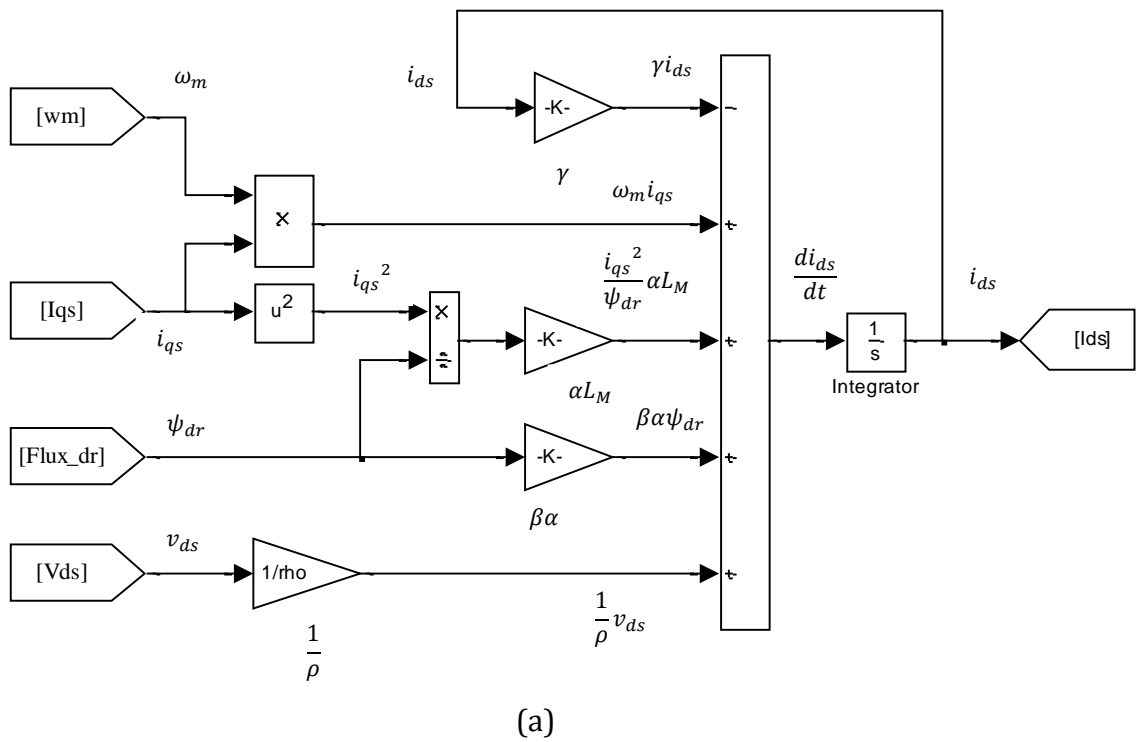


Figure 3-15 (a) Components of the MATLAB/SIMULINK SCIG model: Block C, (b) Components of the MATLAB/SIMULINK SCIG model: Block D

### 3.4.1 Estimation of the Generator Parameter

The parameter values of the equivalent circuit of the induction generator that is used in the Carter wind turbine were estimated based on information from the manufacturer's brochure, including rated power ( $P_{rated}$ ), rated voltage ( $V_R$ ), rated power factor ( $\cos\theta$ ), rated frequency ( $f_R$ ), rated efficiency ( $\eta_R$ ) and online stator resistance ( $R_s$ ). Table 3-1 shows selected parameters that are relevant to the simulation. These parameters are read or recorded from the drive that was installed in the wind turbine system at West Beacon Farm. These details were also reported in Kemsley, R [137].

Table 3-1 Drive parameters

Parameter	Description	Default	Set to
4.13	Current control P Gain	20	20
4.14	Current control I Gain	40	40
5.06	Motor's rated frequency Hz	50	50
5.07	Motor's rated current A	60	60
5.09	Motor's rated voltage	400	400
5.1	Motor's rated power factor	0.92	0.984
5.11	Motor - No. of poles (1=4 POLES)	1	1
5.17	Stator resistance (open loop only) ohms	0	0.287

Using the power flow diagram of a three-phase induction motor as presented in Figure 3-16, the rated current ( $I_R$ ) is determined using Equation (3-38) [138, 139].

$$P_{rated} = P_o = \sqrt{3}V_R I_R \cos\theta \quad (3-38)$$

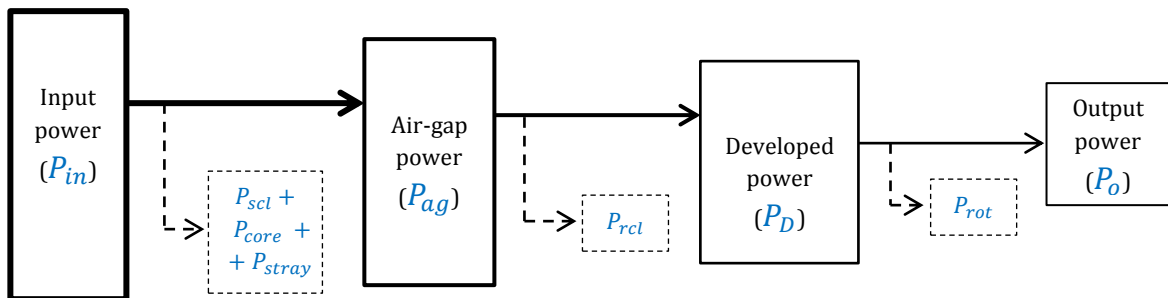


Figure 3-16 Power flow in a three-phase induction motor

Using the motor's rated efficiency and rated power, the total rated input power is determined using Equation (3-39).

$$n_R = \frac{P_o}{P_{in}} \quad (3-39)$$

Based on the IEEE 112-B standard, assuming that the rotational loss ( $P_{rot}$ ), which includes the bearing friction and windage losses, is equal to 0.5% of the total rated input power ( $P_{in}$ ) [ $P_{in}$ ] [140], the developed power ( $P_D$ ) is then estimated using Equation (3-40) [141].

$$P_D = P_{rot} + P_o \quad (3-40)$$

From Figure 3-16 and using the equivalent circuit of a three-phase induction motor as depicted in Figure 3-17, the air-gap power ( $P_{ag}$ ) is calculated as [141]

$$P_{ag} = P_{in} - P_{scl} - P_{core} - P_{stray} = 3I_r^2 \frac{R_r}{s} = \frac{P_D}{(1-s)} \quad (3-41)$$

where

$$P_D = P_{ag} - P_{rcl} = 3I_r^2 R_r \frac{(1-s)}{s} = P_{ag}(1-s) \quad (3-42)$$

$$P_{scl} = 3I_s^2 R_s = \text{stator copper loss} \quad (3-43)$$

$$P_{rcl} = 3I_r^2 R_r = sP_{ag} = \text{rotor copper loss} \quad (3-44)$$

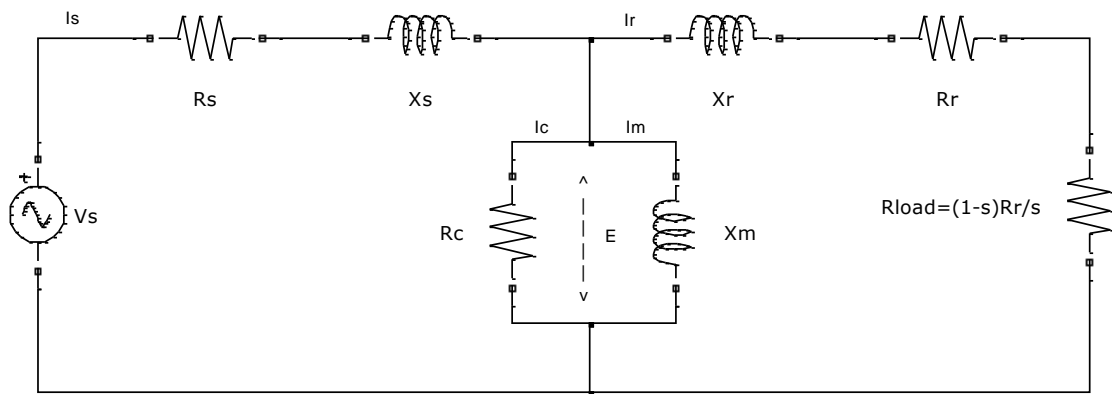


Figure 3-17 Equivalent circuit of a three-phase induction motor

From Equation (3-42), the rotor loss ( $P_{rcl}$ ) is obtained by subtracting  $P_D$  from  $P_{ag}$ . The value of the rotor resistance ( $R_r$ ) can be estimated using Equation (3-44). From the available information, the approximate total losses are given as

$$P_{losses} = \frac{(1-n_R)}{n_R} P_R \quad (3-45)$$

From Figure 3-16, the total losses of the stator copper and core can be calculated as

$$P_{scl} + P_{core} + P_{stray} = P_{losses} - P_{rcl} - P_{rot} \quad (3-46)$$

Numerous studies have assumed that  $P_{core} = P_{stray}$  and that these losses are equal to  $P_{rot}$ . Thus,  $P_{scl}$  can be estimated and used to calculate the stator current ( $I_s$ ) using Equation (3-43) [139]. Using  $I_s$ , the stator voltage ( $V_s$ ) and the voltage drop at the parallel branch ( $E$ ) shown in Figure 3-17 can be estimated using Equations (3-47) and (3-48), respectively. An approximation using a simplified circuit was made in Equation (3-48), where the stator reactance ( $X_s$ ) shown in Figure 3-17 is neglected.

$$P_{in} = \sqrt{3}V_s I_s \cos\theta \quad (3-47)$$

$$E = V_s - I_s R_s \quad (3-48)$$

Therefore, the magnetisation reactance is calculated as

$$x_M = \frac{E}{I_m} \quad (3-49)$$

where

$$I_m = I_s - \frac{E}{R_c} \quad (3-50)$$

$$R_c = \frac{3E^2}{P_{core}} = \text{core resistance} \quad (3-51)$$

Finally, for the stator and rotor reactance values, because the NEMA-design class of the motor is unknown, design class A is assumed which is a quite common type of induction motor [142]. Therefore, these parameters are assumed equal ( $x_s = x_r$ ). NEMA refers to the National Electrical Manufacturer's Association which produces important specifications (such as rated voltage, rated current, rated frequency, rated full load speed, rated horsepower, etc.) found on every motor nameplate. Using Equation (3-52), which was taken from [143], the  $x_s$  and  $x_r$  can be estimated by solving the roots of the equation where only  $x_s$  is unknown. The stator leakage reactance and the rotor leakage reactance can then be calculated using Equations (3-53) and (3-54), respectively.

$$4 * \left( \frac{1}{x_M} - \frac{\tan \theta}{R_c} \right) * x_s^2 + 2x_s + \left( \frac{1}{x_M} - \frac{\tan \theta}{R_c} \right) * \left( R_s + \frac{R_r}{s} \right)^2 - \tan \theta * \left( R_s + \frac{R_r}{s} \right) = 0 \quad (3-52)$$

$$x_{ls} = x_M - x_s \quad (3-53)$$

$$x_{lr} = x_M - x_r \quad (3-54)$$

### 3.5 Summary of Wind Turbine Data/Parameter

The characteristics of the wind turbine based on the parameters estimated in the previous subsections are depicted in Table 3-2.

Table 3-2 Wind Turbine Characteristics

Section	Parameter	Symbol	Value
<b>Rotor</b>	Blade rotor	$R$	5 m
	Hub height	$h$	23.8 m
	Rotor inertia (including hub)	$J_r$	372 kgm <sup>2</sup>
	Rated power output	$P_{rated}$	25 kW
	Maximum power output	$P_{max}$	30 kW
	Maximum power coefficient	$C_{pmax}$	0.478
	Optimum tip speed ratio	$\lambda_{opt}$	6.78
	Air density	$\rho$	1.225 kg/m <sup>3</sup>
<b>Drive train</b>	Gearbox ratio	$G$	12.748
	Total turbine inertia	$J$	3.068 kgm <sup>2</sup> (for the high speed shaft)
<b>Generator</b>	Generator inertia	$J_g$	0.78 kgm <sup>2</sup>
	Rated/base frequency	$f_{rated}$	50 Hz
	Rated/base voltage	$V_{rated}$	400 Volt
	Rated current	$I_{rated}$	60 Amps
	Number of poles	$P$	4
	Number of pole pairs	$P_p$	2
	Stator resistance	$R_s$	0.287 $\Omega$
	Stator inductance	$L_S$	43.1 mH
	Stator leakage inductance	$L_{ls}$	3.916 mH
	Stator leakage reactance	$x_{ls}$	1.23 $\Omega$
	Stator reactance	$x_S$	13.54 $\Omega$
	Rotor resistance	$R_r$	0.125 $\Omega$
	Rotor inductance	$L_R$	43.1 mH
	Rotor leakage inductance	$L_{lr}$	3.916 mH
	Rotor leakage reactance	$x_{lr}$	1.23 $\Omega$
	Rotor reactance	$x_R$	13.54 $\Omega$
	Magnetising leakage inductance	$L_M$	39.184 mH
	Magnetising Reactance	$x_M$	12.31 $\Omega$
	miu	$\mu$	0.296 kg <sup>-1</sup> m <sup>-2</sup>
	alpha	$\alpha$	2.9 $\Omega$ /H
	beta	$\beta$	121.6 H <sup>-1</sup>
	gamma	$\gamma$	52.207 $\Omega$ /H
sigma	$\sigma$	7.476 mH	

Note: Leakage inductance means the leakage component that occurs in the flux linkage.

### 3.6 Validation of the Fixed-Speed SRWT Simulation Model

There is no standard theory or terminology in the area of model verification and validation (V& V) [144]. However, V&V is a necessary tool to evaluate the system accuracy, particularly in the absence of real data test.

As explained in the preceding sections, a modular programming approach was utilised to verify the proposed SRVSWT system model. To validate that the proposed SRVSWT model for this study is sufficiently accurate to represent the

behaviour of the real system, the complete model is tested while operating at a fixed speed. The fixed-speed SRWT is then validated with information from the manufacturer and data from an existing turbine in West Beacon Farm, Loughborough, UK. The modelling results obtained with this methodology are compared with the performance of the turbine at several operating frequencies. A discussion of the results and the ability of the model to accurately simulate relevant phenomena is also provided. The operation of the turbine was simulated at frequencies of 50 Hz and 43.5 Hz:

- 1- Turbine runs at a frequency of 50 Hz: The wind turbine was designed by the manufacturer to run at a fixed-speed of 50 Hz. Hence, the available data such as power versus wind speed curve and the power coefficient versus tip speed ratio were based on this frequency.
- 2- Turbine runs at a frequency of 43.5 Hz: The Carter turbine at West Beacon Farm currently operates at 43.5 Hz to enable a lower cut-in wind speed and to avoid frequent idling [145]. Therefore, the available data set (power versus wind speed curve) is based on this operating frequency.

### **3.6.1 Validation of Turbine Operation at 50 Hz**

To verify the SRWT model, the developed SIMULINK model was used to simulate an operating frequency 50 Hz, and the results were compared with the manufacturer's data. The manufacturer's data were taken from a brochure that is attached in [129]. Figure 3-18(a) shows the manufacturer's data and the generated power from the simulations under two wind speed patterns. The first pattern is a ramp wind speed signal, whereas the second pattern is a realistic wind speed profile that ranges from 3 to 16 m/s, as illustrated in Figure 3-18(b) and Figure 3-18(c), respectively.

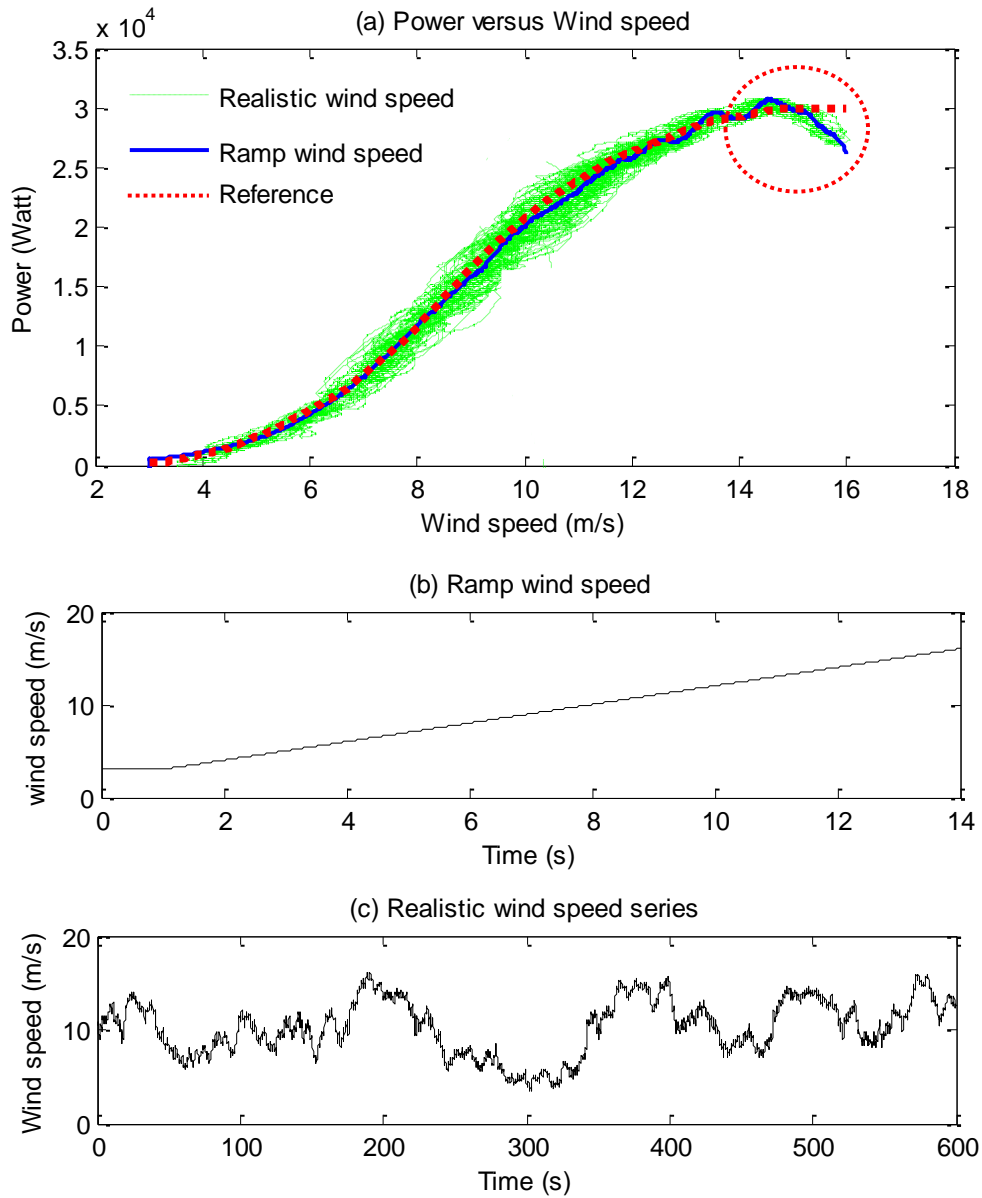


Figure 3-18 (a) Power versus wind speed (b) ramp wind speed (c) realistic wind speed

Figure 3-18(a) shows that the generated power at low and medium wind velocities in the simulations agrees well with the manufacturer's data. As the wind speed increases from the cut-in to the rated wind speed, the simulated power increases at roughly the cube of the wind speed. When the realistic wind speed is run for 600 seconds, the generated power shows a scattered signal around the curves from the manufacturer's and ramp wind speed inputs. This scattered signal represents realistic behaviour, where the power varies due to the rotor responses to changes in wind speed [146]. The inertia of the turbine

rotor and generator affect the rotation speed of the generator through the slip factor even though the turbine is run at a fixed speed.

However, when the wind speed reaches 13 m/s, the simulations begin to behave differently. The simulated curves decrease significantly when the wind speed reaches approximately 15 m/s. This is expected because when the wind speed increases, the turbine experiences a dynamic stall and then goes into a deep stall [147] at higher wind speeds. The dynamic stall at very high wind speeds was not considered in the modelling. Consequently, two observations are made from the response to high winds:

- 1- The first observation is that power fluctuations are shown by the simulations after the turbine reached the rated wind speed (approximately 11.7 m/s). The signals represent the actual behaviour of the turbine during stall conditions, where the power cannot be captured linearly due to the complex loads caused by fluctuations of the wind and turbulence.
- 2- The second observation is that a dynamic stall model is required in the design model to simulate the stall phenomena and determine how a deep stall can be avoided when the wind speed reaches 15 m/s, as shown in Figure 3-18(a). This implies the need to obtain an updated  $C_p - \lambda$  curve with a better model. For this reason, the next subsection describes the adjusted model curve.

### **3.6.1.1 Dynamic stall at high wind speeds (in the FL region)**

As depicted in Figure 3-18(a), one reason that the deep stall occurred too early is that the slope of the  $C_p - \lambda$  curve is very steep in that region. Therefore, a dynamic (adjusted) stall model needs to be included in the design methodology.

A dynamic (adjusted) stall model can be included in the simulation model by modifying the  $\lambda$  term in Equation (2-5). The additional component of tip speed ( $\Delta\omega_{stall}R$ ) needs to be added to the original tip speed, as shown in Equation (3-55).

$$\lambda_{stall} = \frac{\omega R + (\Delta\omega_{stall}R)}{U} = \frac{(\omega + \Delta\omega_{stall})R}{U} = \lambda + \Delta\lambda \quad (3-55)$$

High wind velocities increase the angle of attack, and  $\lambda$  will be influenced by these changes of angle of attack. The addition of the  $\Delta\omega_{stall}R$  term to represent the dynamic stall during high winds is necessary to demonstrate the different  $\lambda$  behaviours during early stall and deep stall. According to Equation (2-4), when  $\lambda$  decreases during high winds in the FL region,  $C_p$  also decreases, meaning that the efficiency of the generated power also decreases. When Equation (3-55) is considered for high winds, the present value of tip speed ratio is now greater than the original value of  $\lambda$  in Equation (2-5). This is due to that the present blade tip,  $(\omega R + (\Delta\omega_{stall}R))$ , is now larger than when the original  $\lambda$  (blade tip =  $\omega R$ ) is used. This situation is illustrated in Figure 3-19.

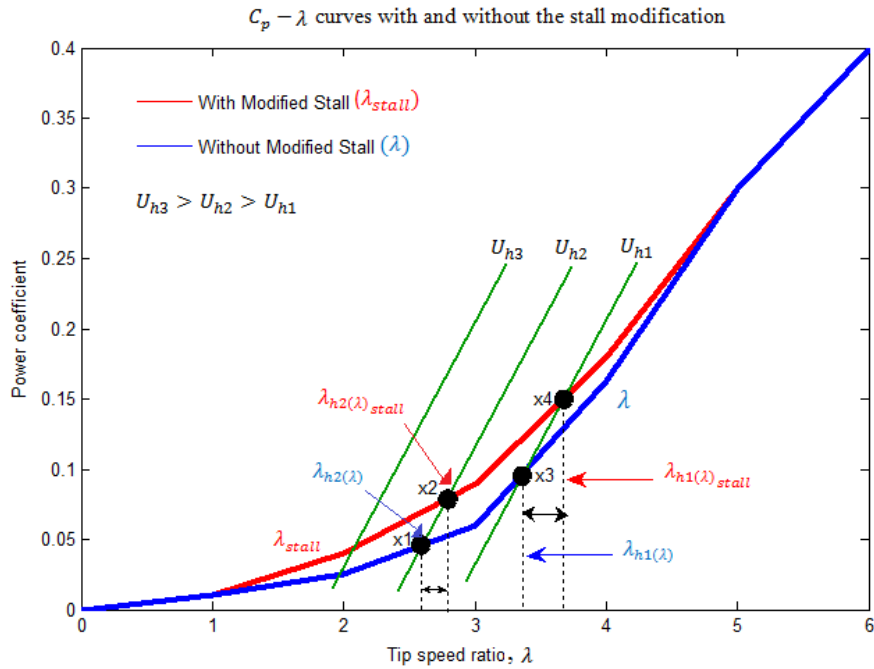


Figure 3-19  $C_p - \lambda$  curves with and without the stall modification

Figure 3-19 shows the difference between the  $C_p - \lambda$  curves before and after being modified to represent a stall in the FL regime. Note that,  $U_{h3} > U_{h2} > U_{h1}$ . Let say, when wind speed experiences a constant speed at  $U_{h1}$ , the tip speed ratio will be located at point  $x3(\lambda_{h1}(\lambda))$  if original  $\lambda$  is used. Conversely, the tip speed ratio will be located at point  $x4(\lambda_{h1}(\lambda)_{stall})$  if  $\lambda_{stall}$  is used (with the same

wind speed;  $U_{h1}$ ). Similarly, when wind speed blows at  $U_{h2}$ , the tip speed ratio will be shifted to the right plane (from  $\lambda_{h2(\lambda)}$  to  $\lambda_{h2(\lambda)_{stall}}$ ) when  $\lambda_{stall}$  is considered. Therefore, power can be shifted upward, in which the efficiency of the turbine will be significantly increased. Sorenson et al. [147] also confirmed that the power signal will increase considerably if a dynamic stall model is included in the simulation. Hence, the behaviour of the dynamic stall also can be expressed in Equations (3-56) and (3-57). At  $\lambda_{stall}$ , power coefficient also increases.

$$\lambda_{stall} \Rightarrow C_{p-stall} \quad (3-55)$$

where

$$C_{p-stall} = C_p + \Delta C_p \quad (3-56)$$

Also, meaning that, when  $\lambda_{stall}$  is considered, the actual rotor speed will be larger than when the original  $\lambda$  is used. In reality, means that turbine will slows down more slowly when wind speed changes from  $U_{h1}$  to  $U_{h2}$ ; and so it goes when wind speed keep increases. This is due to the factor of  $\omega + \Delta\omega_{stall}$  in Equation (3-55). From Figure 3-19, it also can be depicted that when the wind speed increases (let says, from  $U_{h1}$  to  $U_{h3}$ ) as  $\lambda$  decreases, the generated power decreases with the increasing of wind speed, due to the steep slope of  $C_p$  efficiency. Tang et al. [76] also confirmed that the wind turbine will experience a greater power reduction during high winds than during medium winds.

In summary, from illustration that was depicted in Figure 3-19, the significant effect of the dynamic (modified) stall can be observed and understood clearly. Therefore, it is necessary to include the dynamic stall algorithm in the model in the FL region to provide realistic behaviour during high winds. The details of the tip speed ratio and power coefficient when the dynamic stall is included are given in Table 3-3. From the table, the response during high winds for  $\lambda_{stall}$  values between zero and five is provided. When wind speed increases from the state of the optimum tip speed ratio ( $\lambda_{opt} = 6.78$ ) to  $\lambda_{stall} = 5$ , no modification is included, in which at this range of  $\lambda$  values, early stall occurred.

The modification of the tip speed ratio started when tip speed ratio greater than five. From the data given in Table 3-3, it can be observed that the  $C_{p-stall}$  increases with increasing of tip speed ratio, as the increasing of wind speeds. Power coefficient has a significant change when  $\lambda=3$  and the  $\Delta C_p$  narrowed when tip speed ratio larger than 3.

Table 3-3 Details of the new tip speed ratio and power coefficient

$\lambda_{stall}$	$C_{p-stall} = C_p + \Delta C_p$	$C_p$	$\Delta C_p$
1.0	0.001	0.001	0
1.5	0.020	0.0165	0.0035
2.0	0.040	0.025	0.015
2.5	0.067	0.0425	0.0245
3.0	0.090	0.060	0.030
3.5	0.139	0.115	0.024
4.0	0.180	0.163	0.013
4.5	0.245	0.235	0.01
5.0	0.300	0.300	0

As a result of the dynamic stall algorithm being added to the model, the new power versus wind speed curve resembles the manufacturer's curve, as depicted in Figure 3-20. The generated power during high winds is much improved for both the ramp wind speed and realistic wind speed inputs.

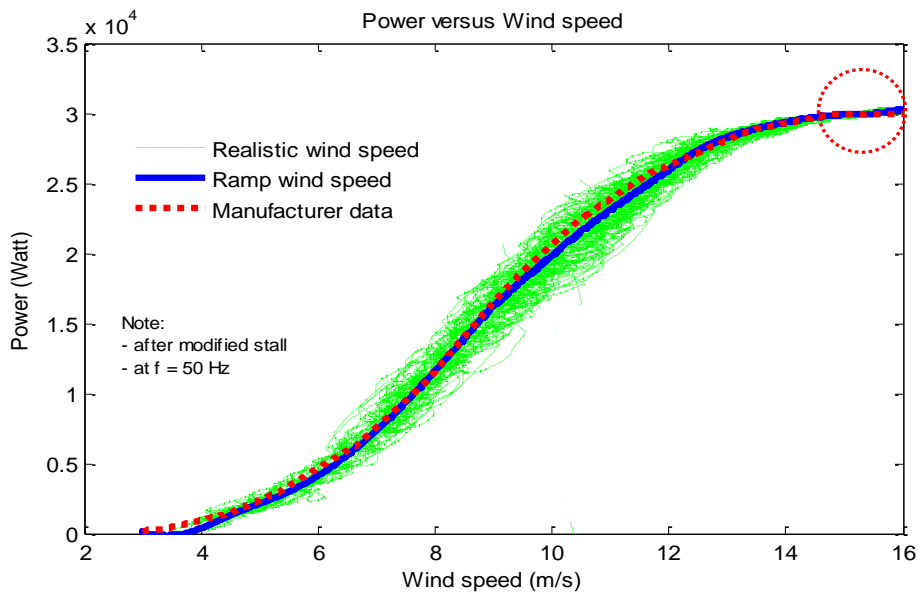


Figure 3-20 Power versus wind speed after the stall modification for high winds

Figure 3-21 shows other important responses that further validate the accuracy of the model when realistic wind speeds were simulated for 600 seconds. The manufacturer's and simulated curves of the  $C_p - \lambda$  response are compared in Figure 3-21(a). The simulation results appear to be identical to the manufacturer's curve. A  $C_{pmax}$  value of 0.478 is achieved at an optimum tip speed ratio,  $\lambda_{opt}$ , of 6.78. The tip speed ratio,  $\lambda$ , versus wind speed is depicted in Figure 3-21(b). The simulated response shows that  $\lambda$  decreases as the wind speed increases (at a fixed rotational speed). When the wind speed increases further and reaches the rated wind speed,  $C_p$  will decrease further, while  $\lambda$  becomes even smaller.

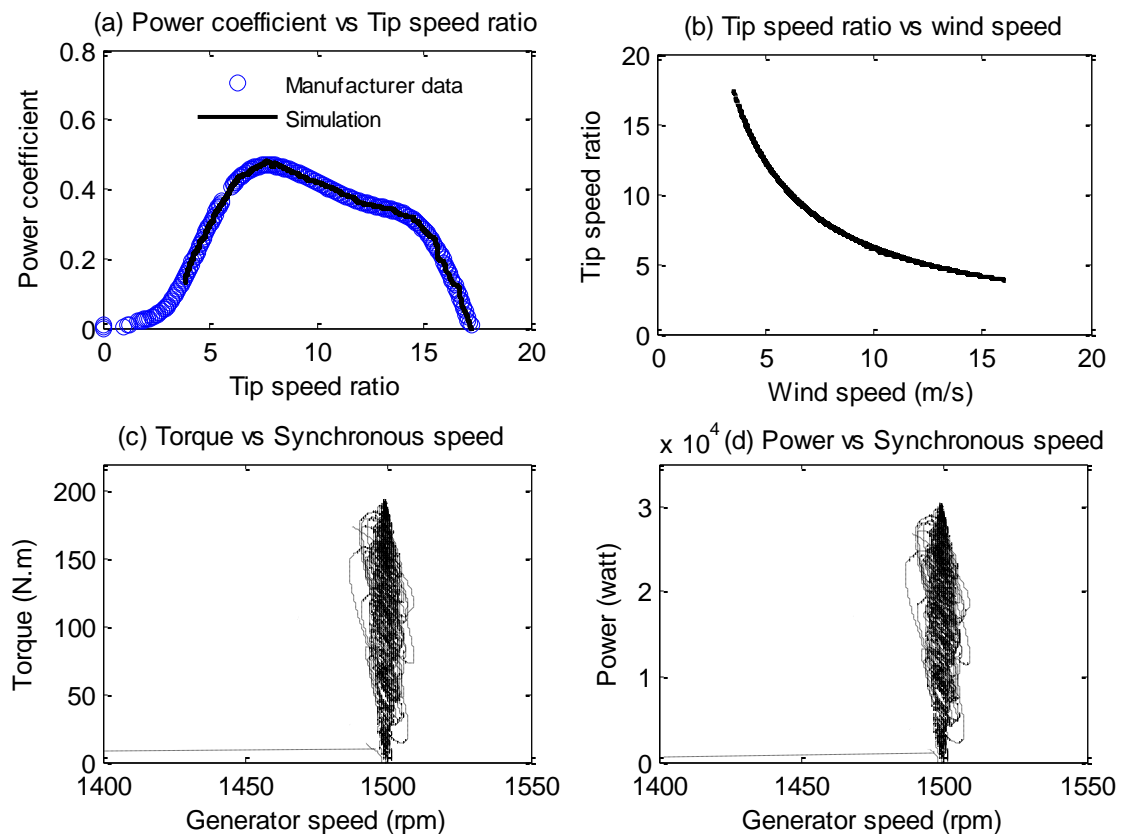


Figure 3-21 (a)  $C_p - \lambda$  curve, (b)  $\lambda$  - wind speed curve, (c) torque - speed curve, (d) power - speed curve

The torque and power versus generator speed in rpm is shown in Figures 3-21(c) and (d), respectively. At very low wind speeds or wind speeds below or close to the cut-in wind speed, the turbine operates at less than 1500 rpm. Approximately 2 kW of power is generated at this speed. However, at low-to-high wind speeds, the turbine runs at a fixed speed, while the generator operates at the nominal speed of 1500 rpm. The uncertainty of the speed deviates from the base speed by approximately  $\pm 1.2\%$ , which is consistent with real generators that have slip magnitudes of up to 2%. The developed torque and power also work below the maximum rated torque (about 300 N.m) and maximum power (about 30 kW), respectively.

In summary, the former fixed-speed SRWT model agrees well with the manufacturer's curve but deviates at very high winds ( $\geq 15$  m/s). By adding a dynamic stall algorithm, the fixed-speed SRWT model better simulated the manufacturer's power versus wind speed curve. Thus, the second model can be considered as valid and will be used for the next validation process, which is presented in the next subsection.

### **3.6.2 Validation of Turbine Operation at 43.5 Hz**

Using the SRWT model with the dynamic stall algorithm, the operating frequency of the generator was then changed from 50 Hz to 43.5 Hz. It is changed to this frequency because the available real data is based on this operating frequency. Therefore, equivalent comparison can be assured in determining the competence of the developed model to present the behaviour of the real system. Figure 3-22 compares the simulation and field measurements of the power generated at wind speeds from 0 to 16 m/s.

Figure 3-22 shows that the model agrees with the field measurements for both the ramp and realistic wind speeds except at wind speeds of approximately 13 to 14 m/s, where the simulation shows lower power production than the field data. This difference is probably caused by abrupt changes in the gust factor, turbulence level and air density while the field data were collected at these wind speeds. Figure 3-22 also shows that at lower operating frequencies, the main effect of a frequency change is a lower generated power. At an operating

frequency of 50 Hz, the power can reach a maximum of approximately 30 kW (as depicted in Figure 3-20), but when the operating frequency is 43.5 Hz, the maximum power is approximately 22 kW.

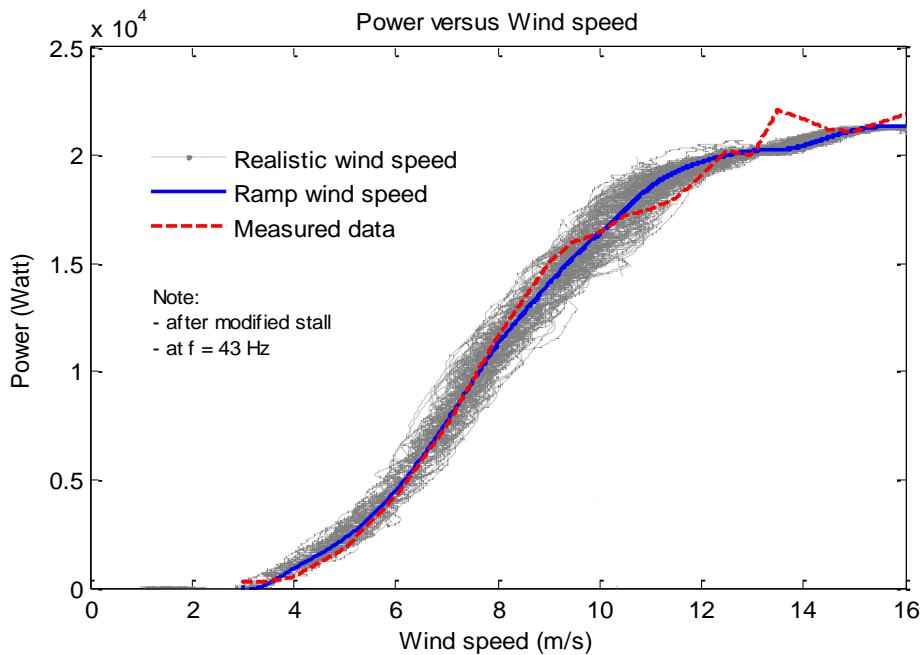


Figure 3-22 Power versus wind speed after the stall modification at an operating frequency at 43.5 Hz

The power and torque versus generator speed at a fixed speed of 43.5 Hz (1305 rpm or 136.66 rad/s) are shown in Figures 3-23(a) and (b). The power and torque increase with increasing wind speed. Figure 3-23(b) shows that the simulated torque agrees with the estimated torque range in [115]. See **Appendix 3B** for the estimated torque that was taken from [115]. The estimated torque was derived by Harson using the current and frequency data that were measured on site by Barton, J. [131]. Figure 3-23 shows that the simulated torque varies from zero and increases up to 156 N.m as the wind speed increases from minimum to rated. Meanwhile, from the figure shown in **Appendix 3B**, it can be seen that the estimated working torque for the Carter machine (the same machine considered in this study) is in a similar range. However, the difference in synchronous speed can be observed in these figures. This is because the operating frequency considered in this study is 43.5 Hz, whereby the operating frequency considered by Harson in [115] is 50 Hz.

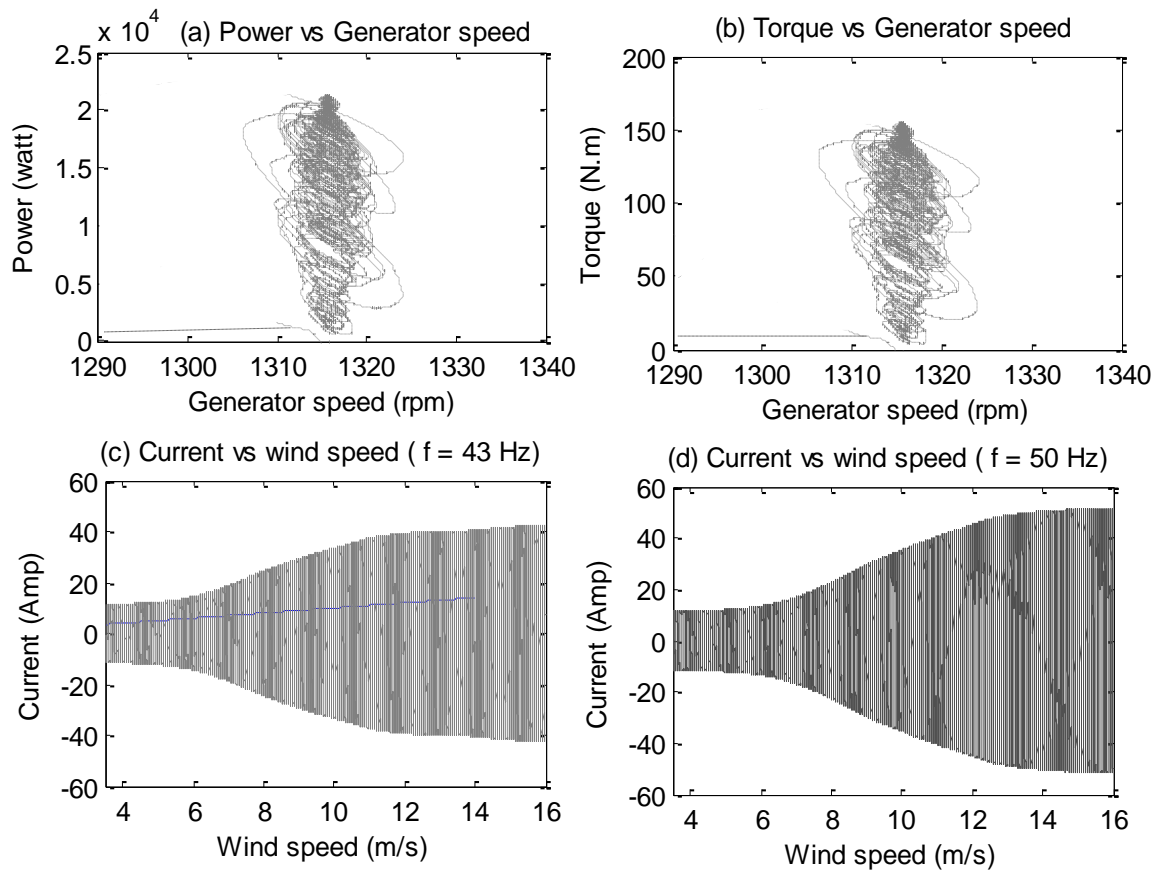


Figure 3-23 (a) Power vs. generator speed, (b) torque vs. generator speed, (c) phase current vs. wind speed (  $f = 43.5$  Hz), (d) phase current vs. wind speed (  $f = 50$  Hz)

Because the generator can operate with a maximum of 2% slip, the generator speed can vary between 1305 and 1331 rpm when the speed is set to 43.5 Hz. Because the wind speed varies from 3 to 16 m/s (and does not reach the cut-out wind speed), the electrical generator speed is estimated to operate at between 1305 and 1325 rpm. This is verified by the simulation signals as shown in Figures 3-23(a) and (b). In practical work, using an adjustable frequency/speed drive, the induction machine can be reconfigured to operate with various base speeds, without changing the physical structure and size of the machine [148]. This means that when using an adjustable frequency/speed drive, the base frequency is not usually restricted to be equal to a particular frequency (such as 50 or 60 Hz). When the voltage is changed proportional to the frequency while the ratio of the Volts/Hertz is maintained constant, the machine can be operated at the same rated torque (using the same machine). However,

this decreases the generated power (as shown in Figure 3-23(a)), as the operating current also decreases, as shown in Figures 3-23(c) and (d). The phase current increases with increasing wind speed. The focused snapshots for these current signals when the frequency is set to 43.5 Hz and 50 Hz are shown in Figure 3-24.

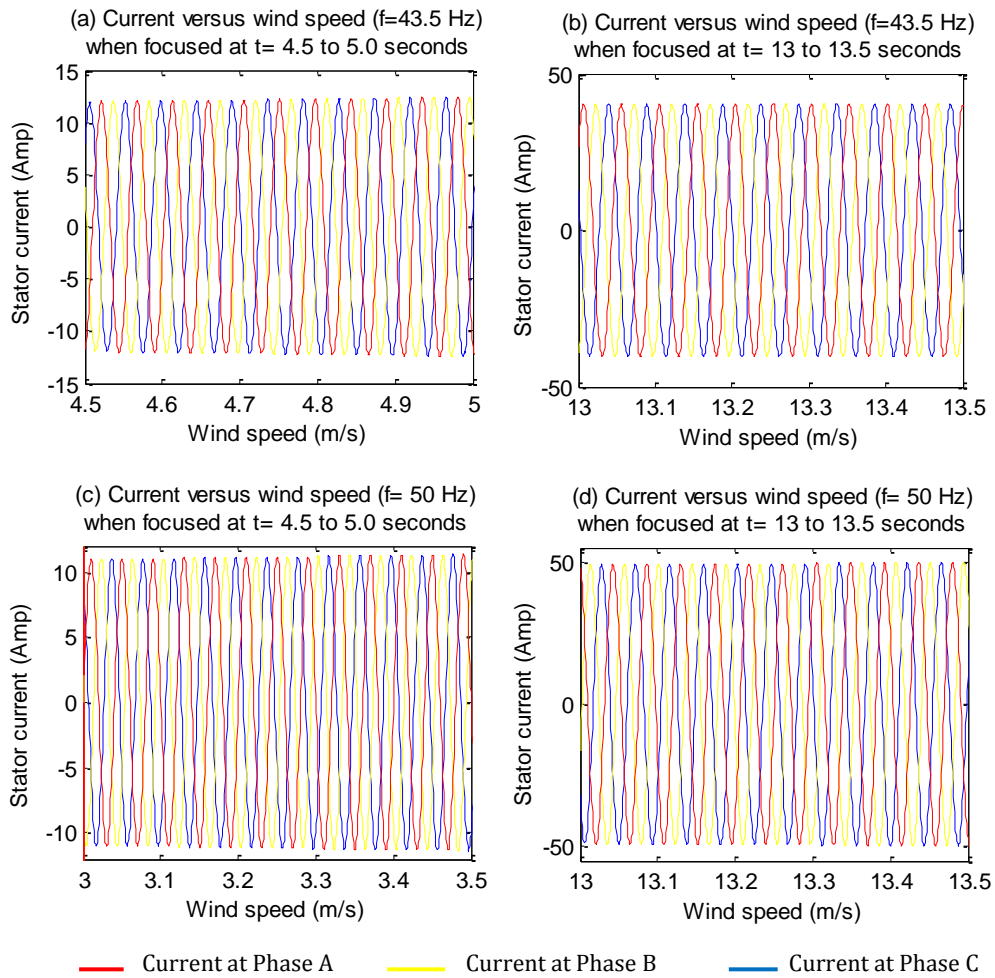


Figure 3-24 Snapshot current vs wind speed (a) at  $t = 3$  to  $3.5$  seconds ( $f=43.5$  Hz) (b) at  $t = 13$  to  $13.5$  seconds ( $f=43.5$  Hz) (c) at  $t = 3$  to  $3.5$  seconds ( $f=50$  Hz) (d) at  $t = 13$  to  $13.5$  seconds ( $f=50$  Hz)

At the higher operating frequency (50 Hz), the current reached 50 amps, whereas at the lower frequency (43.5 Hz), the current reached 40 amps. This scenario showed that the turbine works under normal conditions, where the rated phase is approximately 60 amps, as shown in Table 3-1 [137].

### 3.6.3 Details of the Fixed-speed SRWT Control

The control system that was applied to the fixed-speed SRWT model in this study is shown in Figure 3-25. Several guidelines were used to obtain the appropriate control parameters.

As shown in Table 3-1, the Proportional (P) and Integral (I) current control gains were set to 20 and 40, respectively. These gains were selected and set in the  $I_{qs}$  Current controller. Noting that the rotor flux and the magnetising current ( $i_m$ ) are proportional as shown in Equation (3-56), and considering that the magnetising inductance ( $L_M$ ) is constant, similar gains of P = 20 and I = 40 were also selected for the  $\psi_{dr}$  Flux controller.

$$\psi_{dr} = L_M i_m \quad (3-56)$$

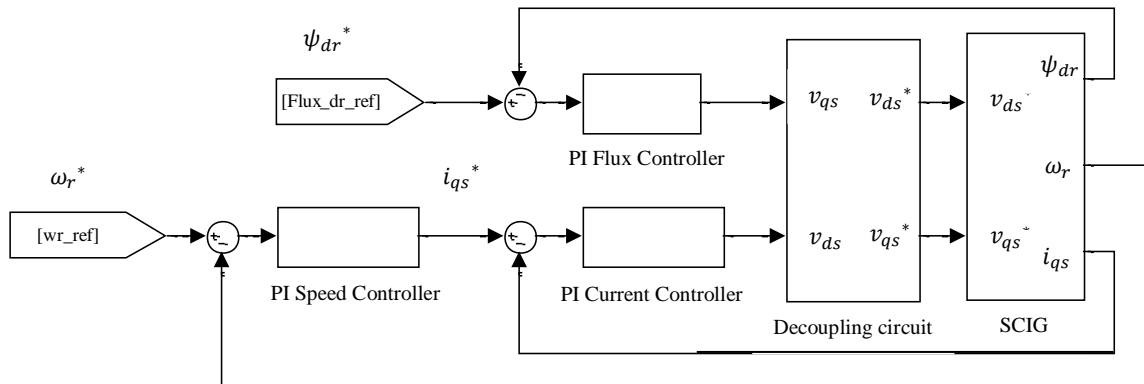
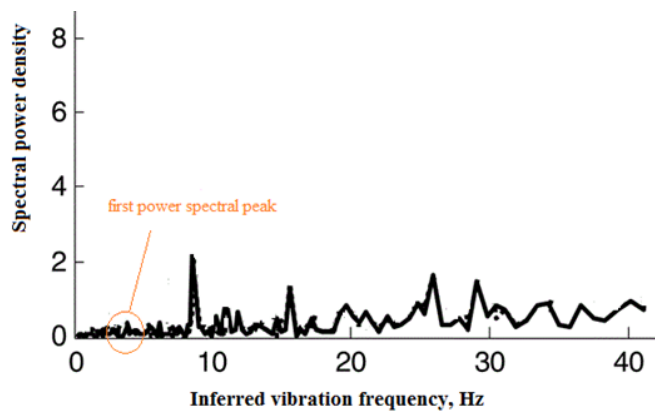


Figure 3-25 Schematic diagram of the fixed-speed SRWT control system

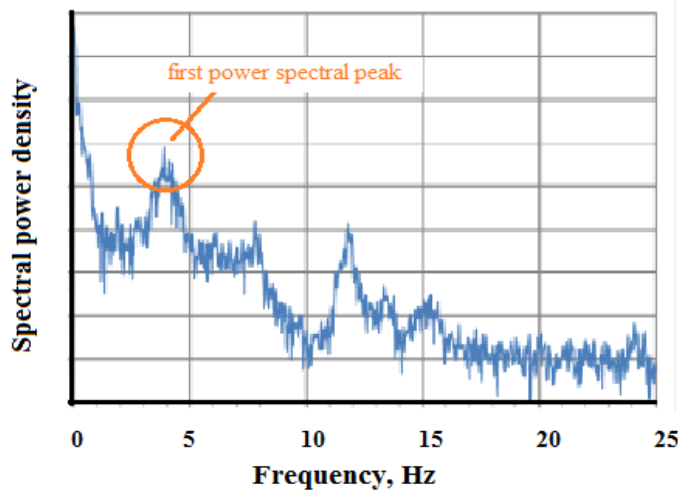
However, for the speed controller, the P and I gains were calculated based on the bandwidth that was appropriate for the natural frequency ( $f_n$ ) of the turbine rotation. Using the natural frequency as a reference, the control system can be improved by choosing a suitable cut-off frequency ( $f_{c,PI}$ ) for the speed controller. The value of  $f_{c,PI}$  should be less than the natural frequency [149, 150] and should provide a sufficiently low bandwidth [151]. A bandwidth that is too large may cause the signal to be dominated by noise when the control system become too active [149], whereas a bandwidth that is too low may result in the control system becoming nearly inactive because the control system becomes

too sensitive to the disturbances [151]. The bandwidth of the speed controller can be derived as follows:

- 1- To determine the  $f_n$  of the turbine rotor, it is common to consider the lower frequency component of the frequency spectrum signal of the turbine vibration [152]. As can be seen in the power spectral density function versus the frequency signal of the Carter turbine, which was taken from [131, 153] and [115] and is depicted in Figures 3-26(a) and (b), respectively, the  $f_n$  of the rotor is approximately 4 Hz. Hence, the natural bandwidth ( $\omega_n$ ) of the turbine rotor is approximately  $2\pi f_n = 25.13$  rad/s.



(a)



(b)

Figure 3-26 Graphs of power spectral density versus vibration frequency of the Carter wind turbine (a) taken from [131, 153] (b) taken from [115].

For the figure shown in Figure 3-26(a), the fast Fourier transform (FFT) spectrum of the accelerometer reflects to the generator frequency derived from the measured three-phase current signals. The generator frequency was then used to infer the blade rotor frequency as the high-speed shaft rotation frequency can be derived from the generator frequency data. Meanwhile, in Figure 3-26(b), the power spectrum reflects the drive train vibration frequency of the Carter wind turbine (as considered in Figure 3-26(a)) in which the vibration frequency was derived using the data obtained for the variation of power in response to wind speed. Interestingly, from these figures, it can be observed that both power spectrums show an identical first power spectral peak component with the peak frequency of 4 Hz. This frequency was therefore assumed to be the natural frequency of the blade rotor.

- 2- The cut-off frequency ( $f_{c,PI}$ ) of the speed controller should be less than  $\frac{1}{p}$  of  $f_n$  as shown in Equation (3-57) [154]

$$f_{c,PI} < \frac{f_n}{p} \quad (3-57)$$

where  $p$  should be greater than 5. If 6 is chosen for  $p$ ,  $f_{c,PI}$  is equal to 0.67 Hz, which can be considered as the cut-off frequency of the speed controller. Hence, the  $\omega_{c,PI}$  of the speed controller is approximately 4.21 rad/s. where  $\omega_{c,PI} < \omega_n$ . Good disturbance attenuation can be achieved using this rule.

- 3- Equation (3-58) [155] was used to verify that the  $f_n$  of the Carter turbine is approximately 4 Hz

$$f_n = \frac{1}{2\pi} \sqrt{\frac{K_s}{J_r}} \quad (3-58)$$

where  $K_s$  is the shaft stiffness and  $J_r$  is the inertia of the rotor.

The low and high speed shafts of the Carter turbine were measured during maintenance. The shaft was divided into several sections. Each section has a different length and diameter. The stiffness of the low speed shaft is estimated using Equation (3-59)

$$K = G \sum_{i=1}^n \frac{d_i^4}{32L_i} \quad (3-59)$$

where  $d$  is the shaft's diameter,  $G$  is the element's modulus of rigidity (90 Gpa for steel) and  $L$  is the element's length. Using Equation (3-59), the estimated stiffness is equal to  $2.35 \times 10^5$  N.m/rad. This value was confirmed by Harson [115], who calculated a stiffness of  $2.36 \times 10^5$  N.m/rad. Using this value of  $K$ , the natural frequency of the turbine rotor is 4 Hz.

$$f_n = \frac{1}{2\pi} \sqrt{\frac{K}{J_r}} = \frac{1}{2\pi} \sqrt{\frac{2.35 \times 10^5}{372}} = 4 \text{ Hz}$$

The final values of the P and I gains for the speed controller are thus equal to 4.6927 and 10.0396, respectively, using a phase margin of  $65^\circ$  from the rule in Equation (3-57). Using the PI gains that were selected for the three controllers as depicted in Figure 3-25, the generated power, flux, stator current and speed when the SRWT model is run with realistic wind speeds for 600 seconds are shown in Figure 3-27. Though no actual time series data can be compared with the simulation results in this figure, observations have made based on the theoretical approach.

Figure 3-27 shows that all of the signals behave normally. The generated power behaves as expected between zero and 22 kW, and the other simulated signals track their reference signals closely. Note that, to make the machine operate efficiently, the rotor flux should work at rated flux. As shown in Figure 3-27(b), the simulated rotor flux,  $F_{rd}$  is successfully maintained to work around the reference rotor flux. The reference rotor flux can be calculated using Equations (2-52) or (2-56). Because the rotor flux can be maintained around the reference rated flux, the direct-axis component of stator current also is limited at a constant current. See Equation 3-56. Using vector control, the magnitude and the phase angle of the stator current could be varied to control the actual stator current. Thus, the actual stator current can be controlled as required, by

controlling the quadrature-axis component; meanwhile maintaining the direct-axis current component. As depicted in Figure 3-27(c), the simulated quadrature-axis of the stator current varies smoothly as estimated by its reference. The reference of the quadrature-axis component of the stator current can be calculated using Equations (2-57).

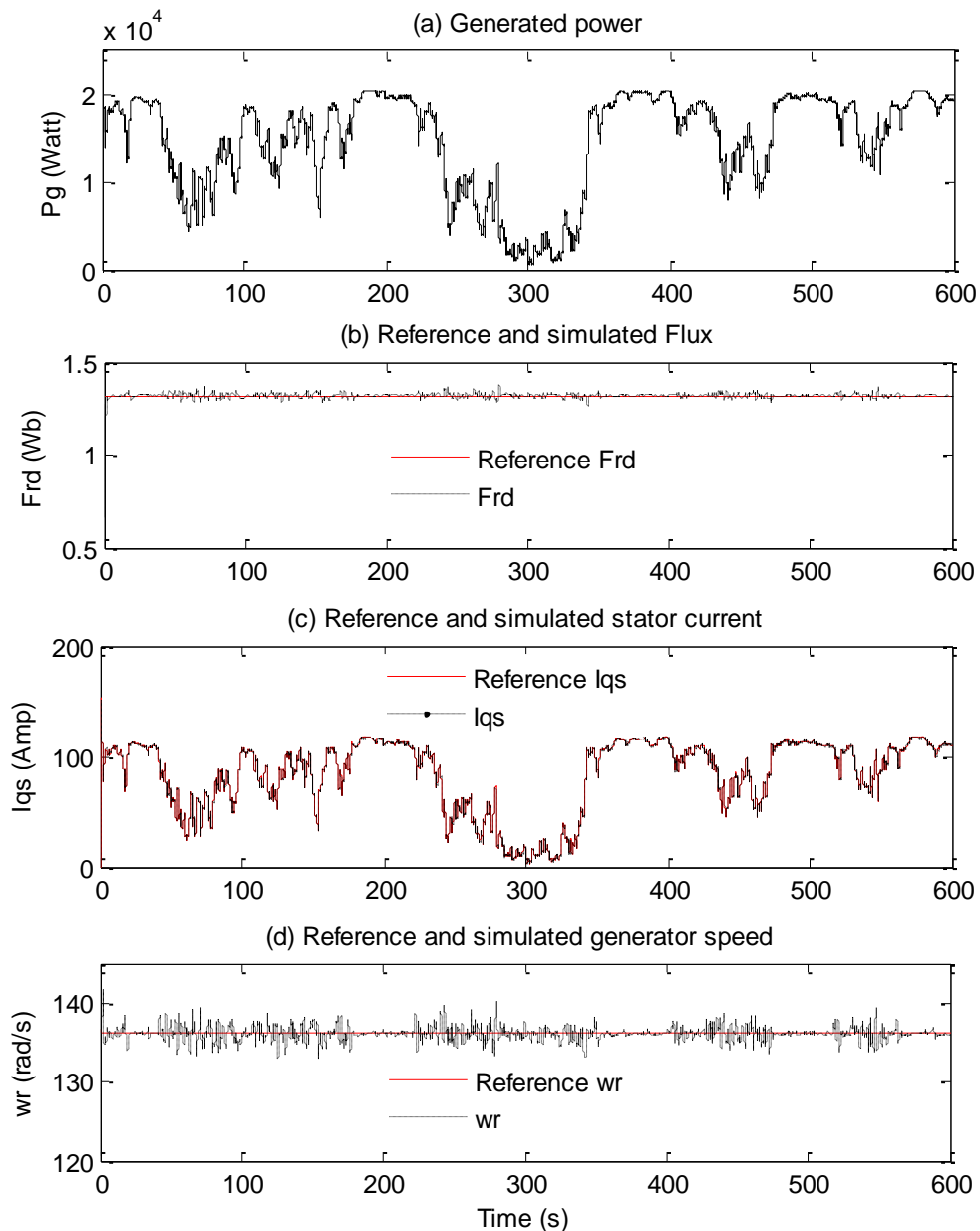


Figure 3-27 Generated electrical power, flux, stator current and speed responses when the fixed-speed SRWT system model is controlled by the  $\psi_{dr}$  flux controller, the  $I_{qs}$  current controller and the speed controller

Figure 3-27(d) depicts the electrical speed of the generator. It can be seen that the simulated electrical rotor speed can be controlled to rotate at the rated speed of approximately 1305 rpm or 136.65 rad/s. This reference electrical rotor speed can be calculated using Equations (2-23) and (2-26), respectively. The positive and negative deviations of the electrical rotor speed from its reference are considered to be due to the slip factor under normal conditions.

### **3.7 Chapter Summary**

This chapter explained the steps involved in the development of a model of the stall-regulated, fixed-pitch, fixed-speed Carter wind turbine and provided a detailed explanation of the development of the SIMULINK model of the fixed-speed SRWT model from the first sub-model to the end sub-model. The method used to estimate the unknown parameters for the drivetrain and SCIG models and the approach specified to design the controllers' gains were also explained, and the method used to improve the complete fixed-speed SRWT model with a dynamic stall algorithm was described. Finally, the dynamic system of this turbine was validated using the manufacturer's specifications for operations at a fixed speed (50 Hz) and using data measured during normal operations (at a frequency of 43.5 Hz). The good responses from the developed fixed-speed SRWT with the dynamic stall model under these two operating conditions greatly increased the confidence in the validity of the model. The fixed-speed SRWT with the dynamic stall model will be then used as the complete SRWT model in later chapters with the addition of designed IVC and SLIVC model algorithms to develop a stall-regulated variable speed wind turbine (SRVSWT) model.

## **4 Description of Controllers, Tuning Procedure and Performance Index**

### **4.1 Chapter Overview**

This chapter describes the research method, the controller tuning procedure and the performance assessment of the modelling study. In this study, two different research methods for vector control are selected, namely, indirect vector control (IVC) and sensorless indirect vector control (SLIVC). In section 4.1, the contents of this chapter are outlined. A description of the proposed research method is provided in section 4.2. A brief history, the working principle, the circuit diagram and the reactions of each controller to the SRVSWT system are also explained. The reasons for selecting the different methods are discussed. In section 4.3, a description of the controller tuning procedure is provided. The method used to confront the interaction problems between the inputs and the outputs of a multiple-input multiple-output (MIMO) system during PI controller tuning is also clarified in this section. In section 4.4, the four methods of the analytical tuning rules for the PI controllers in the IVC and SLIVC models are derived for the general process model by employing the internal model control (IMC) design procedure. The following tuning methods are considered: Ziegler-Nichols (ZN), Tyreus and Luyben (TL), IMC and the proposed method, which was inspired by the IMC and the advantages of an integral-proportional (IP) controller. The performance index to assess the performance of the complete proposed system is explained in section 4.5. The chapter is summarised in section 4.6.

### **4.2 Description of Controllers**

Scalar control (SC) is the first control method introduced in an adjustable speed AC drive, which is based on an induction machine. SC is popular due to the

simplicity and low cost of its application [156], [77]. By implementing appropriate control algorithms, a sophisticated control system can be designed to improve the speed and torque performances and the dynamics of the turbine machine response, e.g., impedance parameters [157]. Using SC, the torque and speed can be controlled by simultaneously varying the stator voltage and its frequency. By increasing or decreasing the stator's supply voltage and frequency, the torque and speed of the machine can be accelerated or decelerated, respectively. The speed variations produce a change in machine reactance, in which the reactance is a function of the operating angular frequency and the machine inductance. This change in machine reactance will also cause the machine impedance to vary. Consequently, the current will increase or decrease. The torque can be controlled by the changes in current. The motor torque will decrease if the current is small, whereas the torque will increase when a large current is applied. When the current increases (voltage also increases) and the frequency decreases, the flux level will exceed its rated flux. Equation (4-1) shows the relationship among the rated flux ( $\psi$ ), the applied voltage ( $E$ ) and the frequency ( $f$ ) of the machine.

$$\frac{E}{f_s} = 4.44\psi N \quad (4-1)$$

where  $E$  is the induced voltage in the machine's stator,  $f_s$  is the fundamental frequency of the supplied voltage,  $\psi$  is the magnetic flux linkage in the stator and  $N$  is the number of turns. The number 4.44 represents the machine constant. By considering the equation for air-gap torque (refer to equation 3-41), a parameter arrangement can be performed, as shown in equation (4-2). From equation (4-2), an inverse relation between torque and frequency is obtained, in which the torque is directly proportional to the voltage ( $I_r R_r$ ).

$$T_{air-gap} = \frac{P_{air-gap}}{\omega_s} = 3I_r^2 \left( \frac{R_r}{\omega_s S} \right)$$

$$T_{air-gap} = 3I_r^2 \left( \frac{R_r}{\omega_s S} \right) = 3I_r^2 \left( \frac{R_r}{2\pi f_s S} \right) = \frac{3I_r}{2\pi f_s S} (I_r R_r) \quad (4-2)$$

As the induction machine is designed to operate at a particular flux density, the limitation of the variation in stator voltage and frequency must be considered. By simultaneously changing the voltage and frequency, the maximum available torque can be maintained at a constant level and the disadvantages of flux saturation and burnt coils can be prevented. A nearly constant torque of the generator is required to ensure a constant supply of electrical power output to the connected grid [158], [78].

However, SC has some drawbacks; for instance, the coupling effect in SC cannot be prevented, i.e., both torque and flux are functions of voltage or current and frequency [72]. As SC provides a sluggish response, its use is not suitable for control systems that require a large precision response at a high frequency. Consequently, vector control (VC) was introduced. Compared with the SC case, VC enables decoupling control with DC-like performance in which the torque and flux can be separately controlled. The VC can be divided into two types: direct vector control (DVC) and indirect vector control (IVC). DVC is also known as feedback vector control. The term DVC originates from the direct estimation of the rotor flux position in the stator coordinates [94], [95]. DVC requires a direct sensing method, such as a Hall effect sensor, to define the rotor flux position and value [159], which may result in a higher cost and problems in practice [160], particularly if the sensor is poorly mounted or damaged.

Compared with DVC, IVC is more common in industrial applications [72] and is extensively used in induction motors due to its simple design and construction [77]. In addition, IVC can provide better control performance due to its ability to operate at low speeds [94],[160]. In certain instances, IVC is also referred to as feedforward vector control. The principle of IVC is similar to DVC; the similarity between these two techniques relates to the manner in which the torque and the flux of a machine are controlled using the vector orientation. In IVC, the manipulated variables, such as voltages or currents, are typically referred to a direct and quadrature synchronous frame. Decoupling of the control of the rotor flux and torque can be established. The phenomenon of this decoupled control is shown in Figure 4-1.

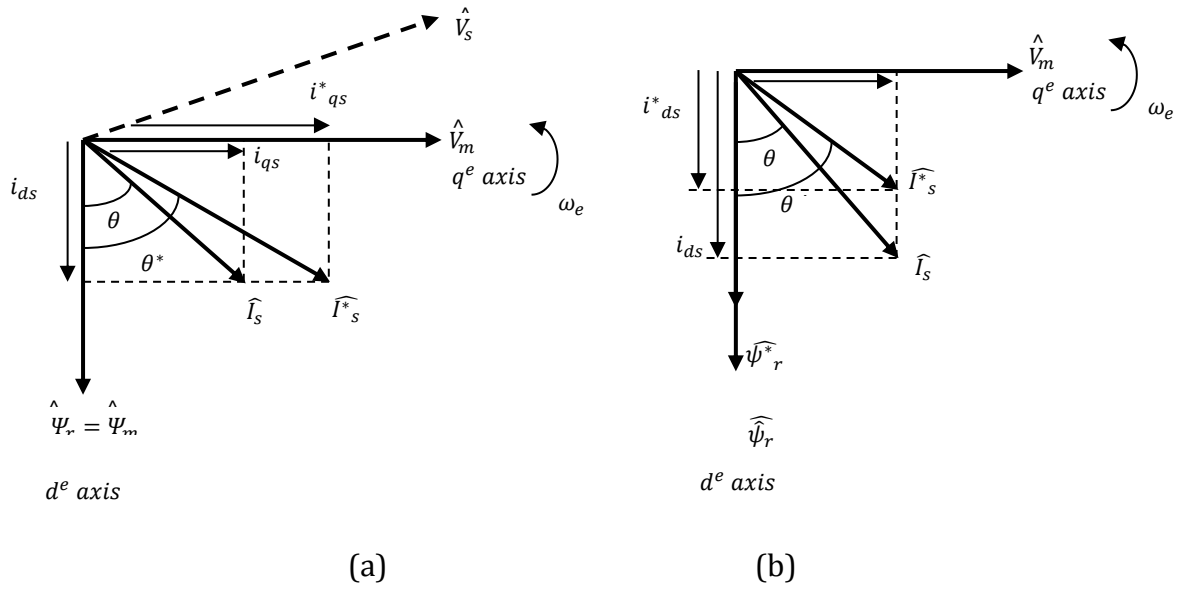


Figure 4-1 Vector control steady-state phasor: (a) Torque component of current control and (b) Flux component of current control [72]

In Figure 4-1, the three-phase system is represented by an equivalent two-phase machine with a quadrature-axis synchronously rotating frame ( $q^e$ ) and a direct-axis synchronously rotating frame ( $d^e$ ), where  $\hat{V}_s$  and  $\hat{I}_s$  are the terminal voltage and the current, respectively, of the induction machine;  $\hat{V}_m$  is the air gap voltage, which is aligned on the quadrature-axis synchronously rotating frame,  $\hat{\psi}_r$  is the rotor flux, which is aligned on the direct-axis synchronously rotating frame, and 'e' represents the synchronous rotating reference frame.

Note that the stator current  $\hat{I}_s$  can be expressed as

$$\hat{I}_s = \sqrt{i_{ds}^2 + i_{qs}^2} \quad (4-3)$$

Equation (4-3) shows that the current of  $\hat{I}_s$  can be controlled, regulated, and/or maintained by changing the variables of the direct-axis current  $i_{ds}$  and the quadrature-axis current  $i_{qs}$ . When operating below the base speed, the rotor flux  $\hat{\psi}_r$  is usually kept constant [157], [72] as

$$\hat{\psi}_r = \hat{\psi}_{dr} = L_M i_{ds} \quad (4-4)$$

where  $\hat{\psi}_r$  can be set at a constant value if  $i_{ds}$  is also limited to a constant value and  $\hat{\psi}_{dr}$  is the rotor flux at the direct axis. The base speed is the rated operating speed, in which the motor will develop a rated power at the rated load and voltage.

In the proposed SRVSWT system, the applied base speed is 50 Hz. Although  $i_{ds}$  is fixed, the stator current  $\hat{I}_s$  can be changed to any required value by changing the quadrature current  $i_{qs}$ , as shown in Figure 4-1(a), in which the stator current can be set at  $\hat{I}_s$  when the quadrature current is set at  $i_{qs}$  with a phasor angle of  $\theta$ . The stator current can also be set at different magnitudes, such as  $\hat{I}_s^*$ , when the quadrature current is set to  $i_{qs}^*$  with a phasor angle of  $\theta^*$ .

However, when the machine operates above the base speed, the voltage must be limited to the rated value [157], [72]. If the voltage is fixed when the speed increases, the rotor flux should be decreased. In this region, the control approach is referred to as the flux-weakening region. In the flux-weakening region, the magnetising current must be decreased proportionally to its speed.

The vector control implementation of the SCIG is shown in Figure 4-2. The vector control orientation on the control side is depicted on the left side of the figure, whereas the vector control transformation on the machine side is depicted on the right side of the figure. On the control side, the inverse transformation was used to translate the input variables from the synchronous reference frame to the stationary reference frame prior to transformation of the variables into a three-phase system. At the machine terminal, the three-phase variables should be passed to the back-to-back converter. For simplicity, the converter is omitted from Figure 4-2. By assuming that the converter has unity current gain, the three-phase variable is subsequently transformed into the synchronous rotating frame on the machine side.

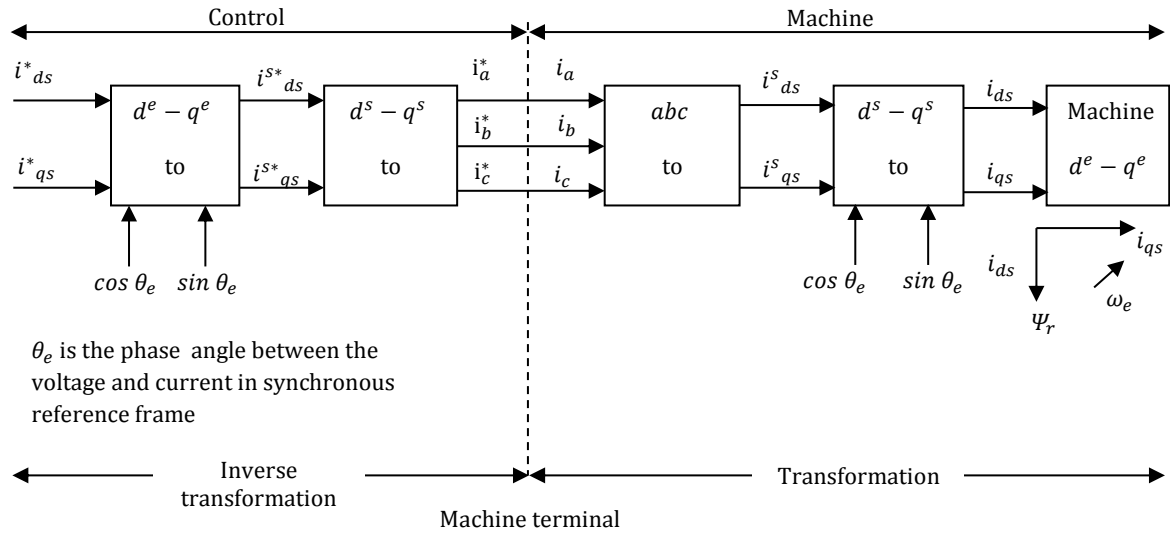


Figure 4-2 Implementation of transformation and inverse transformation of vector control in a machine [72]

#### 4.2.1 Indirect Vector Control

Indirect vector control (IVC) differs from vector control in the method used to calculate the machine rotor flux position. Using IVC, the rotor flux position is not directly calculated. To calculate the position of rotor flux, measurements of the stator currents ( $i_a, i_b, i_c$ ) and the angular mechanical rotor speed ( $\omega_m$ ) are required. The angular electrical rotor speed can be estimated from the measured angular rotor speed. This electrical rotor speed is added to the negative slip speed to determine the instantaneous value of the stator speed ( $\omega_e$ ). Determination of the rotor flux ( $\hat{\psi}_r$ ) is not directly performed; thus, this version of the vector control method is referred to as indirect vector control.

The relation that describes how torque is controlled using IVC is shown in Equation (4-5). For decoupling control,

$$\psi_{qr} = 0 \quad (4-5)$$

is preferred, that is,

$$\frac{d\psi_{qr}}{dt} = 0 \quad (4-6)$$

which generates a total rotor flux ( $\psi_r$ ) directed along the  $d^e$  axis. Thus, the torque can also be expressed as

$$T_e = \frac{3}{2} \left( \frac{P}{2} \right) \frac{L_M}{L_r} (\psi_{dr} i_{qs}) \quad (4-7)$$

where  $P$  is the pole number. Equation (4-7) shows that the torque can be controlled by regulating  $i_{qs}$  and  $\psi_{dr}$ .  $i_{qs}$  can be regulated by controlling the slip speed  $\omega_{slip}$  or  $(\omega_s - \omega_r)$ ; in addition,  $\psi_{dr}$  can be regulated by controlling  $i_{ds}$ , which can be obtained from Equation (4-8)

$$\frac{L_R}{R_r} \frac{d\hat{\psi}_r}{dt} + \hat{\psi}_r = L_M i_{ds} \quad (4-8)$$

With  $\frac{d\hat{\psi}_r}{dt} = 0$ , if the rotor flux  $\hat{\psi}_r = \text{constant}$ , then the equation becomes

$$\hat{\psi}_r = L_M i_{ds} \quad (4-9)$$

Thus, the rotor flux is directly proportional to the current  $i_{ds}$  in the steady state. For slip-speed control  $\omega_{slip}$

$$\omega_{slip} = \frac{L_M R_r}{\hat{\psi}_r L_r} i_{qs} \quad (4-10)$$

Using information from equation (4-9), the slip speed can also be expressed as follows:

$$\omega_{slip} = \frac{R_r i_{qs}}{L_r i_{ds}} \quad (4-11)$$

Detailed explanations of the derivations of equations (4-8) and (4-9) are provided in [157] and [72].

In induction machine control, several methods have been used to perform IVC. Based on the literature review for this study, the IVC can be classified into six designs. The differences among these designs are summarised in Table 4-1.

Table 4-1 Summary of the differences among the designs of IVC

Category	Type of referenced loop control	No. of control loop	Details	Reference
I	Flux loop ( $\hat{\psi}_r^*$ ) Current loop ( $i_{qs}^*$ )	2	Applied in wind turbine control. Extensively used in SCIG torque control. Can use a decoupling circuit. Rapid and accurate torque dynamic response. Small time constant, e.g., in a millisecond.	Munteanu et. al [17]
II	Speed loop ( $\omega_r^*$ )	1	Applied in general machine control. Simple implementation. Satisfactory dynamic response. Can use a decoupling circuit. Overcomes the overshoot problem but produces a slower response.	Vas, P [136]
III	Current loop ( $i_{ds}^*$ ) Current loop ( $i_{sq}^*$ )	2	Applied in wind turbine control. Contains an additional algorithm to eliminate the cross-coupling effect.	Anaya-Lara et. al [152]
IV	Speed loop ( $\omega_r^*$ ) Current loop ( $i_{qs}^*$ ) Current loop ( $i_{ds}^*$ ) } cascade	3	Applied in general machine control. Rapid and accurate torque dynamic response.	Ozpineci, B., and Tolbert, L. M [161]
V	Position loop ( $\theta_r^*$ ) Speed loop ( $\omega_r^*$ ) Torque loop ( $T_e^*$ ) Current loop ( $i_{qs}^*$ ) Flux loop ( $\hat{\psi}_r^*$ ) Current loop ( $i_{ds}^*$ ) } cascade	6	Applied in general machine control. Complex. Uses a decoupling circuit.	Vas, P [136]
VI	Current loop ( $i_{ds}^*$ ) Current loop ( $i_{qs}^*$ )	2	Applied in high-speed operations. Synchronous current control with feed-forward counter electromotive force (CEMF). Contains an additional algorithm to eliminate the cross-coupling effect.	Bose, B.K [72]

In this study, two models of IVC were considered and adapted based on the study setting requirements. During selection, the factors for a large dynamic response and simplicity are the main requirements as the operation under normal conditions can be maintained and the maintenance costs can be significantly reduced. Based on Table 4-1, only Category II uses one sensor and a feedback loop. This approach is simple, produces a satisfactory dynamic

response [136] and requires low simulation times. Although this approach is usually applied in general machines and no examples of wind turbine application are available, this approach may provide satisfactory responses for the SRVSWT modelling. The performance of this approach is similar to the performance of other approaches that employ a larger number of sensors [136].

Categories I, III and VI utilise two sensors with two feedback loops. Both sensors have a similar objective of controlling the stator current components  $i_{qs}$  and  $i_{ds}$ , with the exception of Category I, in which  $i_{ds}$  is replaced with the rotor flux  $\hat{\psi}_r$ . However, the objective of controlling  $i_{ds}$  by controlling  $\hat{\psi}_r$  remains the same, as shown in equation (4-7). However, as Category I and Category III have been used in wind turbine applications, the reliability and confidence levels for these systems are high. For this reason, Category VI is not selected. The approach between Category I and III is similar. However, as Category I, which may provide rapid and accurate torque dynamic response, has a small time constant and functions well at high frequencies; thus, Category I was selected over Category III. In [17], Category I was used for wind turbine power optimisation or for partial loads using speed loop control. In [17], the authors also suggest that this approach may be suitable for power restriction and power limitation zones. For the proposed approach in this study, the addition of a speed loop control was included to closely track the speed. This speed loop is cascaded with the  $i_{qs}$  current loop to obtain a larger dynamic response (speed and current produce torque control). By adding an additional speed loop control in the proposed system and cascading the loop with the  $i_{qs}$  current loop, this new proposed approach is equivalent to Category IV. As Category IV is only used for the general machine and the control algorithm used in Category I is more reliable, Category IV was not considered.

The approach for Category V is complex as six controllers are required to control the induction machine. Although the concept of multivariable control, which may generate a large dynamic response, is employed, this approach is not considered due to the high cost of installation and operation and maintenance issues.

Using a suitable control algorithm and control approach in wind turbine applications, the power and torque responses can be easily controlled under

normal operations along with the wind speed variations, particularly during transition from a low-wind speed region to a high-wind speed region or when subject to disturbances; for instance, gusty with turbulent winds and changes in the supply voltage reference. The generator mechanical speed and the turbine blade speed can be safely controlled without applying excessive stress on the turbine blade during these states.

As shown in Table 4-1, all studies used a feedback system known as a 'closed-loop' control; some of the studies were improved by cascading the closed-loop system. To design a sophisticated control system with high dynamic performance, this feedback system is usually applied as a control system will not always work as desired. A feedback or 'closed-loop' system refers to the continuous measurement of the outcome signal. In the context of machine control, the control system usually uses the difference between the measurements of the rotation speed to set the desired value in determining the next control action and ensure that the machine is working properly. If the speed has not changed by the desired amount, a correction can be made, which renders the machine operation less sensitive to variations and disturbances. Consequently, the system dynamics will be improved.

Compared with the 'closed-loop' system, 'cascade' controls involve multiple control loops that consist of multiple signals for one manipulated variable. To understand this control concept, the definition of the two terms that are commonly found in the control subject should be clarified: 'manipulated variables' and 'control variables' [162]. These terms typically refer to either the input signal or the output signal. In this study, 'control variables' refer to inputs such as voltage readings. 'Manipulated variables' refers to the output signal that is transmitted to the power converter, such as currents, speed, flux and positions.

Generally, cascade-loop control consists of two nested loops—inner loops and outer loops [8],[163],[164]. The outer loop is usually known as the master loop and the inner loop is usually known as the slave loop. The objective of a cascade control loop is to closely control one variable at its set-point; this variable is the outer loop or the master loop process variable. The inner or slave loop also has a process variable. In this work, for the cascade loop design, the inner loop has its own individual control, which expected could provide better

(faster) control of the outer loop process variable. Use of cascade-loop controls enables the system to be more responsive to changes and disturbances [99]. This type of control is recommended when the 'deadtime' (the delay from the time when a control variable signal is issued until the time when the measured variable begins to respond) in the outer master loop is significantly larger than the deadtime in the inner loop [165].

#### **4.2.2 Testing Models**

As effective modelling is essential to perceive the real potential application of a system, an initial study was performed to develop the SRVSWT simulation model and explore the operational behaviour of the developed system. The fully rated converter-based system that is applied to a squirrel-cage induction generator has only been technically presented in the literature and no implementation study has been performed, with the exception of investigations from 1996 to 2000 by NREL [11],[12],[13],[14],[15]. As the SRVSWT has been addressed by some researchers [16],[17],[18], the continuation of this study is important as it may be suitable for offshore applications [19]. The behaviour information obtained from the modelling studies, particularly regarding the efficiency of the selected controllers for the entire operating region (low, medium and high wind velocities), when the SRVSWT system equipped with appropriate control algorithms is useful prior to testing the real system.

The next subsection explains how the two selected control approaches are applied to the proposed SRVSWT system. The first model (Model-1) uses standard indirect vector control, whereas the second model (Model-2) uses the sensorless approach of indirect vector control. For simplicity, each model is designated as follows:

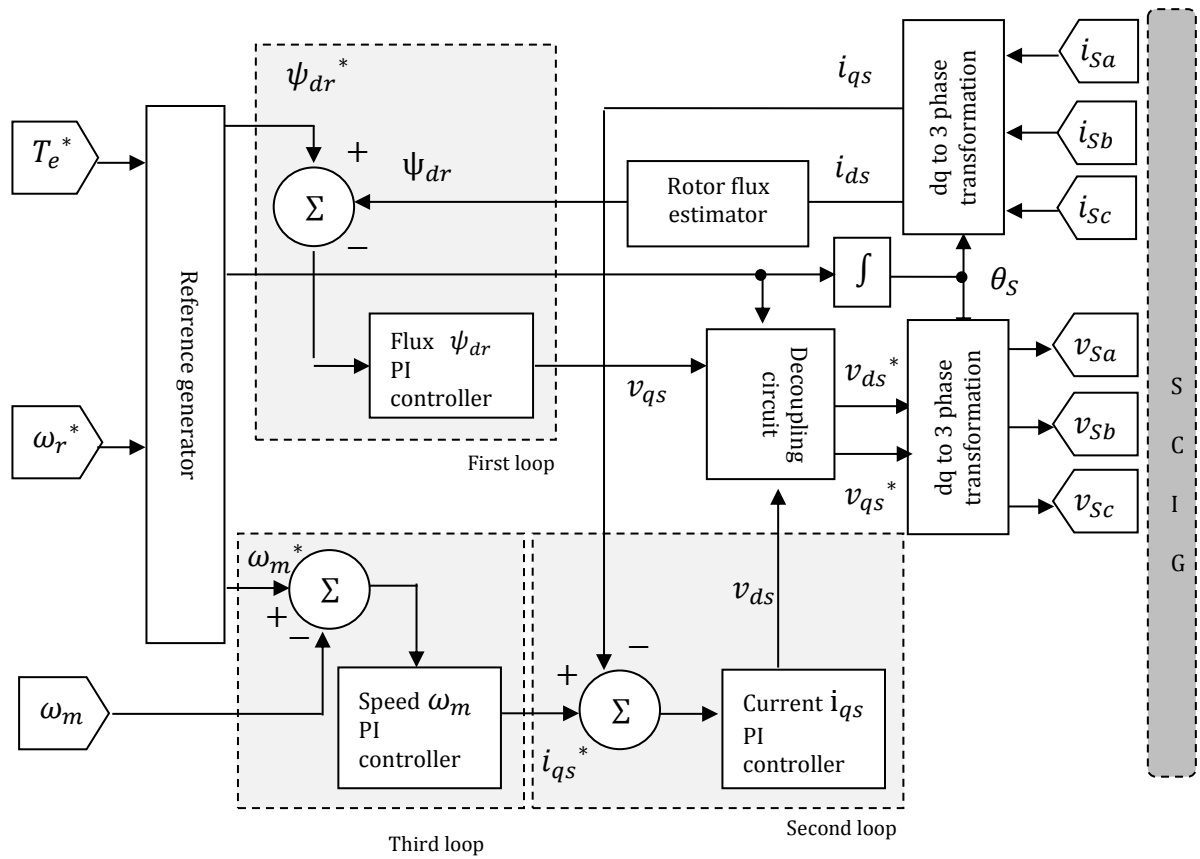
- 1- Model-1 (standard indirect vector control) is denoted as IVC
- 2- Model-2 (sensorless indirect vector control) is denoted as SLIVC

#### 4.2.2.1 Model-1 (IVC)

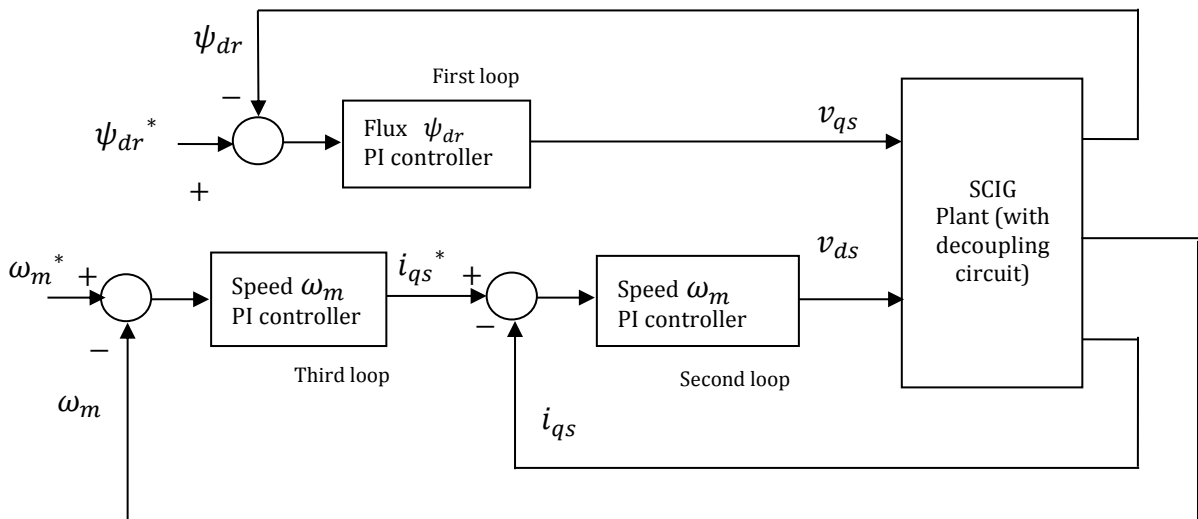
A diagram of the SRVSWT simulation model with indirect vector control (IVC) is shown in Figure 4-3(a). To aid the understanding, the IVC that was revised in a classical control loop is also given, as can be depicted in Figure 4-3(b). In the control approach, three loops of PI control were used. The first loop is the rotor flux control, the second loop is the stator current control of the quadrature-axis and the third loop is the speed loop control. Each loop serves an important role in controlling the stator voltages of  $v_{ds}$  and  $v_{qs}$ . In this method, the flux loop serves as single closed-loop control, whereas the speed loop and the torque loop are cascaded. The speed loop is considered to be an outer loop, whereas the torque loop is considered to be an inner loop.

In the first loop, as shown in Figure 4-3, the reference rotor flux is compared with the estimated rotor flux. The rotor flux estimation is obtained from the three-phase stator current measurement ( $i_{sa}, i_{sb}, i_{sc}$ ). From the measured currents, the three-phase stator currents are transformed to the two-phase d-q stationary frame prior to transforming the signal into the two-phase d-q synchronous frame. Using these d-q synchronous frame variables ( $v_{ds}$  and  $v_{qs}$ ), the d-axis stator current ( $i_{qs}$ ) and the rotor flux ( $\psi_{dr}$ ) are estimated by multiplication with certain model parameters. After the rotor flux ( $\psi_{dr}$ ) is obtained, this variable is compared with its reference and the difference between these two variables is tuned by the Flux  $\psi_{dr}$  PI controller until no difference is detected. This flux controller controls the direct axis variable (flux control).

In the third loop, the mechanical speed ( $\omega_m^*$ ) of the reference generator is compared with the actual machine rotor speed ( $\omega_m$ ). The error between these two speeds serves as an input to the current  $i_{qs}$  PI controller. In the second loop, this current  $i_{qs}$  PI controller reduces the error between the input current reference and the estimated stator current. This current controller controls the quadrature axis variable (torque control).



(a)



(b)

Figure 4-3 (a) Standard indirect vector control for IVC (b) The classical design control loop for standard indirect vector control

When the direct-axis of the rotor flux reference  $\psi_{dr}^*$  is compared with the actual value of  $\psi_{dr}$ , the PI flux loop will produce a new value of quadrature-axis of stator voltage reference of  $v_{qs}^*$ . When the quadrature-axis of the stator current reference  $i_{qs}^*$  is compared with the actual value of  $i_{qs}$ , the PI torque loop will produce a new value of direct-axis of the stator voltage reference of  $v_{ds}^*$ .

Both reference d-q axes of the stator voltages  $v_{ds}^*$  and  $v_{qs}^*$  are transformed into the two-phase stationary frame prior to transformation to the three-phase stator voltages. These stator voltages are input into the power converter to switch the pulse signals.

#### 4.2.2.2 Model-2 (SLIVC)

The working principle of the IVC, as explained in the previous subchapter, was employed as this model is actually based on the concept of the standard IVC. However, the concept of the sensorless approach is analysed in this model. Figure 4-4 represents the diagram of the SLIVC application on the SRVSWT system. As shown in the figure, this method utilises only one control loop with a speed sensor and the reference value of the d-q stator currents ( $i_{ds}^*$  and  $i_{qs}^*$ ) instead of the actual value of the d-q stator currents ( $i_{ds}$  and  $i_{qs}$ ), as in the case of IVC.

By assuming that the wind turbine is operating at a constant rotor flux ( $\psi_r = \psi_{rd}$ ), the d-axis current becomes constant. This current is considered to be the d-axis reference current ( $i_{ds}^*$ ). As in the previous model, the reference mechanical rotor speed ( $\omega_m^*$ ) in the speed loop control will be compared with the actual rotor speed ( $\omega_m$ ) before their errors will be corrected by the PI speed controller. The output of this controller will subsequently serve as the q-axis reference current ( $i_{qs}^*$ ). To create the independent control of each axis, the reference signals of  $i_{ds}^*$  and  $i_{qs}^*$  are subsequently added to the decoupling block, as shown in Figure 4-4. As this study is related to the servo application concept, a small delay term should be incorporated in the decoupling terms to prevent significant overshoot of the electromagnetic torque [136]. Using a first-order lag as the delay term, the effect of the stator transient inductance is included in the

decoupling compensator. Consequently, the improved dynamic response can be attained by delaying  $i_{qs}^*$  using the stator transient time constant ( $T_s' = \frac{L_s'}{R_s}$ ).

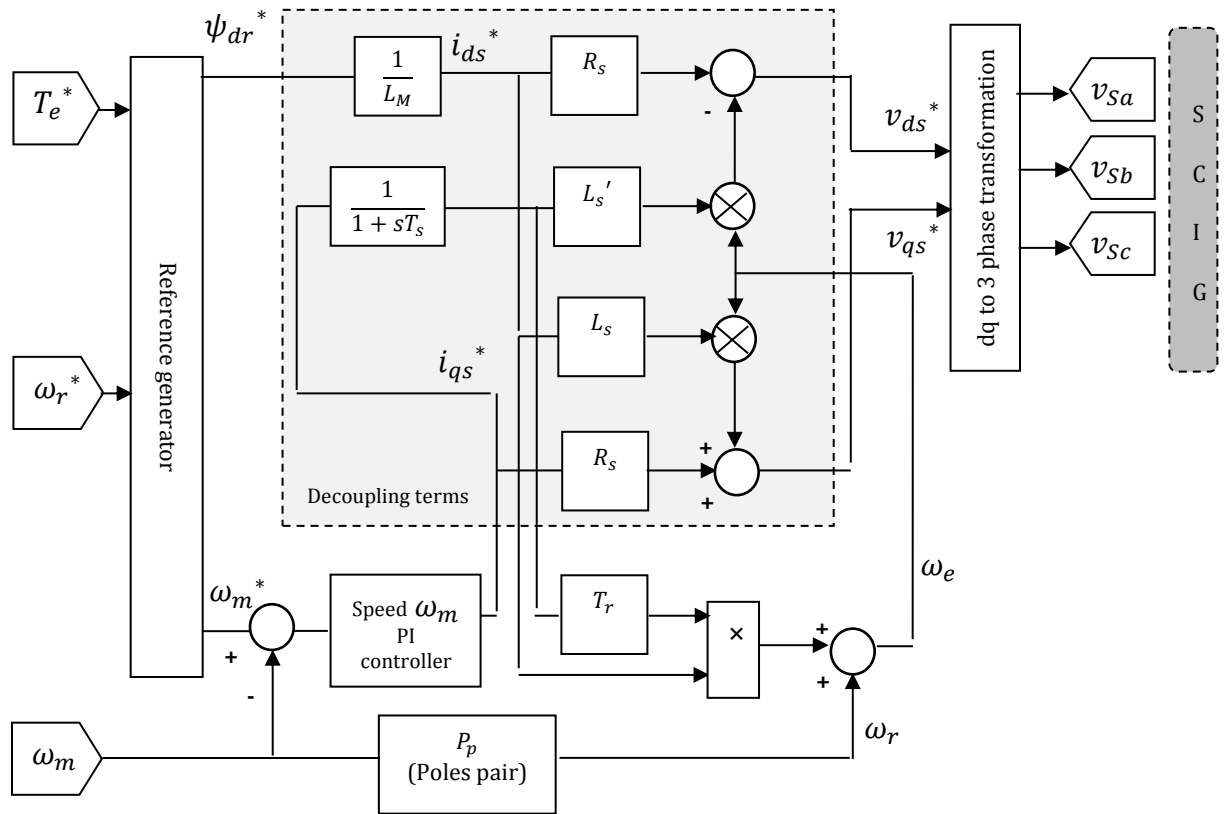


Figure 4-4 SRVSWT with the SLIVC method [136]

### 4.3 Controller Tuning Procedure

As explained in the preceding section, more than one controller is involved in Model-1, which is common in most cases in which the system contains more than one control input and more than one manipulated variable. Generally, this system is referred to as the multiple-input multiple-output (MIMO) system or as a multivariable system. In the MIMO system, each input generally has an effect on each output of the system, in which the interaction between different inputs and outputs exist. Due to the coupling effect between the inputs and the outputs, the signals can interact in unexpected ways, which is one of the most challenging aspects of control in the MIMO system.

In the MIMO system shown in Figure 4-5, a suitable controller can be designed using the concept of input-output (I/O) pairing [166].

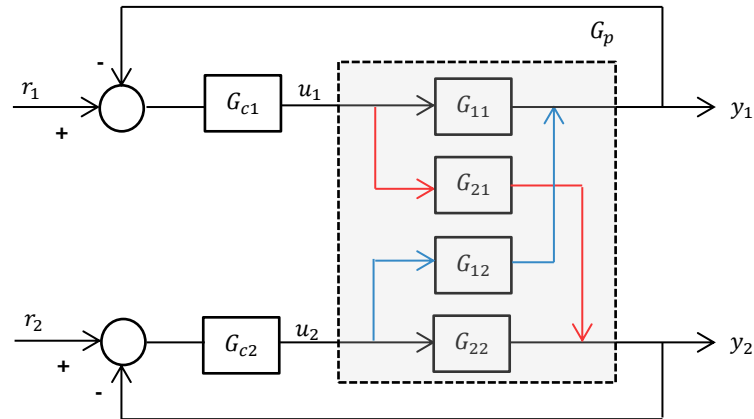


Figure 4-5 MIMO model of the SRVSWT system

Using this concept, the best pairing of controlled and manipulated variables is recommended. In control theory, controlled variable is the variable that is input into the control system (output of a plant). Meanwhile, the manipulated variable is the variable that the controller action influences (input of a plant).

In this study, a method known as the relative gain array (RGA)  $\Lambda$  was used to measure the interaction level for obtaining the appropriate I/O pairing, where

$$\Lambda = \lambda_{ij} = \begin{bmatrix} \lambda_{11} & \lambda_{12} \\ \lambda_{21} & \lambda_{22} \end{bmatrix} = \begin{bmatrix} \lambda_{11} & 1 - \lambda_{11} \\ 1 - \lambda_{11} & \lambda_{22} \end{bmatrix} \quad (4-12)$$

The guidelines for obtaining the two best I/O pairings for the design of the proposed controller in the proposed SRVSWT system are explained in the next section.

### 4.3.1 I/O Pairing Using the RGA Approach

The I/O pairing using the RGA approach is performed in two steps:

### Step 1

Based on Figure 4-3, disregard the speed PI controller. Consider the control inputs flux  $\psi_{dr}$  PI and the  $i_{qs}$  current PI and their two output variables by assuming the measured flux  $\psi_{dr}$  as the output  $y_1$  and the measured current  $i_{qs}$  as the output  $y_2$ , where  $r_1$  is the reference flux  $\psi_{dr}^*$ ,  $r_2$  is the reference  $i_{qs}^*$ ,  $G_{c1}$  is the flux  $\psi_{dr}$  PI controller,  $G_{c2}$  is the  $i_{qs}$  current PI controller,  $u_1$  is the control input 1,  $u_2$  is the control input 2 and  $G_p$  is the process plant, which can also be expressed in matrix form as  $\begin{bmatrix} G_{11} & G_{12} \\ G_{21} & G_{22} \end{bmatrix}$ .

Obtain the first-order plus time delay (FOPTD) transfer function for each possible I/O pairing ( $G_{11}, G_{21}, G_{12}, G_{22}$ ) from the process plant response. Several approaches can be used to obtain the FOPTD transfer function [167]. However, in this study, the following approach has been considered:

- i- Determine the open-loop transfer functions between all inputs and outputs, e.g.,  $G_{11}, G_{21}, G_{12}$  and  $G_{22}$ .
- ii- Determine the open-loop step response for each transfer function using the slope-intercept method. Estimate the FOPTD parameters of  $K_p$ ,  $\theta$  and  $\tau$ , as depicted in Figure 4-6, where  $K_p$  is the model gain ( $\frac{\Delta y}{\Delta u}$ ),  $\theta$  is the time delay and  $\tau$  is the time constant.

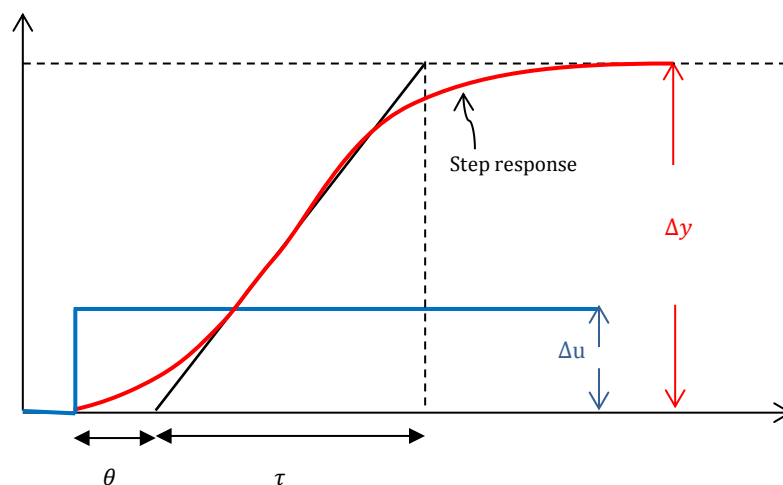


Figure 4-6 Step response of a FOPTD system and the graphical construction used to estimate the FOPTD parameters

iii- Develop the FOPTD transfer function for each model of  $G_{11}$ ,  $G_{21}$ ,  $G_{12}$  and  $G_{22}$  in the form

$$G_{ij} = \frac{K_p e^{-\theta s}}{\tau s + 1} \quad (4-13)$$

### Step 2

Obtain suitable I/O pairings (minimised interaction)  $u_i \leftrightarrow y_j$ :

- $u_1 \leftrightarrow y_1 / u_2 \leftrightarrow y_2$ , or
- $u_1 \leftrightarrow y_2 / u_2 \leftrightarrow y_1$ .

To make it clear, no matter whether we choose pairing  $u_1 \leftrightarrow y_1$  or  $u_2 \leftrightarrow y_2$ , we will get the same answer. Similarly, no matter whether we choose pairing  $u_1 \leftrightarrow y_2$  or  $u_2 \leftrightarrow y_1$ , we will get the same answer. But, note that from either the first or the second I/O pairings we must obtain the best one. Then, design the specific controller for the determined I/O pairing without considering other loops.

Two methods have been executed in this study. Method 1 was executed and subsequently reconfirmed using Method 2.

### **Method 1[168]:**

$$\Lambda = \lambda_{ij} = \frac{\lambda_{open}}{\lambda_{closed}} = \frac{\text{Gain' from } u_1 \text{ to } y_1 \text{ if upper loop is open}}{\text{Gain' from } u_1 \text{ to } y_1 \text{ if upper loop is closed}} \quad (4-14)$$

is close to 1. If  $\lambda_{ij} = 1$ , then  $G_{c1}$  can be designed independently from  $G_{c2}$ .

To obtain  $\lambda_{open}$ , place the step input test at  $u_1$  and open  $u_2$ , as shown in Figure 4-7(a). Record the gain of  $\lambda_{open}$ . Obtain  $\lambda_{closed}$  by placing the step input test at  $u_1$  and close  $u_2$  as depicted in Figure 4-7(b). Record the gain of  $\lambda_{closed}$ .

Subsequently,  $\lambda_{ij}$  can be obtained by inserting the  $\lambda_{open}$  and  $\lambda_{closed}$  values in Equation (4-14). As the testing considered the gains  $u_1$  and  $y_1$ , the obtained  $\lambda_{ij}$  is  $\lambda_{11}$ , which is also equivalent to  $\lambda_{22}$ . The RGA matrix expressed in

Equation (4-12) can be computed. With this final value of this RGA matrix, the I/O pairing can be determined by observing that  $0.5 < \lambda_{ij} < 1$ .

For example, if  $\Lambda$  is  $\begin{bmatrix} 0.667 & 0.333 \\ 0.333 & 0.667 \end{bmatrix}$ , then the  $\lambda_{ij}$  that complies with the rule of  $0.5 < \lambda_{ij} < 1$  is  $\lambda_{11}$  and  $\lambda_{22}$ . Thus, the pairing that should be selected for the additional tuning of the PI controller is  $u_1 \leftrightarrow y_1 / u_2 \leftrightarrow y_2$  (consider transfer function model of  $G_{11}$  and  $G_{22}$ ).

If  $\Lambda$  is  $\begin{bmatrix} 0.47 & 0.53 \\ 0.53 & 0.47 \end{bmatrix}$ , then the  $\lambda_{ij}$  that complies with the rule of  $0.5 < \lambda_{ij} < 1$  is  $\lambda_{12}$  and  $\lambda_{21}$ . Thus, the pairing that should be selected for the additional PI controller tuning is  $u_1 \leftrightarrow y_2 / u_2 \leftrightarrow y_1$  (consider transfer function model  $G_{12}$  and  $G_{21}$ ).

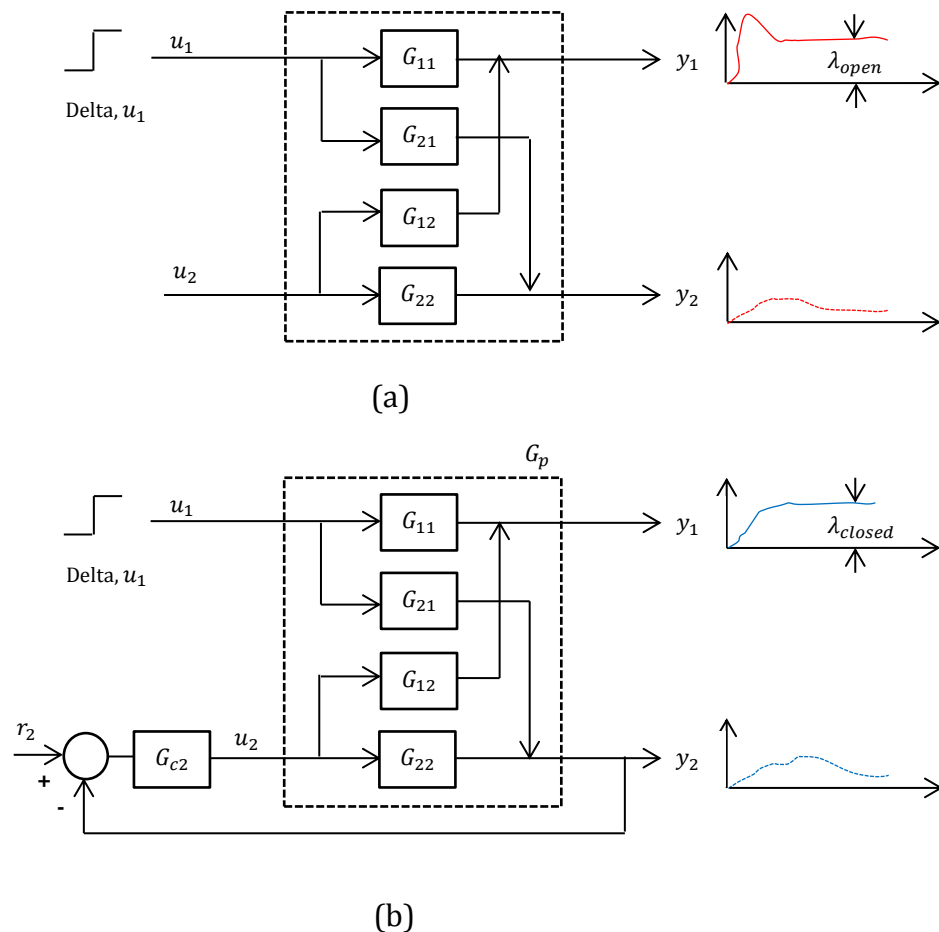


Figure 4-7 Step response of a FOPTD system and the graphical construction used to estimate the FOPTD parameters [168]: (a) Obtaining  $\lambda_{open}$  and (b) Obtaining  $\lambda_{closed}$

## Method 2 [166]:

Assume the system 2 x 2 matrix

$$\begin{bmatrix} y_1 \\ y_2 \end{bmatrix} = \begin{bmatrix} G_{11} & G_{12} \\ G_{21} & G_{22} \end{bmatrix} \begin{bmatrix} u_1 \\ u_2 \end{bmatrix} \quad (4-15)$$

$$\Lambda = G \otimes (G^{-1})^T \quad \text{an } (m \times m \text{ matrix}) \quad (4-16)$$

where  $\otimes$  denotes the element-by-element multiplication and  $G = \begin{bmatrix} G_{11} & G_{12} \\ G_{21} & G_{22} \end{bmatrix}$ .

### 4.4 Proportional (P) and Integral (I) Parameter Tuning Method

To establish a satisfactory response of the PI controller, this study investigates three existing PI tuning methods and proposes a new PI tuning method. PI controllers are extensively used in industrial control systems due to the reduced number of parameters to be tuned. Although PI has only two parameters—proportional (P) and integral (I)—if they are not properly tuned, poor results may be obtained. Thus, a systematic tuning procedure in parameter selection is needed if no gain rescheduling is involved when the operating point changes from one condition to another condition. Thus, a systematic control design method, which reduces the controller commissioning time and the tuning efforts, is proposed in this study. The considered methods include Ziegler-Nichols, Tyreus and Luyben and internal model control (IMC); these methods are compared with a new proposed method, namely, IMC-PI-IP.

The first and second methods use a simple method and are commonly used to estimate the gains of the P and I terms, which are obtained from the process plant step response. In the third and fourth methods, they require a first-order plus time delay (FOPTD) transfer function from the process plant transfer function. The control structures and tuning methods that were investigated in this study are briefly described in the next section.

#### 4.4.1 Ziegler-Nichols (M1)

Based on the Ziegler-Nichols method, two methods can be employed: the ZN reaction curve (open loop) method and ZN oscillation (closed loop) method. In this study, the ZN oscillation method is used when the process's critical characteristics are used to calculate the proportional control gain  $K_p$  and the integral control time constant  $T_i$ . The form of this PI controller is

$$G_c = K_p + \frac{1}{T_i s} = K_p + \frac{K_i}{s} \quad (4-17)$$

where  $K_i = \frac{1}{T_i}$  =integral control gain.

The tuning procedure for this method is performed in five steps as follows:

- 1- Determine whether the required critical gain  $K_c$  is positive or negative by slightly stepping the input signal (positive increment). If the steady-state value of the process output has also moved up (increased),  $K_c$  has to be positive.
- 2- Turn the controller to P-only mode. Turn both the integral mode and derivative mode off by setting  $T_i = \infty$  and  $T_d = 0$ , respectively.
- 3- Initially, set  $K_c = 0$ . Slowly increase  $K_c$  until the loop begins to oscillate.
- 4- When a value of  $K_c$  produces a sustained periodic oscillation in the controller output (or close to it), record this critical value of  $K_c$  as the ultimate gain  $K_u$  and measure the oscillation period of the controller output  $P_u$ .
- 5- Using the values of the ultimate gain  $K_u$ , and the ultimate period  $P_u$ , the proportional control gain  $K_p$  and the integral control time constant  $T_i$  can be computed according to Table 4-2 and the type of desired controller. For the PI control loop,  $K_p$  can be calculated as  $K_u/2.2$ , where  $T_i = P_u/1.2$ .

Table 4-2 Tuning of PID controller parameters according to the ZN method

Controller	$K_p$	$T_i$	$T_d$
P	$K_u/2$		
PI	$K_u/2.2$	$P_u/1.2$	
PID	$K_u/1.7$	$P_u/2$	$P_u/8$

#### 4.4.2 Tyreus and Luyben (M2)

As an alternative to improve the obtained response based on Table 4-2, another set of tuning rules, which have been determined by Tyreus and Luyben (TL) as summarised in Table 4-3, were used to reduce the oscillatory effects and improve robustness. M2 is revised from the M1 method.

Table 4-3 Tuning of PID controller parameters according to the TL method

Controller	$K_p$	$T_i$	$T_d$
PI	$K_u/3.2$	$2.2P_u$	
PID	$K_u/2.2$	$2.2P_u$	$P_u/6.3$

#### 4.4.3 IMC-PI (M3)

M3 is more advanced than the M1 and M2 methods. M3 is a design method based on the internal model control (IMC) design that was introduced by Manfred Morari in 1986 [169]. The equivalent representations of the classical feedback structure and the IMC structure are shown in Figure 4-8. The IMC structure offers more benefits than the classical design in terms of the controller design procedure, in which the IMC is more direct and natural than the classical control and the requirement of solving the roots of the characteristic polynomial  $1 + G_p G_c$  does not apply where only a simple examination of the poles of  $q_c$  (IMC controller) is needed [170, 171].

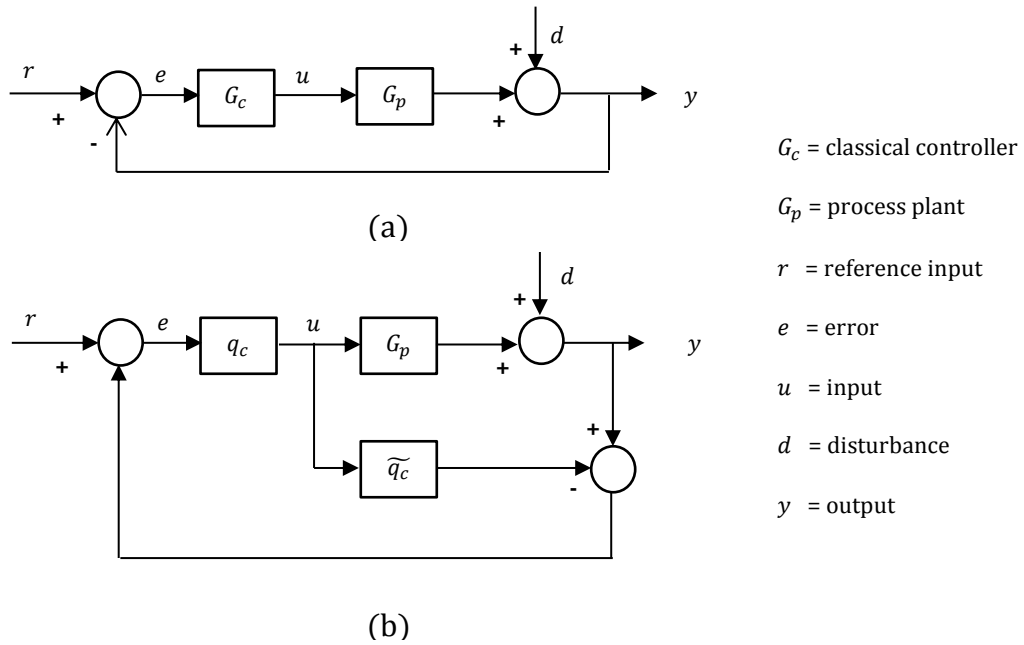


Figure 4-8 (a) Classical feedback structure and (b) IMC structure

#### 4.4.3.1 IMC Design Procedure

To obtain a near-optimal design of IMC, the IMC design procedure involves two main steps:

##### Step 1

Factorisation of the process plant model as

$$G_p(s) = G_{p-}(s)G_{p+}(s) \quad (4-18)$$

where  $G_{p-}(s)$  is an invertible minimum phase and the noninvertible part contains all nonminimum phase elements e.g., delays and the zeros of the right half plane (RHP). However, the process model  $G_p$  must be obtained, which is modelled as (FOPTD) dynamics as

$$G_p(s) = \frac{K}{\tau s + 1} e^{-\theta s} \quad (4-19)$$

or can also be expressed as

$$G_p(s) = \frac{K(-\theta s + 1)}{\tau s + 1} \quad \theta, \tau > 0 \quad (4-20)$$

under the assumption that the inputs are steps, where  $K$  is the gain,  $\tau$  is the time constant and  $\theta$  is the time delay of the FOPTD model of the plant transfer function. Thus,

$$G_{p+} = -\theta s + 1 \quad G_{p-} = \frac{K}{\tau s + 1}$$

The IMC controller is defined as

$$\tilde{q}_c(s) = G_{p-}(s)^{-1}, \quad (4-21)$$

which is stable and causal. Thus,

$$\tilde{q}_c(s) = \frac{\tau s + 1}{K} \quad (4-22)$$

## Step 2

Augment  $\tilde{q}_c$  with an IMC filter,  $f(s)$ . The final IMC controller is defined as

$$q_c(s) = G_{p-}(s)^{-1} f(s) \quad (4-23)$$

where

$$f(s) = \frac{1}{(\lambda s + 1)^r} \quad (4-24)$$

where the parameter  $\lambda$  is the adjustable parameter for the trade-off between the performance and the robustness of the inner loop and  $r$  is the order of the filter, which should be sufficiently large to create a (semi-) proper IMC controller  $q_c$ . A smaller  $\lambda$  provides a faster response but at the expense of more active control inputs; with a larger  $\lambda$ , the control is less aggressive but the closed-loop response is slower. In terms of robustness, the higher is the value of  $\lambda$ , the higher is the robustness of the control system.

To select the filter adjustable parameter  $\lambda$ , several approaches are available in the literature, such as reported by Saxena in [169], Tham in [172],

Rivera in [170] and [171], Vilanova in [173], Lee et. al in [168] and Jeng et. al in [174]. As  $r$  is 1 in this study, the selected  $\lambda$  is set as twice as fast as the open-loop response used by Tham in [172]. However, this selection complies with the rule  $\frac{\lambda}{\theta} > 1.7$ , as proposed by Rivera in [170] and  $\frac{\lambda}{\theta} > 0.2\tau$ , as proposed by Shahrokhi and Zomorodi in [175].

The conventional feedback controller  $G_c$  is related to the IMC controller  $q_c$ , which is denoted as

$$G_c(s) = \frac{q(s)}{1-G_p(s)q(s)} = \frac{\tau s+1}{K} \frac{1}{(\lambda s+1)^r} \quad (4-25)$$

This equivalent controller is not in the form of the PI controller. Therefore, the Maclaurin series expansion formula is applied to obtain a PI controller, which approximates  $G_c$  given in (4-25) as

$$G_c(s) = \frac{1}{s} [f(0) + f'(0)s + \frac{f''(0)}{2}s^2 + \dots] = K_c(1 + \frac{1}{T_i}s + T_d s) \quad (4-26)$$

where  $f(s) = sG_c(s)$ . The PID parameters are obtained as

$$K_c = f'(0); T_i = \frac{f'(0)}{f(0)}; T_d = \frac{f''(0)}{2f'(0)} \quad (4-27)$$

Note that a PI controller or a P controller can be approximated using only the first two terms or the second term, respectively, in (4-26). Thus, the gain for the PI controller can be extracted as

$$K_P = \frac{\tau}{K(\theta+\lambda)} \quad (4-28)$$

$$T_i = \tau \quad (4-29)$$

#### 4.4.3.2 IMC-PI Cascade Controller Design

Cascade control is extensively used in industrial sectors to reduce the effects of possible disturbances that affect the secondary (inner) loop. In cascade

design, the disturbance is effectively compensated prior to affecting the process variable of the primary (outer) loop. Cascade control may improve the dynamic performance of a closed-loop system [32]. This section explains how to obtain the parameters of the PI controllers of the proposed model (IVC and SLIVC) from a well-designed and well-tuned IMC cascade control system. Figure 4-9 shows the configuration of a typical cascade control system, where  $G_{p1}$  and  $G_{p2}$  are the primary process and the secondary process, respectively. The primary process variable  $y_1$  (with setpoint  $r_1$ ) is used by the primary controller  $G_{c1}$  to establish the set-point ( $r_2$ ) for the secondary controller  $G_{c2}$ . The secondary process variable  $y_2$  is subsequently fed to the secondary controller, which fine-tunes the manipulated variable  $u$ . To obtain the PI parameter for the cascade design, the controller tuning began with the secondary controller (inner loop) and continued with the primary controller (outer loop) [168, 174].

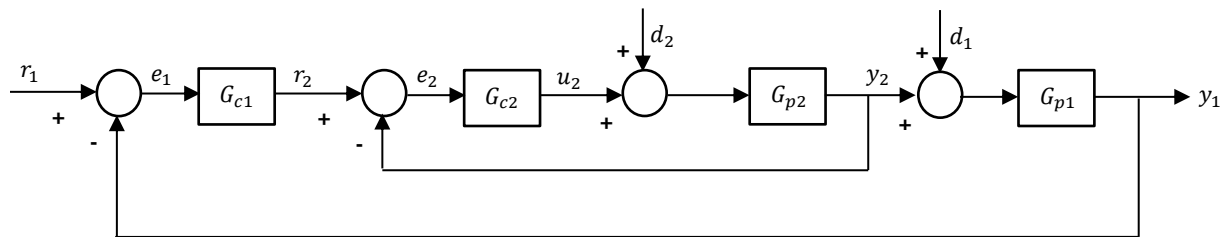


Figure 4-9 Configuration of a typical cascade system

#### 4.4.3.2.1 Design of the Secondary Controller

According to the method presented in the previous section, the secondary process model  $G_{p2}$  must be obtained; it is modelled as (FOPTD) dynamics as

$$G_{p2}(s) = \frac{K_2}{\tau_2 s + 1} e^{-\theta_2 s} \quad (4-30)$$

The IMC controller  $q_{c2}$  is designed as

$$q_{c2}(s) = G_{p2}(s)^{-1} f_2(s) \quad (4-31)$$

where  $G_{p2-}$  is the invertible part of the model  $G_{p2}$  and  $f_2$  is the IMC filter that addresses the robustness issue of the inner loop. In this case, the selected IMC filter is

$$f_2(s) = \frac{1}{(\lambda_2 s + 1)^{r_2}} \quad (4-32)$$

where the parameter  $\lambda_2$  is the adjustable parameter of the secondary filter.

The conventional feedback controller  $G_{c2}$  is related to the IMC controller  $q_{c2}$  as

$$G_{c2}(s) = \frac{q_2(s)}{1 - G_{p2}(s)q_2(s)} = \frac{\tau_2 s + 1}{K_2} \frac{1}{(\lambda_2 s + 1)^r} \quad (4-33)$$

Using Equations (4-28) and (4-29), the PI controller gains for the secondary controller can be obtained when compared with Equation (4-33).

#### 4.4.3.2.2 Design of the Primary Controller

With the designed secondary controller, the primary controller is designed based on the apparent process  $G_{p1}^*$ , as determined by the primary controller as

$$G_{p1}^*(s) = \frac{G_{c2}(s)G_{p2}(s)}{1 + G_{c2}(s)G_{p2}(s)} G_{p1}(s) \quad (4-34)$$

With the model  $G_{p1}^*$ , the IMC design is applied to design the primary controller  $G_{c1}$ . The IMC controller  $q_{c1}$  is designed as

$$q_{c1}(s) = G_{p1-}^*(s)^{-1} f_1(s) \quad (4-35)$$

where  $f_1$  is the IMC filter that addresses the robustness issue of the outer loop.

To maintain the simplicity of the control system, the typical IMC filter design is adopted for  $f_1$ ,

$$f_1(s) = \frac{1}{(\lambda_1 s + 1)^r} \quad (4-36)$$

where  $\lambda_1$  is the adjustable parameter to create a trade-off between the performance and the robustness of the outer loop.

The apparent process for the primary controller design is modelled using FOPTD dynamics as

$$G_{p1}(s) = \frac{K_1}{\tau_1 s + 1} e^{-\theta_1 s} \quad (4-37)$$

In this primary FOPTD model, the conventional feedback controller  $G_{c1}$  is related to the IMC controller  $q_{c1}$  as

$$G_{c1}(s) = \frac{q_1(s)}{1 - G_{p1}^*(s)q_1(s)} = \frac{\tau_1 s + 1}{K^*_{p1} (\lambda_1 s + 1)^r} \quad (4-38)$$

Using Equations (4-28) and (4-29), the PI controller gains for the primary controller can be obtained when compared with Equation (4-38).

#### 4.4.4 IMC-PI-IP (M4)

M4 is actually based on M3. But, in M3, the speed Proportional Integral (PI) controller in M4 is replaced with the Integral Proportional (IP). The structure of this controller is shown in Figure 4-10.

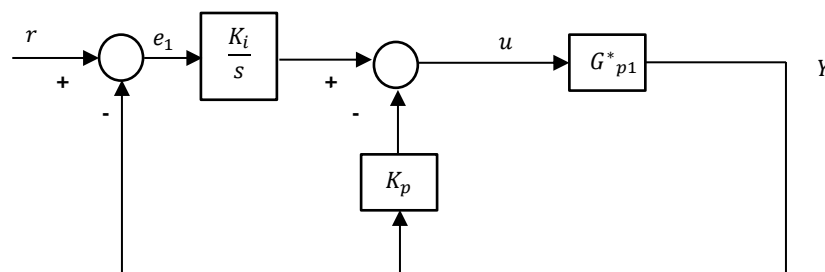


Figure 4-10 Block diagram with I-P controller

The closed-loop transfer function between the output  $Y(s)$  and the input  $r(s)$  is given as [176]

$$\frac{Y(s)}{r(s)} = \frac{K_i G(s)}{s(1 + K_p G(s)) + K_i G(s)} \quad (4-39)$$

where  $G_{p1}^*$  is the transfer function of the plant,  $K_p$  is the proportional gain and  $K_i$  is the integral gain.

#### 4.4.4.1 IP Parameter Tuning Method

To select the proportional and the integral gain for the IP, the following steps have been undertaken:

- 1- Initially set  $K_p = 0$ .
- 2- From the  $G_{p1}^*(s)$  transfer function that was obtained in Equation (4-34), obtain the zero pole gain from the open-loop transfer function matrix  $G_{p1}^*(0)$  plant; consider gain to be the integral gain constant. The integral gain  $K_i$  can be computed as

$$K_i = \varepsilon G_{p1}^*(0) \quad (4-40)$$

where  $\varepsilon$  is the controller tuning parameter, in which  $0 < \varepsilon < 1$ .

- 3- Set the proportional gain  $K_p = 1$ . Observe its response. If the response is not satisfactory, increase the  $K_p$  until a satisfactory result is obtained.

#### 4.4.4.2 Guidelines for the selection of the controller tuning parameter ( $\varepsilon$ )

To select the controller tuning parameter of  $\varepsilon$ , the following steps have been undertaken:

- 1- Initially set  $\varepsilon = 1$ . Observe the output response. If the loop signal shows a sustained periodic oscillation in the controller output (or close to it) as depicted in Figure 4-11, record this value as the controller tuning parameter  $\varepsilon$ .

- 2- If the required response is not achieved, reduce the value of  $\varepsilon$  until a sustained periodic oscillation output signal is achieved. Record this value as the controller tuning parameter  $\varepsilon$ .

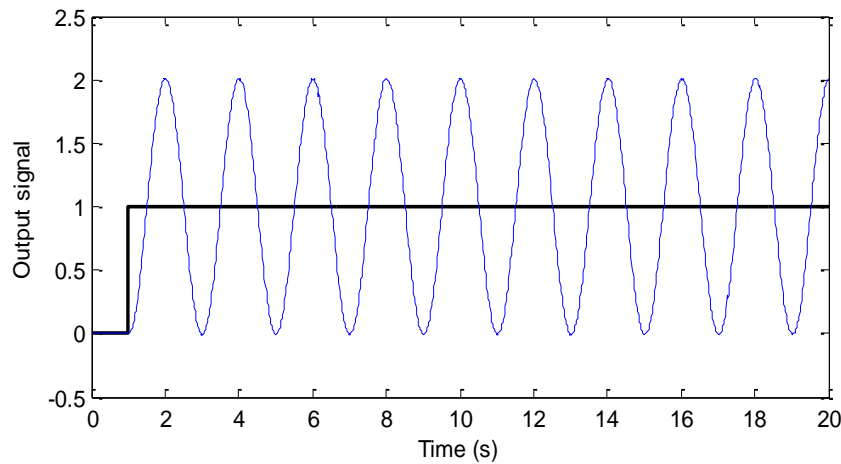


Figure 4-11 Sustained periodic oscillation signal

#### 4.5 Performance Index

The performance of the designed feedback control system is analysed and measured. In this study, the following measures were used:

- 1- Robustness: The maximum sensitivity function  $M_S$ .
- 2- Performance: Output performance and input performance.

It is a general practice to use this type of performance metrics when IMC approach is undertaken, e.g., as can be seen in [166, 168, 169, 173, 174, 177-180]. It has been claimed and proven in [181] by Astrom, K. J that this performance metrics can be used to replace the classical stability criterion; the gain and phase margins.

In any control design, robustness and performance issue is an important key that should be trade-offs. Robustness is the ability of a closed-loop system to be insensitive to component variations. Reasonable robustness that is usually measured using gain and phase margins, alternatively can be determined using a single stability margin, which is known as sensitivity function,  $S(s)$ . Using

information of  $\mathcal{S}(s)$ , both robustness and stability of a loop transfer function also can be measured [181] by inspecting its maximum sensitivity function,  $M_s$  and its complementary sensitivity function,  $\mathcal{T}(s)$ . If the  $M_s$  value closes to one (1), system is more conservative, meanwhile if  $M_s$  value closes to two (2), system corresponds to be more aggressive controller. The employment of sensitivity function in measuring the proposed SRVSWT system's robustness is explained in more detail in section 4.5.1.

Meanwhile, performance of a loop transfer function can be measured using input and output performance measures through load disturbance and noise tests. Also, using sensitivity function information, the controller performance can be described by inspecting the ability to follow reference signal and inspecting the disturbance effects on the controlled output. To achieve good disturbance rejection, the adjustable filter parameter,  $\lambda$  should be designed as small as possible using this approach. The type used to measure the input and output performance of the proposed SRVSWT system is given in section 4.5.2.

#### 4.5.1 Robustness Measure

Using the sensitivity function, the level of sensitivity of a closed-loop system to the changes in the open-loop system can be determined by the relationships among the error, the process and the controller. The sensitivity function, which is denoted as  $\mathcal{S}(s)$ , is usually related to the disturbance rejection properties, which should be made as small as possible. Particularly, if  $\mathcal{S}(s) = 0$  can be achieved, the best performance or perfect control is attained. However, perfect control cannot be achieved for the entire frequency range. In all cases, perfect control can only be achieved for a small range of frequencies (low frequencies). The  $\mathcal{S}(s)$  is bounded between 0 and 1, where 1 is always achieved at high frequencies. The sensitivity function  $\mathcal{S}(s)$  can be measured as

$$\mathcal{S}(s) = \frac{1}{1+G_c(s)G_p(s)} \quad (4-41)$$

The maximum sensitivity function  $M_s$  is the peak value of the magnitude sensitivity function  $S(s)$ . This function indicates the model sensitivity to the modelling errors or the magnitude of the maximum amplification from the reference to the error signal.  $M_s$  is defined as the inverse of the shortest distance from the Nyquist curve of the open loop transfer function to the critical point  $(-1,0)$  [182, 183], as shown in Figure 4-12. All points inside the dashed circle exhibit sensitivities greater than 1.  $M_s$  can also be expressed as

$$M_s(s) = \max \left| \frac{1}{1+G_c(s)G_p(s)} \right| \quad (4-42)$$

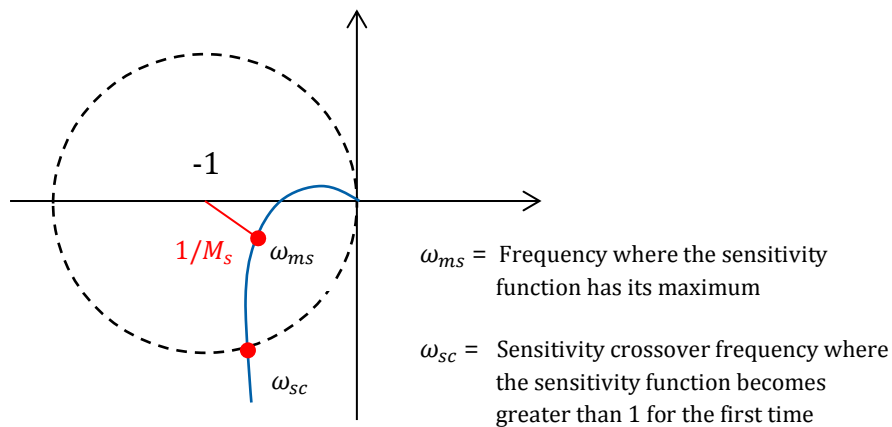


Figure 4-12 Graphical interpretation of the sensitivity function from the Nyquist curve

#### 4.5.2 Performance Measure

The output performance is computed for the process output, which can be measured by computing the integrated absolute error (IAE),  $e = r_{ref} - y$ . This error should be as small as possible, where

$$IAE = \int_0^{\infty} |e(t)| dt \quad (4-43)$$

The input performance is computed for the process input and can be measured by computing the total variation (TV) of the control signal  $u(t)$ . Using the TV, the smoothness of the control signal can be measured; which should be as small as possible. The TV can be measured as

$$TV = \sum_0^{\infty} |u_{i+1} - u_i| \quad (4-44)$$

IAE is computed using Simulink by making the output error absolute (abs) prior to feeding to an integrator, whereas TV is computed using the Matlab command 'sum(abs(diff(u)))'.

## 4.6 Chapter Summary

Detailed descriptions of the indirect vector control (IVC) and sensorless indirect vector control (SLIVC) methods have been presented. The strategies for using the IVC and SLIVC models in the stall-regulated variable-speed wind turbine (SRVSWT) system have been presented. The input/output pairing using the relative gain array (RGA) approach as the controller tuning procedure has also been explained. The guidelines for designing the controller using the Ziegler-Nichols (ZN), Tyreus-Luyben (TL), and the internal model control (IMC) structure IMC-PI and the new structure IMC-PI-IP, which is based on the IMC-PI and the integral-proportional (IP) controller, has also been described. The approaches to assess the performance of the proposed tuning rules are also detailed in this chapter.

## **5 Results and Discussion**

### **5.1 Chapter Overview**

This chapter presents the results from the analyses. This chapter is divided into five sections. Section 5.1 highlights the contents of this chapter. Section 5.2 presents the results of the estimated PI gains that were obtained from the four types of proposed tuning methods (Ziegler-Nichols, Tyreus-Luyben, IMC-PI and IMC-PI-IP) for the SRVSWT with Model-1 (IVC), which were explained in chapter four. The comparison of the results for the step and the realistic wind speed input changes are also demonstrated. The behaviour (performance index) during the step track changes and the disturbance rejection with regards to the proposed SRVSWT system is also demonstrated. Section 5.3 discusses the comparison results between the constant speed (CS) and the modified power tracking (MoPT) during the intermediate load (IL). In section 5.4, the comparison of the results between the IVC and SLIVC model algorithms using the best tuning method, which was presented in the previous sections of this chapter, is presented. A summary of the results obtained in this research is provided in section 5.5.

### **5.2 Results of the Proposed Tuning Methods**

To assess the behaviour and operating performance of the SRVSWT, two tests of the system were conducted. The first test was run under a step input (wind speed) change. In the second test, the system was tested using a realistic input (wind speed) time series. These tests analysed the reliability of the proposed operating system.

### 5.2.1 Step Change Performance Assessment

The step input test is usually important as this test distinctly assesses the behaviour of the outputs of a general system when its reference/input changes from one state to another state. In this section, the performance and robustness of the system are evaluated and compared based on the performance index explained in Section 4.5.

Table 5-1 shows the robustness and performance measure that were applied to the SRVSWT system when the Ziegler-Nichols (ZN), Tyreus-Luyben (TL) and IMC-PI tuning rules are used. In this table, details of the IMC-PI-IP are not included as the arrangement of the P and I controller for the speed controller is not equivalent to the ZN, TL and IMC-PI (refer to Figure 4-10). From Table 5-1, the IMC-PI exhibits better robustness as it yields a smaller  $M_s$  than the ZN and the TL. For the input and output performance measures, the IMC-PI yielded the smallest TV values compared with ZN and TL during the step input test. IMC-PI also yielded lower IAE values for the flux and torque controllers; however, the lowest IAE for the speed controller was given by the TL tuning rule. During the step disturbance test, IMC-PI produces higher IAE values for the torque and speed controllers but yields better TV values compared with ZN and TL.

Table 5-1 Performance measures for the ZN, TL and IMC-PI tuning rules

Tuning	$M_s$	Step Set Point						Step Disturbance					
		IAE			TV			IAE			TV		
		Flux	Torque	Speed	Flux	Torque	Speed	Flux	Torque	Speed	Flux	Torque	Speed
ZN	2.5	0.71	4.73	12	44	168	260	0.59	2.61	3.04	37	139	125
TL	2.3	1.57	110.6	2.05	102	1898	6018	1.52	5.96	1.69	29	162	394
IMC-PI	1.3	0.15	4.04	44.09	20	72	36	0.13	13.94	39.55	18	79	45

In Table 5-2, the details of the tuning parameters ( $K_p, T_i, K_i, K_u, P_u$ ) for the proposed ZN and TL tuning procedures are summarised. The details of the tuning parameters ( $K_p, T_i, K_i, \lambda$ ) and the FOPTD model ( $\varepsilon, K, \tau, \theta$ ) for the proposed IMC-PI and IMC-PI-IP tuning rule are summarised in Table 5-3. Table 5-2 and Table 5-3 reveal that different tuning rules yielded the variable controller gain  $K_p$  and the integral time constant  $T_i$ . In the majority of cases, ZN tuning yielded the highest  $K_p$  values in the flux controller, whereas the IMC-PI exhibited the lowest  $K_p$  values in the speed controller. In terms of the integral time constant  $T_i$  the ZN

tuning rule has the smallest constants compared with the other rules, with the exception of the flux controller, for which the IMCs present the smallest  $T_i$ .

Table 5-2 Details of the tuning parameters for the Ziegler-Nichols and Tyreus-Luyben tuning procedures

Tuning	Controller	$K_p$	$T_i$	$K_i$	$K_u$	$P_u$
ZN	Flux Controller	33.75	0.035	28.57	75	0.042
	Torque Controller	0.450	0.025	40.00	1	0.030
	Speed Controller	3.15	0.0258	38.71	700	0.031
TL	Flux Controller	23.25	0.0924	10.823	75	0.042
	Torque Controller	0.31	0.066	15.152	1	0.030
	Speed Controller	2.17	0.0682	14.663	700	0.031

Table 5-3 Details of the tuning parameters and the FOPTD model for the IMC-PI and IMC-PI-IP tuning rules

Tuning	Controller	$K_p$	$T_i$	$K_i$	$\lambda$	$\varepsilon$	$K$	$\tau$	$\theta$
IMC-PI	Flux Controller (PI)	3.35	0.007	142.86	0.19	-	0.0108	0.007	0.0001
	Torque Controller (PI)	0.60	0.917	1.091	0.2	-	1.41	0.917	0.885
	Speed Controller (PI)	1.282	1.28	0.781	15.95	-	0.06	1.28	0.691
IMC-PI-IP	Flux Controller (PI)	3.35	0.007	142.86	0.19	-	0.0108	0.007	0.0001
	Torque Controller (PI)	0.60	0.917	1.091	0.2	-	1.41	0.917	0.885
	Speed Controller (IP)	25.5	0.015	67.64	-	0.22	-	-	-

Figure 5-1(a) to Figure 5-1(c) show the step responses for the plant output and Figure 5-1(d) shows the plant input (control signal) of the SRVSWT system when a step change is applied to the set point signal. The step change is referenced when the wind speed changes from 4 to 5 m/s, in which the turbine mechanical speed also influenced the change from 52 rad/s to 68 rad/s. Table 5-4 shows details of the step responses for all proposed tuning rules. For this performance measure, the following characteristics are referenced:

- Rise time ( $T_r$ ): The time for the output to attain 90% of its final value.
- Settling time ( $T_s$ ): The time for the output to attain 5% of its final value.
- Overshoot (%OS): The ratio between the peak value and its final value, which should be 1.2 or less than 20%.
- Phase margin: The PM can estimate the “safety margin” for closed-loop stability. The larger are the stability margins, the more stable is the system. PM is used to determine the required amount of phase lag at the gain crossover frequency prior to the loss of stability. The gain crossover

frequency is the frequency in which the loop transfer function attains a magnitude of 1.

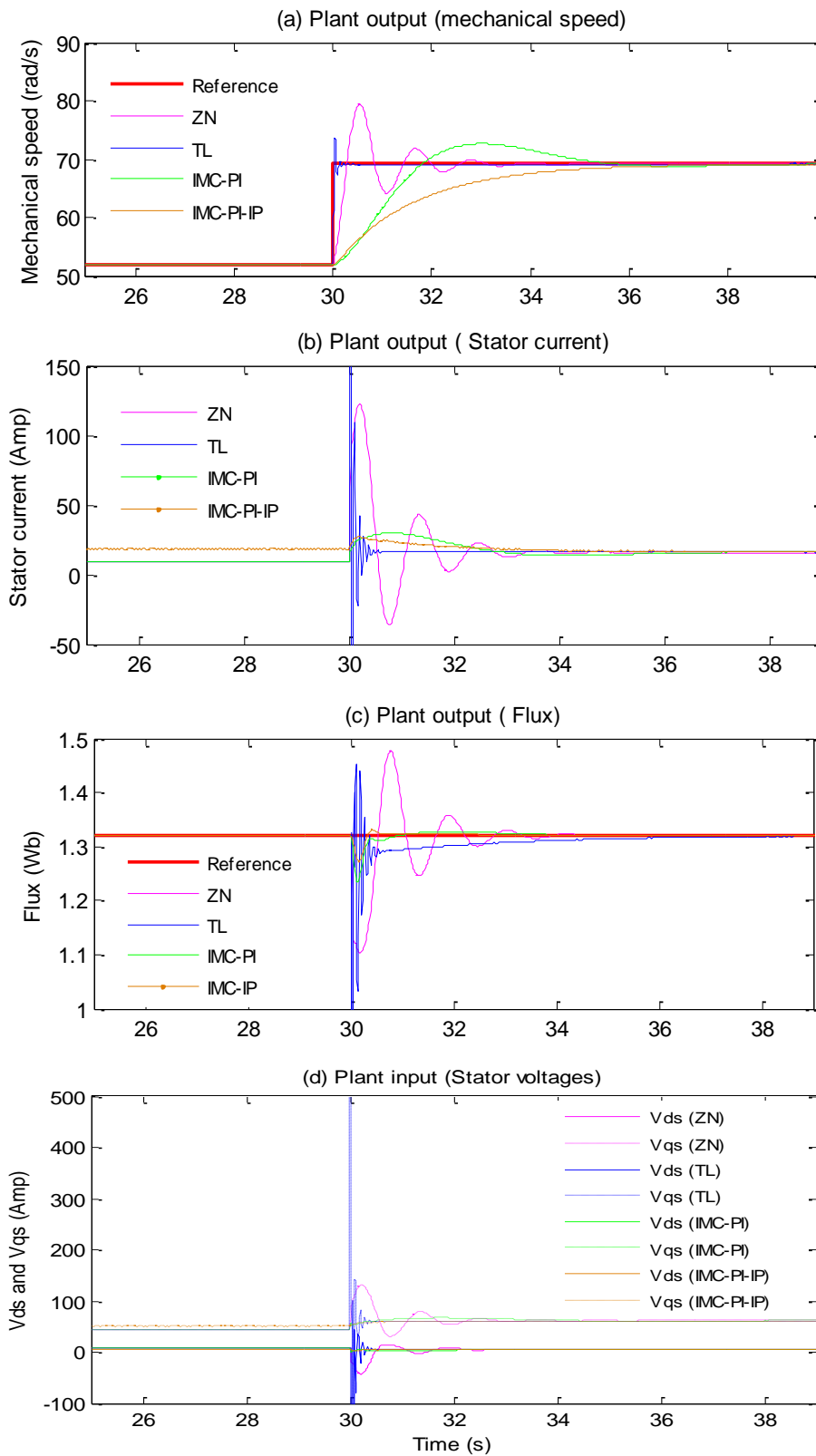


Figure 5-1 Step change response at the set point

Table 5-4 Details of the transient response for the ZN, TL, IMC-PI and IMC-PI-IP tuning rules

Tuning	Controller	Rise time, $T_r$ (s)	Settling time, $T_s$ (s)	Overshoot, OS (%)	Phase margin
ZN	Flux	0.30	3.72	2.55	48°
	Torque	0.20	3.30	21.7	53°
	Speed	0.18	2.91	55.8	24°
TL	Flux	0.04	6.36	9.84	53°
	Torque	0.12	0.36	49.8	24°
	Speed	0.02	0.36	45.5	20°
IMC-PI	Flux	0.10	0.38	7.83	61°
	Torque	0.40	0.42	15.1	70°
	Speed	1.60	5.96	6.21	62°
IMC-PI-IP	Flux	0.18	0.23	6.00	90°
	Torque	0.30	0.22	11.7	65°
	Speed	4.20	6.44	0	62°

As shown in Figure 5-1 and Table 5-4, the high gain of  $K_p$  and the excessively low  $T_i$  from the ZN tuning rule produces an unstable process in which overshoots with large amplitudes (greater than 25%) and oscillations exist. A similar situation occurs when TL is used. Although TL generates a lower  $K_p$  and a higher  $T_i$  than ZN, these parameters are considered large compared with the proposed tuning rules of the IMCs. Thus, TL tends to present oscillatory results and high overshoots are produced in some cases, such as for the current control (refer to Figure 5-1(b)). Consequently, the inputs of the plant ( $v_{ds}$  and  $v_{qs}$ ) produce a large resonant peak, which must be prevented in the control system. This finding is confirmed by the large values of TV when TL is employed, as depicted in Table 5-1. Although considerably low IAE values (fast response) with high TV values are identified during a step point change, the stability of the system is reduced.

Compared with the ZN and TL tuning rules, no oscillation is produced with the IMC design. Satisfactory robustness for diminishing errors and oscillation responses is usually achieved with a phase margin between 45° to 60°. With the IMC design, more robust control with a better stability phase margin is obtainable, as shown in Table 5-4. The phase margin for the IMC design is greater than 45° for all controllers; this result is not achievable by ZN and TL. This finding is also verified by the low values for the  $M_s$ , IAE and manipulated input variable usage (TV), as shown in Table 5-1. Although no oscillation is produced for the output signal when IMC-PI is used, an overshoot is produced. The

overshoot is considered to be acceptable when the percentage overshoot value does not exceed 20%.

With the IMC-PI-IP tuning rule, no oscillation and almost no overshoot is produced for the output signals. For example, as shown in Figure 5-1(a), no overshoot or oscillation occurs for the speed signal. Although IMC-PI-IP produces no oscillation or overshoot, the speed takes a while to settle compared with the IMC-PI. As shown in Table 5-4, the IMC-PI-IP required approximately 6.44 seconds to settle, whereas IMC-PI required 5.96 seconds to settle. However, for the current torque and flux control, IMC-PI-IP achieves a faster settling time and lower percentage overshoot compared with IMC-PI. The inputs of the plant signals ( $v_{ds}$  and  $v_{qs}$ ) are also smooth (refer to Figure 5-1(d)).

Figure 5-2 shows the step response when a disturbance of 6 seconds is applied to the input plant. The examples of disturbance include reductions in aerodynamic torque and changes in voltage, such as fault voltage, voltage-dip and voltage sag in the integration system. As shown in Figure 5-2, the ZN and TL tuning rules result in a better load disturbance rejection compared with IMC-PI and IMC-PI-IP but in the presence of clearer noise in the current and flux signals. Additionally, the figure shows that the IMC-PI and IMC-PI-IP tuning rules produce some overshoots in speed ( $\approx 0.2\%$ ), current ( $\approx 2.8\%$ ) and flux ( $\approx 1.2\%$ ). The overshoots presented by these tunings are considerably small and provide a fast response during the disturbance rejection and manage to produce smoother signals (free from noise) compared with ZN and TL.

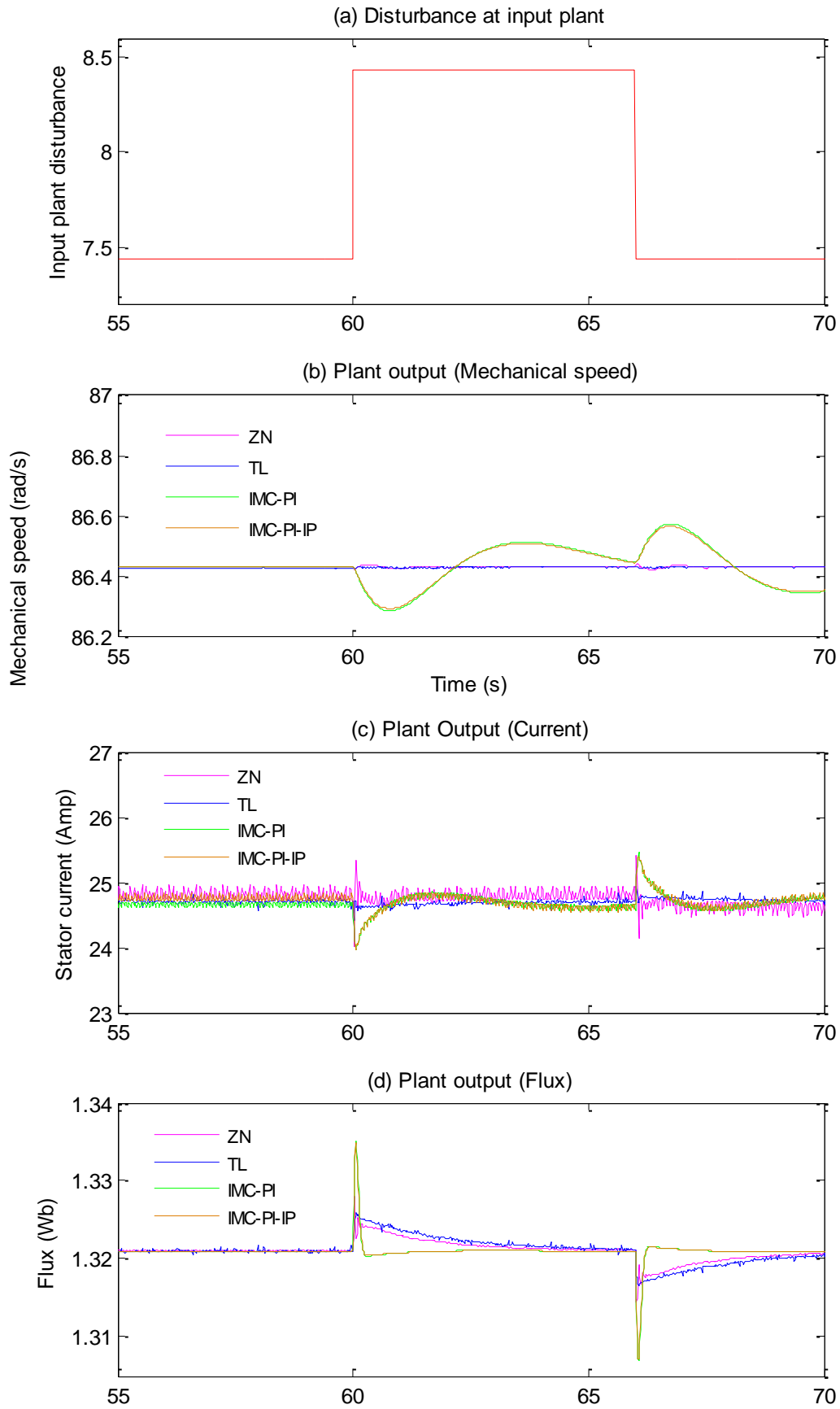


Figure 5-2 Disturbance response at the input plant

For the FOPTD transfer function that is used in the proposed IMC models, details of the high-order transfer function and the estimated reduced-order model transfer functions (FOPTD) for the MIMO process plant  $G_p$  are summarised in Table 5-5.

Table 5-5 Details of the high-order and reduced-order model transfer function for the MIMO plant

MIMO Plant	High-Order Equation	FOPTD Equation
$G_{11}$	$\frac{84.84s^2 + 1.259e004 s + 9941}{s^4 + 296.8 s^3 + 3.857e004 s^2 + 8.855e005 s + 9.284e005}$	$\frac{0.0108e^{-0.0001s}}{0.015s + 1}$
$G_{12}$	$\frac{-1.421e004 s^2 - 1.665e006}{s^4 + 296.8 s^3 + 3.857e004 s^2 + 8.855e005 s + 9.284e005}$	$\frac{-1.793e^{-0.01s}}{0.95s + 1}$
$G_{21}$	$\frac{1.234e004 s + 7829}{s^4 + 296.8 s^3 + 3.857e004 s^2 + 8.855e005 s + 9.284e005}$	$\frac{0.0108e^{-0.0001s}}{0.015s + 1}$
$G_{22}$	$\frac{195.4 s^3 + 2.901e004 s^2 + 1.143e006 s - 1.311e006}{s^4 + 296.8 s^3 + 3.857e004 s^2 + 8.855e005 s + 9.284e005}$	$\frac{-1.41e^{-0.885s}}{0.917s + 1}$

In this study, using SIMULINK environment, the high-order transfer functions are obtained from the nonlinear SRVSWT model (as depicted in Figure 4-3) after executing linearization at an appropriate operating point. However, to obtain the process plant  $G_p = \begin{bmatrix} G_{11} & G_{12} \\ G_{21} & G_{22} \end{bmatrix}$  for the I/O pairing purpose (as depicted in Figure 4-5), only “First loop” and “Second loop” are involved. Since an IMC design is used in this study (for the reasons of simplicity, robustness and ease of computation/procedure) to find the PI parameters of the proposed SRVSWT system, these linearized transfer functions are then estimated to be in the form of the FOPTD transfer functions. Through this, a more direct and natural controller design procedure than the classical approach can be applied, where the requirement of solving the roots of the characteristic polynomial  $1 + G_p G_c$  can be avoided. Only simple analysis of the pole of  $q_c$  is considered when IMC controller is used (see Figure 4-8(b)). Furthermore, the proposed IMC offers a simple and effective method to attain the PI controller rules for parallel cascade control system which takes into account the interaction between primary and

secondary control loops, as needed when designing the speed controller of the proposed SRVSWT system (“Third loop”) as shown in Figure 4-3(b).

The comparison signals for the high-order transfer function and the estimated FOPTD for the MIMO plant are shown in Figure 5-3. Using Equations (4-14) to (4-16), the RGA matrix  $\Lambda = \begin{bmatrix} 0.995 & 0.005 \\ 0.005 & 0.995 \end{bmatrix}$  is obtained and the I/O Pairing of  $G_{11}$  and  $G_{22}$  was selected for the controller tuning. The approximation of these signals ( $G_{11}$  and  $G_{22}$ ) is identical. Although the  $G_{11}$  model approximation does not capture the resonant peak of the high-order signal, this approximated FOPTD signal describes the process gain, time delay and time constant of this process.

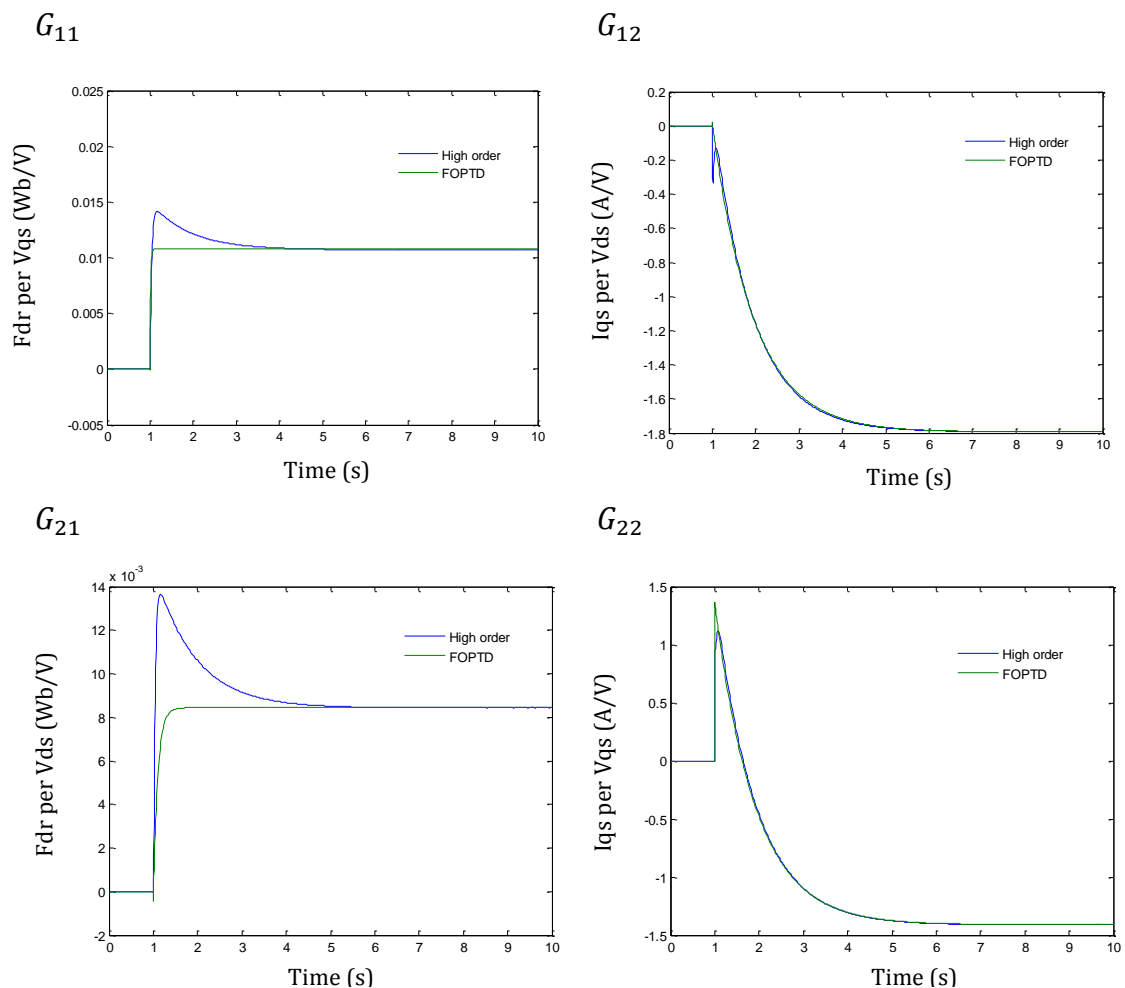


Figure 5-3 Comparison between high-order model and the FOPTD model

For the IP parameters of the speed controller for the IMC-PI-IP tuning rule, the controller tuning parameter of  $\varepsilon$  is 0.22. The effect of the different controller

tuning parameters ( $0 < \varepsilon < 1$ ) during tuning parameter selection is shown in Figure 5-4, which shows that when  $\varepsilon$  is 1, an unstable oscillation is created. However, when  $\varepsilon$  is reduced by 0.25, the peak of the oscillation signal is also reduced. With  $\varepsilon = 0.25$ , the output signal almost exhibits a sustained periodic oscillation signal. After additional testing ( $\varepsilon < 0.25$ ), a pure sustained periodic oscillation signal is obtained when  $\varepsilon = 0.22$ , as depicted in Figure 5-5.

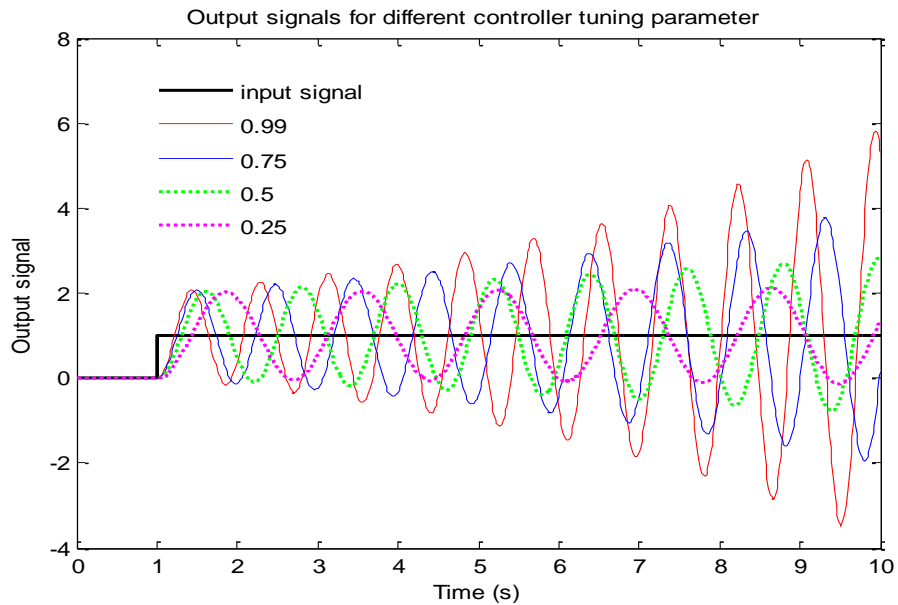


Figure 5-4 Different output signals based on different values of the controller tuning parameter  $\varepsilon$

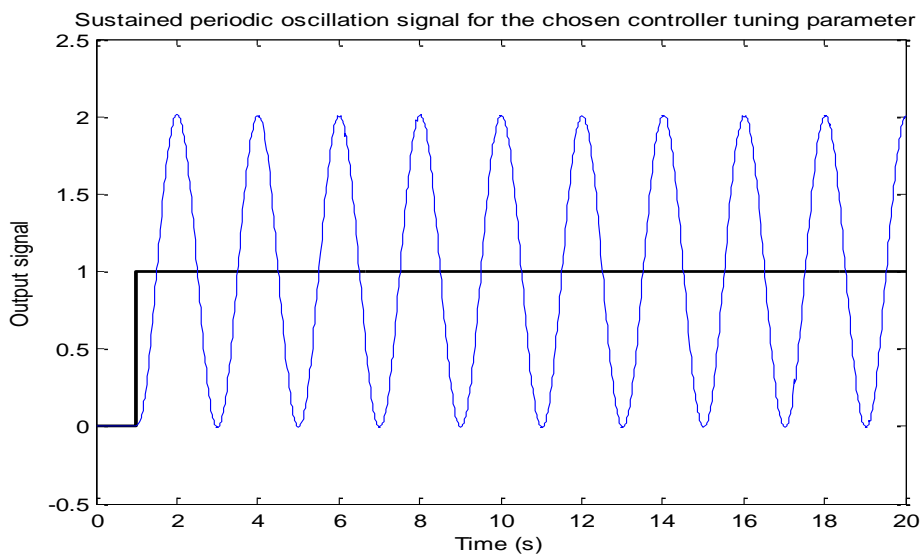


Figure 5-5 The sustained periodic oscillation signal for  $\varepsilon = 0.22$

## 5.2.2 Dynamic Performance Assessment

This section presents the simulation results for the SRVSWT system behaviour when the system is subjected to a 1000-second realistic wind speed time series as the input signal. The wind speed has a time step of 1 second. The details of this time series model are presented in subchapter 3.1.1 To assess the real behaviour of the SRVSWT system, a random wind speed time series was tested to demonstrate the closed-loop system behaviour of the SRVSWT. The profile for an extensive range of wind speeds from 3 to 20 m/s is shown in Figure 5-6(a). The generator mechanical speed response to the created wind speed is shown in Figure 5-6(b) and the tip-speed ratio (TSR) and the power coefficient ( $C_p$ ) evolutions are shown in Figures 5-6(c) and 5-6(d), respectively.

Figure 5-6 shows that the SRVSWT system is successful for an extensive range of wind speeds using all tuning rules. All rules can track the speed reference (as shown in Figure 5-6(b)) and almost no significant deviation can be observed, with the exception of the signal carried by the TL. TL tends to create overshoot in speed when wind speeds change their directions. This scenario is also shown in Figure 5-6(d), in which the tip speed ratio experiences a similar trend of overshoot signals. This property is also shown in Figure 5-1 and Table 5-4 in the preceding subsection, in which TL exhibits a large overshoot during speed change.

The  $C_p$  signals show similar performance in all tunings, as depicted in Figure 5-6(c). However, differences in the performances of the proposed approaches are distinct when the simulation results are closely examined. The explanation will be divided into 3 snapshots. The first snapshot will focus on the low wind speed region, whereas the second snapshot and third snapshots will focus on the medium wind speed and high wind speeds regions, respectively.

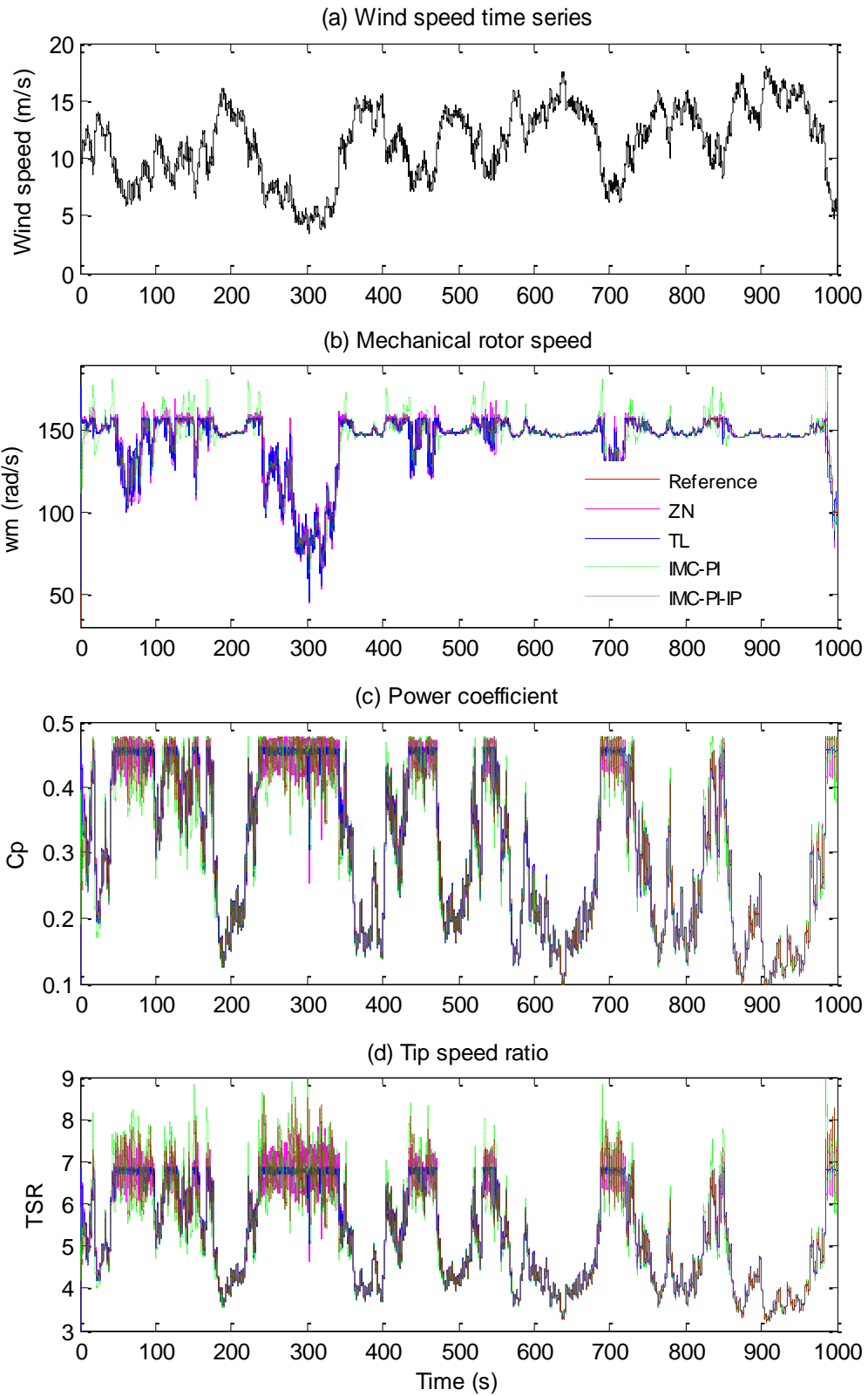


Figure 5-6 The SRVSWT behaviour in a realistic wind speed profile: (a) the realistic wind speed profile, (b) the generator mechanical speed, (c) the power coefficient, and (d) the tip-speed ratio

When the observation is focused on the period from 300 to 340 seconds, the turbine experiences a low wind speed profile, which ranges from 3 to 8 m/s. In this situation, the wind speed falls within the optimal tracking region. The focused snapshot of this region is shown in Figure 5-7(a) and 5-7(b). During this time, TL tracks the generator speed reference more closely than the design of the ZN and IMCs. The power coefficients can also be better maintained in the peak area of the curve, as presented in Figures 5-7(c). Therefore, TL also shows better performance for maintaining the TSR at the optimum value of 6.78, as distinctly shown in Figures 5-7(d). Using the IMC design, the speed changes are less oscillatory compared with ZN and TL. Between IMC-PI and IMC-PI-IP, the latter performs better where the signals track the reference more closely.

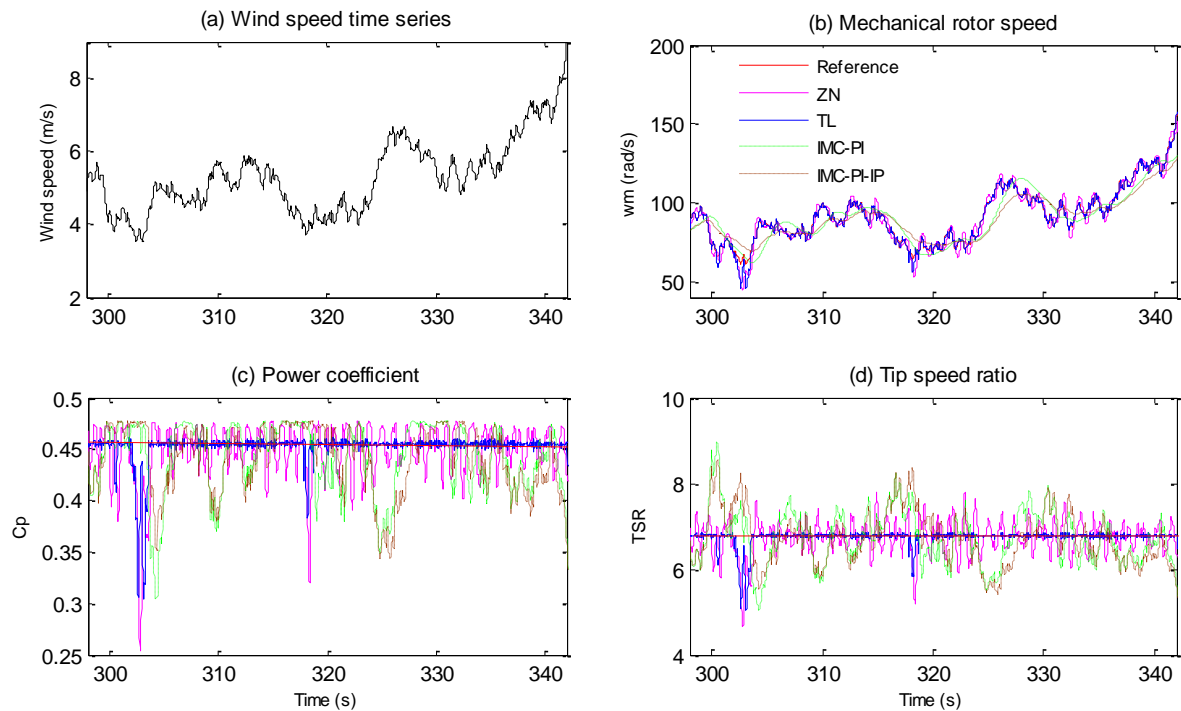


Figure 5-7 The SRVSWT behaviour in the low wind speed region: (a) the realistic wind speed profile, (b) the generator mechanical speed, (c) the power coefficient, and (d) the tip speed ratio

In the medium wind speed region, the power is restricted by following the maximum power locus. This region covers wind speeds from 8 to 11 m/s, as depicted at time  $t = 546$  to 555 seconds and as shown in Figure 5-8(a). For this

condition, the speed is fixed at the maximum permitted value. The behaviour of the wind speed, the angular mechanical speed, the power coefficient and the tip speed ratio in this region is illustrated in Figure 5-8(a) to 5-8(d).

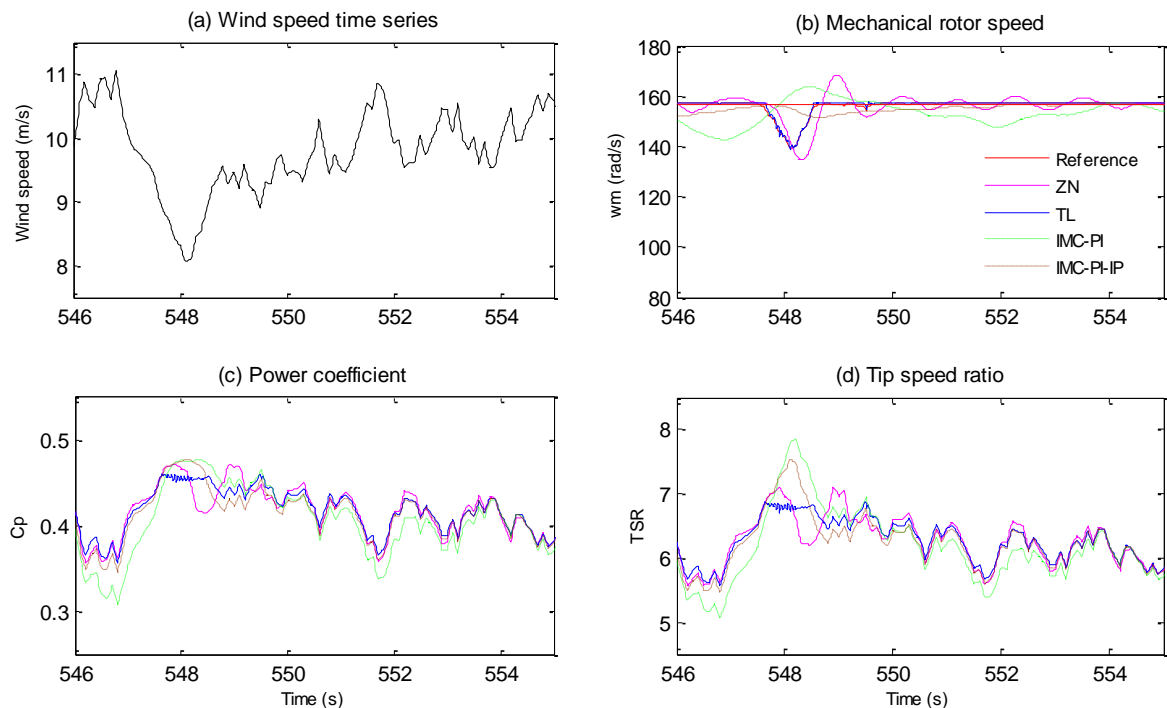


Figure 5-8 The SRVSWT behaviour in the medium wind speed region: (a) the realistic wind speed profile, (b) the generator mechanical speed, (c) the power coefficient, and (d) the tip speed ratio

Figure 5-8(b) shows that IMC-PI-IP performs better in limiting the rotor speed to a fixed speed (157 rad/s) as demanded by the reference, regardless of the size of the changes/fluctuations in wind speeds. IMC-PI-IP has the smallest maximum percentage error of deviation of 2% compared with IMC-PI, which exhibits deviations larger than the ZN, TL and IMC-PI-IP (approximately 15%). Therefore, IMC-PI-IP yields smoother curves of the  $C_p$  and the TSR. However, all tuning rules can control the  $C_p$  and TSR to function below the  $C_{pmax}$  and  $\lambda_{opt}$  values in this medium wind speed region. The validity relationship formulated by Equation (2-5) also demonstrates which TSR will be reduced when the rotor speed is maintained at the constant value and the wind speed increases. These results are observed at time  $t = 548$  to  $t = 555$  seconds. Conversely, the TSR will

increase when the wind speed decreases, as observed in the period from time  $t = 547$  to  $t=548$  seconds. For the  $C_p$ , the curves operate below  $C_{pmax}$ , as expected for wind speeds in the medium wind speed region.

As the generated power must be rated at 25 kW in the high wind speed region, the generator speed needs to be prevented from accelerating above the maximum permitted speed (157 rad/s) and must be reduced below this maximum speed when the wind speed exceeds 11 m/s. In the high wind speed region, the IMC-PI fails to limit the generator speed to this maximum speed as it attains a maximum speed of 160 rad/s for wind speeds of approximately 11.5 m/s, as shown in Figure 5-9(a) and 5-9(b). This result is observed at time  $t = 965$  seconds. This finding is confirmed by the large values of IAE during the set point change in speed when IMC-PI is used, as shown in Table 5-1. The ZN, TL and IMC-PI-IP perform better in restricting the speed although the wind speed falls near the low wind speed region, in which the control algorithm needs to be switched to the optimal rotor control target if a wind speed below 11 m/s is attained.

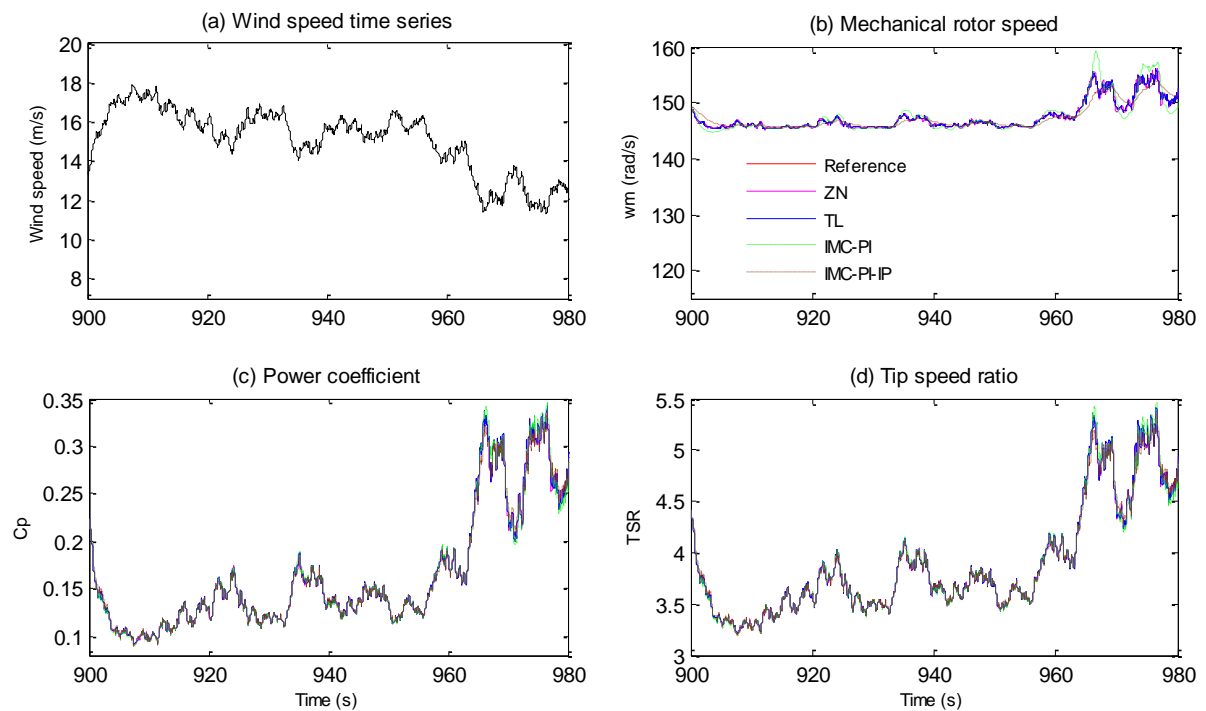


Figure 5-9 The behaviour of the SRVSWT in the high wind speed region: (a) the realistic wind speed profile, (b) the generator mechanical speed, (c) the power coefficient, and (d) the tip speed ratio

However, in this wind speed region,  $C_p$  is reduced lower than it does during the medium wind speed region, as shown in Figure 5-9(c) and Figure 5-8(c). The  $C_p$  can be reduced from 0.33 to approximately 0.1 when the wind speed increases from 11.5 m/s to 18 m/s. This is due to the controller's success in reducing the tip speed ratio, as shown in Figure 5-9(d) and Figure 5-8(d). The tip speed ratio also shows a similar trend in which all tunings successfully reduce the tip speed ratio value compared with the medium wind speed region, in which the maximum wind speed exceeds 11 m/s, as shown in Figure 5-9(d).

As an induction machine is designed to operate at a particular flux density, the limitation on the variation of the stator voltage, stator current and frequency that can be practically achieved must be considered and the operating stator voltage and the operating stator current must not exceed their rated values [142]. Using the same wind speed profile as depicted in Figure 5-6(a), the behaviours of the dq-stator voltage, the three phase stator voltage, the dq-stator current and the three phase stator current for a 1000 realistic wind speed time series are shown in Figure 5-10(a) to Figure 5-10(d).

Figure 5-10(b) and Figure 5-10(d) show that the stator voltage and stator current operate well within normal conditions and with their rated values when IMC-PI and IMC-PI-IP tunings are employed. The three-phase voltage is successfully controlled to operate below 415 volts, whereas the three-phase current operates below 60 amps. Figure 5-10(b) and Figure 5-10(d) also show that IMC-PI and IMC-PI-IP use a lower voltage and current compared with ZN and TL due to the tracking precision on the torque-current component in the inner loop and the phase control of the flux and torque for the current components.

To prevent flux saturation, the rotor flux d-axis is controlled at the rated flux, which causes the d-axis of the stator current component to be limited to a constant current. As shown in Figure 5-10(c), the stator current ( $i_{ds}$ ) can be operated constantly using the IMC design at the reference level with wind speed variations. Using the IMCs approach, the  $i_{ds}$  can function on the nominal level.

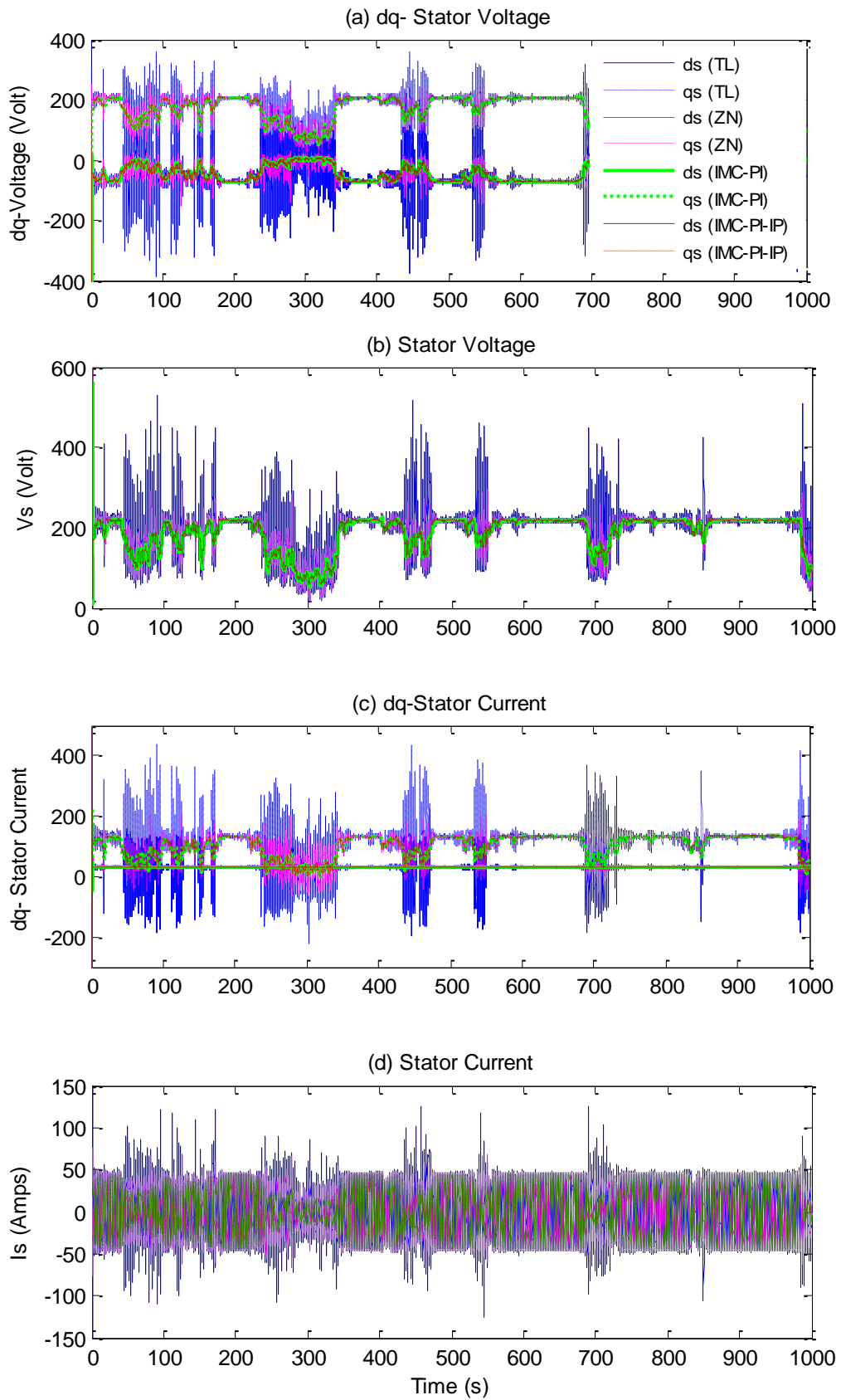


Figure 5-10 The behaviour of the SRVSWT in a realistic wind speed profile: (a) the dq-stator voltage, (b) the stator voltage, (c) the dq-stator current, and (d) the stator current

Meanwhile, from Figure 5-10(a) to 5-10(d), it can be seen that the TL presents poor results for the stator voltage and current signals. The signals are frequently dominated by excessive noise, in which high frequency vibrations can be observed particularly when turbine experiencing wind speeds lower than the rated wind speed, for instance at time 50s to 80s, 235s to 235s, 430s to 470s and 680s to 750s. This is presumably occurred because of the fast speed response offered by TL as shown by the rise time and settling time in Table 5-4. Too fast controller response could trigger signal pulsations or oscillations where the system becomes too sensitive to any actions. This oscillatory signal is also confirmed by the large TV values when TL is employed as shown in Table 5-1. Therefore, this also leads to the noise and spike signals of the stator voltages and currents.

In Figure 5-11, the evolution of the generated torque, the generated active power, the rotor flux and the stator angular frequency for the 1000-second realistic wind speed time series are shown. Using the IMC-PI and IMC-PI-IP approaches, the torque and power are acceptable at their rated levels of 190 N. m and 25 kW, respectively; they exhibit normal behaviour. Conversely, using TL and ZN, these responses exceed the rated level by several times; for example, at  $t = 50$  to 150 seconds and  $t = 250$  to 350 seconds, which occurs when the wind speeds change from one transition region to another transition region, using TL and ZN, the rotor flux cannot be easily maintained at the rated value. However, TL provides weaker flux control and a larger flux error along the simulation time. This finding is confirmed by the largest IAE values for the flux control compared with the remaining IAE values, as shown in Table 5-1. In addition, Figure 5-11(d) shows that the synchronous speed is controlled similar to the fixed speed, in which the speed operates around another base speed when TL is used; approximately 150 rad/s with 7% slip. Therefore, stressing more the wind turbine torque, in which this effect is shown in Figure 5-11(a). Thus, creates significant noise to the power output and this similar trend is also shown in the rotor flux signal when TL is used as depicted in Figure 5-11(b) and Figure 5-11(c), respectively.

In Figure 5-11(d), it shows that the stator angular frequency for all tuning types remains within the permitted range below 157.1 rad/s. In terms of synchronous speed, IMC-PI-IP follows the stator angular frequency reference better than ZN, TL and IMC-PI. Using IMC-PI-IP, the synchronous speed works as expected, in which this behaviour shows the real situation that should occur when the variable speed strategy is applied in the proposed SRVSWT system. Good flux response as exhibited in Figure 5-11(c) is achieved when this tuning rule is used, in which the rotor flux can be controlled to work at the constant level with very minimum percentage error (approximately 1.5%). Hence, the generated power can be controlled smoothly between zero to 25 kW. IMC-PI and ZN also show similar trends, but these signals look like rather influenced by noise, particularly during frequent speed changes; for example at time,  $t = 230$  to 330 seconds. However, noise is more dominated by ZN compared to IMC-PI, in which the rotor flux is slightly weakened from its rated level. The error up to 17.5 % was created during this time period, as can be seen in Figure 5-11(c). Therefore, torque and power signals are more dominated by the noise, as depicted in Figure 5-11(a) and Figure 5-11(b).

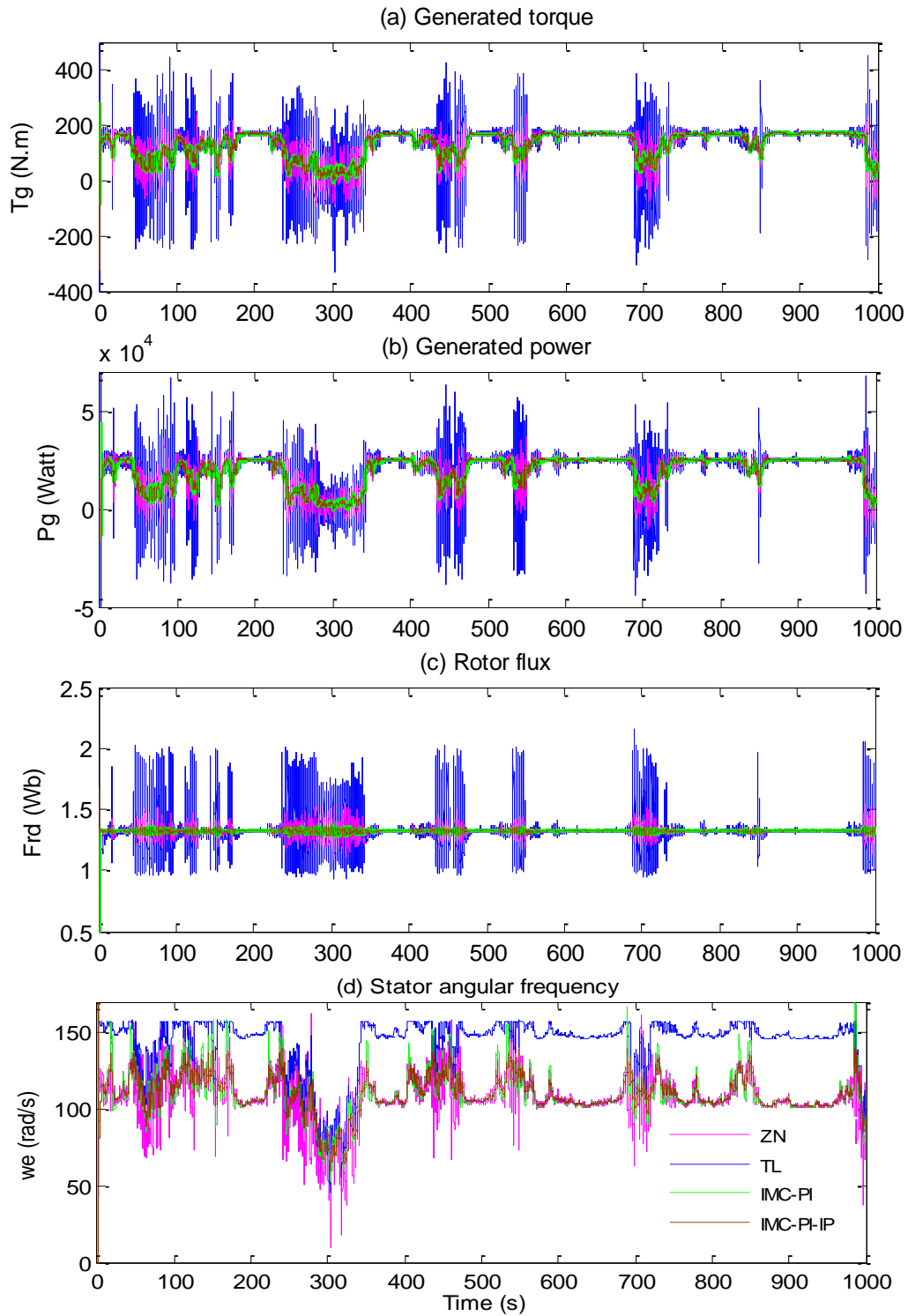


Figure 5-11 The behaviour of the SRVSWT in a realistic wind speed profile: (a) the generated torque , (b) the generated power, (c) the rotor flux, and (d) the stator angular frequency

The results of the ‘torque-wind speed’ curve of the SRVSWT are depicted in Figure 5-12. The difference in the efficiency of the control action is clear. Using ZN and TL, the electromagnetic torque scatters exceeded the rated torque level during low and medium wind speeds. Additionally, the torque variations are unacceptable where the electromagnetic torque can assume opposite sign values where the machine can operate in the motoring regime when ZN or TL is used, particularly at low wind speeds. Although this situation is not shown, the torque is observed to pass below the zero level of the y-axis numerous times when the wind speed ranges from 3.7 m/s to 9 m/s, as shown in Figure 5-12(a) and Figure 5-12(b). These conditions produce abnormal regimes of the electrical signal. Using IMC-PI and IMC-PI-IP, the closed-loop system operates in normal condition along the wind speed variations. However, the system performs better in high winds compared with low winds; for instance, above 12 m/s, particularly when IMC-PI-IP is used. However, during low and medium wind speeds, the torque can also be satisfactorily managed between zero and the maximum permitted torque level, as shown in Figure 5-12(c) and Figure 5-12(d).

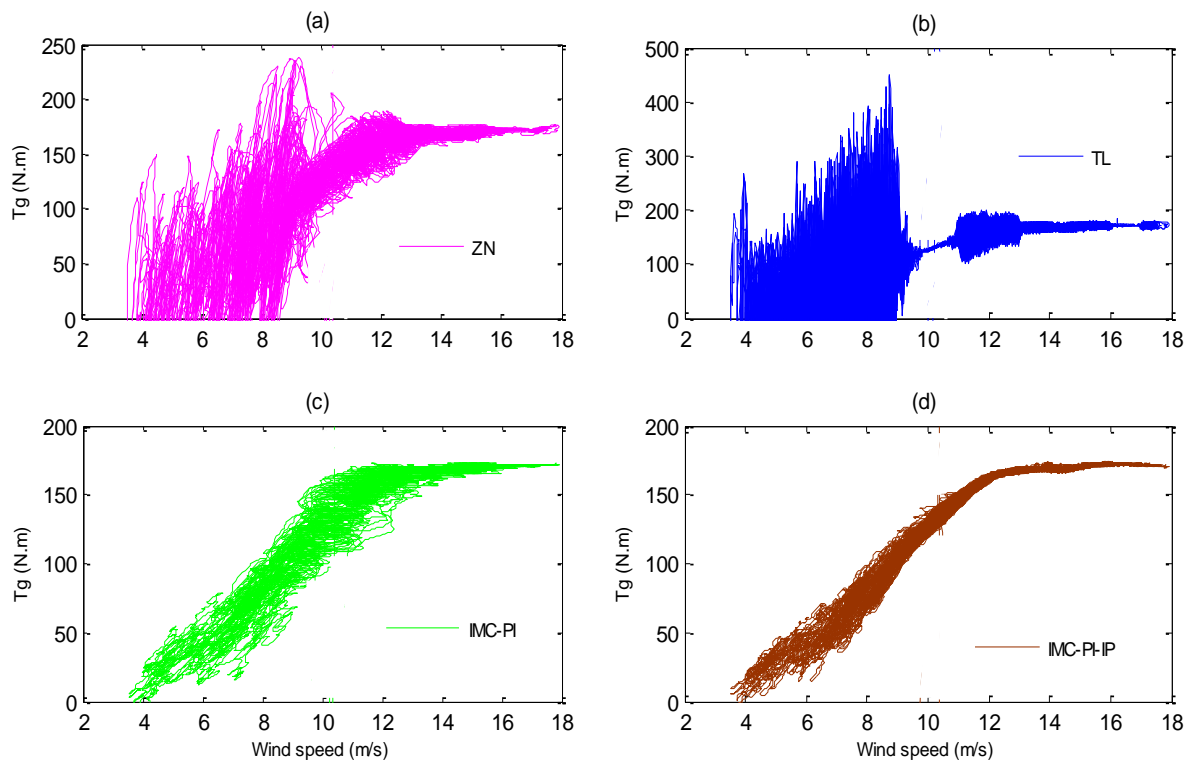


Figure 5-12 Generated torque versus wind speed

The results of the ‘power-wind speed’ curve of the SRVSWT are shown in Figure 5-13. If ZN or TL is imposed, the power variations become unacceptable, which produces abnormal regimes of the power flow. This situation occurs for low wind speeds and some medium wind speeds, as shown in Figure 5-13(a) and Figure 5-13(b). In certain conditions, the power tends to be absorbed from the grid instead of supplied to the main grid. The power also significantly goes above the rated level. For example, a maximum power excursion of 37 kW can be attained using ZN, whereas the power excursion can exceed 60 kW for a wind speed of 9 m/s. During this time, the control goal changes from optimal rotor control to speed constant control. During this transition regime, controller switching is typically employed to enable operation of the turbines at the corresponding operating points.

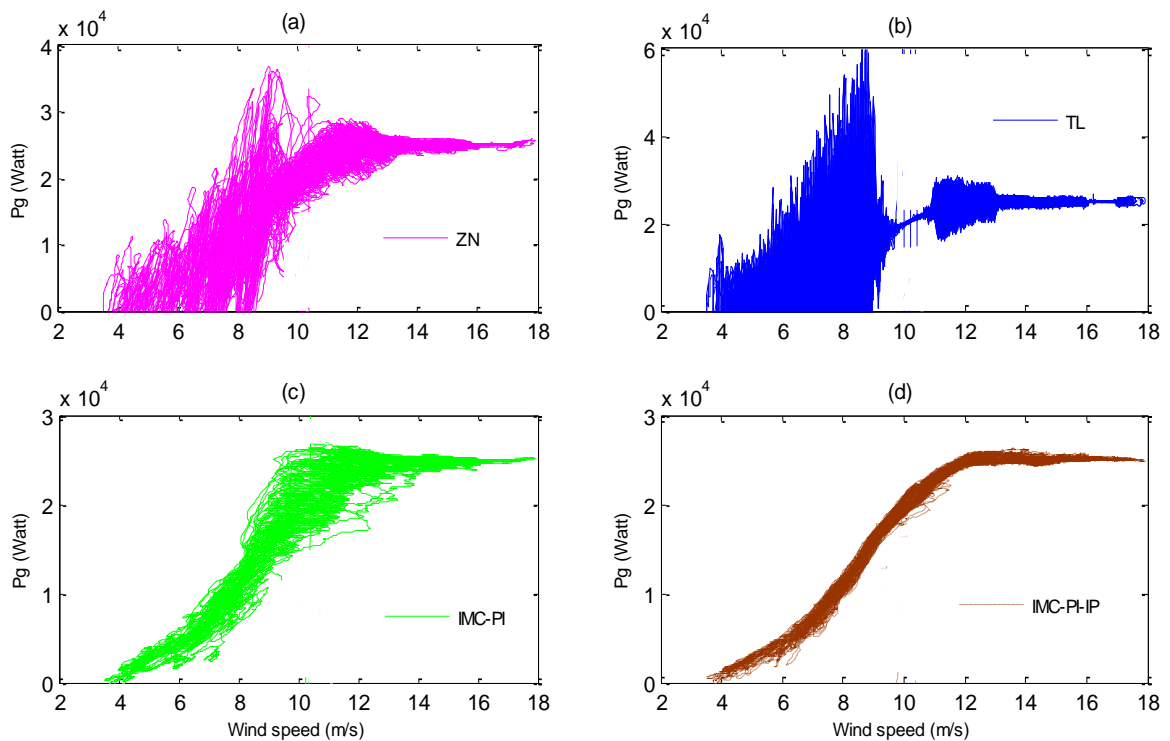


Figure 5-13 Generated power versus wind speed

Figure 5-13(c) and Figure 5-13(d) show that the IMC-PI, which is similar to the IMC-PI-IP, manages to limit the energy extraction around the rated power of 25 kW in the high wind speed region. The IMC design results in significant improvement of power control compared with ZN and TL. IMC-PI-IP exhibits

smoother power control along the wind speed variations from the cut-in to cut-out wind speed. The use of separate integral and proportional terms controlled structures eliminate the oscillatory nature of the system's response at low and medium wind speeds. Power excursion between 8 m/s to 14 m/s from IMC-PI is improved when IMC-PI-IP is used. The speed restriction is indirectly achieved in the presence of persistence disturbances. The excursions of the operating points from one state to another state do not cause considerable power loss during rapid changes in wind speed. This is because the single proportional term was applied to the feedback signal; meanwhile the single integral term was applied to the cumulative errors between the reference signal and the feedback signal. See Figure 4-10. Subtracting the proportional output from the integral output simplifies the torque control action and reduces the proportional kick when the reference signals change abruptly.

The 'power-angular mechanical rotor speed' curve is shown in Figure 5-14.

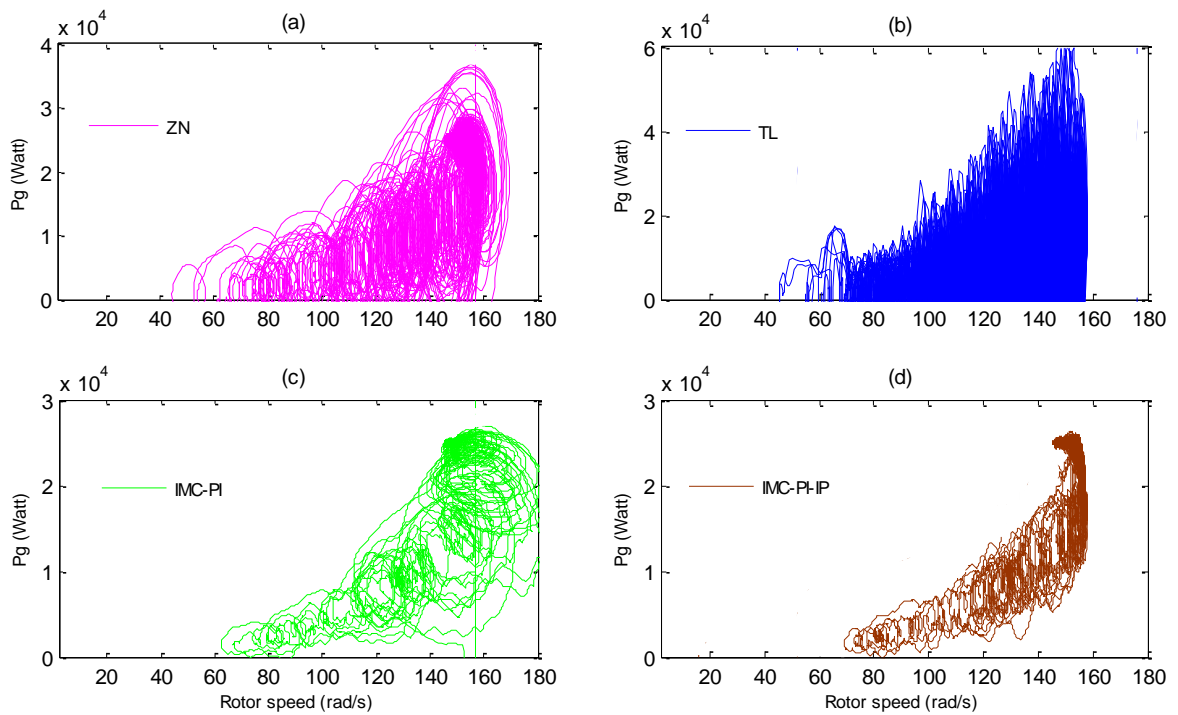


Figure 5-14 Generated power versus mechanical rotor speed

Figure 5-14(c) clearly shows that the generator operates beyond the maximum permitted constant speed level when IMC-PI is used (greater than 157.1 rad/s). ZN also shows a similar trend in which ZN fails to restrain the generator from overspeeding to a maximum speed of 170 rad/s, as illustrated in Figure 5-14(a). The generated power cannot be controlled below the maximum level. The power peaks are high and on the order of 160% of the nominal value. Of all the controllers, IMC-PI-IP exhibits the best precision in maintaining the mechanical rotor speed at its reference, followed by TL as TL can limit the speed around the constant value despite an abnormal power excursion. The TL exhibits the worst performance in power limitation due to the high amplification of the noise produced in the power signal. Figure 5-14(b) shows that the power goes much higher than the maximum power of 30 kW. The speed can be better controlled using IMC-PI-IP at lower generator speeds and at low wind speeds compared with ZN, TL and IMC-PI.

From the results discussed in Section 5.2, the IMC design offers better control compared with the design of ZN and TL as this design offers more robust control with low maximum sensitivity  $M_s$ . Greater stability of the phase margin also obtained. Besides, IMCs provide better input and output performance with lower values of IAE and TV for the step change and less affected by disturbance. With small values of TV, the manipulated input signals are not influenced/dominated by the oscillations; however, with smaller IAE, error can be reduced.

Among the IMCs, the IMC-PI-IP offers better control compared with IMC-PI for the proposed SRVSWT system as no overshoot of speed control is produced and it yields a faster and smaller overshoot or oscillation on the rotor flux and current torque control. Although slower speed responses were observed for IMC-PI-IP, this tuning rule does not exhibit the robustness and stability problems for the SRVSWT system. This speed response helps the turbine to prevent the problem of overspeeding during abrupt input changes. The excursion of the electromagnetic torque and the generated power that produces abnormal behaviour, such as exceeding the maximum rated level and absorbing power from the grid during the operation can also be avoided. Thus, the torque and power are better controlled and are free from noise due to the speed tracking

response, flux maintenance, precision of current-torque control and lower control effort. With less control effort, the control inputs ( $v_{ds}$  and  $v_{qs}$ ) perform adequately for the extensive wind speed range.

### 5.3 Results for the Proposed Control Strategies during Intermediate Load (IL)

To assess the performance of the SRVSWT in the IL region, the performance comparison of two strategies (CS and MoPT) that were applied to produce smoother power control during region transition is shown. For the CS, this strategy was used during the simulation that was presented in the preceding sections. In Figure 5-15, the comparison strategies that were proposed during the transition region from low winds to high winds are depicted. A brief explanation of these strategies is provided in Section 1.2.2 and Section 2.2.1.2.

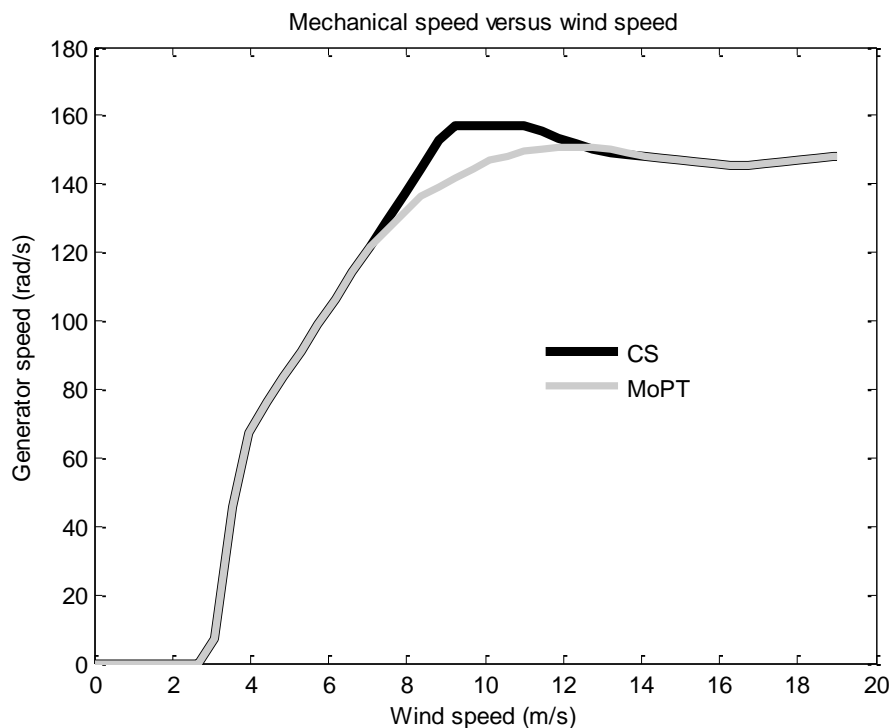


Figure 5-15 The mechanical rotor speed strategies: constant speed (CS) and modified power tracking (MoPT)

The power and torque evolutions of the proposed SRVSWT system, when the CS strategy and MoPT strategy, respectively, are applied, are shown in Figure 5-16 and Figure 5-17.

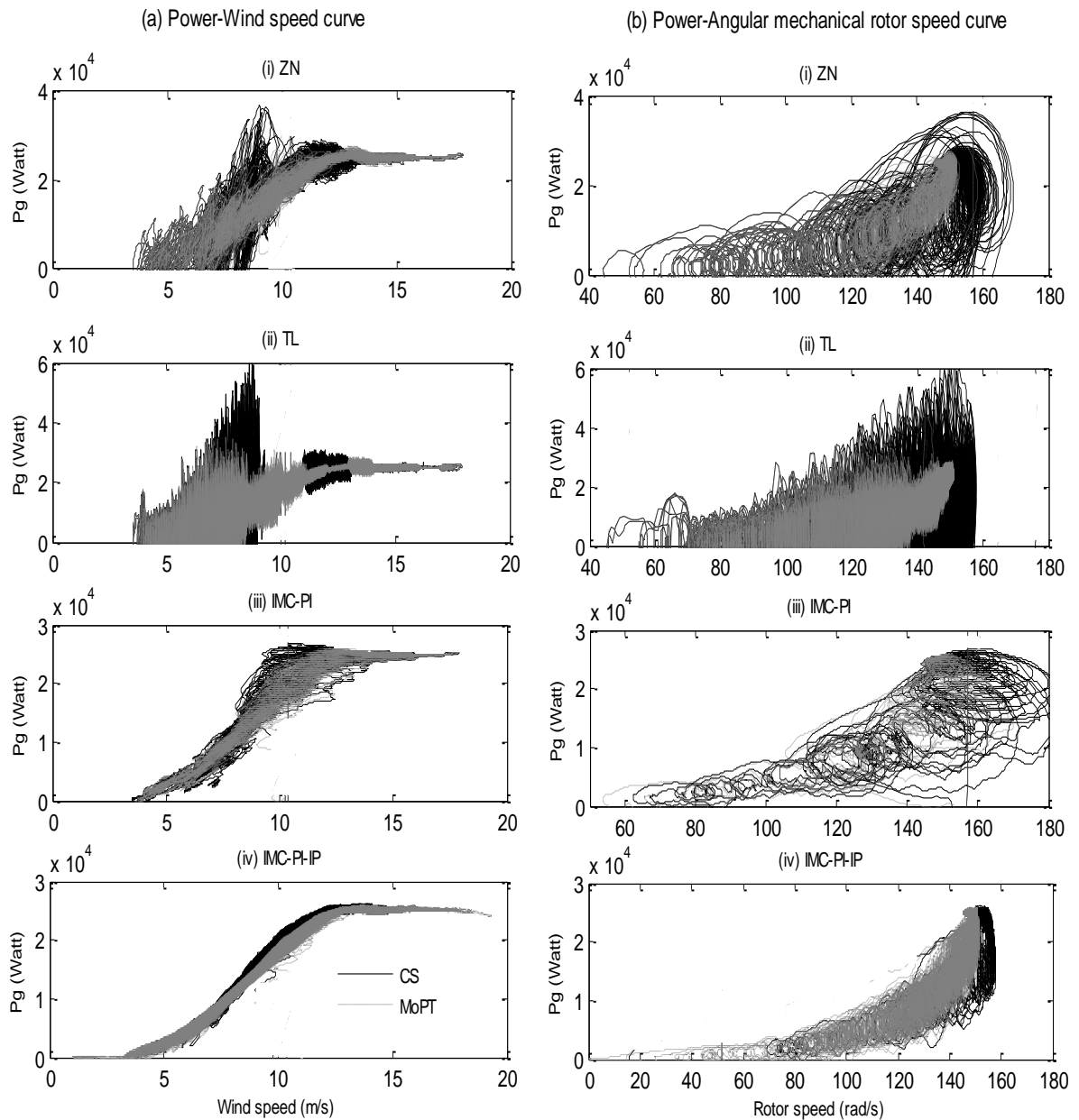


Figure 5-16 The control performance of the SRVSWT system using CS and MoPT strategies: (a) power-wind speed curve and (b) power-angular mechanical rotor speed curve

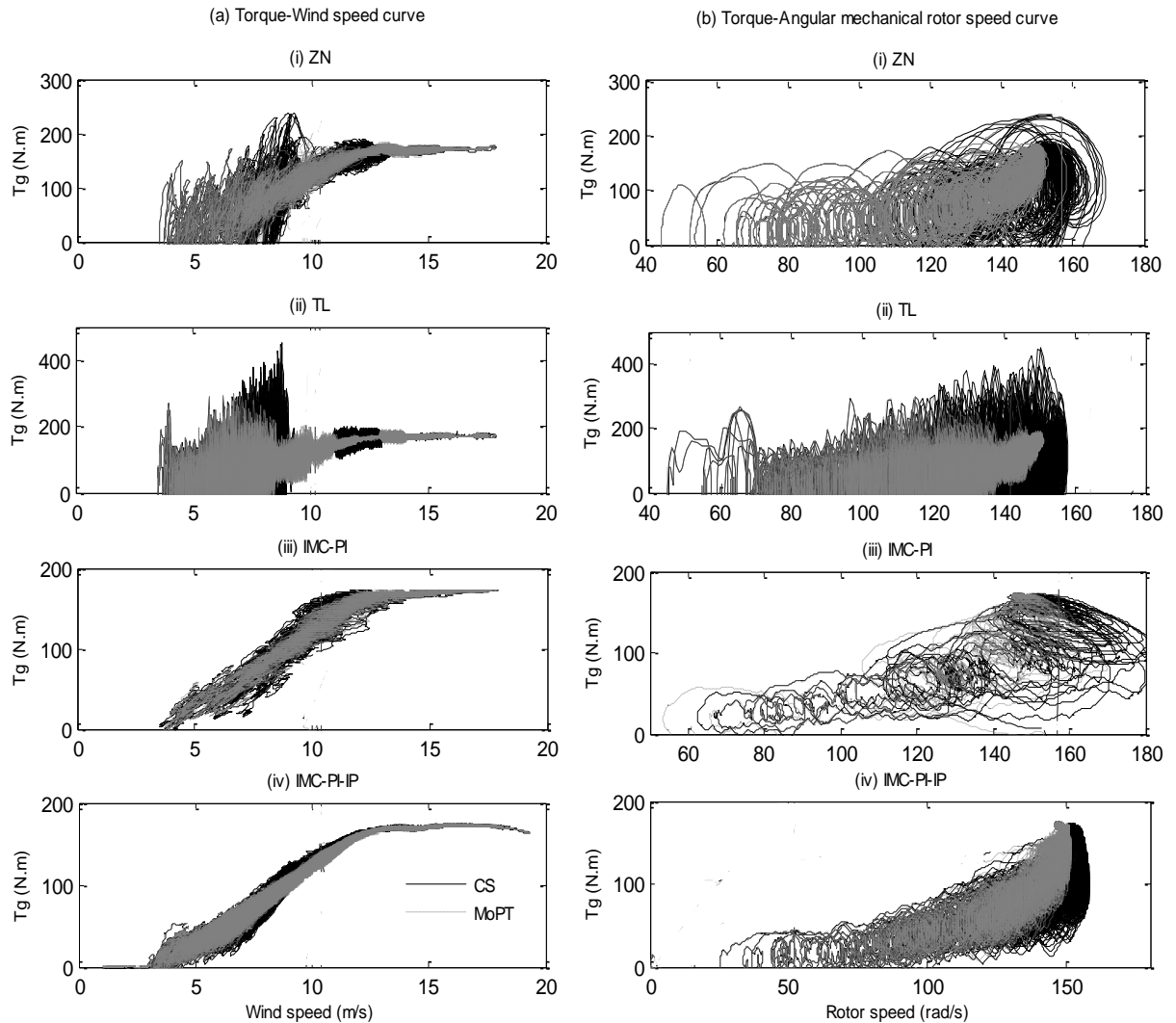


Figure 5-17 The control performance of the SRVSWT system using the CS and MoPT strategies: (a) torque-wind speed curve and (b) torque-angular mechanical rotor speed curve

Figure 5-16(a) shows that the power efficiency is reduced for medium winds (from 8 m/s to 15 m/s) with MoPT strategy compared with the CS strategy. Using ZN, the maximum power peak during stall conditions can be reduced from 37 kW to 23 kW, whereas the excessive power can be reduced more than 50% from its maximum peak using TL, as depicted in Figure 5-16(a)(i) and Figure 5-16(a)(ii). Using the IMC design, the maximum achieved power is reduced from 5% to 9%, as shown in Figure 5-16(a)(iii) and Figure 5-16(a)(iv). Figure 5-16(b) reveals that the strategy that incorporates MoPT design principles

results in an acceptable speed limit below the rated speed level in the IL region, if the use of ZN, TL or IMCs tuning is disregarded. Figure 5-17(b) also yields similar conclusions regarding the success of this limitation. Consequently, the stress torque can be reduced significantly as torque varies in a lower speed range during the transition from the PL to the IL region, as shown in Figure 5-17(a). Therefore, power can also be controlled but with power losses.

Based on the data shown in this section, for the power control strategy during medium wind velocities or in the IL region, the excessive power can be significantly reduced when MoPT is applied to replace the CS strategy, particularly when ZN and TL are used. Although IMC-PI prevents power excursion by exceeding the rated level when MoPT is applied, which replaces the CS strategy, no significant improvement is shown when IMC-PI is used for the IMC design. With the IMC-PI-IP tuning rule, the CS strategy generates better power extraction than MoPT. Although the torque stress is reduced with MoPT, the turbine continues to operate in normal conditions in which the stress level or rated level (in terms of power, torque and speed) is managed securely with the CS strategy and the IMC-PI-IP tuning rule. The power is successfully controlled for an extensive range of wind speed variations.

#### **5.4 Results for the Indirect Vector Control (IVC) and Sensorless Indirect Vector Control (SLIVC) Model Algorithms**

This section discusses the comparison results for the SRVSWT model with the proposed IVC model algorithm (that was presented in the preceding sections) and the SLIVC model algorithm, in which the controllers involved are tuned with the best tuning rule as revealed in the preceding sections. For the controller tuning method, only IMC design was considered as this tuning provides satisfactory performance measures. For an equivalent comparison, all model algorithms were tested using the 1000-seconds of realistic wind speed time series, as depicted in Figure 5-6(a). For this comparison, only the power-wind speed curve is shown. For the SLIVC model with the application of IMC-PI and

IMC-PI-IP tuning rules, the ‘power-wind speed’ response of the SRVSWT system is shown in Figure 5-18.

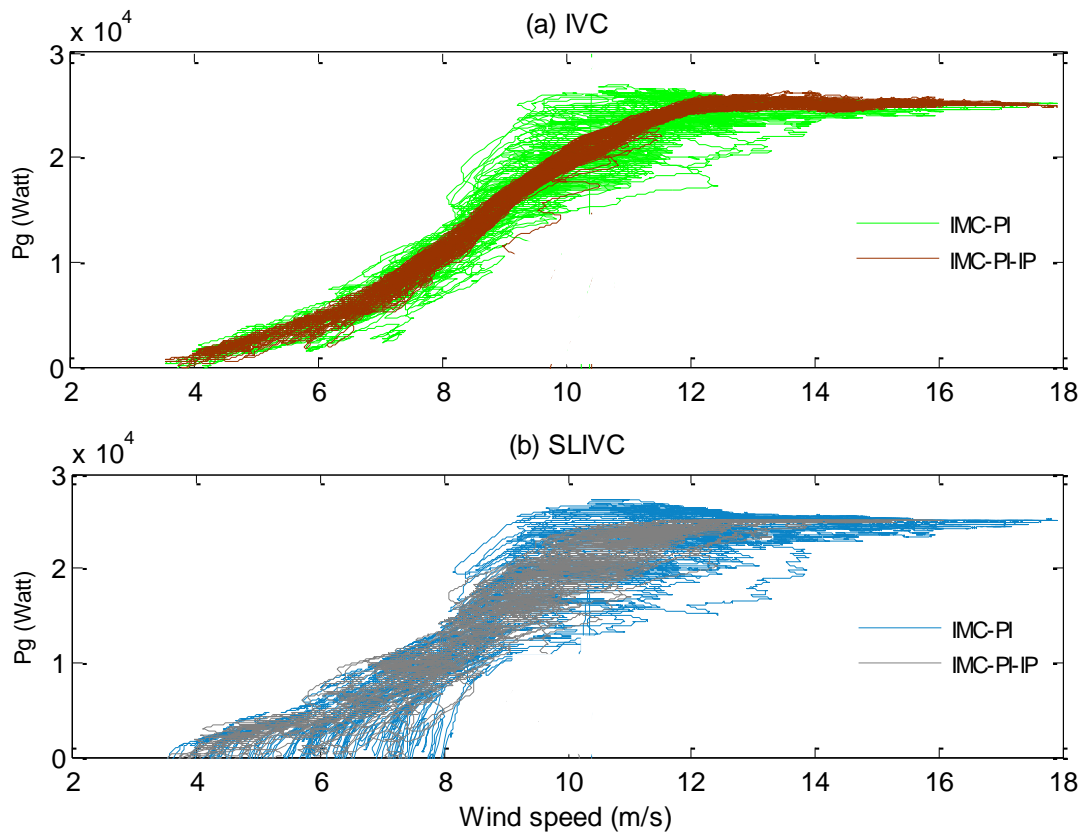


Figure 5-18 ‘Power-wind speed’ curve: (a) IVC and (b) SLIVC

Figure 5-18 shows that the IMC-PI-IP control tracks the power curve better than IMC-PI, which corresponds with the previous results for the IVC and the SLIVC models. Substantial improvement is obtained by the IMC-PI-IP compared with the IMC-PI, particularly for medium winds (8 to 14 m/s) in which the turbine experiences stall conditions where power is restrained from following the maximum power locus. In this condition, the electromagnetic torque can be better controlled when the transient peak of the torque-current component is successfully controlled through greater rising and settling times in the speed control (due to single integral control as shown in Figure 4-10). However, when the performances of the two different control algorithms are compared when IMCs tuning rule is used, as shown in Figure 5-19, the SLIVC

model algorithm exhibits poor performance compared with the IVC model algorithm.

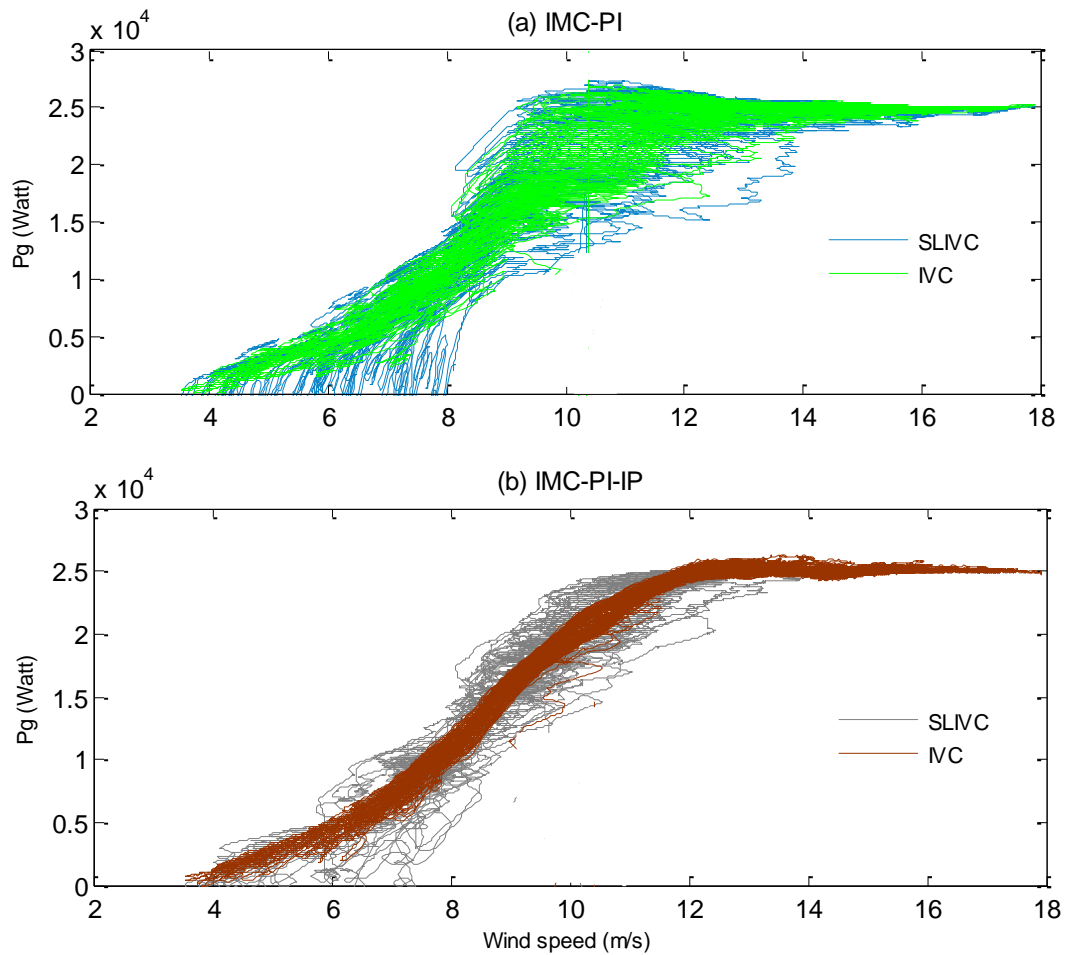


Figure 5-19 'Power-wind speed' curve: (a) IMC-PI and (b) IMC-PI-IP

When the SLIVC algorithm is considered, as shown in Figure 5-19(a), tracking maximum power locus at low winds may not be attainable when IMC-PI is used. With IMC-PI-IP tuning in the SLIVC model, the power can be controlled only slightly better and motoring conditions can be prevented as the SLIVC model only uses one controller: speed control. When the IVC model algorithm is used to control the proposed SRVSWT system, smoother power control involving maximum power control (at low winds), constant speed control (at medium winds) and closer tracking of the restricted power (at high winds) is obtainable, regardless of whether IMC-PI-IP or IMC-PI is employed. However, the IVC model

algorithm with the IMC-PI-IP tuning rule yields the best performance. Figure 5-19(b) shows that the IMC-PI-IP was required as it improved the power control along the wind speed variations by narrowing the power scatters by one-third, particularly from 3.7 m/s to 14 m/s. This outcome significantly lessens the stress on the turbine components, such as the gearbox, the shafts, and the generator.

## 5.5 Chapter Summary

The simulation results for the SRVSWT system when applied to the step input and the realistic wind speed profile are presented in this chapter. Four types of controller tuning rules that employ the IVC model algorithm have been compared: the ZN, TL, IMC-PI and IMC-PI-IP. For the entire wind speed region, the IMC tuning rules resulted in better control performance compared with ZN and TL. The IMC design provides the best robustness, and the input and output performance measures provide a larger stability phase margin due to the lower values of  $M_s$ , IAE and TV. However, IMC-PI-IP provides the most convincing approach for controlling the proposed SRVSWT system, in which no overshoot of speed control is produced, as it results in the fastest and smallest overshoot/oscillation on the flux and the current producing torque control.

To suppress the power peaks during region transition, the proposed MoPT strategy successfully suppressed the power excursion from exceeding the rated level during early-stall in the IL region, regardless of the tuning type. However, for the MoPT strategy, no significant difference among the different IMCs tuning rule was observed. When the CS strategy with the IMC-PI-IP tuning is used, the power excursions can be avoided naturally, in fact, this gave the smoothest power extraction under normal conditions without reducing the power production as happened when MoPT was used. The IVC model algorithm is significantly more reliable than the SLIVC model algorithm for controlling the SRVSWT system.

## **6 Conclusions, Contributions to Knowledge and Suggestions for Future Studies**

### **6.1 Chapter Overview**

This chapter completes the thesis by providing conclusions, a summary of the contributions to the field and suggestions for future studies.

### **6.2 Conclusions**

This study presented simulations of the working principle of a stall-regulated variable-speed wind turbine system. The study looked at a squirrel-cage induction machine within a 25 kW two-bladed wind turbine.

The objective of this research was to study the application of internal model control (IMC) to the squirrel-cage induction generator (SCIG) of a stall-regulated variable-speed wind turbine (SRVSWT) system. It involved the estimation of proportional-integral (PI) and integral-proportional (IP) parameter values, which tracks the angular mechanical generator speed, the stator-current producing torque and the rotor flux.

Prior to executing feasibility and reliability studies of the variable-speed application on the stall-regulated wind turbine (SRWT), the validation study of the SRWT system performance was performed by computer simulation with fixed speeds prior to using the SRWT model for variable speed application, which is referred to as the stall-regulated variable-speed wind-turbine (SRVSWT). After applying the modified dynamic stall curve to the SRWT model, the power versus wind speed curve that was created from the study resembles the curve that was provided by the turbine manufacturer and obtained from the measurement field test. This validity study increases the confidence level of the SRWT model that will be used for the performance study of the SRVSWT system.

The indirect vector control (IVC) approach was adopted to enable faster responses and the decoupling of torque and flux control in the closed-loop feedback system. This method employs three sensors to determine the actual existing speed, current and flux. The internal model control (IMC) approach is relatively easy, simple and robust. This approach is applicable to the estimation of the PI parameter values. An estimation parameter tuning rule of the IVC model algorithm, which is based on this approach and referred to as the IMC-PI and IMC-PI-IP, were proposed. The PI controller used in the IMC-PI and the IMC-PI-IP approaches was based on the standard IMC design using the first-order plus time delay (FOPTD) model of the SCIG. The IP controller design was based on the sustained periodic oscillation during searching the integral (I) parameter gain and used the approach of the increment of gain from lower to higher gain to search the proportional parameter gain (with consideration of the percent overshoot below 20%). This IP control is designed for the IVC model algorithm to overcome power dispersion or scatter problems of the SRVSWT system operation during stall conditions, in which excessive power needs to be restricted from reaching or exceeding the generator's rated power, for smoother power tracking and lower torque stress. As IP control ensures an attenuated rotor speed, overspeeding or underspeeding can be prevented during abrupt changes in wind speed e.g., direction or velocity.

The design of the PI and IP controller was based on the fourth-order model of the SCIG that is directly coupled to a full-rated power converter through the machine stator, whereas the machine rotor is connected to the turbine rotor via a gearbox. The PI controller was directly applied to the SRVSWT system in the rotor flux and current-producing torque controllers, whereas the IP controller is applied in the speed controller. During PI parameter estimation, the input/output pairing approach with the relative gain array (RGA) method simplifies the controller design process in the MIMO model. As a result, less time is required during controller design. The employed cascade design, which involves the current controller as the inner loop and the speed controller as the outer loop ensures faster current tracking and a smaller overshoot/oscillation speed signal.

The effectiveness of the four tuning rules used to obtain the proportional and integral values—the Ziegler-Nichols (ZN), Tyreus-Luyben (TL), internal model control-based PI control (IMC-PI) and internal model control-based PI and IP control (IMC-PI-IP) methods—were compared. For the entire wind speed region, the IMC-based tuning rule provides better control performance than ZN and TL. IMC-based design provides the best robustness and input and output performance measures due to its lower values of  $M_s$ , IAE and TV and a larger stability phase margin. For a SRVSWT system operation from cut-in to cut-out wind speed with the IVC model, the IMC-PI-IP tuning rule exhibited the best performance, whereas the IMC-PI tuning rule exhibited the second-best performance as the IMC-PI tuning performance for the SRVSWT was lower than the IMC-PI-IP tuning performance at medium winds, particularly during region transition from the partial load (PL) region to the intermediate load (IL) region. Due to the IP parameters in the speed controller, the turbine/generator speed was reduced prior to the current/torque excursions/surges to mitigate the effect of abrupt changes in wind speeds and the load disturbances. Therefore, the IP speed controller produced smoothed and improved power tracking performance for the SRVSWT by reducing the dispersion of power by one-third during medium winds and improved or almost retained its performance during low winds compared with the performance of the SRVSWT with PI speed control. IMC-PI-IP has also worked well during high winds.

The constant speed (CS) control goal that was set for wind speeds in the intermediate load region was changed to the modified power tracking (MoPT) design strategy in the IVC model algorithm, in which the objective was to suppress the power peaks and minimise the stress torque on the drive train during early stall conditions. Power peaks during the wind region transition were successfully suppressed below the rated level when the MoPT was applied at a several operating points at the intermediate load region. However, the CS strategy produces higher energy capture than the MoPT strategy and generates a curve that resembles the ideal power curve. In fact, the power/torque/speed can be controlled without exceeding the rated level. This finding shows that a SRVSWT system that employs the IVC model algorithm with the IMC-PI-IP tuning rule considering with the CS strategy is more profitable than a SRVSWT with the

MoPT strategy. Thus, a longer life span and lower maintenance cost can be maintained by this wind turbine designed by the manufacturer due to the smoother power/torque control along the wind speed variations from low to high winds.

When the same IMC-PI-IP tuning approach was applied to the speed controller in the sensorless indirect vector control (SLIVC) model algorithm, both the IVC and SLIVC model algorithm exhibited equally satisfactory performance in the power limitation region (FL region). During low and medium winds, the IMC-PI-IP tuning performance for the SLIVC model algorithm of a SRVSWT system was less effective than the IMC-PI-IP tuning performance for the IVC model due to the degradation of power capture performance and excessive scatter power when the SLIVC model algorithm was used. This finding shows that the turbine fails to track the maximum power locus during low wind speeds when the SLIVC model is used. When the IMC-PI tuning method was applied to the same SLIVC model algorithm of a SRVSWT system, no significant difference was observed between the performance of the IMC-PI and the performance of the IMC-PI-IP.

These results conclude that a reasonable number of sensors are required to ensure better power control/tracking. The right placement of the P and I controller in the model algorithm also enables a smoother and slower speed response to the SCIG that is directly coupled to the fully-rated power converter of a SRVSWT system. For instance, by applying a single proportional term to the feedback signal and by applying a single integral term to the cumulative errors between the reference signal and feedback signal, a more robust speed controller can be obtained. This is necessary, particularly when abrupt changes occur when winds change their velocities or directions or the control goal is switched from one region to another region. A reasonable number of sensors would allow smoother power control over a large range of wind speeds. Additionally, the IVC model algorithm is more reliable than the SLIVC model algorithm in controlling the SRVSWT system.

Therefore, the contributions of this research can be concluded as follows:

1. Estimation of the modified tip speed ratio ( $\lambda_{stall} = \frac{\omega R + (\Delta\omega_{stall} R_{stall})}{U}$ ) of the dynamic stall model of the fixed-speed stall-regulated wind-turbine (SRWT) system.
2. Validation of the modified dynamic stall curve in the SRWT system by computer simulation. The comparison of the power curve performance has been executed on the SRWT system when the frequency is set to 50 Hz (from manufacturer data) and when the frequency is set by the wind turbine owner at 43.5 Hz (from field measurement).
3. Estimation of the proportional-integral (PI) parameter values of the squirrel-cage generator system of the SRVSWT system for the PI flux controller, the PI current controller and the PI speed controller using the IMC approach based on the first-order plus time delay (FOPTD) model.
4. The new design method of the estimation of the integral-proportional (IP) parameter values of the squirrel-cage generator system of the SRVSWT system for the speed controller.
5. Use of the PI and IP parameters estimates (in the flux, the current and the speed controllers, respectively) in the IVC model algorithm of the induction generator of the SRVSWT system.
6. Modified power tracking (MoPT) strategy at medium wind speeds has been proposed and the success of its reduction peak power has been proven. Additionally, the performance of the MoPT strategy has been compared with the used constant speed (CS) strategy for this wind speed region.
7. Validation of the IVC model algorithm performance using the IMC design method with two PI controllers (for the flux and the current controllers) and one IP controller (for the speed controller) by extensive computer simulation and the evaluation of the IMC design performance due to the nonlinearity of the profiled wind speed. Additionally, the performance of the validated IVC model has been compared with the sensorless indirect vector control (SLIVC) model algorithm based on the power-wind speed curve.

Based on these contributions, the proposed technology (SRVSWT system) positively impacts the development of wind turbine technology enhancements. This study numerically demonstrates that the proposed SRVSWT system is feasible for future implementation. From the power-wind speed curve profile that was demonstrated by the SRVSWT system when the IVC model algorithm with IMC-PI-IP tuning rule is used, the power-wind speed curve that resembles the ideal power-wind speed curve was produced. This finding indicates that the simplest variable-speed wind turbine technology/configuration using a stall-blade is commercially feasible when coupled to the full-rated power converter. For this configuration, a full-rated power converter handles all supplied power to the utility grid, which differ from the wind turbine that uses pitching-blade technology, in which the doubly fed induction generator (DFIG) is usually employed. This DFIG uses a partial-rated converter, in which only one-third of the generator size power is available and managed. In addition to the cost of the electronics mechanism for the pitching blade, this configuration can be very expensive due to the cost of the slips rings, brushes and maintenance. The findings in this study indicate that the SRVSWT technology, which uses a simple and low-cost variable speed configuration with less maintenance costs, exhibits significant potential for commercialisation. Previous constraints to use full-rated power converter is due to the availability of low-cost large power converters and its efficiency. The recent rapid development of power converter technology has enabled inexpensive large power converters and higher efficiency. Due to the advantage of extensive speed control, this technology can be applied to a large-size wind farm; for instance, the offshore wind turbine farm, which usually uses a large blade diameter, generator capacity and power converter. At this time, it is useful to test the system characteristics in a small-sized turbine (as considered in this study) before scaling up the turbine to a larger system to eliminate risks and also learn experience from the small-scaled design. Not only time can be saved, but also costs can be minimised. Therefore, the application of the proposed SRVSWT system is projected to be more beneficial as the power can be managed 100% (passes through the converter) and a larger speed range is available when a fully-rated power converter is connected between the generator and the grid. A smaller generator size than that required if a partial-rated or half-rated

converter is used can be offered in the proposed system to generate power of similar size. The proposed system also enables the capital and maintenance costs to be significantly reduced, the complex electronic actuators systems can be removed and the power-wind speed curve resembling an ideal power curve is achieved. Besides that, a system configuration that provides safer and convincing power management in which the frequency of mechanical shocks due to the faults/disturbances from the grid can be reduced can be achieved.

As this is a feasibility study to investigate the feasibility of IMC-based PI and IP controllers for the squirrel-cage induction generator (SCIG) system using the indirect vector control (IVC) model algorithm of a stall-regulated variable-speed wind-turbine (SRVSWT) system, practical implementation will require other issues to be addressed, such as the power converter technology or the design and safety features.

### 6.3 Suggestions for Future Studies

Several opportunities can be delivered from this research study for future works:

1. **Simulation model:** For the purpose of simplicity, some parameters have been omitted in the sub-models. For an example, in the drivetrain model, only rotor and generator inertias have been considered in Equation (3-15) and (3-16). For a more detailed model, study can be investigated further by considering the stiffness and damping in the equations. Also, the developed model could be further studied by considering two- or additional- mass in the drive train model, with nonlinearities included in the system. This study has only considered the single mass of the drive train model. Besides, an additional of power converter model may be included in the modeling system in the future work where the control side of the grid side converter can be comprised. Also, with grid side converter, the issues of active and reactive power control, the power quality issue, the network faults and the complete operational issues can be investigated while considering the total potential of SRVSWT.
2. **IMC-PI-IP controller:** During IMC designing, the first-order filter has been used in the second step as written in Equation (4-24) on page 132. Another

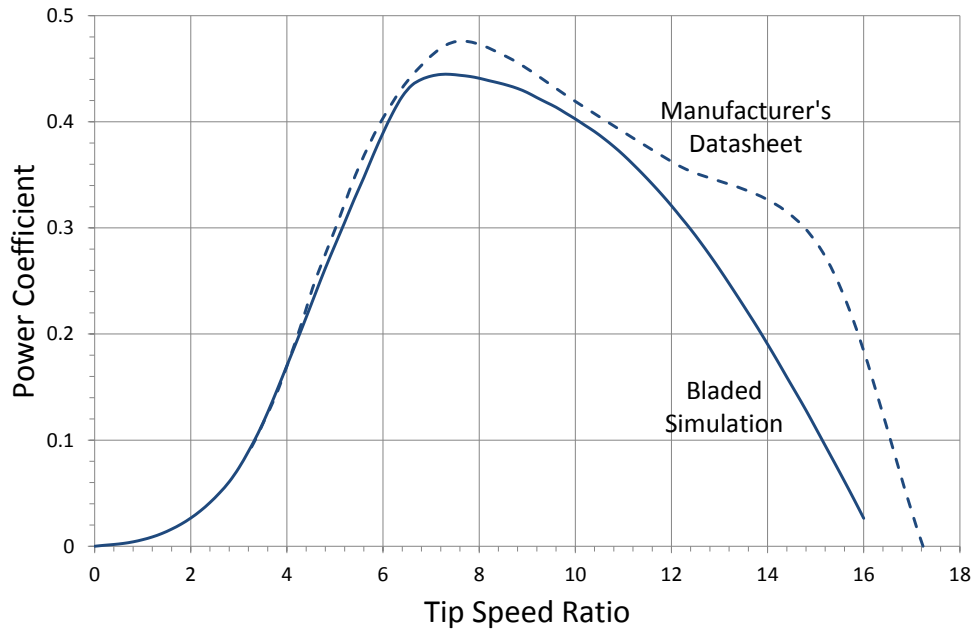
approach that possibly could improve in the estimation of PI parameter values based on the IMC design in the future is by use the higher-order filter of  $\frac{1}{(s+\lambda)^n}$  e.g.,  $n > 1$ . Also, in this study, to estimate the PI parameter values, the first-order plus time delay (FOPTD) approach was used. In the future, the effectiveness of the proposed SRVSWT system could be tested and compared with the second-order plus time delay (SOPTD) approach. Besides, IMC-PID based with filter also could be investigated further replacing the IMC-PI and IMC-PI-IP controllers. Application of other control algorithms in the SRVSWT system e.g., gain-scheduling approach, genetic algorithm, and detailed/advanced SLIVC model algorithm.

3. **IP Parameter Tuning Method:** There is no explicit tuning method has been proposed in tuning the IP controller. This is still an open issue. The proposed method shows good tracking properties particularly for the speed controller. It showed, by simulation, the power peaking during early rated wind speed was improved by smoothing the generator speed response. The results, however, could be further be investigated by performing some possible analytical analysis of how system stability can be improved. Improvement during tuning also possibly could be achieved by considering several switching methods with an IP controller e.g., bumpless switch.
4. **Performance analysis:** Performance analysis has been measured using sensitivity function. In the future, performance analysis can be confirmed by performing frequency response analysis where the stability and robustness could be measured using details of gain and phase margins. Besides, the output and input performance of the step change also has been performed to measure system performance. In this study, IAE was used to measure output performance meanwhile TV value was used to measure input performance, as explained in Section 4.5.2. The results for the output performance, however, could be further be explored by considering other measurement approach such as integral-square error (ISE), least-square error (LSE) and least-absolute error (LAE).
5. **Validation on a real machine:** The identification algorithms and controllers executed in this simulation studies can be tested and validated in the real SRVSWT plant.

## APPENDIXES

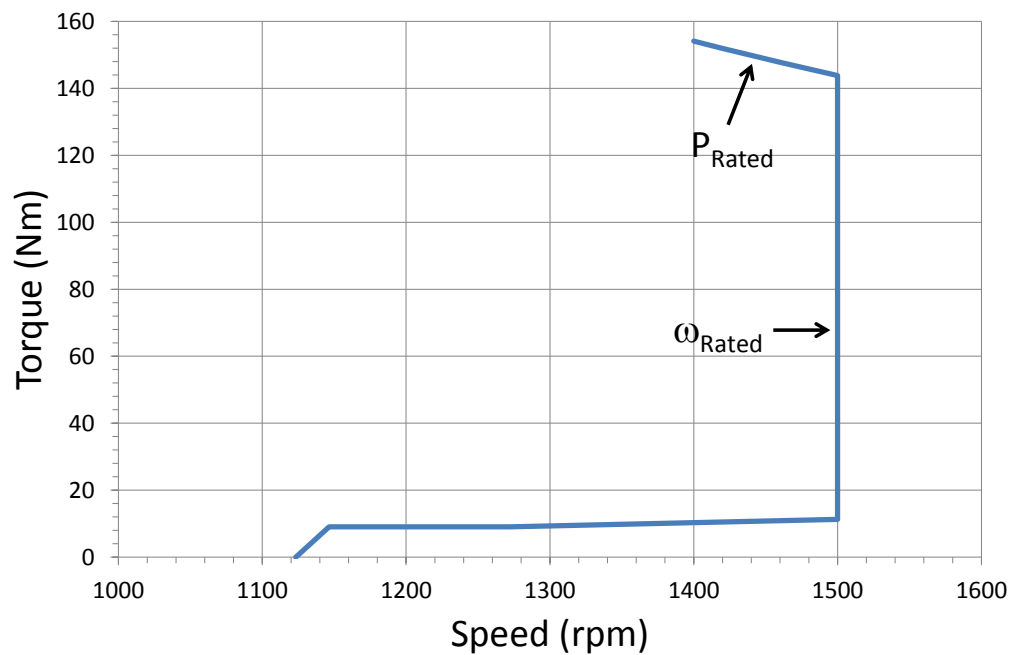
### Appendix 3A

$C_p - \lambda$  curve taken from [115].



### Appendix 3B

Estimated generator torque-speed characteristic curve taken from [115]



## LIST OF PUBLICATIONS

### Journals

1. **N. Rosmin**, S. Samsuri, M.Y. Hassan, A.H. Musta'amal and F. Hussin (2013) "Wind Turbine Power Limitation using Power Loop: Comparison between Proportional-Integral and Pole Placement Method," *International Journal of Education and Research*, volume 1, Issue 10, page 1-15.
2. **N. Rosmin**, S. Samsuri, M.Y. Hassan and H.A. Rahman (2012) "Power Control for a Small-sized Stall-regulated Variable-speed Wind Turbine using power loop and speed loop control method". *Archive Des Sciences Journal*, Volume 65, Issue 7, page 162-174.
3. **N. Rosmin**, S. Samsuri, M.Y. Hassan, A.H. Musta'amal and H.A. Rahman (2012) "Power Control for a Small-sized Stall-regulated Variable-speed Wind Turbine using speed loop control method". *Archive Des Sciences Journal*, Volume 65, Issue 7, page 567-581.
4. **N. Rosmin** and S.J.Watson (2011) "Performance analysis of indirect vector control algorithm for small-sized wind turbine induction generator", *Journal of Energy Procedia, Elsevier*, Volume 14, page 964-970.
5. **N. Rosmin**, S.J.Watson and M.Tompson (2010) "Power Limitation at High Wind Speed for a Variable Speed Fixed Pitch Wind Turbine using Close-Loop Scalar Control," *Renewable Energy & Power Quality Journal (RE & PQJ)*, No. 8, April 2010.

### Journals in submission:

1. **N. Rosmin** and S.J.Watson (2014) Review of Fixed-Pitch Wind Turbine Control: Principles, Progress and Challenges. *Renewable & Sustainable Energy Reviews, Elsevier*.
2. **N. Rosmin** and S.J.Watson (2014) Power Control for a Stall-regulated Variable-speed Wind Turbine using Internal Model Control (IMC) Design. *Renewable Energy, Elsevier*.
3. **N. Rosmin** and S.J.Watson (2014) Fixed-Speed Stall-Regulated Wind-Turbine (FSSRWT) System: modelling approach. *Energies journal*.
4. **N. Rosmin** and S.J.Watson (2014) Fixed-Speed Stall-Regulated Wind-Turbine (FSSRWT) System: validation approach. *Applied Energy, Elsevier*.
5. **N. Rosmin** and S.J.Watson (2014) Power Limitation at High Wind Speed for a Variable-Speed Fixed-Pitch Wind Turbine using Internal Model Control (IMC) Design. *IET Renewable Power Generation, Elsevier*.
6. **N. Rosmin** and S.J.Watson (2014) Integral Proportional (IP) Tuning for speed control applied to a Fixed-Pitch Wind Turbine. *IET Control Theory and Applications*.

### Conference Proceedings

1. **Rosmin, N**, Watson, S.J. and Mustaamal, A. H (2013) " Power Optimization for a Variable-speed Stall-regulated Wind-turbine using Scalar Control." *4<sup>th</sup> International Conference on Clean Electrical Power (ICCEP 2013)*, 11-13<sup>th</sup> June 2013, Alghero, Sardinia, Italy.
2. **Rosmin, N**, Manaf, M. S. A, Mustaamal, A. H and Hassan, M. Y (2013) "Does Tidal Energy using Double-Emptying Scheme has a Good Prospect in Malaysia?." *1st Malaysian Ocean Renewable Energy Symposium 2013 (MORES 2013)*, 6th June 2013, Maritime Centre, Putrajaya, Malaysia.
3. **Rosmin, N**, Watson, S.J. and Mustaamal, A. H (2013) " Stall-regulated Variable-speed Wind Turbine Simulink Model." *IEEE International Power Engineering and Optimization Conference 2013 (PEOCO 2013)*, 3-4<sup>th</sup> June 2013, Langkawi Island, Kedah, Malaysia.

4. **Rosmin, N**, S. Samsuri, Hassan, M. Y and Rahman, H. A (2012) "Power Optimization for a Small-sized Stall-regulated Variable-speed Wind Turbine". *IEEE International Power Engineering and Optimization Conference 2012 (PEOCO 2012)*, 6-7<sup>th</sup> June 2012, Melaka, Malaysia, page 373-378.
5. **Rosmin, N**, Samsuri, S and Hassan, M. Y (2012) "Comparative study on power limitation of a Stall Regulated Variable Speed Wind Turbine". *The Proceeding on Brunei International Conference on Engineering and Technology (BICET) 2012: Sustainable Development through Advances in Engineering and Technology*, 25-56<sup>th</sup> January 2012, Bandar Seri Begawan, Brunei, page 221-229.
6. **Rosmin, N** and Watson, S. J (2011) "Performance analysis of indirect vector control algorithm for small-sized wind turbine induction generator". *Proceeding on 2nd International Conference on Advanced in Energy Engineering (ICAEE 2011)*, 27-28<sup>th</sup> December 2011, Bangkok, Thailand.
7. **Rosmin, N**, Watson, S.J. and Tompson, M (2010) "Speed Control at Low Wind Speeds for a Variable Speed Fixed Pitch Wind Turbine," *Proceedings of Modelling, Identification & Control (MIC)*, Innsbruck, Austria, February, 2010.
8. **Rosmin, N**, Watson, S.J. and Tompson, M (2010) "Power Limitation at High Wind Speed for a Variable Speed Fixed Pitch Wind Turbine using Close-Loop Scalar Control," The European Association for the Development of Renewable Energies, Environment and Power Quality (EA4EPQ), *Proceeding of an International Conference on Renewable Energies and Power Quality (ICREPQ'10)*, Granada, Spain, 23<sup>th</sup> to 25<sup>th</sup> March, 2010.
9. **Rosmin, N** and Watson, S. J (2010) "Speed Control at High Wind Speeds for a Variable Speed Fixed pitch Wind turbine," *Proceeding on European Wind Energy Conference and Exhibition (EWEC)*, Warsaw, Poland, 20<sup>th</sup> to 23<sup>rd</sup> April 2010.
10. **Rosmin, N** and Watson, S.J (2010) "A comparison control strategy for variable speed, fixed-pitch stall regulated wind turbine," *Proceeding of UK- Malaysia Engineering Conference 2008(UK-MEC08)*, London, UK, 8-9 April 2010.
11. **Rosmin, N**, Watson, S.J. and Tompson, M (2009) " Power Limitation at high wind speeds for a variable speed stall-regulated fixed pitch wind turbine". *The Proceeding on The European Academy of Wind Energy: 5<sup>th</sup> PhD seminar on Wind Energy in Europe*, Durham, UK, 30 September – 1 October 2009.
12. **Rosmin, N**, Watson, S.J. and Tompson, M (2009) "Power Limitation at High Wind Speeds for a Variable Speed Fixed Pitch Stall-Regulated Wind Turbine by using Cascade Control". *International Conference: Electrical Energy and Industrial Electronic Systems (EEIES2009)*, 7-8 December 2009, Penang, Malaysia.
13. **Rosmin, N**, Watson, S.J. and Tompson, M (2008) " Stall regulated variable speed wind turbine: Control strategies, design model and analysis to improve wind turbine performance". *Proceeding on UK-Malaysia Engineering Conference 2008*, London, UK, 14-15 July 2008.

#### Book Chapter

1. **Rosmin, N**, "Speed Control at Low Wind Speeds for a Variable Speed Fixed-Pitch Wind Turbine" in *Advances in Power Engineering*, Penerbit UTM Press, Johor Bahru, Malaysia, 2013.

## REFERENCES

1. Tsili, M., and Papathanassiou, S. (2009) A review of grid code technical requirements for wind farms. *IET Renewable Power Generation*, **3**(3): p. 308-332.
2. Pepermans, G., Driesen, J., Haeseldonckx, D., Belmans, R and D'haeseleer, W. (2005) Distributed Generation: Definition, Benefits and Issues. *Energy Policy*, **33**(6): p. 787-798.
3. Jager-Waldau, A., and Arantegui, R. L. (2011) *2011 Snapshot on European Wind Energy*. European Commission, Joint Research Centre. p. 1-4.
4. Nicolas, C.V., Ramirez, D., Lafoz, M., and Iglesias, J. (2002) Guidelines for the design and control of electrical generator systems for new grid connected wind turbine generators in *28th Annual Conference of the IEEE Industrial Electronics Society 2002*, Sevilla, Spain.
5. Secretariat, R.G.C. (2012) *Grid connection code for renewable power plants (RPPs) connected to the electricity transmission system (TS) or the distribution system (DS) in South Africa*. Germiston: Eskom Transmission Division. p. 1-61.
6. Teodorescu, R., Liserre, M. and Rodriguez, P. (2011) *Grid converters for photovoltaic and wind power systems*. West Sussex, United Kingdom: John Wiley & Sons, Ltd.
7. Blaabjerg, F., Liserre, M., and Ma, K. (2012) Power Electronics Converters for Wind Turbine Systems. *IEEE Transactions on industry applications*, **48**(2): p. 708-719.
8. Blaabjerg, F., Chen F.Z., Teodorescu, R and Iov, F. (2006) Power Electronics in Wind turbine systems in *The International Power Electronics and Motion Control Conference 2006 (IPEMC 2006)*, Shanghai, China.
9. Anzum, A., and Changlani, S.S. (2013) Performance analysis of DFIG based wind farm connected to weak distribution system. *International Journal of Advanced Research in Science and Engineering*, **2**(6): p. 103-111.
10. Erlich, I., Wrede, H. , and Feltes, C. (2007) Dynamic Behavior of DFIG-Based Wind Turbines during Grid Faults in *Power Conversion Conference 2007*, Nagoya, Japan. p. 1195-1200.
11. Jha, B., and Rao, K. R. M. (2011) Compensation techniques for improving FRT capability on DFIG. *International Journal of Engineering Science and Technology (IJEST)*, **3**(1): p. 514-524.
12. European Wind Energy Association (2009) The Facts: A guide to the technology, economics and future of wind power in *Wind Energy - The Facts*. Earthscan: London.
13. Farret, F.A., and Simoes, M.G. (2006) *Integration of alternative sources of energy*. Hoboken, New Jersey: A John Wiley & Sons, Inc-IEEE Press.
14. Rahmann, C., Haubrich, H.J., Vargas, L., and Salles, M.B.C. (2009) Investigation of DFIG with Fault Ride-Through Capability in Weak Power Systems in *International Conference on Power Systems Transients 2009 (IPSTS2009)*, Kyoto, Japan.

15. Hansen, A.D., and Michalke, G. (2007) Fault Ride-Through Capability of DFIG Wind Turbines. *Renewable Energy*, **32**(9): p. 594-1610.
16. Pokharel, B., and Wenzhong, G. (2010) Mitigation of Disturbances in DFIG-based Wind Farm Connected to Weak Distribution System Using STATCOM in *North American Power Symposium (NAPS) 2010*, Arlington, Texas, USA.
17. Munteanu, L., *et.al* (2008) *Optimal Control of Wind Energy Systems*. London: Springer-Verlag London Limited.
18. Manwell, J.F., McGowen, J.G., and Rogers, A.L. (2002) *Wind Energy Explained: Theory, Design and Application*. John Wiley & Sons Ltd.
19. Spera, D.A. (2009) *Wind Turbine Technology: Fundamental Concepts of Wind Turbine Engineering, Second Edition* New York, USA: ASME Press.
20. Wagner, H.-J., and Mathur, J. (2009) *Introduction to wind energy systems: Basics, technology and operation*. Berlin;Heidelberg: Springer-Verlag
21. Tangler, J.L., and Somers, D.M. (1995) *NREL Airfoil families for HAWTs*. National Renewable Energy Laboratory Colorado. p. 1-13.
22. Klimas, P.C. (1985) *Tailored Airfoils for Vertical Axis Wind Turbines*. New Mexico: Sandia National Laboratories.
23. Rooij, R.V., and Timmer, N. (2004) *Design of Airfoils for Wind Turbine Blades*. Delft University of Technology: Netherlands.
24. Drela, M., and Giles, M. B. (1987) Viscous-inviscid analysis of transonic and low Reynolds number airfoils. *AIAA Journal*, **25**(10): p. 1347-1356.
25. Timmer, W., and van Rooy, R. (1992) Thick airfoils for HAWTs. *Wind Engineering and Industrial Aerodynamics*, **39**: p. 151-160.
26. Obayashi, S., and Takanashi, S. (1996) Genetic Optimization of Target Pressure Distributions for Inverse Design methods. *AIAA Journal*, **34**(5): p. 881-886.
27. MacPhee, D., and Beyene, A. (2011) A flexible turbine blade for passive blade pitch control in wind turbines in *IEEE Power Engineering and Automation Conference (PEAM) 2011*, Wuhan, China.
28. Botasso, C.L., Campagnolo, F., Croce, A., and Tibaldi, C. (2012) Integrating active and passive load control in wind turbines in *EWEA 2012*, Copenhagen, Denmark.
29. Senjyu, T., Ryosei, S., Urasaki, N., Funabashi, T., Fujita, H., and Sekine, H. (2006) Output power leveling of wind turbine generator for all operating regions by pitch angle control. *IEEE Transactions on Energy Conversion*, **21**(2): p. 467-475.
30. Muljadi, E., and Butterfield, C. P. (2001) Pitch-controlled variable-speed wind turbine generation. *IEEE Transactions on Industry Applications*, **37**(1): p. 240-246.
31. Polinder, H., Bang, D., van Rooij, R.P.J.O.M., McDonald, A.S., and Mueller, M. A. (2007) 10 MW wind turbine direct-drive generator design with pitch or active speed stall control in *IEEE Electric Machines & Drives Conference 2007*., McDonal, USA.
32. Muljadi, E.B., Butterfield, C.P., and Marshall L.B. J. (1997) Effect of Turbulence on Power Generation for VariableSpeed Wind Turbines in *the ASME Wind Energy Symposium 1997*, Reno, NV.

33. Murthy, S.S., Singh, B., Goel, P.K., and Tiwari, S.K. (2007) A Comparative Study of Fixed Speed and Variable Speed Wind in *7th International Conference on Power Electronics and Drive Systems*, Bangkok, Thailand.
34. World Wind Energy Association-WWEA (2011) *The World Wind Energy Association: Half-Year Report 2011*. Bonn, Germany: World Wind Energy Association. p. 1-7.
35. Bianchi, F.D., Mantz, R. J., Battista, H.D. (2007) *Wind Turbine Control System: Principles, Modelling and Gain Scheduling Design*. Springer-Verlag London Limited.
36. Leithead, W., and Connor, B. (2000) Control of variable speed wind turbine: design task. *International Journal of Control*, **73**(13): p. 1189-1212.
37. Neammanee, B., Sirisumrannukul, S., and Chatratana, S. (2010) Control Strategies for Variable-speed Fixed-pitch Wind Turbines, in *Wind Power*, Mueeen, S.M. (Ed). Croatia:InTech
38. Pierce, K.G., and Migliore, P.G. (2000) Maximizing energy capture of fixed-pitch variable-speed wind turbines in *The 38th AIAA Aerospace Sciences Meeting and Exhibition (ASME) Wind Energy Symposium*, Reno, Nevada.
39. Novak, P., Ekelund, T., Jovik, I., and Schmidtbauer, B. (1995) Modeling and control of a variable-speed wind-turbine drive system dynamics. *IEEE Control System Management*, **15**(4): p. 28-38.
40. Bianchi, F.D., Mantz, R. J., Christiansen, C. F. (2005) Gain scheduling control of variable-speed wind energy conversion systems using quasi-LPV models. *Control Engineering Practice*, **13**(2): p. 247-255.
41. Bianchi, F.D., Battista, H., and Mantz, R.J. (2007) *Wind turbine Control Systems: Principle, Modelling and Gain Scheduling Design*. Heidelberg: Springer Verlag.
42. Muljadi, E., Pierce, K., and Migliore, P. (1998) Control strategy for variable-speed stall-regulated wind turbines in *American Controls Conference 1998*, Philadelphia, PA.
43. Muljadi, E., Pierce, K., and Migliore, P. (2000) Soft-stall control for variable-speed stall-regulated wind turbines. *Journal of Wind Engineering and Industrial Aerodynamics*, **85**(3): p. 277-291.
44. Muljadi, E., Pierce, K., and Migliore, P.(2000) A conservative control strategy for variable-speed stall-regulated wind turbines in *The 19th American Society of Mechanical Engineers (ASME) Wind energy Symposium*, Reno, Nevada.
45. Salameh, Z.M. (1986) Interfacing a fixed-pitch-angle wind turbine with a double-output induction generator. *Energy*, **11**(10): p. 941-947.
46. Battista, D.H., Puleston, P.F., Mantz, R.J., Christiansen, C.F (1997) Sliding mode control of wind energy systems with DOIG- power efficiency and torsional dynamics optimization. *IEEE Transaction of Power Systems*, **15**(2): p. 728-734.
47. Peter, M., Bongers, M., and Dijkstra, S. (1992) *Control of Wind Turbine Systems for Load Reduction*. Wind Energy: Technology and Implementation in *Proceedings of the European Wind Energy Conference, EWEC*: p. 1710-1714.

48. Cardenas, R., Asher, G. M., Ray, W. F., and Pena, R. (1996) Power Limitation in variable speed wind turbines with fixed pitch angle. *IEEE Conference Publication*, **419**: p. 44-48.
49. Vihriälä, H. (2002) *Control of Variable Speed Wind Turbines*. Tampere University of Technology.
50. Boukhezzar, B., Siguerdidjane, H. (2005) *Nonlinear Control of Variable Speed Wind Turbines for Power Regulation*. in *Proceedings of the 2005 IEEE Conference on Control Applications*. 2005. Toronto, Canada.
51. Ekelund, T. (1994) Speed control of wind turbines in the stall region in *The 3rd IEEE Conference on Control Application 1994*, Glasgow, UK.: p. 227-232.
52. Leithead, W.E., and Connor, B. (1990) Dependence of performance of variable speed wind turbines on the turbulence, dynamics and control. *IEE Proceedings*, **137**(6):P. 403-413.
53. Xin-fang, Z., Da Ping, X., and Yi-bing, L. (2004) Adaptive optimal fuzzy control for variable speed fixed pitch wind turbines in *Proceedings of the 5th World Congress on Intelligent Control and Automation*, Hangzhou, China.
54. Datta, R., and Ranganathan, V.T. (2002) Variable-speed wind power generation using doubly-fed wound rotor induction machine- a comparison with alternative scheme. *IEEE Transaction on Energy Conversion*, **17**: p. 414-421.
55. Senjyu, T., Ochi, Y., Kikunaga, Y., Tokudome, M., Yona, A., Muhando, E. B., Urasaki, N., and Funabashi, T. (2009) Sensor-less maximum power point tracking control for wind generation system with squirrel cage induction generator. *Renewable Energy* **34**: p. 994-999.
56. Pournaras, A.S., Papathanassiou, S., and Kladas, A. (2004) *Robust controller for variable speed stall regulated wind turbines*. in *Proceedings ICEM'04*, Krakow, Poland.
57. Thiringer, T., and Linders, J. (1993) Control by variable rotor speed of a fixed-pitch wind turbine operating in a wide speed range. *IEEE Transactions on Energy Conversion*, **8**(3).
58. Bourlis, D. (2012) A Complete Control Scheme for Variable Speed Stall Regulated Wind Turbines in *Fundamental and Advanced Topics in Wind Power*, Leicester. p. 300-338.
59. Arnaltes, S. (2003) Comparison of variable-speed wind turbine control strategies in *International Conference on Renewable Energies and Power Quality*, Vigo, Spain.
60. Novak, P., Ekelund, T., Jovik, I., and Schmidtbauer, B. (1995) Modeling and control of a variable-speed wind-turbine drive system dynamics. , **15** **4**: p. 28-38.
61. Pao, L.Y., and Johnson, K. E. (2009) A Tutorial on the Dynamics and Control of Wind Turbines and Wind Farms in *American Control Conference*, St. Louis, MO
62. Battaiotto, P.E., R.J. Mantz, and P.F. Puleston. (1996) A wind turbine emulator based on a dual DSP processor system. *Control Engineering Practice*, **4**(9): p. 1261-1266.
63. Bossanyi, E.A. (2000) The Design of Closed Loop Controllers for Wind Turbines. *Wind Energy*, **3**: p. 149-163.

64. Dam, J.V., Jacobson, E., Link, H., and Wilde, S (2003) *Wind turbine generator system safety and function test report for the Atlantic Orient 15/50 wind turbine*[Pdf]. National Wind Technology Center, National Renewable Energy Laboratory: Cole Boulevard, Colorado. p. 1-19.
65. Morren, J., J. Pierik, and S.W.H. de Haan. (2006) Inertial response of variable speed wind turbines. *Electric Power Systems Research*, **76**(11): p. 980-987.
66. Tielens, P., and Dirk, V. H. (2012) Grid Inertia and Frequency Control in Power Systems with High Penetration of Renewables in *Young Researchers Symposium in Electrical Power Engineering*, Delft, Netherlands.
67. Leithead, W.E., and Connor, B. (2000) Control of variable speed wind turbines: dynamic models. *International Journal of Control*, **73**(13): p. 1173-1188.
68. Jonas, N.H., Nygaard, T. A., and Duque, E. P. N. (2004) Passive Pitch Control of Small Horizontal Axis Wind Turbines in *42nd AIAA Aerospace Sciences Meeting and Exhibit*, Reno, Nevada.
69. Crowder, R. (2006) *Electric Drives and Electromechanical Systems*. Great Britain: Elsevier.
70. Albers, A., and Gerhard, D. (1999) Wind Farm Performance Verification in *DEWI Magazine Nr.* p. 1-10.
71. Maria, A. (1997) Introduction to Modelling and Simulation. in *Winter Simulation Conference*, Atlanta, GA, USA.
72. Bose, B. (2002) *Modern power electronics and AC drives*. Upper Saddle River, NJ: Prentice Hall, Inc.
73. Razzaghi, K., Jalali, A. A. (2011) A New Approach on Stabilization Control of an Inverted Pendulum using PID Controller in *International Conference on Control, Robotics and Cybernetics*, New Delhi, India. p. 1-6.
74. Rani, M.R., Selamat, H., Zamzuri, H and Ahmad, F. (2011) PID Controller Optimization for a Rotational Inverted Pendulum using Genetic Algorithm in *Modelling, Simulation and Applied Optimization 2011*, Kuala Lumpur, Malaysia. p. 1-6.
75. Ackermann, T. (2005) *Wind Power in Power Systems*. City: John Wiley & Sons.
76. Tang, C., Pathmanathan, M, Soong, W. L., and Ertugrul, N (2008) Effects of Inertia on Dynamic Performance of Wind Turbines in *Australasian Universities Power Engineering Conference (AUPEC 08)*, Sydney, New South Wales, Australia.
77. Chouhan, H., Kumawat, R., and Verma, H.K. (2012) Comparative analysis of scalar and vector control induction machine drive through modeling and simulation. *International Journal of Electrical Engineering and Technology (IJEET)*, **3**(2): p. 39-50.
78. Srilad, S., Tunyasrirut, S., and Shuksri, T. (2006) Implementation of a scalar controlled induction motor drives in *SICE-ICASE International Joint Conference 2006*, Bexco, Busan, Korea. p. 1-6.
79. Mallesham, G, Ramana, K. B. V. (2007) Improvement in Dynamic Response of Electrical Machines with PID and Fuzzy Logic Based Controllers in *Proceedings of the World Congress on Engineering and Computer Science 2007*, San Francisco, USA.

80. Rancilio. *What is a temperature PID control doing for the Rancilio Silvia Espresso Machine?* . [Assessed on 4th July 2013]; Available from: [http://www.pidsilvia.com/What\\_is\\_PID.htm](http://www.pidsilvia.com/What_is_PID.htm).
81. Archana, D., Kalyani, K., Prasad, B. S. (2012) Efficiency Optimization Control of Induction Motor Using Fuzzy Logic. *International Journal of Soft Computing and Engineering (IJSCE)*, **2**(3): p. 327-332.
82. Simoes, M.G., Farret, F.A. (2008) *Alternative Energy Systems:Design and Analysis with Induction Generators*, Second Edition. Boca Raton, Florida, United States: CRC Press,Taylor & Francis Group.
83. Krein, P.T., Disilvestro, F., Kanellakopoulos, F., Loannis., and Locker, J. (1993) Comparative analysis of scalar and vector control methods for induction motors in *24th Annual IEEE Power Electronics Specialists Conference*, Seattle, WA.
84. Ohyama, K., Arinaga, S., and Shigemizu, T. (2007) Sensorless Vector Controlled Converter for Variable Speed Wind Generation System Using an Induction Generator. *Electrical Engineering in Japan*, **159**(4): p. 62-75.
85. Idjdarene, K., Rekioua, D., Rekioua, T., and Tounzi, A (2008) Vector control of autonomous induction generator taking saturation effect into account. *Energy Conversion and Management*, **49**(10): p. 2609-2617.
86. Cardenas, R., Pena, R., Asher, G., and Clare, J. (2001) Control Strategies for Enhanced Power Smoothing in Wind Energy Systems Using a Flywheel Driven by a Vector-Controlled Induction Machine. *IEEE Transactions on Industrial Electronics*, **48**(3): p. 625 - 635
87. Babu, B.C., and Mohanty, K.B (2010) Doubly-Fed Induction Generator for Variable Speed Wind Energy Conversion Systems- Modeling & Simulation. *Journal of Computer and Electrical Engineering*, **2**(1): p. 1793-8163.
88. Mugica, M.S., Urkiola, A. M., Vidal, M. R., and Redondo, R. R. (2004) Comparison of dynamic models for wind turbine grid integration studies in *European Wind Energy Conference 2004*, London, United Kingdom.
89. Davijani, H.K., Sheikholeslami, A., Livani, H., and Davijani, M. K. (2009) Fuzzy Logic Control of Doubly Fed Induction Generator Wind Turbine. *World Applied Science Journal*, **6**(4): p. 499-508.
90. Ibrahim, A. (2009) Vector control of current regulated inverter connected to grid for wind energy applications. *International Journal of Renewable Energy Technology*, **1**(1): p. 17-28.
91. Xu, H., Zhang, W., Nian, H., and Li, N. *Improved vector control of DFIG based wind turbine during grid dips and swells*. in *International conference on Electrical Machines and Systems 2010 (ICEMS 2010)*, Incheon, South Korea.
92. Thakre, K. (2009) *Dynamic performance of DFIG wind turbine under unbalance grid fault condition* .Rourkela: National Institute of Technology.
93. Rosmin, N., Watson, S. J., and Mustaamal, A. H. (2013) Power Optimization for a Variable-speed Stall-regulated Wind-turbine using Scalar Control in *International Conference on Clean Electrical Power (ICCEP) 2013*, Alghero, Sardinia, Italy.
94. Onea, A., Horga, V., and Ratoi, M. (2006) Indirect vector control of induction motor in *The 6th International Conference on Simulation, Modelling and Optimization 2006*, Lisbon, Portugal.
95. Rashid, M.H. (2010) *Power Electronics Handbook*. Second Edition. USA: Elsevier Science.

96. Zaragoza, J., Pou, J., Arias, A., Spiteri, C., Robles, E and Ceballos, S. (2011) Study and experimental verification of control tuning strategies in a variable speed wind energy conversion system. *Renewable energy*, **36**: p. 1421-1430.
97. Hillston, J. (2012) *Performance Modelling*. Edinburgh: University of Edinburgh.
98. Arduino. *LINUSBot - Line Follower Robot - with PID control*. [Assessed on 4th July 2013]; Available from: <http://www.instructables.com/id/LINUSBot-Line-Follower-Robot-with-PID-control/>.
99. Wolff, E.A., and Skogestad, S. (1996) Process Design and Control: Temperature cascade control of distillation columns. *Industrial Engineering Chemical Res*, **35**: p. 475-484.
100. Raptis, I.A., Valaanis, K. P. (2011) *Review of Linear and Nonlinear Controller Designs in Linear and Nonlinear Control of Small-Scale Unmanned Helicopters*. Springer: London. p. 13-19.
101. Gohardani, A.S. (2013) A synergistic glance at the prospects of distributed propulsion technology and the electric aircraft concept for future unmanned airvehicles and commercial/military aviation. *Progress in Aerospace Sciences*, **57**: p. 25-70.
102. Boukhezzar, B.A.S. (2009) Comparison Between Linear Strategies for Variable Speed Wind Turbine Power Capture optimization in *Ecologic Vehicles Renewable Energies*, Monaco. p. 1-8.
103. Okoro, O.I. (2003) Steady state and transient analysis of induction motor driving a pump load. *Nigerian Journal of Technology*, **22**(1): p. 46-53.
104. Spakovszky, Z.S. (2002) *Definitions and Fundamental Ideas of Thermodynamics*. [Assessed on 4th July 2013]; Available from: <http://web.mit.edu/16.unified/www/FALL/thermodynamics/notes/node11.html>.
105. Pace, D.K. (2004) Modeling and Simulation Verification and Validation Challenges in *Johns Hopkins Apl Technical Digest*. p. 163-173.
106. Muyeen, S.M., Tamura, J., and Murata, T. (2010) *Stability augmentation of a grid-connected wind farm*. London: Springer.
107. Muljadi, E., Gevorgian, V., Singh, M., and Santoso, S. (2012) Understanding Inertial and Frequency Response of Wind Power Plants in *IEEE Symposium on Power Electronics and Machines in Wind Applications*. Denver, Colorado.
108. Dukkupati, R.V. (2006) *Analysis and Design of Control Systems using MATLAB*. New Delhi: New Age International (P) Limited.
109. Billy, M.E., Senjyu, T., Urasaki, N., Yona, A., Kinjo, H., and Funabashi, T. (2007) Gain scheduling control of variable speed WTG under widely varying turbulence loading. *Renewable Energy*, **32**(14): p. 2407-2423.
110. Weather2.com. *Local Weather Forecast. Country Overview for United Kingdom. Yearly Trends: Weather average & Extreme*. [Assessed on 31th October 2013]; Available from: [www.myweather2.com?City-Town?United-Kingdom?Leicestershire?Loughborough?climate-profile.aspx](http://www.myweather2.com?City-Town?United-Kingdom?Leicestershire?Loughborough?climate-profile.aspx).
111. Eldoradoweather. *Your source for world weather*. [Assessed on 31th October 2013]; Available from:

[www.edldoradocountyweather.com/forecast/Enngland?L?Loughborough?Loughborough.html](http://www.edldoradocountyweather.com/forecast/Enngland?L?Loughborough?Loughborough.html).

112. Barton, J.P., *A probabilistic method of modelling energy storage in electricity systems with intermittent renewable energy*, in *Electronic and Electrical Engineering*. 2007, Loughborough University, United Kingdom: Loughborough.
113. Barth, V., *Micrositing using Rotor Equivalent Wind Speed – One Step Forward or Aside?*, in *Dewi Magaziner*. 2014, p. 1-10.
114. Ray, M.L., Rogers, A. L., and McGowan, J. G. *Analysis of wind shear models and trends in different terrains in American Wind Energy Association Windpower 2006*. 2006. Pittsburgh, PA, USA.
115. Harson, A.H., *Modelling of vibration in a 25 kW wind turbine*. 2012, Loughborough University: Loughborough. p. 1-16.
116. Gammon, R. (2006) *The integration of hydrogen energy storage with renewable energy systems*, in *Department of Eletronics and Electrical*. Loughborough University: Loughborough.
117. Muyeen, S.M., Ali, M.H., Takahashi, R., Murata, T., Tamura, J., Tomaki, Y., Sakahara, A., Sasano, E. (2007) Comparative study on transient stability analysis of WT generator system using different drive train models. *IET Renewable Power Generation*, **1**(2): p. 131-141.
118. Muyeen, S.M., Hasan Ali, Md., Takahashi, R., Murata, T., Tamura, J., Tomaki, Y., Sakahara, A., Sasano, E. (2006) Transient stability analysis of wind generator by using six-mass drive train model in *The 2006 International Conference. on Electrical Machines and Systems (ICEMS 2006)*, Nagasaki, Japan.
119. Muyeen, S.M., Mannan, M.A., Ali, M.A., Takahashi, R., Murata, T., Tamura, J., Tomaki, Y., Sakahara, A., Sasano, E. (2006) Fault Analysis of Wind Turbine Generator System Considering Six-Mass Drive Train Model in *4th International Conference on Electrical and Computer Engineering (ICECE 2006)*, Dhaka, Bangladesh.
120. Thiringer, T. (1996) *Power quality measurements performed on a low-voltage grid equipped with two wind turbines*. *IEEE Trans. Energy Converters*, **11**(3): p. 601-606.
121. Papathanassiou, S.A., Papadopoulos, M.P. (2001) Mechanical stresses in fixed speed wind turbines due to network disturbances. *IEEE Trans. Energy Converters*, **16**(4): p. 361-367.
122. Rabelo, B., Hoftman, W., and Gluck, M. (2004) Emulation of the static and dynamic behaviour of a wind-turbine with a DC-Machine in *35th Annual IEEE Power Electronics Specialists Conference 2004*, Aachen, Germany.
123. Wu, S., *Development and validation of machinery health monitoring, diagnostic and prognostic methodology and tools*. 2007, Ann Arbor: ProQuest Information and Learning Company.
124. Rao, J.S (2004). *Rotor dynamics*. Third ed. 2004, New Delhi: New Age International (P) Limited.
125. Lesieutre, G.A., and Kauffman, J. L. (2013) A Viscous `Geometric' Beam Damping Model for Nearly Constant Modal Damping. *AIAA Journal*, **5**(7): p. 1688-1694.
126. Takacs, G., and Rohal, B.(2012) Basics of vibration dynamics in *Model Predictive Vibration Control*. Springer-Verlag London Limited: London.

127. Adamson, S. (2004) Improved Approaches to the Measurement and Analysis of Torsional Vibration in *SAE 2004 World Congress and Exhibition*, Rotec GmbH. p. 23-32.
128. Martins, M., Perdana, A., Ledesma, P., Agneholm, E., and Carlson, O. (2007) Validation of fixed speed wind turbine dynamic models with measured data. *Renewable Energy*, **32**: p. 1301-1316.
129. Marino, R., Tomei, P and Verreli, C. M. (2010) *Induction Motor Control Design*. London: Springer-Verlag.
130. Rasila, M. (2003) *Torque- and Speed Control of a Pitch Regulated Wind Turbine*. Chalmers University of Technology: Goteborg, Sweden. p. 61-7.
131. Barton, J.P. (2012) *Vibration analysis of gearbox and generator of a 25 kW wind turbine*. Supergen Meeting Presentation.
132. Perahia, J., and Nayar, C. V. (1994) Simulation of a fixed-pitch wind turbine powered induction generator in EMTP. *International Journal of Electrical Engineering Education*, **31**: p. 362-374.
133. Elert, G. (2008) *The Physics Hypertextbook*. [Assessed on 10th September 2008 ]; Available from: <http://hypertextbook.com/physics/mechanics/rotational-inertia/>.
134. *List of moments of inertia*. [Assessed on 14th September 2008]; Available from: [http://en.wikipedia.org/wiki/List\\_of\\_moments\\_of\\_inertia](http://en.wikipedia.org/wiki/List_of_moments_of_inertia).
135. *Carter Wind System Model 25*. (1982), Burkburnett: Texas.
136. Vas, P. (1998) *Sensorless vector and direct torque control*. Tokyo, Japan: Oxford University Press.
137. Kemsley, R. (2002) *Inverter Configurations for Stand Alone Wind Turbines*. University of Loughborough.
138. Sen, P.C. (1997) *Principles of electric machines and power electronics*. Second Edition. , USA.
139. Akbaba, M., Taleb, M., and Rumeli, A. (1995) Improved estimation of induction machine parameters. *Electric Power System Research*, **34**: p. 65-73.
140. Daut, I., Anayet, K, Irwanto, M., Gomesh, N., Muzhar, M., Asri, M., and Syatirah. (2009) Parameters calculation of 5 HP AC Induction motor in *International conference on Applications in mechanical Engineering and design 2009 (ICADME 2009)*,. Batu Ferringhi, Penang, Malaysia.
141. Haque, M.H. (1993) Estimation of three-phase induction motor parameters. *Electric Power System Research*, **26**: p. 187-193.
142. Trzynadlowski, A.M. (2001) *Control of induction motors*. 2001, United State of America: Academic Press.
143. Ozyurt, C.H. (2005) *Parameter and speed estimation of induction motors from manufacturers data and measurements*, in *The Graduate School of Natural and Applied Science, Department of Electrical and Electronics Engineering*. The Middle East Technical University.
144. Kleijnen, J.P.C. (1995) Verification and validation of simulation models. *European Journal of Operational Research*, **82**: p. 145-162.
145. Barton, J.P.(2013) *Reason why operating frequency of Carter turbine is changed from 50 Hz to 43.5 Hz*. Loughborough, UK.
146. Muljadi, E., Singh, M., and Gevorgian, V. (2013) Fixed-Speed and Variable-Slip Wind Turbines Providing Spinning Reserves to the Grid in *IEEE Power and Energy Society*. Vancouver, British Columbia.

147. Sørensen, P., Hansen, A, Janosi, L., Bech, J., and and B. Bak-Jensen. (2001) *Simulation of Interaction between wind farm and power system*. Risø National Laboratory, Roskilde: Denmark. p. 1-66.
148. Melfi, M.J. (1995) Application and Selection of Adjustable Speed Motors to Optimize Spares in *Pulp and Paper Industry Technical Conference*. Vancouver, BC, Canada: IEEE.
149. Leithead, W.A.E.A. (1990) *Wind Turbine Modelling and Control*. University of Strathclyde: Glasgow.
150. Xu, Z., Hu, Q., and Ehsani, M. (2012) Estimation of Effective Wind Speed for Fixed-Speed Wind Turbines Based on Frequency Domain Data Fusion. *IEEE Transactions on Sustainable Energy*, **3**(1): p. 57-64.
151. Fischer, B. (2013) Reducing rotor speed variations of floating wind turbines by compensation of non-minimum phase zeros. *IET Renewable Power Generation*, **7**(4): p. 413-419.
152. Anaya-Lara, O., Jenkins, N., Ekanayake, J., Cartwright, P., and Hughes, M. (2009) *Wind Energy Generation: Modelling and control*. West Sussex: John Wiley & Sons, Ltd.
153. Barton, J.P., and Watson, S. J. (2012) Analysis of electrical power data for condition monitoring of a small wind turbine. *IET Renewable Power Generation*, **7**(4): p. 341 - 349.
154. Qiao, W., Zhou, W., Aller, J. M., and Harley, R. G. (2008) Wind Speed Estimation Based Sensorless Output Maximization Control for a Wind Turbine Driving a DFIG. *IEEE Transactions on Power Electronics*, **23**(3): p. 1156-1169.
155. Walker, D.N. (2003) *Torsional vibration of turbomachinery*. USA: McGraw Hill Professional.
156. Blaabjerg, F., Chen, Z., Teodorescu, R., and Iov, F. (2006) Power Electronics in Wind turbine systems,, in *CES/IEEE 5th International Power Electronics and Motion Control Conference (IPEMC 2006)*.. Shanghai, China.
157. Kohlrusz, G., and Fodor, D. (2011) Comparison of scalar and vector control strategies of induction motors. *Hungarian Journal of Industrial Chemistry VESZPREM*. **39**(2): p. 265-270.
158. Nayar, C.V., and Bundell, J. H. (1987) Output Power Controller for a Wind-Driven Induction Generator in *IEEE Transactions on Aerospace and Electronic Systems* (AES). **23**(3): p. 388-401.
159. Viramontes, E. (2010) BLDC Motor Control with Hall Effect sensors using the 90S08MP, in *Systems and Applications Engineering*. Freescale Technical Support. p. 1-13.
160. Dominguez-Garcia, J.L., Gomis-Bellmunt, O., Trilla-Romero, L., Junyent-Ferre. (2010) A Vector Control of Squirrel Cage Induction Generator for Wind Power, in *International Conference on Electrical Machines (ICEM 2010)*, Rome, Italy.
161. Chengaiah, C., and Prasad, I. S. (2013) Performance of induction motor drive by indirect vector controlled method using pi and Fuzy controllers. *International Journal of Science, Environment and Technology*. **2**(3): p. 457-469.
162. Nise, N.S. (1995) *Control Systems Engineering*. Second Edition The Benjamin/Cummings Publishing Company, Inc.

163. Boyle, G. (2001) Power for a Sustainable Future. *Renewable Energy*. **19**(6): p. 603-626.
164. Fox B, F.D., Bryans L, Jenkins L, Milborrow D, O'Malley M, Watson R and Anaya-Lara, O. (2007) *Wind Power Integration: Connection and system operational aspects*. London: The Institution of Engineering and Technology.
165. Woolf, P. (2013) *Control Architectures Feed Forward, Feedback, Ratio, and Cascade*. University Michigan: Michigan.
166. Skogestad, S., and Postlethwaite, I. (2005) *Multivariable Feedback Control: Analysis and Design*. Singapore: John Wiley & Sons.
167. Basilio, J.C., and Matos, S. R. (2002) Design of PI and PID Controllers with Transient Performance Specification. *IEEE Transactions on Education*. **45**(4).
168. Lee, Y., Skliar, M., and Lee, M (2006) Analytical method of PID controller design for parallel cascade control. *Journal of Process Control*. **16**: p. 809-818.
169. Saxena, S., and Hote, Y. V.(2012) Advances in Internal Model Control Technique: A Review and Future Prospects. *IETE Tech Rev* **29**: p. 461-472.
170. Rivera, D.E., Morari, M., and Skogestad, S. (1999) *Internal Model Control: A Comprehensive Review*. Arizona State University: Arizona. p. 1-12.
171. Rivera, D.E., Morari, M., and Skogestad, S. (1986) Internal Model Control. 4. PID controller Design. *Industrial Engineering Chemical Process Des. Dev.* **25**: p. 252-265.
172. Tham, T.(2002), *Internal Model Control*., New Castle University. p. 1-9.
173. Vilanova, R.(2008) MC based Robust PID Design: Tuning guidelines and automatic tuning. *Journal of Process Control*. **18**: p. 61-70.
174. Jeng, J.-C., and Lee, M-W. (2012) Identification and Controller Tuning of Cascade Control Systems Based on Closed-Loop Step Responses. in *The 8th IFAC Symposium on Advanced Control of Chemical Processes, The International Federation of Automatic Control*., Furama Riverfront, Singapore.
175. Shahrokhi, M., and Zomorodi, A. (2012) *Comparison of PID Controller Tuning Methods*. 2012 [Assessed on 18th January 2014]; Available from: <http://ieeexplore.ieee.org/stamp/stamp.jsp?tp=&arnumber=6618130>.
176. Zanjani, M.A., Shahgholian, G. H., and Eshtehardiha, S. (2007) Gain Tuning PID and IP Controller with an Adaptive Controller Based on the Genetic Algorithm for Improvement Operation of STATCOM. in *7th WSEAS International Conference on Electric Power Systems, High Voltages, Electric Machines 2007*. Venice, Italy.
177. Jayachandra, P., and Dilip, K. M (2012) A comparison of multi-loop PI/PID controller design with reduction and without reduction technique. *International Journal of Instrumentation, Control and automation (IJICA)*. **1**(3): p. 91-96.
178. Lee, M., Shamsuzzoha, M., and Vu, T. N. L. *IMC-PID Approach: An Effective Way to Get an Analytical Design of Robust PID Controller*. in *International Conference on Control, Automation and Systems 2008*. 2008. COEX, Seoul, Korea.

179. Jeng, J.-C., and Lee, M-W. *Identification and Controller Tuning of Cascade Control Systems Based on Closed-Loop Step Responses*. in *The 8th IFAC Symposium on Advanced Control of Chemical Processes*. 2012. The International Federation of Automatic Control, Furama Riverfront, Singapore.
180. Skogestad, S.,(2003) Simple analytic rules for model reduction and PID controller tuning. *Journal of Process Control*. **13**: p. 291-309.
181. Astrom, K.J. *Control System Design*. 2002, University of California: Santa Barbara. p. 269.
182. Ali, A., and Majhi, S,(2009) PI/PID controller design based on IMC and percentage overshoot specification to controller setpoint change. *ISA Transactions*, . **48**: p. 10-15.
183. Tavakoli, S., Griffin, I., and Fleming, P. J. (2005) Robust PI controller for load disturbance rejection and setpoint regulation. in *IEEE Conference on Control Applications 2005*, Toronto, Canada.